Fundamental study of plasma-catalytic surface interactions for CO2 conversion andapplication of fluidized bed reactors

Carolina Garcia Soto

INSTITUT POLYTECHNIQUE DE PARIS

NNT : 2023IPPAX039

Thèse de doctorat

Fundamental study of plasma-catalytic surface interactions for CO_2 conversion and application of fluidized bed reactors

Thèse de doctorat de l'Institut Polytechnique de Paris et l'Université de Bucarest préparée à l'École polytechnique

École doctorale n°626 École doctorale de l'Institut Polytechnique de Paris (EDIPP)
Spécialité de doctorat : Optique, Laser et Plasma

Thèse présentée et soutenue à Palaiseau, le 28/04/2023, par

CAROLINA ALEJANDRA GARCIA SOTO

Composition du Jury :

Dr. François Ozanam Dir. de recherche CNRS, Ecole Polytechnique, France	Président
Dr. Frédéric Thibault-Starzyk Dir. de recherche CNRS, ENSICAEN, Université de Caen, France	Rapporteur
Dr. Maria Victoria Navarro Lopez Tenure Researcher, Instituto de Carboquimica, CSIC, Spain	Rapporteur
Dr. Vasco Guerra Associate Professor, Instituto de Plasmas e Fusão Nuclear, Instituto Superior Técnico, Portugal	Examinateur
Dr. Maria del Carmen Bacariza Rey Researcher, Instituto Superior Técnico, Portugal	Examinateur
Prof. Camelia Bala Professor, University of Bucharest, Romania	Examinateur
Dr. Olivier Guaitella Ing. de recherche, École polytechnique, LPP, France	Directeur de thèse
Prof. Vasile I. Parvulescu Professor, MC Romanian Academy, University of Bucharest, Romania	Co-directeur de thèse

Fundamental study of plasma-catalytic surface interactions for CO_2 conversion and application of fluidized bed reactors

Carolina Alejandra Garcia Soto

Supervisor: Dr. Olivier Guaitella
Co-Supervisor: Prof. Vasile I. Parvulescu

A thesis presented for the degree of
Doctor of Philosophy, (Physics and Chemistry)

Laboratoire de Physique des Plasmas
Ecole Polytechnique
Institute Polytechnique de Paris

Department of Organic Chemistry,
Biochemistry and Catalysis
University of Bucharest

This project has received funding from the European Union's Horizon 2020 research and innovation programme under the Marie Skłodowska-Curie grant agreement No. 813393.

RÉSUMÉ

Le réchauffement climatique est attribué en premier lieu aux émissions de dioxyde de carbone (CO_2). Plusieurs stratégies sont explorées pour fermer le cycle du carbone en transformant le CO_2 en combustibles synthétiques. Les plasmas froids peuvent fournir un environnement unique, hors équilibre, permettant la conversion du CO_2 avec un coût énergétique minimal, mais avec une mauvaise sélectivité. Le couplage du plasma avec un matériau catalytique pourrait offrir un avantage significatif en améliorant sélectivité et performances de conversion. Les réacteurs à lit fluidisé sont un moyen innovant d'associer un plasma et un catalyseur pour la conversion du CO_2. Ils permettent d'augmenter la surface de contact avec le plasma et améliorent le transfert de chaleur. Ce travail consiste d'une part à étudier l'interaction plasma/catalyseur d'un point de vue fondamental, et d'autre part à comprendre les mécanismes spécifiques qui peuvent intervenir dans une configuration de réacteur plasma à lit fluidisé afin d'en améliorer les performances.

Si le plasma peut fournir des espèces réactives pour déclencher une réaction chimique sur la surface catalytique, le catalyseur peut également affecter le développement du plasma. Pour comprendre la complexité de cette interaction mutuelle, des expériences dédiées à basse pression permettant des mesures résolues en temps des espèces adsorbées et en phase gaz ont été réalisées avant d'analyser les performances de réacteurs à pression atmosphérique.

Des décharges de type " glow " à basse pression (1-6 mbar) ont d'abord été utilisées en raison de leur homogénéité. Les réactions de surface catalysées par le plasma ont été étudiées en détail sur CeO_2 pendant l'exposition au plasma de CO_2 seul, puis de CO_2-CH_4 par des mesures *in situ* de FTIR en transmission. Des carbonates ont été identifiés lors de l'exposition au plasma de CO_2. Le phénomène de "désorption assistée par plasma" a été clarifié en identifiant trois contributions principales : l'augmentation de température, les variations de pressions partielles, mais aussi l'effet des espèces excitées à courte durée de vie uniquement possible sous exposition à un plasma. Les mêmes études sous plasma de CO_2-CH_4 mettent en évidence la formation de formates par réaction entre les carbonates et les hydroxyles adsorbés à la surface de CeO_2. Ce même mécanisme est suggéré par des expériences *ex situ* réalisées à l'Université de Bucarest en utilisant un réacteur à décharge à barrière diélectrique (DBD) à pression atmosphérique. Ces résultats posent les bases de l'identification des mécanismes permettant d'améliorer les catalyseurs adaptés à la conversion du CO_2.

L'étude de l'interaction d'un matériau catalytique avec un plasma de CO_2 en lit fluidisé a également été réalisée d'abord dans un réacteur de décharge glow à basse pression avant d'examiner les performances d'une DBD avec lit fluidisé à pression atmosphérique. La "glow-lit fluidisé" a été étudiée avec et sans particules d'Al_2O_3 par spectroscopie d'émission optique. L'interaction d'un matériau chimiquement inerte dans la zone de décharge permet de mettre en évidence l'influence de particules diélectriques sur les propriétés du plasma. Les résultats indiquent une diminution de la densité d'atomes d'oxygène par la fluidisation d'Al_2O_3, probablement en raison d'une augmentation de la surface disponible où O se recombine en O_2, permettant d'éviter la reformation de CO_2. Dans le même temps, la concentration de CO augmente, ce qui est confirmé par mesure FTIR en aval du réacteur. La température rotationelle du système Angström de CO a aussi été mesurée. La température n'augmente pas dans le lit fluidisé bien que la présence de particules d'Al_2O_3 tend à confiner le plasma dans l'espace. Cette augmentation des performances est également observée dans la DBD à la pression atmosphérique en comparant le lit fluidisé à une configuration dite de " packed bed ". Même sans activité catalytique, Al_2O_3 a donc un effet physique qui modifie la chimie du plasma et améliore la conversion du CO_2.

En comparant les décharges à basse pression, qui permettent des mesures *in situ*, aux performances

des réacteurs à pression atmosphérique, ce travail a pu mettre en évidence le rôle des états excités produits par le plasma sur la réactivité à la surface du catalyseur, et l'influence de la présence de particules diélectriques sur la conversion du CO_2 dans le plasma lui-même. Les spécificités du couplage plasma/catalyseur et les avantages qu'elles peuvent apporter pour une conversion efficace du CO_2 ont ainsi pu être identifiées pour permettre l'optimisation future des réacteurs plasma à lit fluidisé, qui s'avèrent très prometteurs.

ABSTRACT

The increase in global temperature is attributed to the greenhouse gas effect especially from carbon dioxide (CO_2) emissions. Several strategies are explored to close the carbon cycle either by transforming CO_2 into platform molecules or synthetic fuels. Non-thermal plasmas can provide a peculiar environment out of equilibrium allowing for CO_2 conversion with minimal energy cost, but they are poorly selective. Therefore, coupling the plasma with a catalytic material could offer a significant advantage by improving the conversion performance and the selectivity. Fluidized bed (FB) reactors are an innovative way to combine a plasma and a catalyst for CO_2 conversion. FB increase the surface contact area with the gas/plasma phase and improve the heat transfer to improve CO_2 dissociation. This work consists on the one hand of studying the plasma/catalyst interaction from a fundamental point of view, and on the other hand of understanding the specific mechanisms that can intervene in a fluidized bed plasma reactor configuration in order to ultimately improve its performance.

If the plasma can provide reactive species to trigger chemical reaction on the catalytic surface, the catalyst can also affect the plasma development. To understand the complexity of this mutual interaction dedicated experiments at low pressure allowing for time resolved measurements of both adsorbed and gas phase species were first performed before analyzing the performances of atmospheric pressure reactors.

DC glow discharges at low pressure (1-6 mbar) were first used due to the homogeneity of the plasma and the previous plasma kinetic studies done in similar configuration. The plasma-catalytic surface reactions were studied in detail on CeO_2 during CO_2 only and CO_2-CH_4 plasma by *in situ* FTIR transmission experiments. Carbonates species were identified upon exposure to CO_2 gas. During CO_2 plasma exposure, the phenomenon of "plasma-assisted desorption" was further clarified by identifying three main contributions: increase in temperature, variations in partial pressures but also effect of short live excited species specific to plasma exposure. The same studies under CO_2-CH_4 plasma highlight the formation of formates by reaction between carbonates and hydroxyls adsorbed on the surface of CeO_2. This same mechanism is suggested by *ex situ* experiments carried out at the University of Bucharest using a Dielectric Barrier Discharge (DBD) reactor at atmospheric pressure and DRIFTS for surface analysis. These results lay the groundwork for identifying the type of reaction mechanism that would improve catalysts suitable for CO_2 conversion.

The study of CO_2 plasma interacting with a fluidizing catalytic material has also been done first in a DC glow discharge-FB reactor before looking at the performance of a FB-DBD at atmospheric pressure. The FB-glow discharge was investigated with and without Al_2O_3 particles with aid of Optical Emission Spectroscopy. The interaction of a chemically inert material in the discharge zone has a special interest to highlight the influence of the particles on the properties of the plasma. The results indicate a decay in Oxygen atom density through the fluidization of Al_2O_3 probably to an increase in the available surface where O recombine into O_2 potentially preventing the reverse reaction. At the same time, the CO concentration increases, which is confirmed by FTIR spectroscopy analysis of the downstream gas. In addition, temperature of rotation was calculated by CO Angstrom system. The temperature does not increase significantly although the presence of Al_2O_3 particles seems to constrain the plasma spatially. This increase in performance is also observed in DBD at atmospheric pressure comparing fluidized bed to a packed bed configuration under the same conditions. Even without catalytic activity, Al_2O_3 has a physical effect modifying the chemistry and therefore, improving the conversion of CO_2.

By comparing low-pressure discharges, which allow *in situ* measurements, with the performance of atmospheric pressure reactors, this work was able to highlight the role of the excited states produced by the plasma on the reactivity on the surface of the catalyst, and the influence of the presence of dielectric

particles on the conversion of CO_2 in the plasma itself. The specificities of the plasma/catalyst coupling and the advantages they can bring for an efficient conversion of CO_2 could thus be identified to allow future optimization of fluidized bed plasma reactors, which are proving very promising.

List of publications and oral presentations

Papers

- C. A. Garcia-Soto, E. Baratte, T. Silva, V. Guerra, V. I. Parvulescu and O. Guaitella. "CO_2/CH_4 glow discharge plasma. Part II: Study of plasma catalysis interaction mechanisms on CeO_2". Plasma Chemistry and Plasma Processing. *(Submitted)*
- E. Baratte, C. A. Garcia-Soto, T. Silva, V. Guerra, V. I. Parvulescu and O. Guaitella. "CO_2/CH_4 glow discharge plasma. Part I: Experimental and numerical study of the reaction pathways". Plasma Chemistry and Plasma Processing. *(Submitted)*
- A. Salden, M. Budde, C. A. Garcia-Soto, O. Biondo, J. Barauna, M. Faedda, B. Musig, C. Fromentin, M. Nguyen-Quang, H. Philpott, G. Hasrack, D. Aceto, Y. Cai, F. Azzolina Jury, A. Bogaerts, P. Da Costa, R. Engeln, M. E. Gálvez, T. Gans, T. Garcia, V. Guerra, C. Henriques, M. Motak, M. V. Navarro, V. I. Parvulescu, G. Van Rooij, B. Samojeden, A. Sobota, P. Tosi1, X. Tu and O. Guaitella. "Meta-analysis of CO_2 conversion, energy efficiency and other performance data of plasma-catalysis reactors with the open access PIONEER database". Journal of Energy Chemistry. *(Accepted)*

Oral contributions

- C. A. Garcia Soto : "Study of CO_2-CH_4 plasma surface interactions on cerium oxide using *in situ* FTIR transmission experiments". LPP Seminar, Palaiseau Cedex, October 2022.
- C. A. Garcia Soto, P. Thevernet, D. Sadi, M. Fondaneche, E. Baratte, V. I. Parvulescu and O. Guaitella. "DC Glow Discharge - Fluidized Bed Reactor for CO_2 Recycling". International Symposium Plasma Catalysis for CO2 Recycling, Kraków, September 2022.
- C. A. Garcia Soto, E. Baratte, V. I. Parvulescu and O. Guaitella. "Study of plasma-surface interactions of CO_2-CH_4 plasma on CeO_2 using *in situ* Infrared Transmission experiments'. GEC 2021, Online, October 2021.

Posters

- C. A. Garcia Soto, P. Thevernet, D. Sadi, M. Fondaneche, E. Baratte, V. I. Parvulescu and O. Guaitella. "DC Glow Discharge – Fluidized Bed Reactor for CO_2 Recycling". WE-Heraeus-Seminar Non-Thermal Plasmas for Sustainable Chemistry, Bad Honnef, April 2023.
- C. A. Garcia Soto, E. Baratte, V. I. Parvulescu and O. Guaitella. "Study of CO_2-CH_4 plasma-surface interactions on cerium oxide using *in situ* FTIR transmission experiments". ESCAMPIG, Paris, July 2022.

- C. A. Garcia Soto, E. Baratte, V. I. Parvulescu and O. Guaitella. "*In situ* FTIR transmission experiments through catalytic pellets under CO_2-CH_4 plasma exposure". FLTPD XIV, Levico Terme, May 2022.

Acknowledgments

I would like to start giving thanks to the person that made this work possible: Olivier Guaitella. I don't know how to thank you properly because the PIONEER project has changed my life for good. When I think about it, I am glad we had that informal call by Skype in summer of 2019 and discussed with you about your project. Of course, I feel blessed that you selected me to be your student. I learned so much from you, everything i know about plasma physics is because of you! It was hard work but I wouldn't have done it differently (except breaking less stuff in the lab, oops). Everything that I did was because of your support and motivation. Besides being the best supervisor I ever had, you are truly an amazing person. You are so kind and friendly. I feel I was very lucky to work with you and I hope I get to continue collaborating with you in the future. Je te remercie sincèrement.

I want to thank my PIONEER family. To all ESRs: thank you so much for everything! I am so happy I had the fortune to meet each one of you. You are all amazing and unique. It was really sad we couldn't meet until 2 years after the project started but we managed to hangout even by zoom and then in real life. I want to give special thanks to Jairo for helping me in Bucharest with all the peculiarities of the country and for becoming my friend. I will never forget our discussions and how we managed to build a reactor with scrap pieces of glass. Obrigada por tudo :). I want to thank Maik and Toine for being my best database buddies. It was a pleasure to work closely in such tedious but fascinating project. You two are so smart and I appreciate everything we did together. To the girls of the project, Marzia, Chloe, Beatrice and Golshid: I am so grateful I got to know you all because you are amazing and spending time together was so fun and refreshing. I am so glad we met and I hope we can stay in touch in the future. Also, I want to thank the supervisors for your support and feedback. I want to thank you Marivi for being so sweet and helpful when I needed especially for the fluidized bed. Also, thank you for accepting to be my rapporteur ;) Thank you Frederic for your feedback and thank you so much for your patience with all the doubts and questions I had. It was really a pleasure to discuss with an expert like you.

To all my colleagues in Romania, Sabina, Zinnia, Magdi and Andrada, I don't know how to properly express my gratitude because you helped so much to navigate the labs, the administration and the country. It was a pleasure to learn more about your culture and enjoy my stay in Bucharest. Really, thank you thank you thank you.

To my LPP family, I got the best colleagues ever because I got know many of you and I am so glad I did because you are so fun! Tarek, thank you for being so welcoming to the office we shared and for opening your circle so I could join you and experience more about the life in Paris. You are one of the kind. Dihya!!!!!!!! For some reason I have the fortune to meet angels during the labs where I have worked and let me tell you that you are the sweetest person in the lab ever. You are the reason the chapter of FB-glow discharge is complete, without you I couldn't have done it. You are so smart and kind, really. I am sure you will do great during your phd as you did great during your internship. I want to also thank Paloma and Marie for the good job done in the lab during your internship and I am certain you will do great in the future. Victor, you are so weird and funny haha I am glad you don't hate me when I mean to you, I am mean just because I like to bother you and I think I do it very well. Finally, to Edmond, my constant partner in the lab for the last 3 years. Thank you so much for your help navigating LPP and for sharing the project we have in common. Also, thank you for letting me experience a bit more of the french culture, I certainly learned a lot from you. I am sure you will get far in whatever you propose to, MERCI BEAUCOUP! The lab would not have been the same without Andrey, Shu, Kunkin, Zhan, Benjamin, Federico and all the PhD students, postdocs and interns I had the fortune to meet during my

three years at LPP.

To my office neighbours Emmanuele and Mhedine. I am so glad I got to share the office with you, we had really interesting discussions and I feel you are already my friends. I hope you don't forget me because I would definitely never forget you.

I don't think I would have been able to survive these 3 years and a half without the support of my dearest friends. Paula <3, you are an incredible friend to me, you have been there when i needed you the most and I am so proud to call you my friend. You deserve only good things in life and I am sure you will get them. Frannie : I am so glad you replied to my message in GGI and we manage to get to know each other. You are such a cool and kind friend, thank you for not forgetting me while I was gone writing this thesis haha. I can't wait for our trip together and many more adventures to come. Para mi familia chilena, gracias por hacerme parte de su grupo. Nunca pense que me haria amiga de personas tan lindas como ustedes. Agradezco haberme inscrito al curso de frances en polytechnique y haber conocido a Cristian y luego a Karla y luego a Nati, Nico y finalmente Natu <3 Aunque a veces no entendia lo que decian, tuvieron paciencia conmigo y aprendi chileno forzadamente hahah. Espero sigamos compartiendo mas en los años venideros. To Olivia, I cannot find the words to express how much your friendship means to me. I am so happy we remained friends for so long and to have you around since I left my country. I will cherish all the trips and adventures we had together and looking forward for the future ones. You know I love you and I wish you the best always.

Para mi corazon que deje en Mexico (mi familia y amigos). Cuando me fui, pense que volveria y todo seria como siempre pero me agarro la loquera y no volvi. Aun asi nunca me dejaron y aprecio tanto que apesar de la distancia, todo siguiera como siempre. Para mis amigos de la uni, Ruben y Karla, gracias por la amistad de tantos años. Espero sigamos en contacto por el resto de nuestras vidas. Para mis amigos de MDM, Nico y Ana, gracias por no olvidarse de mi. Siempre es un gusto volverlos a ver y compartir mas que nada comida hahah. Nico, gracias por todo, tu apoyo incondicional, por apoyarme cuando sentia que no podia mas estar en Francia, por estar para mi en los momentos mas dificiles de mi vida. Desearia que estuvieras aqui en mi presentacion pero se que cuento contigo a todo momento. Parte de esta tesis es tuya. Para mis tias y primos que han estado ahi para mi, gracias por ser una familia tan linda conmigo. Les mando un abrazo a todos, los quiero. Para mis papas, no se por donde empezar porque de verdad que es dificil expresar todo el amor que tengo por ustedes. Siempre me han apoyado en todas mis decisiones incluso cuando me fui de Mexico y me quede en Francia. Yo se que me extrañan pero yo los extraño mas (y a los gatos y perros), todos los dias. Agradezco haberlos tenido como mis padres y agradezco mas que me hayan dado a Fernando como mi hermano. Fer, todas las veces que no sabia que hacer o que decir, siempre pensaba en que es lo que tu harias. Nunca olvidare las veces que platicabamos y como emocionado me mostrabas algunos experimentos de optica. Siempre pense que seriamos amigos de adultos. Me haces tanta falta y no puedo esperar el dia que te vuelva a ver. Esta tesis es tuya. Espero no te disguste tanto dado que es en Fisica pero con mucho de quimica. Te quiero mucho.

Doing this thesis has been the one of the best experiences I ever had in life and I am grateful I managed to do such satisfactory work along with amazing people. Thank you all.

Carolina Alejandra Garcia Soto

List of Figures

Contents

Chapter 1

Introduction and state of the art

Contents

1.1 Importance of CO_2 recycling

The increasing concentration of carbon dioxide (CO_2) in the atmosphere represents a major threat to human society. As in a chain reaction, due to anthropogenic activity, CO_2 concentration has risen to unprecedented levels leading to increase in temperature which directly affects the climate and ocean acidification. According to the United Nations Emissions Gap report from 2021, fossil CO_2 emissions dominate growth and total greenhouse gas (GHG) emissions. CO_2 emissions reached a record 37.9 gigatons of CO_2 in the beginning of this project (2019), but dropped to 36.0 $GtCO_2$ in 2020 [1]. This has been leading to the development of technologies to reduce CO_2 emissions and/or to capture and store.

An attractive approach to mitigate the effects of global warming is CO_2 recycling. Recycling refers to utilize a waste product from the industry, in this case carbon dioxide, to transform it into valuable compounds as precursors for chemical industries or in the production of fuels and plastics. Subsequently, the disposal or consumption of such products generates CO_2 which can enter again in the recycling process [20]. This is what is called closing the carbon cycle. With the aid of renewable energies and other hydrogenated co reactants, it is possible to create neutral carbon processes. The schematic is shown in figure 1.2. The distinct stages of CO_2 recycling represent a challenge on their own.

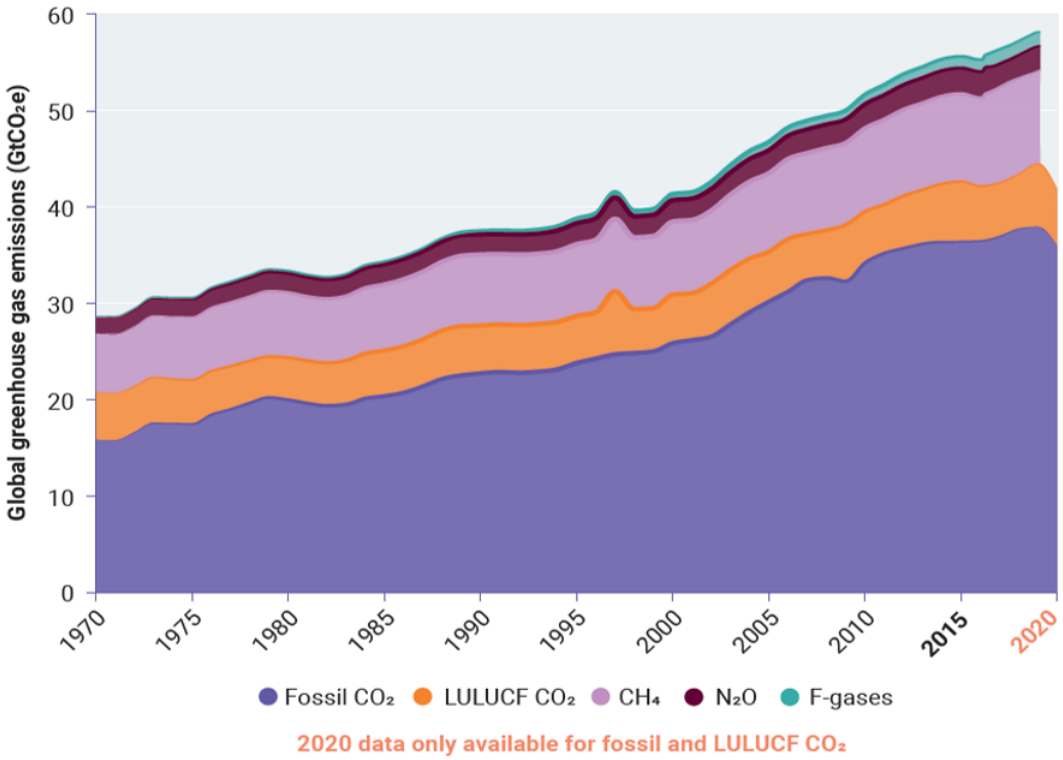

Figure 1.1: Global greenhouse gas emissions from all sources, 1970–2020. LULUCF – land use, land-use change and forestry. Figure extracted from [1].

1.1.1 Approach to CO_2 conversion

Eunice Foote in 1856 demonstrated that carbon dioxide could adsorb heat and assumed that different concentrations in the atmosphere (based on geological evidence) might impact the atmospheric temperature and therefore, the climate [21]. Five years later, Tyndall reported his experiments with different gases and he determined that molecules of higher complexity and lower symmetry such as water vapor and carbon dioxide were the best absorbers and radiators of heat radiation [22]. The infrared active vibrations of carbon dioxide are directly responsible for its role as a greenhouse gas. They did not know the important role vibrational excitation could play on the mechanism for CO_2 conversion.

Carbon dioxide is a triatomic molecule very stable with high oxidation state. This represent the need for high energy input and efficient catalysts to reach competitive yields. Different technologies are under development and these are classified into biological and chemical transformations. The first involves CO_2 fixation by natural photosynthesis, algae production or the use of microorganisms [23]. Chemical transformation involves a diverse range of technologies for CO_2 conversion as electrochemical, thermal, photocatalytic and biochemical approaches through a wide range of CO_2 reactions [24–28]. Each technology represents advantages and disadvantages but no single one is able to tackle completely the conversion of CO_2 efficiently. Several reviews describe better in detail these technologies [27, 29, 30]. Nonetheless, plasma-catalysis offers combined advantages.

Plasmas are a complex mixture characterised by the simultaneous presence of ions, electrons, atoms, electronically and vibrationally excited species, and molecular and radical species in their fundamental state. Non-thermal or low temperature plasmas are characterized by high temperature electrons meanwhile the rest of the molecules/atoms remain at relatively low temperature in contrast to thermal plasmas where electrons and gas molecules/atoms have almost the same temperature. For the sake of simplicity, in the rest of the text **Plasmas** will be used to refer to non-thermal plasmas (*i.e.* low-temperature

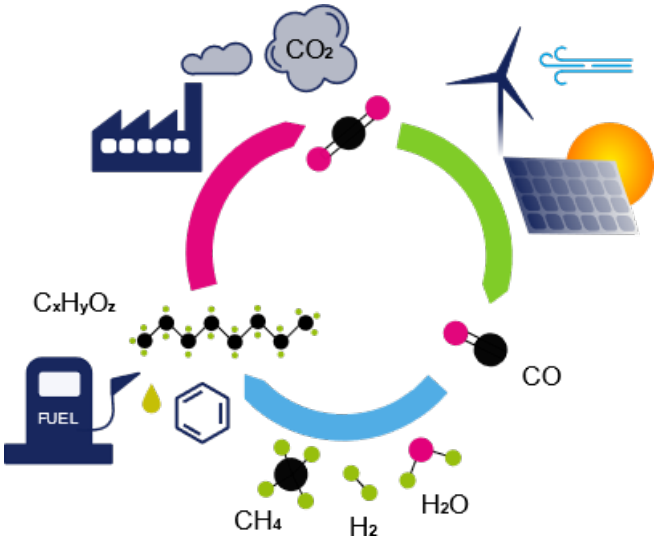

Figure 1.2: Ideal closed carbon cycle. Inspired from figure taken from [2].

plasmas or out of thermodynamic equilibrium plasma). Catalysts are materials or molecules that help to reduce the activation energy and allow the reactants to convert into the corresponding products. As it will be discussed throughout this thesis, materials that are not considered as a catalyst in thermal catalysis, can sometimes play such a role when placed in contact with a plasma.

1.2 Plasma-catalysis

Plasma-catalysis (or plasma-assisted catalysis) is not a new term and early works on the field could be traced back to the middle of the 20th century as reported in the review by Kim et al. [31]. Definitely plasma catalysis has become an emergent field since then with promising real applications. Many publications have reported the synergistic effect of plasma-catalysis for several purposes: VOC abatement [32], indoor air cleaning [33], ammonia synthesis [34], H_2 production [35], water treatment [36], carbon coupling [37] and carbon dioxide recycling [38], for naming some.

Regardless of the application, a synergy is given as an explanation for the enhanced performance in terms of conversion, selectivity and/or energy efficiency. Synergy is explained as the effect of coupling plasma with a catalyst resulting in a greater effect than plasma and catalyst alone [39]. However, given the complex nature of plasmas, it is difficult to assign this so called synergy to a specific characteristic of the non-thermal plasmas or to the catalyst. In one or several ways, the plasma can affect the catalyst, for example, by modifying the morphology or altering the charge in the surface. At the same time, the presence of the catalyst in the discharge area can affect the gas composition or the electric field. Plasma-catalyst coupling is therefore a peculiar and quite complex case of plasma-surface interaction.

1.2.1 Plasma-surface interaction

Given the particular properties of plasmas, these interact differently with a surface than a neutral gas would. The energy is mostly deposited in the electrons which could later be transferred to other species and lead to specific processes like etching, deposition, surface charging and heating.

Plasma etching is one of the main applications of plasma treatment and is commonly used in production of semiconductor devices [40]. During plasma etching, the highly energetic and reactive species produced from a selected process gas, such as O_2 or a fluorine bearing gas, bombard and react with the

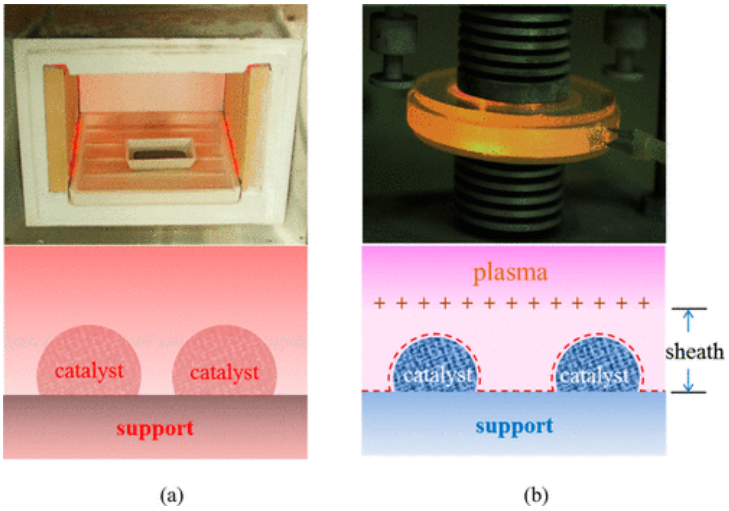

Figure 1.3: Example of interaction in a) thermal catalysis and b) plasma catalysis. Figure extracted from [3].

sample surface and, as a result, the materials at the surface are broken down to volatile and/or smaller molecules which are then removed by the vacuum system. It is possible to etch off parts or the entire top layer of the surface. The objective of etching is to transfer a given pattern onto a functional layer deposited on a substrate. Deposition of thin films or other structures onto a surface is also possible with the aid of plasma [41]. Nowadays, for catalysts preparations, metal deposition by plasma deposition results on enhanced dispersion which ultimately gives higher conversions on thermal dry reforming of methane [42].

When a material is inside the plasma region, the surface exposed is subject to negative charge by plasma derived electron flux. This could lead to accumulation of the charge in the surface that affects the surfaces reactions (like adsorption and desorption) [43, 44]. At atmospheric pressure experiments suggest that charges can accumulate in the surface of dielectric materials resulting on re-ignition of filamentary discharges by in surface charge memory [45]. Such effect could somewhat be translated to catalytic materials, many being dielectrics as well. In the particular case of CO_2 conversion, the negative charge accumulating onto the surface could make the surface more Lewis basic, especially for alumina, enhancing adsorption of CO_2 [44].

1.3 Innovative routes for CO_2 conversion

The plasma conversion of carbon dioxide with hydrogenated molecules like water, methane and other light hydrocarbons is regarded as one of the possible ways for making the utilization of natural gas resources more efficient from both economic and ecological points of view [46]. Within the framework of PIONEER (a European project involving 15 research groups dedicated to the conversion of CO_2 by plasma-catalysis and of which this thesis is a part), various types of novel reactor configurations for non-thermal plasmas are explored for CO_2 recycling. Nanosecond repetitively pulsed discharges are used to study the time evolution of excited species for CO_2 conversion [47]. Microwave plasmas are used to promote the stretching vibration of CO_2 in combination with N_2 [48]. Also, water as an impurity in gas exhausts mixtures is under study in CO_2 plasmas using DC glow discharges [49]. Interestingly liquid water can also serve as H donor in bubbling plasma-liquid phase interactions. The goal is to synthesize hydrocarbons and organic acids using CO_2 as carbon source. All these approaches are interesting but the objective of the work presented here is to explore another route, by studying the potential of fluidized

beds for plasma-catalysis coupling.

Combining plasma discharges and fluidized bed into one system seems an excellent approach to solve the mixing and heat transfer problem of plasma process for gas-solid processing. While fluidized beds-plasma reactors range a number of applications as coating of powders, surface modification, inactivation of microorganisms, etc. [50–52], very few works are investigating this possibility for CO_2 conversion.

1.3.1 Fluidized bed - plasma reactors

Regarding CO_2 conversion, promising results under plasma-catalytic systems coupled with a fluidized beds are already reported. For example, voltaic arc plasma reactor coupled with a fluidized bed for carbon dioxide conversion only was tested by Pou et al. They expected the efficiency to be increased by using a fluidized bed that can have two functions: (1) to catalyze the CO_2 decomposition; (2) to enhance the distribution of the plasma discharges in the reactor [53]. Using a life cycle assessment approach in the use of photovoltaic energy it was estimated that with the best conditions obtained in this work it would be possible to compensate 67% of the CO_2 emissions associated to the process. In another study for simulated biogas (CO_2 and CH_4 admixture), a coaxial DBD plasma reactor coupled with a fluidized bed is tested. A homogenous system (catalyst free) was used as a reference and a heterogeneous system (fluidized bed system) with two kinds of catalysts (Pd/Al_2O_3 and Cu/Al_2O_3) was used to test the activity of catalysts. Both catalysts change the product composition significantly. Under homogenous conditions the maximum synthesis gas ratio (H_2/CO) was 1.3, whereas the highest ratio is found with the fluidized Cu-based catalyst with up to 1.7 ratio [54]. Also, the performance of plasma packed bed reactor vs plasma fluidized bed reactor has been assessed. Wang et al. compared Dielectric barrier discharge (DBD) plasma fluidized bed with DBD plasma packed bed. In the plasma fluidized bed, the synergetic effect of the catalyst and the plasma was clearly identified from 648 K to 798 K. The synergetic effect characterized by the conversion ratio of synergetic results to the sum of the results of only using plasma and only using catalyst showed that the plasma fluidized bed behaved better than the plasma packed bed within a certain temperature range [55]. However, the characteristics of the catalysts have a clear impact on how the reactors are operated: packed bed vs fluidized bed. Bouchoul et al. tested different Al_2O_3 materials with a specific surface area on a fluidized bed-DBD reactor and packed bed-DBD reactor. They found that large surface Al_2O_3 favored the deposition of organic products in fluidized bed but the stacking of particles in the fixed bed limits this effect [56].

1.4 *In situ* FTIR spectroscopy for the study CO_2 recycling

Plasma-catalytic interactions represent a complex system to study. Gas-plasma phase reactions and plasma-surface reactions occur simultaneously making the analysis challenging. For CO_2 conversion, it is critical to understand gas-plasma-surface interaction and only *in situ* techniques can help to elucidate the physical and chemical mechanisms at stake. Operando and *in situ* measurements can be challenging but slowly Infrared spectroscopy is more and more used for *in situ* studies.

CO_2 hydrogenation/methanation plasma reactions deal solely with CO_2 conversion along with H_2. CO_2 hydrogenation and CO_2 methanation plasma-assisted catalytic reactions are mostly performed using DBD as plasma source and the *in situ*/operando studies are reported respectively in [57–61] and [62–64]. However, Azzolina-Jury and Thibault-Starzyk were the first to report the use of glow discharges to study by operando time-resolved FTIR spectroscopy the active species in Zeolite H-USY doped with nickel for CO_2 hydrogenation [65]. They claim that vibrationally excited CO_2 molecules are then adsorbed on nickel forming formates rather than carbonates. In another similar study performed in their group, they found that a considerable amount of CH_4 was released from the catalyst after the plasma was off when

testing several Ni-zeolites (USY and ZSM type) [66].

Beyond CO_2 hydrogenation reactions, carbon dioxide can work as an oxidant on reforming of methane. Dry Reforming of Methane (DRM) reaction offers the advantage to utilize carbon dioxide as oxidant agent while transforming another greenhouse gas (CH_4) into synthesis gas (H_2/CO) commonly known as syngas. However, this reaction is highly endothermic:

$$CO_2 + CH_4 \longrightarrow 2\,CO + 2\,H_2 \qquad \Delta H_{298\ K} = 247\ kJ/mol$$

In addition, side reactions can occur (*e.g.* Reverse-Water-Gas-Shift) resulting in a significant fraction of water. The improvement of the performance in terms of conversion and selectivity of DRM reaction can only be achieved by understanding fundamental mechanisms. In this aspect, *in situ* infrared spectroscopy can help to explain the surface reactions occurring on a catalyst and clarifying the role of each component of a catalytic system. The main findings of several studies using *in situ* infrared techniques, mostly by DRIFTS, are described below for thermal-catalytic and to lesser extend on plasma-catalytic systems.

1.4.1 Thermal-catalytic DRM reaction

Almost 20 years ago, Ferreira-Aparicio et al. studied in detail the DRM reaction over Rh catalysts at 450-550°C. *In situ* DRIFTS showed that when CO_2 was sent to Ru/Al_2O_3, carbonate/bicarbonate species were formed which changed upon methane introduction displaying bands corresponding to formates. When carbon dioxide was removed from the mixture, these bands were depleted. Besides, no adsorbed intermediate species were seen on ruthenium phase probably because of low dispersion of the metal. These results suggested that CH_4 was activated on the metallic surface diffusing hydrogen species to the support while CO_2 was hydrogenated on the alumina to yield formate species finally decomposing to CO. Oxygen species continuously provided during the CO_2 activation process, diffuse from the support to the metal surface to oxidize carbonaceous deposits formed during methane decomposition. In addition, it was discussed the origin of hydrogen carbonates which were suggested to be formed by carbonates and OH^- adsorbed species on the support which later promote the generation of formates. Also, formates could be formed by carbonate species reacting with surface adsorbed H. Emphasize was made on the importance of hydroxyls key role on Ru/Al_2O_3 for the oxidation of the carbonaceous adspecies located on the metallic surface in contrast to Ru/SiO_2 catalyst activity where inevitably coke was formed [67].

Upcoming research on this area slowly increased in time, mostly on thermal-catalysis testing different materials with different metallic active species. Liu et al. studied the two step-wise reaction of CH_4 direct carboxylation with CO_2 using Cu-Co as catalyst in time-resolved FTIR transmission spectroscopy. Results showed that CH_4 was dissociated to atomic hydrogen and M-CH_x species on catalyst surface when it was first introduced in the system. Interestingly, negative peaks appeared in the region 3200-3800 cm^{-1} suggesting an interaction of CH_x and adjacent OH species. Then CO_2 was inserted into the intermediate species directly into carboxylate. Finally, the subsequent CH_4 adsorption provided active hydrogen for the species of previous surface reaction, thus leading to the formation of acetic acid, according to the authors. However, it was discovered that the addition of CO_2 first instead of CH_4 had detrimental effect on CH_4 catalytic conversion [68].

The activity of MnO_x species on Ni/CeO_2 was evaluated by *in situ* DRIFTS on DRM reaction at 550°C. Continuous flow of CO_2 and 6 pulses of CH_4 were performed during the IR study. Three bands were particularly observed (2020, ∼2100 and ∼2170 cm^{-1}) which were assigned to the surface adsorbed carbonyl species, linear CO and gaseous carbon monoxide, respectively on Ni/CeO_2. However, on MnO_x-doped/CeO_2, the band at 2020 cm^{-1} assigned to surface adsorbed carbonyl (CH_xO) was not present either because of fast consumption (highly reactive) or because it was not produced. In any

case, the absence of this specific intermediate could explain the lower coke formation in comparison to the undoped catalyst. Hydrogen carbonates were formed but formates did not. Two reactions pathways were proposed: one where CH_4 decomposes into CH_x and H species on Ni sites; and the second, where surface carbonyl intermediate was formed by methane decomposition and available mobile oxygen. In both cases, hydrogen carbonates are formed and later decomposed into CO, H_2O and H_2 [69].

On another approach, the calcination treatment of ZrO_2 (zirconia) support was submitted to H_2, N_2 and O_2 at 750°C and later studied on CO_2 *in situ* DRIFTS. The zirconia treated by H_2 resulted in slightly stronger bands assigned to linearly or physically adsorbed CO_2 molecules in comparison to those treated by N_2 and O_2. Similar results are obtained for the bridged and bicarbonates formed on the surface. The catalytic testing in DRM at 700°C concluded a superior performance on CO_2 and CH_4 conversion, syngas formation and H_2 selectivity. It was subsequently corroborated that the ZrO_2 treated by H_2 possessed the most active adsorbed oxygen species and highest mobility of lattice oxygen [70].

Electric field was applied to a reactor containing Ni/La-ZrO_2 as catalyst to study DRM reaction in [71]. By increasing the temperature to 300°C and applying a direct input current of 3 mA, CO and H_2 were observed as products. During *in situ* DRIFTS characterization, formates and carbonates were not observed assuming a faster reaction than CH_4 and CO_2 dissociation. TPD-DRIFTS with CO_2 showed in more detailed the bands corresponding to carbonates/bicarbonates/formates in the region of 2000-1000 cm^{-1}. Moreover, the peak for differential spectra in/after application of the electric field, which was assigned to rotation of the adsorbed water (850 cm^{-1}), was observed only when an electric field was applied. This peak is regarded as having a strong relation with the Grotthuss mechanism, as derived from proton conduction. Surface protonics, the mechanism by proton collision derived from its surface conduction, occur in DRM with the electric field over Ni/La-ZrO_2 catalyst, resulting in activation of both CH_4 and CO_2 dissociation. However, it was concluded that lattice oxygen defects also contributed to the dissociation [71].

1.4.2 Plasma-catalytic DRM reaction

Very few articles have been published dealing with the study of plasma/catalyst interaction *in situ* for CO_2 recycling and specifically for DRM reaction. Vakili et al. tested several catalysts where Pt nanoparticles (Pt NPs) supported on UiO-67 (a type of metallic-organic-frameworks MOF) showed the best performance in a Dielectric Barrier discharge (DBD) plasma reactor. *In situ* DRIFTS characterization showed an increased adsorption of CO on Pt NPs after plasma ignition. CO_2 adsorption and decomposition formed carbonates further decomposed to formates which later where decomposed to CO and OH on Pt NPs. An interesting feature was the observance of bands appearing at 1415 and 1610 cm^{-1} revealing the dehydrogenation of C_2H_4 on the catalyst surface. The adsorbed C_2H_4 was dehydrogenated to C_2H_3 on Pt NPs. The signal was weak as it was rapidly dehydrogenated to C_2H_2 and the gas phase band overlapped with C-H vibrational band of CH_4 but detected on the Gas Chromatograph online after the DBD reactor [72].

In another study, *in situ* DRIFTS was used to characterize the surface of La-modified Ni/Al_2O_3 catalyst on a DBD plasma reactor. Firstly, CO_2 plasma was used to evaluate carbonate formation on the catalyst. The intensity of carbonate peaks formed was much stronger on La-Ni/Al_2O_3 than that of Ni/Al_2O_3. Then, methane was added to the system but in this step, plasma was not ignited and the temperature maintained at 600°C. A weak broad band at 1750 cm^{-1} appeared and it was assigned to C=O stretching vibration in surface CH_xO* species (an intermediate already noticed in DRM reaction) which was expected as intermediate for generating CO and H_2. Comparing La-Ni/Al_2O_3 and Ni/Al_2O_3 catalysts, they suggest that CH_4 chemisorption could be interrupted by carbonate formation. They established a good correlation between CH_4 conversion and carbonate formation, although, CH_4

conversion in plasma phase was not mentioned. Methane is decomposed in the surface of the catalyst further reacting with carbonates leading to CO and H_2 release [73].

While many of the works presented here are done on a diffused reflectance mode, recent work has been published using *in situ* plasma-catalysis analysis on transmission mode. The interesting part of this particular work is that they were able to measure the temperature of their catalyst using $BaSO_4$ as an internal standard following the band at 1965.9 cm^{-1} finding that the temperature of the pellet (Ru/SiO_2) does not go above 423 K in $CO_2/CH_4/Ar$ in DBD [74].

On another *in situ* study, Kim et al. evaluate CO (product from DRM reaction) in plasma in contact with ZnO (a reducible material) for CO oxidation in a DBD reactor. They apply *in situ* transmission infrared adsorption to evaluate the rotational and vibrational temperatures of CO and their role in CO oxidation. They found that only vibrationally excited CO, and not the ground state, is adsorbed in ZnO resulting in the appearance of bands attributed to carbonates and bicarbonates. The adsorption of CO (2155 and 2106 cm^{-1}) occurs in Zn^{2+} subsequently reacting with lattice oxygen suggesting a Mars-van Krevelen mechanism [75].

1.5 What is unknown?

Many approaches are reported in the literature dealing with plasma-catalysis for CO_2 conversion. Either by adding H_2 or CH_4, changing the type of catalyst (specially the metal deposited in the support), type of plasma discharges or the coupling of plasma reactor with the chemical one. However, many fundamental processes remain poorly understood or not described in detail in the literature.

I. **Plasma-support interaction**

An heterogeneous catalyst is a material capable to perform catalytic reactions in a different phase to the reactants or products. Typically, heterogeneous catalysts involves solid materials reacting with fluid phase reactants. In many cases, the catalysts are mainly composed of three parts:

(a) *Metal active sites.* Usually it is presented as pure metal (Ni, Co, etc.) and some other cases could deal with metal oxides, mixed oxides, carbonates, etc.

(b) *Promoter.* The role of promoter is to aid in the reaction occurring in the main active site. It can be composed of distinct pure metal phase or metal oxides.

(c) *Support.* The goal is to provide a surface to sustain the active sites where the catalysed reaction takes place. Usually, it is composed of metal oxides or mixed oxides (*e.g.* Al_2O_3, TiO_2, zeolites) but can also be a wide variety of complex structures like Metal-Organic-Frameworks (MOFs), cellulose, carbon nanotubes, etc.

Supports are considered sometimes as an inactive surface in plasma reactions, however they could play a crucial role in the surface reactions. Under plasma conditions, supports could accumulate surface charges or provide reactive species to the near environment but more importantly, the support can also interact with vibrational and electronically excited species in the plasma phase. Indeed, certain material are considered only as a 'support' and not a 'catalyst' because they do not induce surface reaction with just neutral molecules in their ground state. However, that does not mean that excited species and radicals can not trigger surface reactions on these so called 'support' materials. Most of the studies dealing with plasma catalysis for CO_2 conversion deal with complex catalysts (like Pt-UiO-67 or La-Ni/Al_2O_3) without studying the chemical and physical effect of the support on the surface reactions or in the plasma properties [72, 73]. For example, Al_2O_3 is considered inactive in CO_2 plasma reactions but CeO_2 is very well studied for mild reactions of CO_2

in thermal catalysis but very little has been reported for CO_2 conversion by plasma-catalysis [76]. In addition, no detailed *in situ* or operando studies have been reported dealing with solely supports as catalytic surfaces either for DRM reaction or even for CO_2 only.

II. **Type of discharges coupled with Fluidized beds**

As described in the section 1.3, most of the plasma reactors coupled with fluidized beds utilise dielectric barrier discharges as plasma source. DBD is widely used in plasma-catalysis field easing the comparison of catalyst performance across different research groups. Nonetheless, the study *in situ* of DBD plasmas for catalytic conversion of CO_2 is difficult. Implementing spectroscopy techniques like infrared spectroscopy or optical emission spectroscopy giving reliable results of what occurs in the surface of the catalyst or in the gas phase remain challenging. By the filamentary nature of dielectric barrier discharges the plasma region is not homogeneous. In addition the light emission of CO_2 plasmas at atmospheric pressure is very weak. For fundamental studies, other type of plasmas reactors can be beneficial to study to isolate specific plasma/catalyst interaction mechanisms. As the catalyst can also modifies the plasma properties, plasma characterization while in contact with the catalyst is necessary for cross checking among several plasma reactors and configurations. Another aspect to be elucidated in the specific case of fluidized bed configurations is the physical effect of moving particles in the plasma region has on the plasma properties. Conversion and selectivities are not enough to comprehend the synergy described and expected of plasma-catalysis and *in situ* measurements are needed.

III. **Spectroscopy techniques for *in situ* studies**

Basically, all studies reporting plasma-surface mechanisms use infrared spectroscopy as principal diagnostic on DRM reaction. DRIFTS is commonly use for the ease of sample preparation for measurement. Since this technique relies only on the partial exposure of the sample powder in contact with plasma phase, complete exposure can only be achieved in transmission mode. The scattering of the IR beam does not allow to be quantitative in terms of concentrations.

Additionally, despite the previous studies described in section 1.4.2, detailed evidence of catalytic surface reactions and vibrational measurements of reaction intermediates in contact with a well characterized CO_2-CH_4 plasma phase (gas, rotational and vibrational temperatures, reactive species concentration, intermediary species, electric field, etc.) is scarcely reported in the literature.

1.6 Objectives and approach of the thesis

The purpose of this thesis covers two objectives:

1. Provide significant insights on the mechanisms of the plasma interaction with a catalytic surface.
2. Test a fluidized bed - plasma reactor as an innovative configuration for CO_2 recycling.

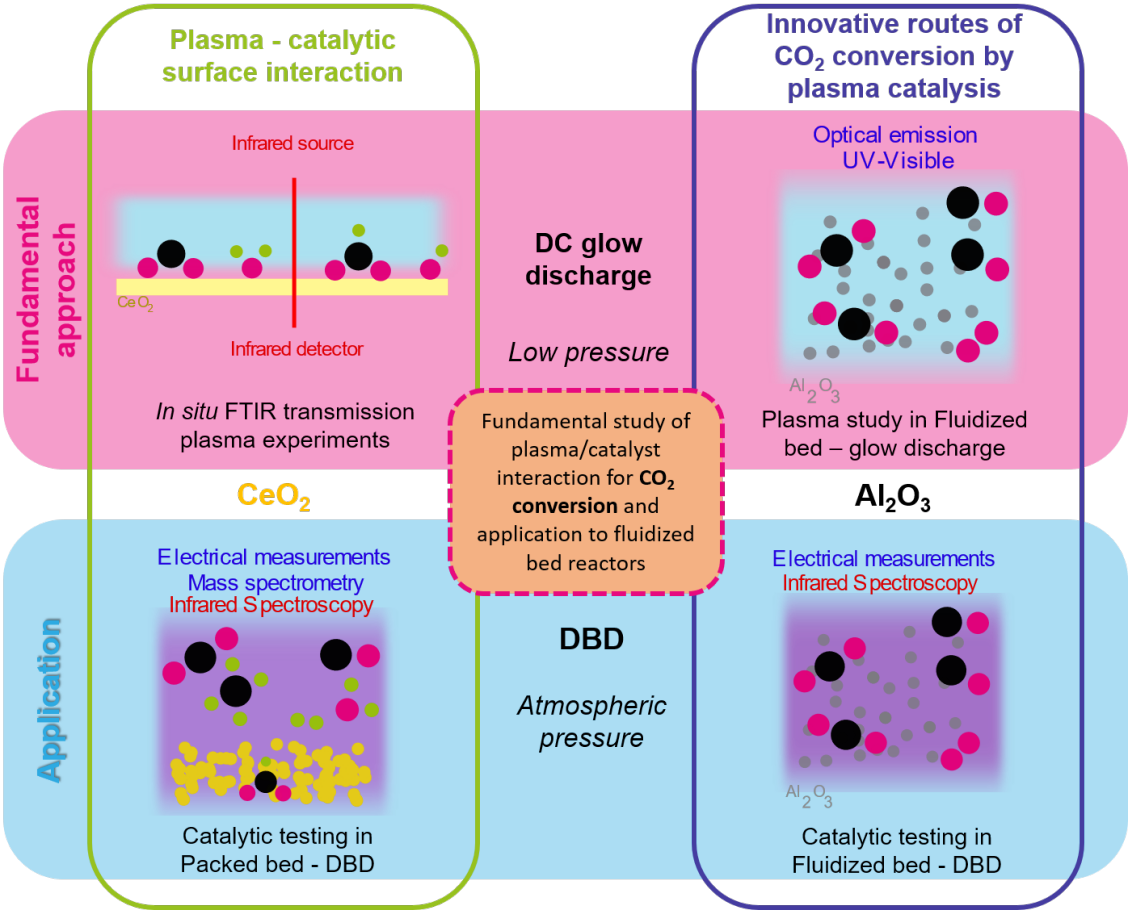

Figure 1.4: Schematic correlating the fundamental approach and application study for plasma-catalytic surface interaction with fluidized bed plasma reactors as innovative route for CO_2 conversion by plasma catalysis described in this thesis work.

The first objective is done with the use of *in situ* experiments using FTIR spectroscopy in transmission mode to try to discriminate different mechanisms of plasma-catalyst interaction. To achieve this, a well characterized plasma source (a **DC glow discharges** at low pressure) is used to interact with a well known catalytic surface as CeO_2 (see top left corner of the schematic on figure 1.4). The DC glow discharge has been chosen for this part of the work because it allows for numerous gas phase characterization providing the temperature, electric field, and all the densities of neutral molecules and atoms. It is also a discharge easier to compare with 0D kinetic models. Ceria has been chosen because often it is used as support and even as 'support', it may not be only a simple spectator, as it can offer different functionalities and play an important role in a catalytic reactions [77]. In this case, CeO_2 was chosen for its easy oxidation/reducibility and subsequently oxygen storage capacity, which is directly linked to the presence of oxygen vacancies that can possibly be created under plasma conditions. Such properties have made it suitable for a wide range of applications as water-gas-shift reaction [78], hydrogenation of alkynes [79], three way automotive exhaust catalysis [80] and electrochemical reductions [81]. In order to study the effect of CeO_2 in CO_2-CH_4 plasma reaction at atmospheric pressure, catalytic testing was performed using **Dielectric Barrier Discharge** reactors in *packed bed* configuration (bottom left corner on figure 1.4). The surface and bulk was analyzed after plasma exposure with a wide variety of characterization techniques providing further insights on the plasma-catalytic interaction. The information obtained in the glow discharge interacting with the same CeO_2 materials will be used to try gaining more understanding of the results obtained in the DBDs.

The second objective is done testing Fluidized Bed (FB) reactors coupled with plasma reactors as *innovative route* for CO_2 conversion. Again, a DC glow discharge is first used for studying fundamental mechanisms before evaluating performances with DBD reactors. Al_2O_3 particles are tested as fludizing material. Al_2O_3 is a metal oxide known for its acid-basic properties due to the degree of hydroxylation of the surface. It is considered an inert material but capable to adsorb CO_2 making it perfect to evaluate the effect of a fluidizing material with a reduced catalytic activity in the plasma properties. FB-glow discharge provides fundamental insights on the modification of plasma properties by Optical emission spectroscopy in UV-Visible range and FTIR spectroscopy analysis on the downstream gas. This study is complemented by results performed in CO_2 plasmas (already reported in the literature) and CO_2-CH_4 plasmas at low pressure [16, 82–85]. FB-DBD reactor offers additional information to conventional configurations reported in several studies dealing with CO_2 reactions at atmospheric pressure [53,54,56,86]. In addition, a comparison is done with results obtained in packed bed (PB)-DBD configuration with Al_2O_3 as catalytic material. The combination of these two type of plasma sources provide valuable information on the plasma itself still giving catalytic parameters comparable to the application reported in literature. Figure 1.4 displays a schematic correlating the fundamental approach and application study for plasma-catalytic surface interaction with fluidized bed plasma reactors as innovative route for CO_2 conversion by plasma catalysis.

The fundamental approach provides detailed information on the catalytic surface reactions which is complemented by a rigorous characterization of the gas and plasma phase contributed by Edmond Baratte in his PhD thesis [87]. In this way, we provide information on the detailed processes occurring on the surface interacting with CO_2 and CO_2-CH_4 plasmas. However, proof that catalytic materials (either metal supported catalysts, bare supports like CeO_2, Al_2O_3 or any other tested here) increase the conversion or selectivity is out of the scope this work. Evidence to support such claim is already stated in the literature through several studies dealing with plasma-catalysis for CO_2 conversion [88–90].

On the scheme of MSCA-ITN goals for the CO_2 PIONEER project, a new joint collaboration was established between the Laboratoire de Physique des Plasmas (LPP) in Ecole Polytechnique, France under the supervision of Dr. Olivier Guaitella and the Department of Organic Chemistry, Biochemistry and Catalysis in the University of Bucharest, Romania under the direction of professor Vasile I. Parvulescu. Such collaboration allowed:

- To performed *in situ* FTIR tranmission experiments on a catalytic surface under different controlled parameters (flow, pressure, current, etc.).
- To characterize the catalytic surface before and after plasma exposure and elucidate any change on the structure that plasma can have on the catalytic material.
- To test the catalytic performance of CeO_2 based catalysts on a packed bed DBD reactor.
- To test the effect of a catalytic material on plasma characteristics and viceversa on a fludized bed - plasma reactor.

Other collaborations were also established with the Instituto de Carboquimica in Zaragoza, Spain and Instituto Tecnico de Lisboa in Lisbon, Portugal in the aim to explore Ni-based catalysts in our configurations and its proper material characterization.

The outcome of this thesis meets the need of in depth plasma-surface characterization while providing information on the performance of plasma-catalytic systems.

1.7 Outline of the thesis

This thesis is divided in three parts:

- **Part I: Description of gas and surface characterization.** Chapter 2 describes the experimental material used along with the characterization techniques employed to characterize the plasma, gas and catalytic materials. Chapter 3 presents the results from the downstream gas of CO_2-CH_4 plasma reactions and the effect of concentration of CO_2, flow rate and presence of ceria pellets in the plasma region in the glow discharge. In addition, the identification of surface adsorption bands in CeO_2 as catalytic material is discussed under CO_2 and CO_2-CH_4 plasmas.

- **Part II: *In situ* FTIR transmission experiments.** Chapter 4 presents the plasma-surface interaction of CO_2 plasma only with CeO_2 with *in situ* experiments enriched with downstream gas and adsorption tests. The investigation is further extended to CO_2-CH_4 plasmas in chapter 5. Characterization of the CeO_2 pellet before and after plasma is described. Chapter 6 provides information to complement and enrich the previous chapters with O_2-CH_4 plasmas. Ar, He and N_2 tested to on the interaction with adsorbates resulted from CO_2-CH_4 plasmas.

- **Part III: Innovative routes for CO_2 conversion by plasma-catalysis.** Chapter 7 presents the results of CO_2 and CO_2-CH_4 plasmas in a fludized bed - DC glow discharge at low pressure using Al_2O_3 particles. A packed bed-DBD is used to test the catalytic performance of CeO_2 used in part II and other ceria-based materials. The results are presented in chapter 8 showing a comparison as well with the literature. A fludized bed-DBD reactor at atmospheric pressure is tested with Al_2O_3 and the results compared with PB mode.

Part I

Description of gas and surface characterization

Chapter 2

Description of experimental diagnostics and plasma reactors

Contents

2.1 Introduction

This chapter gives a general description on the principles of the diagnostics used to study the downstream gas, the plasma and characterization techniques for the catalytic material. Detailed information on the equipment and data treatment used for each diagnostics is given. Subsequently, a description on the types of plasma reactors used is presented along with information on experimental equipment used. In the end, a short overview on the principles of chemical reactors used during this thesis is described for a better comprehension on the combination of plasma, catalysis and chemical engineering fields.

2.2 Diagnostics for gas, plasma and surface

2.2.1 Fourier Transform Infrared (FTIR) Spectroscopy

Principles

FTIR Spectroscopy is a technique widely used to obtain an infrared spectrum of absorption or emission of a solid, liquid or gas. FTIR spectrometers are based on a Michelson interferometer (figure 2.1). The main advantage is the simultaneous measurement of radiation of all wavelengths leading to a faster data acquisition than by conventional dispersive instruments. A continuous source generates IR light over a wide range of infrared wavelengths. The infrared light is sent to the interferometer and splits the light into two paths: one path length is fixed and the other is moving. The light is recombined before sending it to the sample. The detector measures the intensity of the combined infrared beams as a function of the moving mirror displacement, the so called 'interferogram'. The Fourier transform converts the interferogram into the infrared spectrum we all recognize and use. The mid infrared region ranging from 2.5 to 25 μm (4000 - 400 cm^{-1}) shows most of the fundamental molecular vibrations making this region rich in chemical information. Large database and literature contain information for almost every ro-vibrational transition [4].

The Beer-Lambert-Bouguer law states that the absorption of light by a compound depends on the concentration of the absorbing species, the wavelength of the light and the thickness of the sample [91].

$$log\left(\frac{I_0}{I}\right) = \epsilon bc \tag{2.1}$$

I_0 is the intensity of the incident radiation and I the intensity of the transmitted radiation. ϵ refers to the molar absorptivity coefficient, b is the thickness of the sample and c the concentration of the compound in moles. Note that ϵ is specific for each compound at a particular wavelength. The term $log(I_0/I)$ is the absorbance, A, although, most of the spectrometers measure the ratio of the intensity of transmitted radiation and incident radiation (I/I_0) known as Transmittance.

$$A = -log\frac{I}{I_0} \tag{2.2}$$

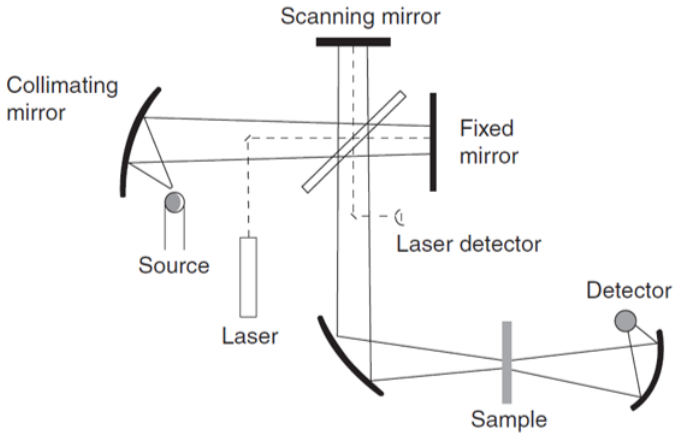

Figure 2.1: The optical arrangement of an FT-IR spectrometer. Figure extracted from [4].

This relationship implies that the intensity of the band observed in the spectrum is correlated to the concentration of the absorbing species at a given wavelength, either in the gas phase or in a surface.

The main reactants of plasma reaction, CO_2 and CH_4, have three and four fundamental vibration modes, respectively. Asymmetric and bending vibrations induce a variation in the dipole moment which are infrared active (the others will be active in Raman) [92]. Water, carbon monoxide and other short hydrocarbons are infrared active, too. However, H_2 (one of the main products of DRM reaction) and O_2, are not infrared active and can only be measured by Mass Spectrometry or Gas Chromatography. H_2 and O_2 density can be calculated when these techniques are not available by atom balance. An alternative technique is to measure *in situ* the atomic H and O densities in plasma by 'Actinometry' (see Appendix A).

When we perform IR transmission through gas/plasma, the good spectral resolution of the FTIR (0.2 cm^{-1}) allows to observe peaks from the rotational structure of each vibrational modes. When looking at IR spectra taken in transmission through a pellet, we observe the molecular vibrations of the species adsorbed in the surface. The absorption bands are broadened by the environment onto the surface of each absorbing molecule. The IR beam passes through the solid material, the reflection and diffusion are small enough to have a transmitted light recollecting information on the vibrations. Care should be taken when preparing an adequate pellet because a thick pellet can absorb the whole infrared beam or the adsorption bands intensity can saturate the signal. However, if the pellet is too thin, the wafer does not hold itself and can break easily, depending the material. Also, the absorption bands intensity could be very weak affecting the study of the surface.

Equipment and data treatment

Two FTIR spectrometers are used in this work. The FTIR spectrometer mainly used for DC-glow discharge sources was a Vertex 70v from Bruker. The glow discharge plasma reactor is adapted inside the sample compartment of the FTIR so that the IR beam passes through it. Absorption measurement can then be done either through the plasma or downstream the plasma in which case the reactor is only used as an IR absorption cell. The IR cell used CaF_2 windows resulting on transparency on the 4000 - 900 cm^{-1} region. The raw spectra were recorded in transmittance from 500 to 5000 cm^{-1} with a resolution of 0.2 cm^{-1}. The FTIR spectrometer is used for two purposes in this work:

a) measurement of molecule densities in the downstream gas from plasma reaction

b) *in situ* IR transmission experiments through a catalytic pellet exposed to plasma conditions.

In the first case, the downstream gas is sent to the IR cell located in the FTIR spectrometer. The script previously developed by Bart Klarenaar in LPP is used to estimate the gas fraction of CO_2, CO, CH_4, H_2O, C_2H_6, C_2H_4, C_2H_2, formic acid, methanol, formaldehyde and other molecules based on the HITRAN database [93, 94]. Figure 2.2 shows two representative fitted IR spectra. The resulting characterization of the gas phase is described in chapter 3 and briefly compared with the work of Edmond Baratte in his PhD thesis [87].

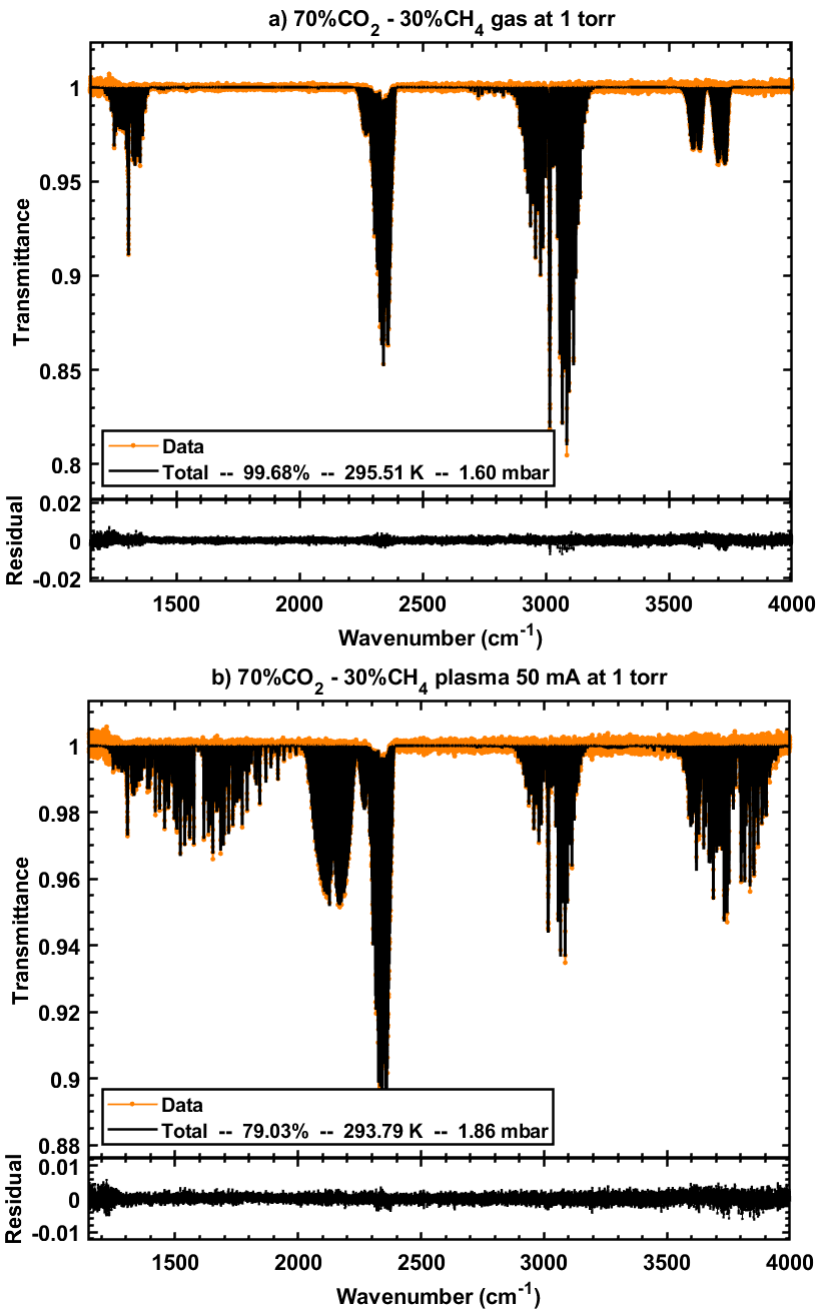

Figure 2.2: Fitted IR spectra of the downstream gas from 70%CO_2-30%CH_4 a) gas and b) 50 mA plasma at 1 Torr.

For the second case, a pellet of a given material is prepared by pressing around 50 - 90 mg between two disks of mica film with 1 ton of pressure. The resulting pellet had an average thickness of 411 μm. Then, the pellet is placed inside a glow discharge reactor having the shape of a cross, with a glass holder perpendicular to the path of the infrared beam (see figure 2.13 below). The spectra were taken using 'Rapid scan' mode through the whole set of experiments approximately every 8 seconds with 20 average scans and the diaphragm aperture was set to 8 mm. Using a Matlab script, the spectra was extracted, the transmittance converted to absorbance by equation 2.2 and the area of the bands was calculated by trapezoidal method after using linear regression for the baseline correction (figure 2.3). When the gas phase bands were overlapping with the surface adsorption bands, a polynomial fit was used to simulate the band shape and subsequently, the area was calculated as previously mentioned. The area of the

bands are plotted as a function of time. More information on the data treatment is provided in chapter 3 as well the validation of the data treatment for time evolution.

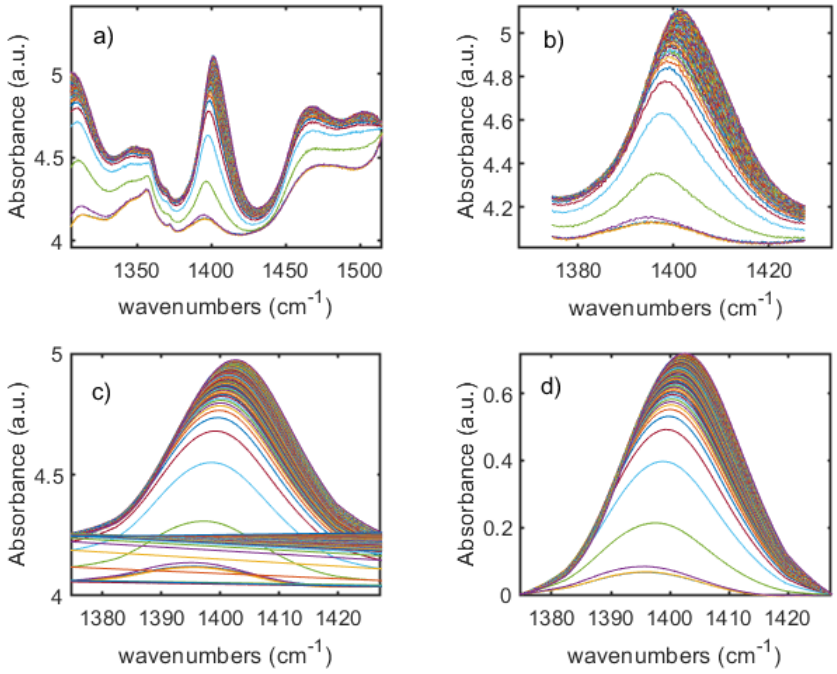

Figure 2.3: Simplified example of area calculated from bands observed in the IR transmission spectra, here the band HC: 1396 cm^{-1} is shown. a) The range in wavenumbers of the band was selected and b) cut, then c) a linear regression was drawn from one side of the band to the other. d) The linear regression was subtracted from the baseline leaving it at zero absorbance.

The second FTIR spectrometer is used for DBD plasma reactions. The fiber FTIR spectrometer used was a FT-MIR Rocket from Arcoptix. The optical fibers were installed in an IR cell with CaF_2 windows. The raw spectra were recorded in transmittance in the range 1700-5000 cm^{-1} with a spectral resolution of 1 cm^{-1}. The resulting spectra is the average of 10 infrared spectra. A spectra was recorded with the IR source off and this was called a 'dark'. Then, the IR source was on and stabilized for few minutes. With the reactor and IR cell empty, an IR spectra was recorded and used as a background. After, IR spectra were recorded for a given experimental condition. The dark spectra was subtracted to the background and experimental spectra. The experimental spectra was normalized by the background to obtain a corrected spectra with transmittance set to 100%. The transmittance was converted to absorbance to ease the estimation of area of the absorption bands. This FTIR spectrometer and method was used to measure the CO fraction in the downstream gas of DBD plasmas performed in chapters 8 and 9. The band in the range 2143-2222 cm^{-1} corresponding to CO vibration was extracted and the area estimated by trapoized method. The experimental area was used to later estimate the CO fraction according to the calibration described below.

Calibration

The calibration was done by sending small known amounts of CO diluted in O_2. The spectra was recorded at 750 and 450 Torr to account for the pressure broadening. The area of the band from 2143-2222 cm^{-1} corresponding to CO vibration was estimated with the trapezoid method using a Matlab script. Figure 2.4 shows the measurements and the linear regression of the CO area band as a function of

the CO fraction. The linear regression (dotted line) represents the fit of y values into the linear equation shown in the figure 2.4. The coefficient of determination R^2 is calculated to assess the linear relationship between concentration and area of the band 2143-2222 cm^{-1}.

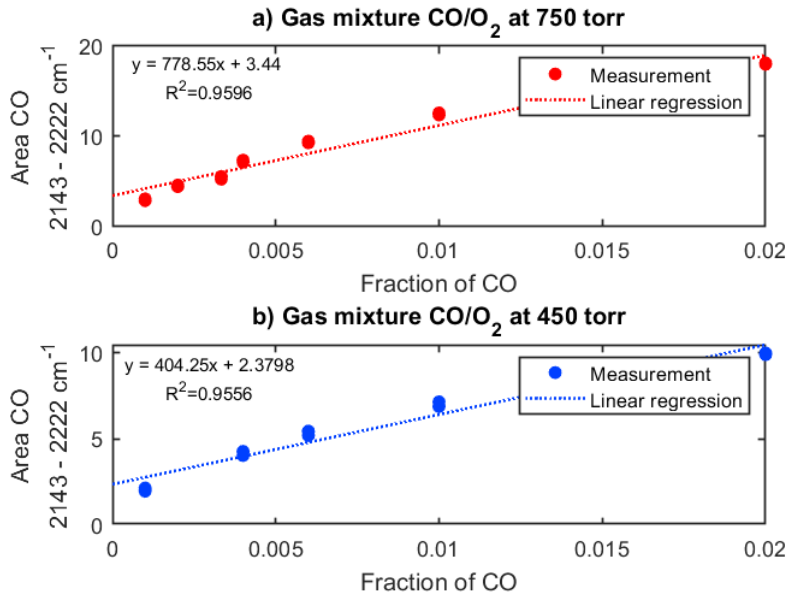

Figure 2.4: Calibration of CO by FTIR spectroscopy in a gas mixture CO/O_2 at a) 750 Torr and b) 450 Torr. The area of CO was extracted from the range 2143-2222 cm^{-1}. Total gas flow: 500 sccm.

In this case, R^2 is around 0.95 in both concentrations. To have a rough estimate of the CO fraction at 550 and 650 Torr, an extrapolation was done using the slopes and intercepts of the linear regressions at 750 and 450 Torr.

2.2.2 Optical Emission Spectroscopy (OES)

Optical Emission Spectroscopy relies on the collection, spectral dispersion and detection of light emitted by the plasma. The light detected comes from the de-excitation of an electronic state of a molecule or atom releasing a photon with a characteristic wavelength. The spectrometer generally consists of entrance slit, collimator, a dispersive element such as a grating or prism, focusing optics and a detector. Spectrometers tend to be in a compact format and detect a wide range of wavelengths which suits several applications like elemental analysis in ICP-OES or VOC detection in environmental sciences.

This technique remains very useful to study the electronic transitions occurring in the non-thermal plasmas in the UV and visible range. In many CO_2 plasmas, the predominant dissociation mechanism is direct electron impact which can lead to the excitation of certain electronic levels that are later studied in de-excitation processes. Figure 2.5 shows the transitions studied by OES in the energy level diagram of the main vibrational and electronic states of neutral components in CO_2 plasmas. Several de-excitation processes can be studied to give an insight on the composition and reduced electric field [95]. With Actinometry, the density of a reactive species of interest (like atomic O) is determined from the ratio of the intensity of emission from an excited state of the probed species to that from a rate gas (actinometer), which is added in a small quantity to the gas mixture. The details on the principles and calculations are described in Appendix A. A simplified equation from A.7 is represented as:

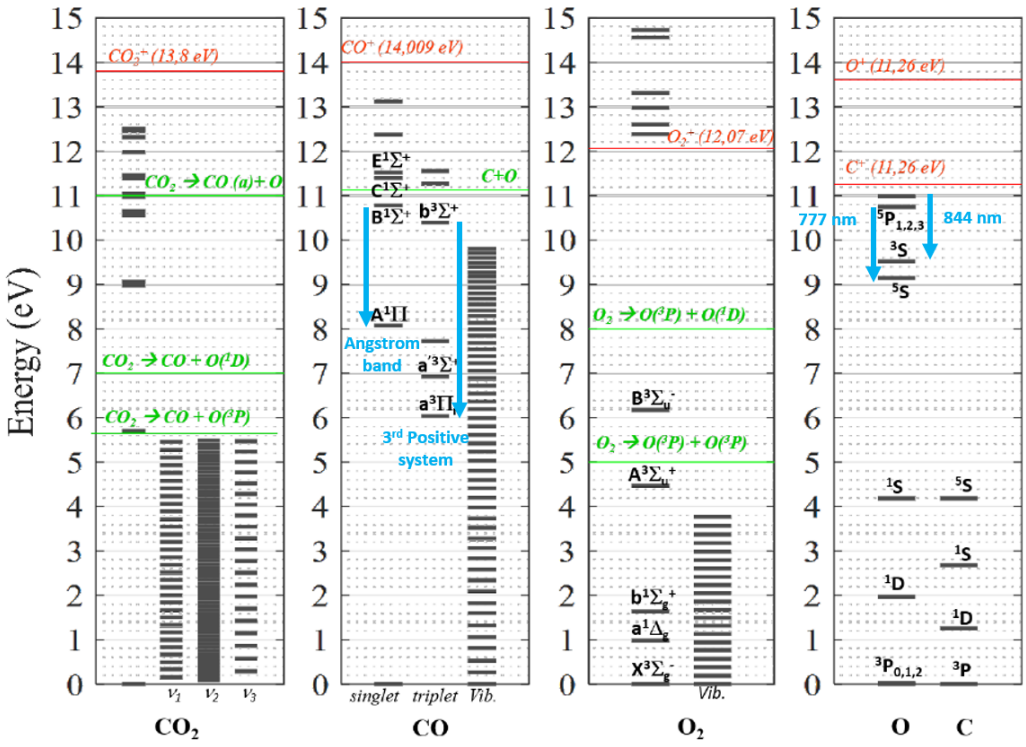

Figure 2.5: Diagram of energy levels of the main vibrational and electronic states of neutral components in CO_2 plasmas. The transitions observed by OES for CO and O are indicated in light blue arrows.

$$[O] = \frac{I_O^{\lambda(nm)}}{I_{Ar}^{\lambda(nm)}} \tag{2.3}$$

Equipment and data treatment

Two spectrometers were used: an AvaSpec-DUAL Avantes and Maya 2000 PRO spectrometers with moderately high spectral resolution. The spectra were taken from 200 to 800 nm with a spectral resolution of 0.1 nm. The emission from CO 3rd Positive System band 3PS ($B^3\Sigma+ \rightarrow a^3\Pi$), CO Angstrom band ($B^1\Sigma+ \rightarrow A^3\Pi$) at 483.5 nm, two O atom emission lines at 777 nm ($^5P_{1,2,3} \rightarrow {}^3S$) and 844 nm ($^3P_{0,1,2} \rightarrow {}^5S$) and H atom emission line at 656 nm (H_α) were evaluated and shown in figure 2.6. CO rotational temperature was obtained by fitting of ($\nu1$,$\nu2$) = (0,1) optical transition of CO Angstrom band as seen in figure 2.7. The procedure followed is described in [5].

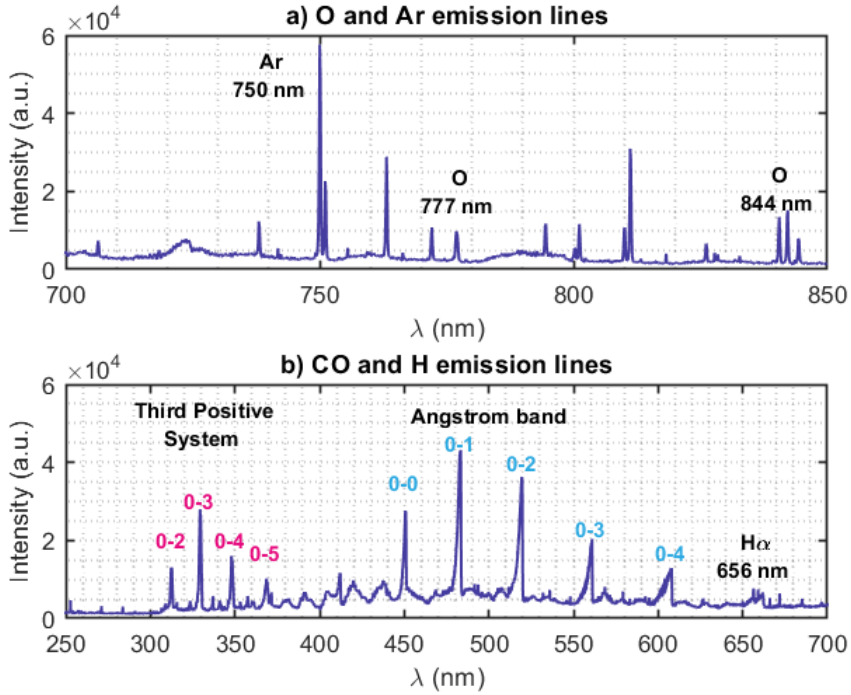

Figure 2.6: Example of Optical Emission Spectra of 95%CO_2-5%CH_4 plasma in Fluidized bed - glow discharge with 4 g Al_2O_3, 1.8 Torr and 30 mA. The spectra shows a) the O and Ar emission lines and b) CO and H emission lines. 3%Ar was added to the total gas flow.

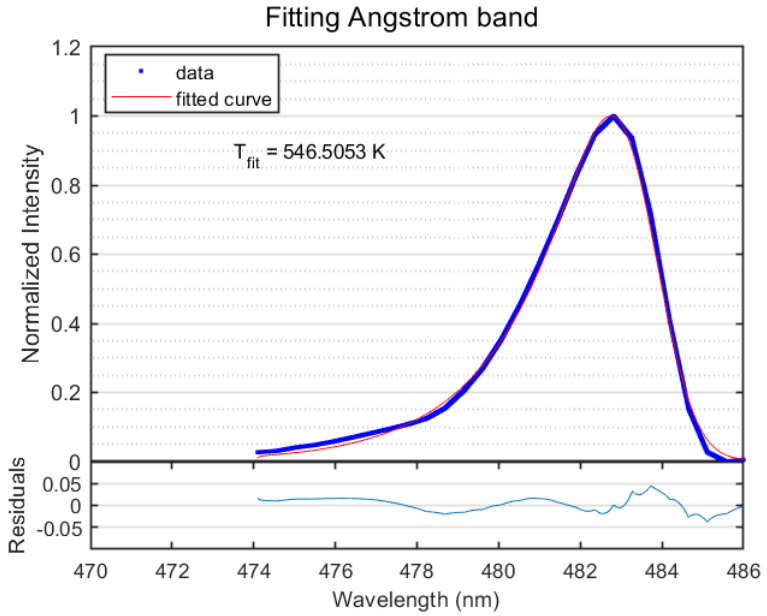

Figure 2.7: Example of fitting of CO Angstrom band for the calculation of the rotational temperature [5].

2.2.3 Mass Spectrometry (MS)

Principles

A Mass Spectrometer (MS) analyzes the chemical composition of a sample by mass-to-charge (m/z) separation. For gases, the sample is introduced through the inlet system to the MS instrument via a capillary or metering valve and pumped down with a vacuum system. Then, the neutral gas particles are ionized by an ion source and subsequently separated in a mass filter on the basis of their m/z.

Four types of mass filters are widespread use nowadays:

1. *Sector field* devices bend the trajectories of the ions as they pass through the mass filter with an electric and/or magnetic field.

2. *Time-of-Flight* (TOF) spectrometers utilizes an electric field to accelerate ions with the same potential and measures the time they take to reach the detector.

3. *Ion traps* confine the ions with high radio-frequency (RF) field and sequentially ejected in order of m/z ratio to the detector.

4. *Quadrupole mass filter* uses the resonance of the moving ions in a high frequency field similar to ion traps except that ions are continuously formed, accelerated and analyzed [96].

Quadrupole mass analyzers were firstly used for the analysis of residual gas until nowadays. Because only light gases are generally involved, the mass range of the quadrupole needed is around 1 – 200 m/z making it suitable for DRM reaction composition. Usually compact and robust. Since the mass scale is linear to the applied amplitude of the RF voltage it has a better ion-ratio precision in comparison to other mass analyzers (*e.g.* ion trap).

The ions are created by electron bombardment ionization in the ion source, then directed to the quadrupole mass filter. As the name suggests, the quadrupole consist of 4 parallel rods arranged in the form of a square. Each opposing rod pair (designed + or -) is connected to each other. Between the two pairs of rods, an electrical voltage consisting of a DC portion U and an AC portion with amplitude V and frequency $f = \omega/2\pi$ applied:

$$U_{quad} = U + V * cos\omega t \tag{2.4}$$

An electrical quadrupole field is formed between the rods. Ions of varying mass are injected axially into the rod system at approximately equal energy and move through the rod system at uniform velocity. The applied quadrupole field deflects the ions in the X and Y directions. If the combination of RF and direct voltages applied to the rods is correctly chosen, only ions of one particular m/z will be successfully transmitted to the detector. However, many ions are lost in the quadrupole mass filter, the majority do not reach the detector loosing sensitivity and resolution. Nonetheless, they are simple, compact and widely used in combination with other techniques like Gas Chromatography or Inductively Coupled Plasmas.

Equipment and data treatment

Two mass spectrometers were used to analyze the downstream gas of the plasma reactions performed in DC glow discharges and DBD reactors. The mass spectrometer used for the catalytic screening on the coaxial DBD reactor in Bucharest was a Prolab from Thermo Scientific with an open ion source with Tungsten filament. The measurements were performed in a mass range 1-50 m/z using a Faraday detector. The vacuum pressure at the inlet of the instrument was around 1 e^{-6} torr for all the measurements performed. The data from the resulting m/z ratio pattern is extracted using a Matlab script. The

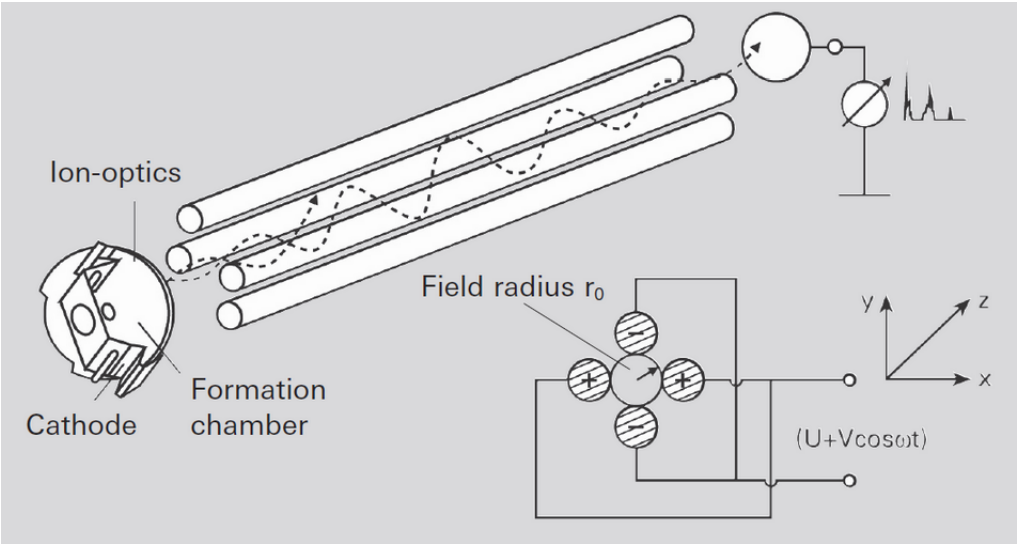

Figure 2.8: Schematic of the analysis of ions in a quadrupole mass analyzer. Ions are created through electron bombardment ionization in the ion source, then they are separated by the m/z ratio in the rod system (quadrupole) and the ions are detected at the exit by the ion detector. Figure extracted from website of Pfeiffer vacuum (www.pfeiffer-vacuum.com/en/, date of extraction: 15/12/2022).

masses of interest (15, 16, 18, 28, 32 and 44) that correspond to CH_3, O/CH_4, H_2O, N_2/CO, O_2 and CO_2, respectively, are extracted. Only ^{12}C and ^{16}O are considered. No calibration was performed using this instrument and only the ion current signals obtained during plasma OFF and plasma ON are compared and used to estimate conversion of CO_2 and CH_4. More details are described in chapter 8.

The mass spectrometer used for the glow discharge reactors in LPP was a QMG 220 from Pfeiffer Vacuum with a grid ion source with tungsten filament. The measurements were performed in a mass range 1-50 m/z, a scan speed of 500 ms/amu and voltage of 1000 V. The detector used is a SEM detector. The vacuum pressure at the inlet of the instrument range 1 e^{-6}-1 e^{-5} mbar for all the measurements performed. The data from the resulting m/z ratio pattern is extracted using a Matlab script. The masses of interest (1, 2, 4, 12, 15, 16, 18, 26, 28, 30, 32 and 44) that correspond to H, H_2, He, C, CH_3, O/CH_4, H_2O, C_2H_2, N_2/CO, C_2H_6/H_2CO, O_2 and CO_2, respectively, are extracted. Only ^{12}C and ^{16}O are considered. For non-infrared active molecules (H_2 and O_2), a calibration was done by sending known amounts of the given molecules in a gas mixture similar to the experimental downstream gas. The details are given in the next subsection. For other molecules which are infrared active like CO_2, CH_4, C_2H_6/H_2CO, C_2H_2 the concentrations were compared by IR absorption results. Specifically the relative concentrations of C_2H_6/H_2CO and C_2H_2 in the downstream gas are discussed by MS and IR absorption in subsection 3.2 of chapter 3.

Calibration

The calibration of the mass spectrometer at LPP is done using gases of the molecules of interest: O_2 and H_2. The calibration was performed roughly every two weeks during the experimental campaign of the downstream gas characterization reported in section 3.2. Mass 32 and 2 are considered for the measurement of O_2 and H_2, respectively. The gas line is set at 2 Torr and the pressure of measurement in the MS is set at 1 e^{-6} mbar for O_2. The total flow is fixed to 7.4 sccm and the O_2 fraction was set by varying pure O_2 gas flow mixing in CO_2 gas. Figure 2.9a) shows an example of calibration for O_2 ranging 0 (no O_2 gas flow) to 1 (pure O_2 gas flow) fraction. The linear regression (dotted line) represents the fit of y values into the linear equation and R^2 the coefficient of determination as shown in the figure

2.9a. In the case of O_2, R^2 is more than 0.98 indicating a strong relationship and the linear equation $y = mx + b$ obtained is used to estimate the O_2 fraction during the downstream gas characterization in CO_2-CH_4 plasmas.

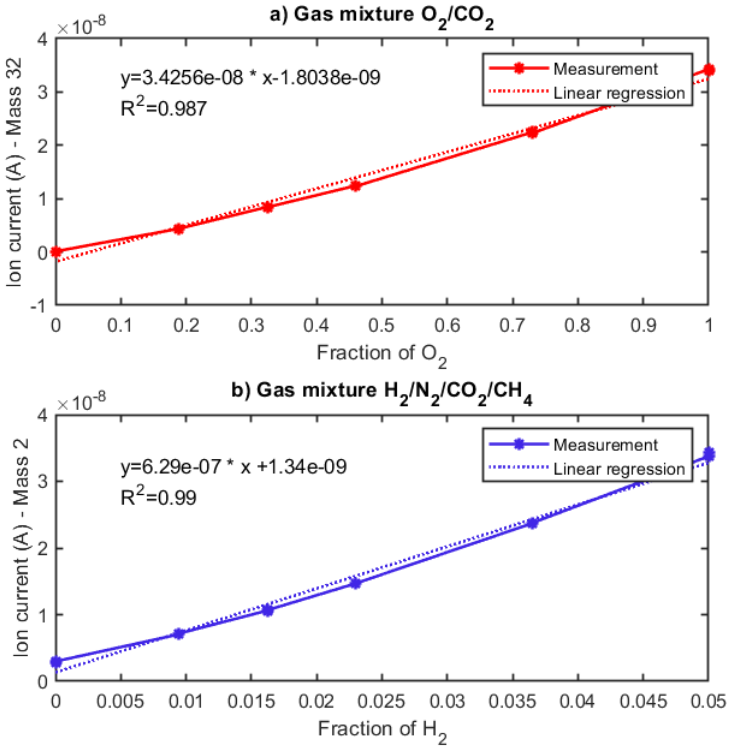

Figure 2.9: Example of MS calibration of a) O_2 in a gas mixture of O_2/CO_2 and b) H_2 in a gas mixture of $H_2/N_2/CO_2/CH_4$. Mass 32 and 2 are considered for the measurement of O_2 and H_2, respectively. The gas line is set at 2 torr and the inlet pressure to the MS is set at 1 e^{-6} mbar for O_2 and 1 e^{-5} mbar for H_2. Total gas flow: 7.4 sccm. Solid line: measurement, dashed line: linear regression fit.

In the case of H_2 calibration, $5\%H_2/95\%N_2$ gas bottle is used. The pressure of measurement in the MS is set at 1 e^{-5} mbar. The total flow is set to 7.4 sccm and the H_2 fraction was set by varying the $5\%H_2/95\%N_2$ gas flow mixing into equal parts of CO_2 and CH_4 gas. The mixing CO_2 and CH_4 gas intended to somewhat replicate the gas mixture in which into H_2 fraction would be detected. Figure 2.9.b) shows an example of calibration for H_2. The maximum H_2 fraction that could be reached was 0.05 ($5\%H_2$). The linear regression shown in the figure is used to extrapolate ion current signals from the MS. The R^2 estimated is around 0.99 indicating a strong relationship between concentration and signal. However, the range of calibration is limited to maximum 0.05 fraction of H_2 which could not longer apply at larger concentrations of H_2 in the gas mixture. This is considered on the interpretation of the results obtained during downstream gas characterization in section 3.2.

2.3 Characterization of catalytic materials

Non-thermal-plasmas (NTP) are known to be mild plasmas: with (relatively) low temperature neutral gas molecules meanwhile the electrons have high temperature (1-10 eV). Nevertheless, the exposure of catalytic materials to NTP can modify their structure, composition, oxidation state, etc. Hereinafter, the characterization techniques are described, along with the advantages and limitations, and the general

parameters for the testing. The techniques mentioned were performed to analyze the sample materials used before and before plasma reaction throughout this thesis work. The instruments are located in the Department of Organic Chemistry, Biochemistry and Catalysis in the University of Bucharest, Romania. Most of the analysis were performed by me, except SEM-EDX and XPS analysis which were performed by other analysts and they are credited in section 2.3.5 along with a brief description of the purpose and limitations of the given technique.

2.3.1 DRIFTS

Diffuse Reflectance Infrared Fourier Transform Spectroscopy (DRIFTS) is a special reflection sampling technique combined with IR absorption spectroscopy [6]. It is usually applied to solid samples that are difficult to analyze in transmission. The principle of FTIR absorption spectroscopy has already been described in 2.2.1. Instead of measuring the IR beam transmitted passing through the sample (pellet or plasma/gas), DRIFTS relies on the scattering of the incident light within the sample (figure 2.10). In this work, DRIFTS is used to analyse solid samples before and after plasma experiments.

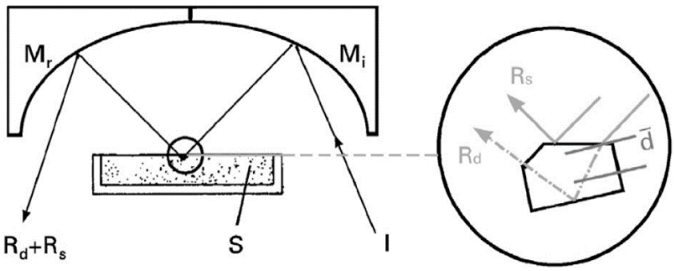

Figure 2.10: Schematic of diffuse reflection measurements. Figure extracted from [6].

The model mostly used to describe the diffuse reflection is the Kubelka-Munk (KM) model [97]. Considering the ratio of reflectance of the sample of infinite depth and the reflectance of a reference powder (KBr or KCl) measured by the instrument,

$$R_\infty = \frac{R_{sample}}{R_{standard}} \tag{2.5}$$

we can obtain the Kubelka-Munk function of the diffuse reflectance:

$$f(R_\infty) = \frac{(1-R_\infty)^2}{2R_\infty} = \frac{\alpha}{S} \tag{2.6}$$

where α is the absorption coefficient and S is the scattering coefficient.

The advantage of this technique is the ease to analyse powder samples without the need to prepare pellets for transmission measurements. However, the scattering coefficient depends on the particle size and refractive index of the sample, and it does not have a strong function to the wavelength so the KM model considers it as constant. Although, care should be taken when preparing samples as reproducible as possible. Nonetheless, KM model can also be applied as well for UV spectroscopy to calculate the band gap of certain materials [98].

DRIFT spectra was recorded with a Bruker Tensor II spectrometer. The spectra were taken in Reflectance mode resulting in Kubelka-Munk arbitrary units as a function of wavenumbers. The spectra

were collected from 4000 - 400 cm^{-1} range with 32 scans average and 4 cm^{-1} resolution. Powder KBr is used as reference material.

2.3.2 X-Ray Diffraction (XRD)

X-Ray Diffraction is a non destructive technique used for the characterization of crystalline samples. XRD works on the principle of Bragg's equation, which can be described in terms of reflection of X-ray beam incidence on a crystal plane of the sample [99].

$$\lambda = 2d_{hkl}sin\theta \tag{2.7}$$

d_{hkl} is the lattice spacing of the diffracting hkl plane, λ is the wavelength of the x-ray beam and θ the diffraction angle.

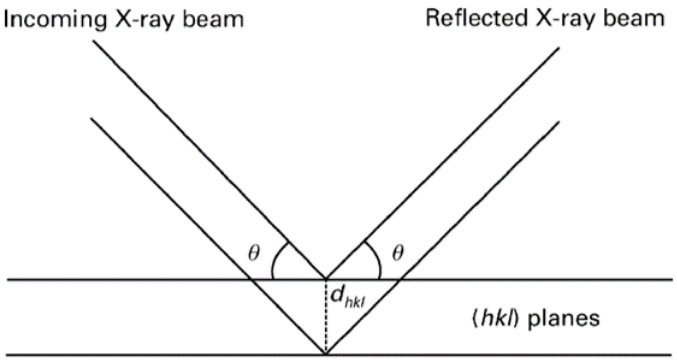

Figure 2.11: Reflection from the planes (hkl) with interplanar spacing d_{hkl}. Figure extracted from [7].

A beam of X-rays is passed through the specimen and is scattered, or diffracted, by the atoms in the path of the X-rays investigated. The interference occurring due to scattering of X-rays with each other is observed applying Bragg's law and a suitably positioned detector, and crystalline structure characteristics of the material are determined.

XRD comes very handy to study a permanent change on the crystalline structure specially after being in contact with reducing agents in plasma conditions (*e.g.* electrons, H_2). The materials used during DRM plasma reaction were analyzed by XRD and compared to the pristine material. XRD patterns were recorded at room temperature with a Shimadzu XRD 7000 diffractometer using a Cu Kα radiation source with $\lambda = 1.540562$ Å, 40 kV, 30 mA, 2θ scan range 10°-80° and a scan speed 2° per minute.

2.3.3 Surface area analysis by BET theory

The Brunauer-Emmett-Teller (BET) theory is a common approach to calculate the surface area from an equilibrium adsorption isotherm, measured at the normal boiling point of the adsorbate (usually N_2 at 77 K). BET theory extends the Langmuir monolayer molecular adsorption model to multilayer layers and assumes the adsorption energy to be independent from the adsorption sites [100].

The BET equation describes the relationship between the number of gas molecules adsorbed on the first monolayer of adsorbate at a given relative pressures of the actual and saturated vapor pressure of the adsorbate $x = (P/P_0)$:

$$\frac{x}{W(1-x)} = \frac{1}{C * W_{ml}} + \frac{C-1}{C * W_{ml}} * x \tag{2.8}$$

W is the mass adsorbed at relative vapour pressure, W_{ml} is the required mass of adsorbate forming a complete monolayer adsorbed on a given sample and C is a constant expressing the differences in the heat of adsorption of the first and second or higher layers. According to equation 2.8, the linear regression of $y = (P/P_0)/W(1 - (P/P_0))$ versus $x = (P/P_0)$ results on intercept b and slope m:

$$b = \frac{1}{C * W_{ml}} \tag{2.9}$$

$$m = \frac{C - 1}{C * W_{ml}} \tag{2.10}$$

The mass of the gas adsorbed in the monolayer is obtained by the sum of the intercept and the slope:

$$\frac{1}{W_{ml}} = m + b \tag{2.11}$$

Knowing this value, the specific surface area SSA ($m^2 \cdot g^{-1}$) can be estimated:

$$SSA = \frac{W_{ml}}{M * m} * N * A \tag{2.12}$$

where M is nitrogen molar mass, m the sample mass, A is the cross sectional area (0.162 nm^2) of nitrogen and N is Avogadro's number.

Before performing the adsorption step, a physical removal of water and other volatile molecules should be removed from the sample. 50 to 150 mg of sample are introduced into a tube cell connected to the degassing station from the physisorption analyzer. After degassing around 300°C for few hours, the tube cell with the sample is connected to the adsorption station. The adsorption is done by adding incremental introduction of the adsorbate: the difference between the measured pressure and that of the empty cell correlate to the moles of N_2.

A long term exposure to NTP could change the material characteristics such as the surface area or the pore size. These measurements were carried out using an Micromeritics ASAP2010 apparatus. Around 0.1 g of powder sample is used for testing. The pore size distribution is possible to obtain from the measurements using the BJH (Barrett, Joyner and Halenda) method.

2.3.4 Temperature Programmed Desorption (TPD)

Temperature programmed desorption is a technique widely used in catalysis because the technique allows to study the interaction of reaction gases with solid surfaces resulting in a powerful technique for the evaluation of active sites including adsorption, surface reaction and desorption. Acid-base properties can also be probed. Routine techniques assess the distribution of the quantity and strength of acidic and basic sites including NH_3 and CO_2, respectively. In a typical TPD run, a small amount of sample (usually powder) is placed in a U-shaped tubular reactor. After an inert gas flows into the sample, a probe gas is adsorbed on the catalyst surface. Then the sample is heated at a linear heating rate under the carrier gas flow. The change of the reaction gas that is desorbed from the surface upon heating is monitored with a downstream detector as a function of temperature. The desorption temperature is taken as a qualitative measure of the strength of interaction. The same principle can be applied to reduction (usually TPR-H_2) and oxidation (TPO-O_2) to assess the reduction/oxidation capacity of a catalyst as a function of temperature [101].

Temperature programmed desorption is experimentally simple to do in chemisorption analysers, inexpensive and ease to analyse powders. The main feature of this technique is that the sample reaches the thermal equilibrium with the system, however, this does not represent what occur in testing conditions

(high pressure or vacuum, high electron temperature, etc.). Nonetheless, the results aid to compare different catalysts and help describe the surface mechanisms in such materials.

TPD-CO_2 experiments were carried out in an AutoChem II 2920 station from Micromeritics. The samples, placed in a U-shaped quartz reactor with an inner diameter of 0.5 cm, were pretreated under He (Purity 5.0, from Linde) at 300°C for 30 min and then exposed to a flow of CO_2 (99.998%, SIAD) for 1 h. After that, the samples were purged with a flow of He (50 ml/min) for 30 min at 25°C in order to remove the weakly adsorbed species. TPD started with a heating rate of 3°C/min until 400°C and remained at constant temperature for 20 min. The desorbed products were analysed with a TC detector. The desorbed CO_2 molecules concentration was determined using a calibration curve expressed as mmol per gram of catalyst. The mmol g^{-1} were converted to molecules g^{-1} by multiplying by Avogadro's number (6.0221415 x 10^{20} $mmol^{-1}$).

2.3.5 Other characterization techniques

In this subsection, a brief description on additional techniques used to analyze the catalytic materials tested during this thesis. These techniques were performed by other laboratories aiming to help elucidating the effect of plasma on the catalytic materials.

SEM-EDX

Scanning Electron Microscopy (SEM) with Energy Dispersive X-Ray Analysis (EDX) was performed by Instituto de Carboquimica (ICB) in Zaragoza, Spain. SEM provides detailed high resolution images of the sample by rastering a focussed electron beam across the surface and detecting secondary or backscattered electron signal. This technique allows to analyse materials from mm range size to around 50 nm. On the nanometric scale, covering the sample with gold nanoparticles can help to improve the resolution but Transmission Electron Microscopy (TEM) might be necessary on such cases. EDX is used to provide elemental identification from the sample bulk and allows to quantitatively and qualitatively determine the composition of the material tested. It can detect up to 0.1% weight. The resulting spectrum is in KeV versus counts per second (*cps*). The peaks are characteristic of each element but some might overlap. Therefore, several peaks are needed to confirm the presence of a given element on the sample.

The main purpose is to obtain images on the Al_2O_3 used in fluidized bed - DC glow discharge and CeO_2 used on *in situ* FTIR transmission experiments. In addition, information regarding the composition and impurities that might be present before and after plasma reaction. The analysis was performed by Nuria Ferrer Santolaria along with Maria Victoria Navarro.

X-ray Photoelectron Spectroscopy (XPS)

XPS is a quantitative technique for measuring the elemental composition of the surface of a material, chemical and electronic state. It permits the identification of particular elemental species on the basis that each element has a characteristic set of binding energies. XPS is a surface technique that normally probes to a depth of 10 nm and requires ultra vacuum conditions [102]. Overall, XPS allows to characterize the surface of catalysts involved in chemical reactions. However, overlap of certain bands might occur and correct deconvolution of the bands must be done for proper identification.

The composition and the oxidation state are important information regarding the effect of non-thermal plasmas on the catalytic material, specifically on CeO_2 which is known to oxidize and reduce quite easily. The XPS analysis and data treatment were performed by Laura Abramiuc in the National Institute of Materials Physics in Măgurele, Romania.

2.4 Plasma discharge types and reactors used

2.4.1 DC Glow discharge

Glow discharge is described as a self-sustained continuous DC discharge with a cold cathode, which emits electrons as a result of secondary emission mostly induced by positive ions bombardment [8]. The electrons are ejected around at 1 eV from the cathode, the electric field increases leading to electronic excitation. Subsequent acceleration of electrons results in ionization of atoms/molecules, and charged species multiply in the cathode dark space. Then, there is a decrease in the electric field, electron energy and ionization rate but an increase in radiation. This is the brightest region (negative glow). The plasma density decrease, the electric field slowly grows and the electrons reach an average electron energy up to 1-2 eV and light is emitted. The electron density is then typically around 10^9-10^{11} cm^{-3} in what is called the *positive column*. This part of the discharge, considered homogeneous and electrically neutral, is the largest part of the plasma (if the electrodes are distant enough). Finally, approaching the anode, the ions are repelled and the electrons pulled out from the positive column creating a negative space charge which leads to an increase in the electric field in the anode layer. [8]. The homogeneity of the positive column is what makes this discharge ideal for fundamental studies as will be seen later.

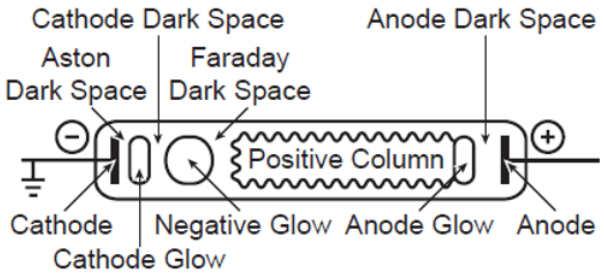

Figure 2.12: Schematic of structure of a glow discharge in a long tube. Figure extracted from [8].

Equipment and experimental conditions

Three different DC glow discharge reactors are used throughout this work:

1. A simple DC glow discharge is used to characterize the downstream gas by FTIR spectroscopy. The reactor has an inner diameter is 2 cm with a outer distance of 23 cm between electrodes enclosed by CaF_2 windows. The plasma volume is around 57.17 cm^3. This reactor was placed upstream to the IR cell placed in the sample compartment of the FTIR spectrometer. Other measurements were made at LPP using this version of DC glow discharge reactor but in that case, the discharge axis is collinear with the infrared beam axis to allow rotational and vibrational temperature measurements directly in the plasma as performed in Edmond Baratte's thesis [87].

2. A cross shaped glow discharge reactor made of glass is used to study *in situ* the surface adsorption of a catalytic material (figure 2.13). The reactor has an inner diameter is 2 cm with a outer distance of 18.2 cm between electrodes enclosed by CaF_2 windows. The plasma volume is around 41.78 cm^3. The pellet sample is sustained in a glass holder and placed in the path of the infrared beam. This reactor is used for 3 types of experiments in chapters 4 and 5:

    I *in situ* experiments. The purpose is to look at the surface adsorption bands under plasma conditions mainly CO_2, CO_2-CH_4, O_2 plasmas and others gases.

II downstream gas experiments. The effect of the plasma composition is evaluated without the presence of electric field, ion bombardment, temperature, etc.

III adsorption tests. The aim is to observe the adsorption of stable molecules over time using CO_2, CO and CO_2-CH_4 gases, along with water impurities inherent to the gas line and gas bottle.

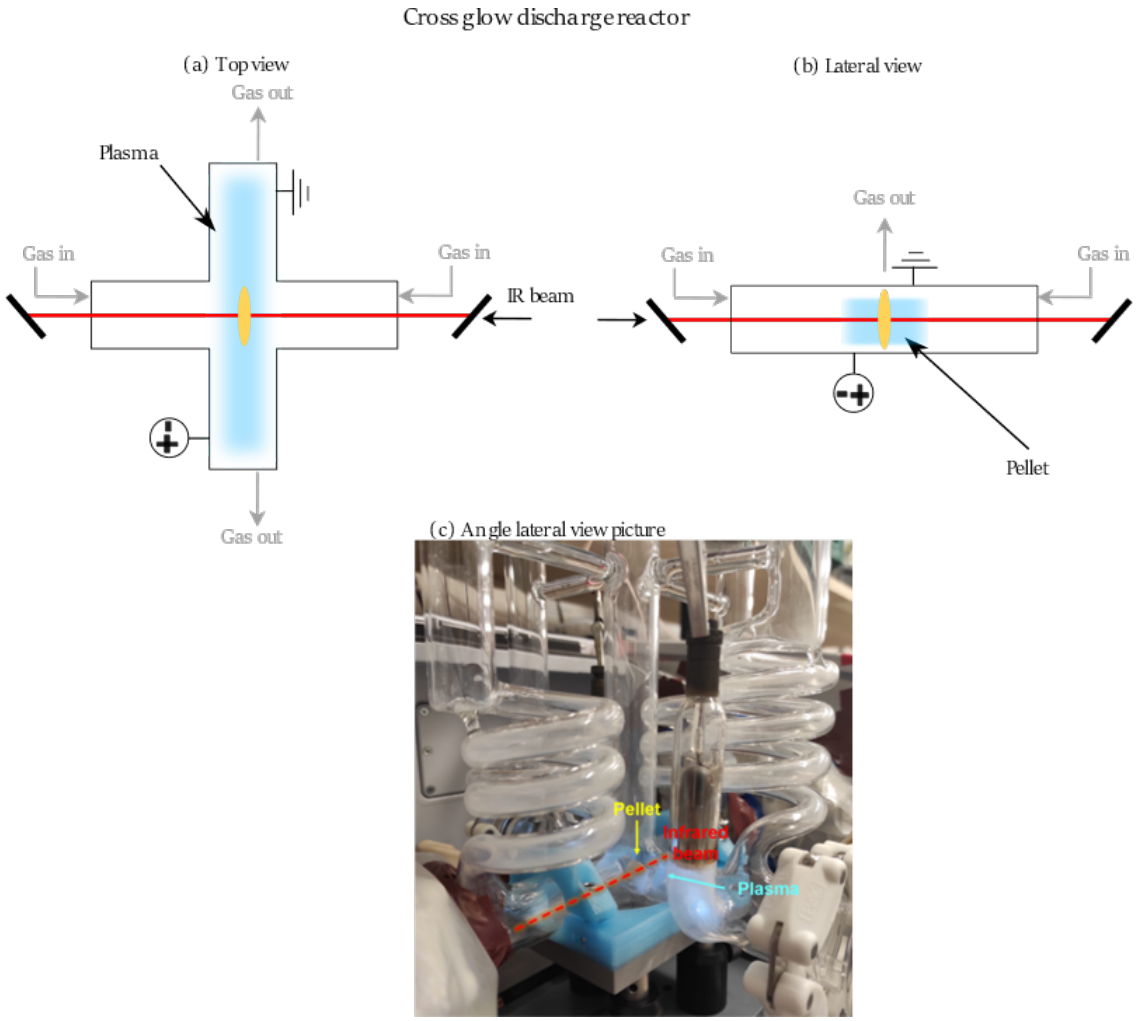

Figure 2.13: (a) top view and (b) lateral view of the schematic of Cross DC glow discharge for *in situ* FTIR transmission experiments, (c) angled lateral view picture of the actual reactor.

In this work, the interest of the cross configuration is to be able to expose the catalyst pellets to exactly the same plasma while having the infrared beam perpendicular to the plasma axis. Thus, the contribution of the gas phase in the measured spectra is simpler because it is essentially thermalized gas and not vibrationally excited one, which is easier to decouple from the absorption bands of the adsorbed species we are trying to study here.

3. Another variant of the DC glow discharge reactor with exactly the same diameter is used to obtain a plasma with a fluidized bed. A porous glass disk is embedded across the section of the 2 cm diameter tube in order to hold catalyst powder and be able to obtain a fluidized bed - glow discharge reactor (figure 2.14). The discharge is established between two electrodes separated by 23 cm. The plasma volume is around 57.17 cm^3. The electrodes are slightly offset to the side of the main tube to ensure that only the positive column of the discharge fills the main part of the reactor where the fluidized bed reactor (FBR) is located (this was also the case in the cross reactor). The powder

particles are hold inside the reactor by the porous disk embedded across the tube around 6.5 cm from the outer side of the bottom electrode. Above the discharge region, a cyclone is placed to allow the particles to fall back into the reactor. A pressed glass wool was installed at the exit of the FBR to prevent any possible particle to reach the gas line.

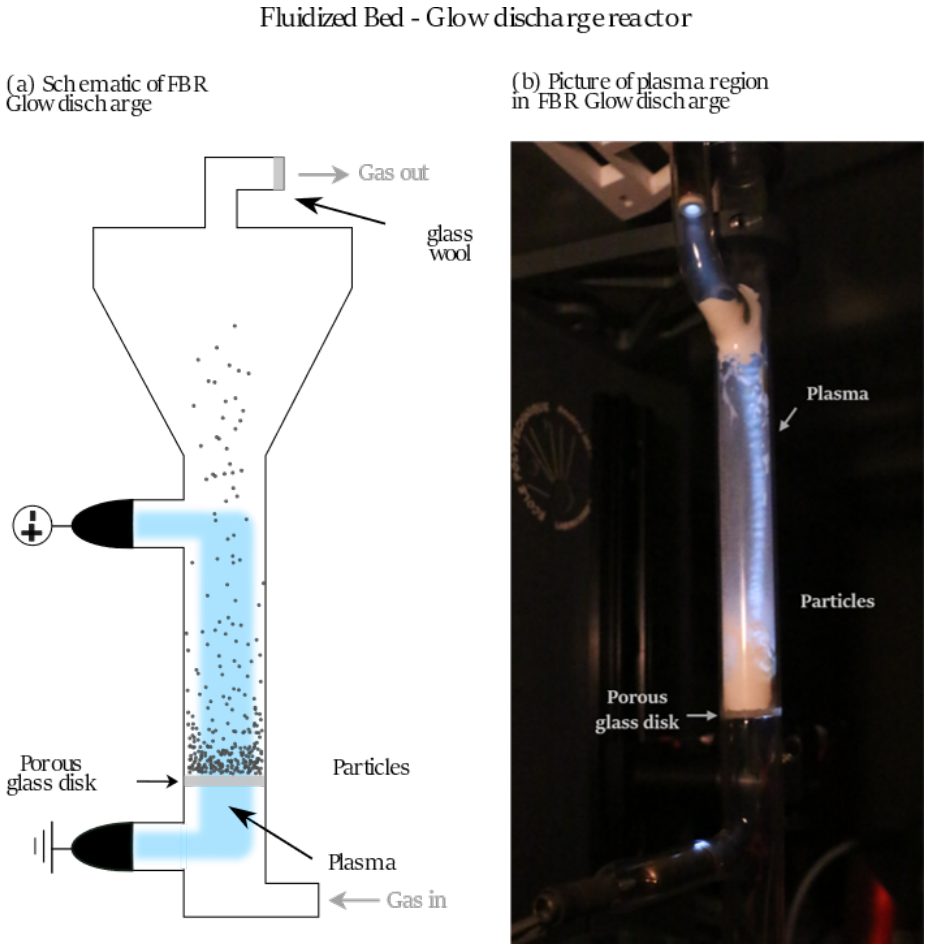

Figure 2.14: (a) Schematic of the Fluidized Bed Reactor FBR - Glow discharge and (b) picture of the actual FBR - Glow discharge

A continuous DC power supply is used for all measurements varying the current from 10 to 50 mA. The gas was evacuated by a scroll pump (Edwards, XDS35) maintaining a low pressure in the system. The flow is supplied by Bronkhorst flow controllers from different capacities using gas from bottles of pure CO_2, CO, O_2, CH_4, Ar, He and 5%H_2-N_2.

2.4.2 Dielectric Barrier Discharge (DBD)

Dielectric Barrier Discharges are self sustained electrical discharges between two electrodes separated by an insulating dielectric material. DBD were initially used for the industrial production of ozone but nowadays they could be applied in a diverse range of applications such as treatment of liquids for antimicrobial purposes, decontamination of biological surfaces or even the treatment of fabric surfaces [103–105]. DBDs do not have an homogeneous discharge region since they are dominated by streamers but they can operate easily at atmospheric conditions.

When a high enough electric field is applied to cause a breakdown in the discharge gap, *micro-discharges* are formed (figure 2.16). In case of DBD, this electrical breakdown occurs because of the

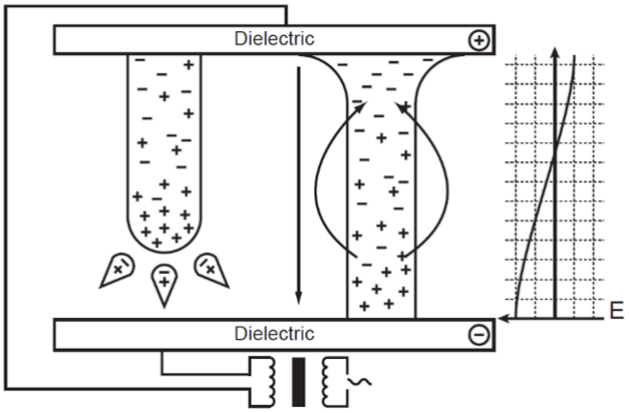

Figure 2.15: Schematic of the formation of a streamer and the plasma channel. Figure extracted from [9].

charging of the insulator surface. The charge previously adsorbed on the surface of the dielectric can help the breakdown by providing the initial seed electron necessary to start the streamer mechanism. The insulator limits the amount of charge and average current density in the gas preventing a spark or arc discharge keeping the plasma in non-thermal-plasma regime [106]. At atmospheric pressure (or even higher), electron avalanches create a space charge and thus, an additional electric field which enhances the growth of secondary electron avalanches locally. The repetitive generation of these micro-discharges visually appear as thin discharge channels often named filaments [106]. In this filamentary mode, the electric conductivity is restricted to the micro-discharges and the gas that is not ionized serves as a reservoir to absorb the energy in the form of heat dissipated and to collect and transport the long-lived species [10].

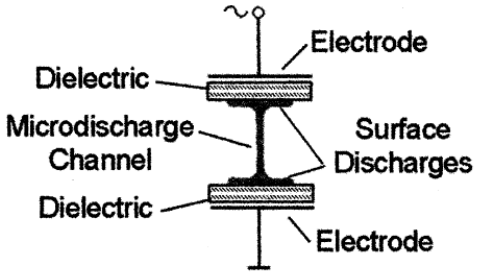

Figure 2.16: Schematic of a micro-discharge in a DBD. Figure extracted from [10].

A DBD plasma at normal pressure with moderate high voltage amplitudes is operated with a discharge gap typically in the range of 0.5–10 mm. The high voltage amplitude is in the range of 1-100 kV [106]. At atmospheric pressure, electron densities of 10^{14} to 10^{15} cm^{-3} and current densities in the range of 100 to 1000 A cm^{-2} are reached. The total charge transferred in a micro-discharge depends on the gas properties and can be influenced by the gap spacing and by the properties of the dielectric [10].

Equipment and experimental conditions

Innovative configurations have been developed to fit several applications but here I focus on coaxial double layer DBD configuration. The three DBD reactors used are described in the following:

1. A coaxial DBD was constructed to support cerium oxide powder for catalytic performance testing

in the packed bed (PB) mode at the University of Bucharest. The high voltage (HV) electrode is composed of a glass tube of outer radius of 0.7 cm with a metal long flat stick of stainless steel inside along with an electrolyte solution of 1 M of NaCl. The level of the electrolyte solution was 5.5 cm. The HV electrode was placed inside another glass tube concentrically. The outer tube has an inner radius of 0.74 cm and it is surrounded by copper wire serving as ground electrode. The schematic is shown in figure 2.17. The discharge volume was calculated to be 1.045 cm^3. The outer tube has a glass base with pores of $\sim$ 0.1 cm radius embedded in the bottom part of the tube where several glass beads where placed to supported glass wool which prevented the fall of powder material during catalytic testing. The catalytic tests were performed with a ns pulsed power supply of 300 Hz and 20 kV capacity.

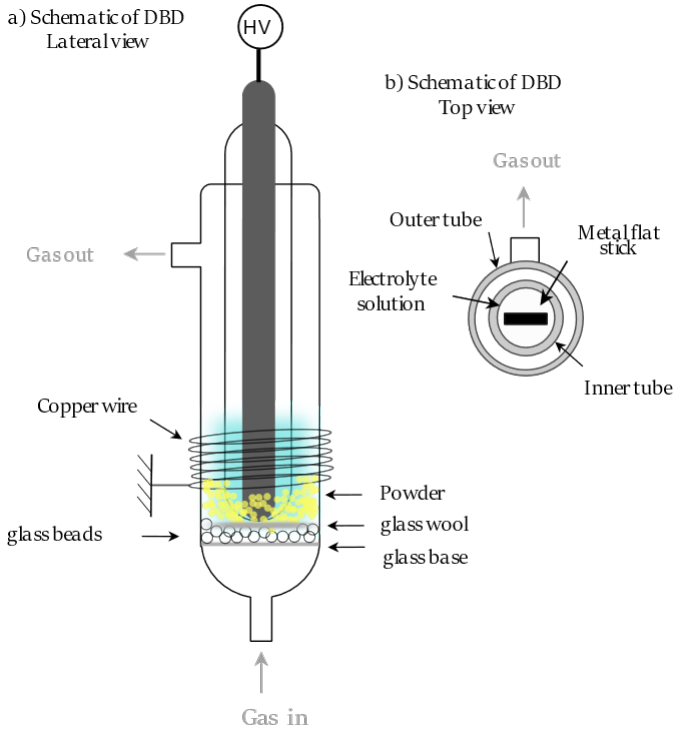

Figure 2.17: Schematic of the DBD packed bed for catalytic testing (a) lateral and (b) top view. Reactor used in University of Bucharest, Romania.

2. A coaxial DBD was constructed to serve as a packed bed - DBD plasma reactor (PB-DBD) located at LPP. The high voltage electrode is composed of a thin glass tube of outer radius of 0.4 cm with a metal long stick well adjusted in diameter to prevent ignition inside this inner tube. The HV electrode was placed inside another glass tube concentrically. The outer tube has an inner radius of 1 cm and it is surrounded by copper tape serving as ground electrode of 2.1 cm height. The schematic is shown in figure 2.18. The discharge volume was calculated to be 1.38 cm^3. The outer tube has a porous glass disk embedded and on top a layer of glass wool was placed to prevent the fall of powder material during catalytic testing.

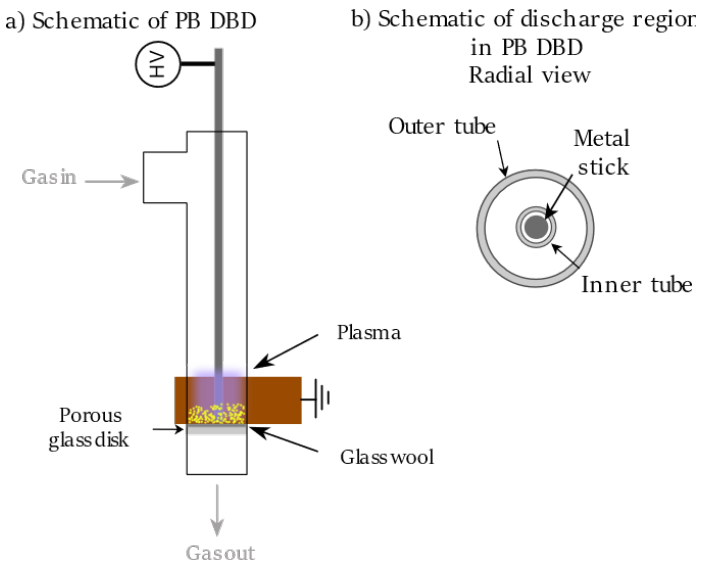

Figure 2.18: Schematic of the DBD packed bed for catalytic testing (a) lateral and (b) top view. Reactor used in LPP, France.

3. A coaxial DBD was constructed to serve as a fluidized bed plasma reactor (FB-DBD) having the same dimensions as the PB-DBD except that a small cyclone was embedded to allow the particles to fall back in the discharge zone. This reactor was located at LPP, as well. The schematic is shown in figure 2.19. The discharge volume was calculated to be 1.38 cm^3. The tests were performed with a power supply of 1 kHz and 30 kV capacity.

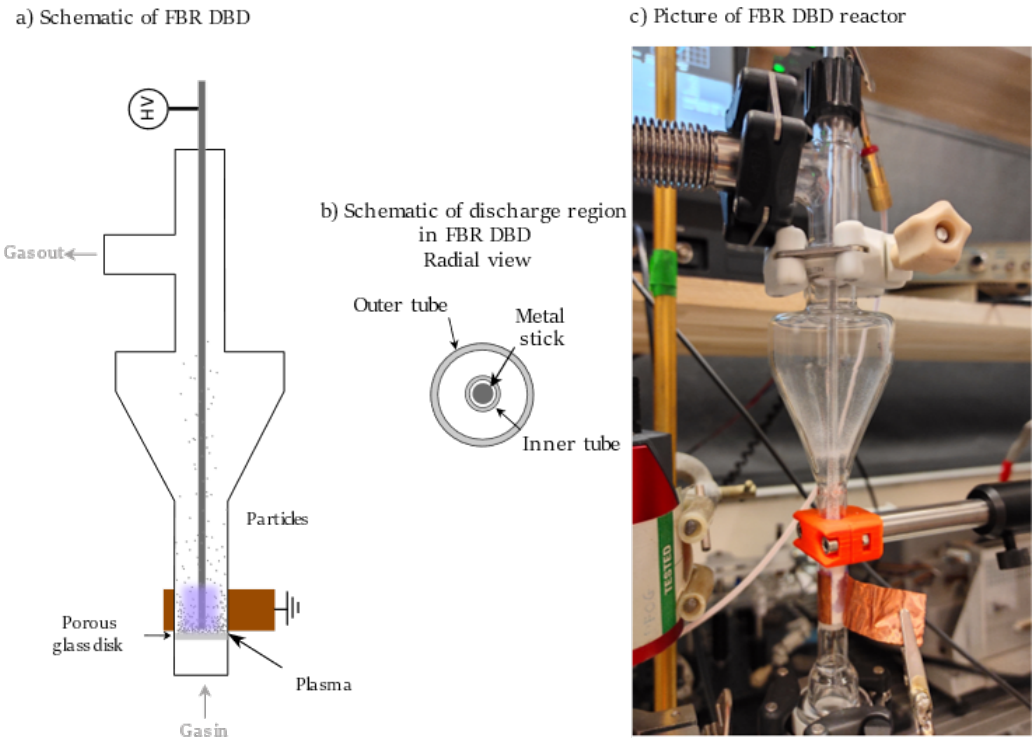

Figure 2.19: a) Schematic of the DBD fluidized bed for catalytic testing b) with a radial view and c) a picture of the reactor used. Reactor used in LPP, France.

2.5 Description of chemical reactors

Chemical reactors can be complex to design, build and operate however, reactors like batch reactor, continuous stirred tank reactors (CSTR) and plug flow reactors are very common. Batch reactors are the simplest configuration of a reactor. Reactants are introduced in a vessel with specific volume where the reactant concentrations decrease and product concentrations increase with time. Then, the reaction is stopped or finished. CSTR has continuous input and output of material. It is also assumed good mixing with no dead zones or bypasses in ideal operation prevailing in a diffusion process. However, with CSTR, low conversion per unit volume is obtained and primarily used for liquid-phase reactions.

Plug flow reactors have continuous input and output of material through a tube dominating the diffusion by the flowing gas. It is assumed that material passes through the reactor in incremental slices (each slice is perfectly mixed radially but has no forward or backward mixing between slices), composition and conversion vary with residence time and can be correlated with reactor volume or reactor length, and the reactor operates at steady state. A plug flow reactor can become a packed bed (also called a fixed-bed) reactor (with a catalytic material) or a fluidized bed. Packed bed reactors, and then fluidized bed theory are described in detail in the following subsections.

2.5.1 Packed bed reactor

Packed bed configuration is an heterogeneous reaction system mostly used to catalyze gas reactions. Many applications on plasma catalysis have been reported and as seen in section 1.2, it is a staple configuration for CO_2 catalytic conversion testing. The advantage of the packed bed reactor is that for most reactions it gives the highest conversion per weight of catalyst of any catalytic reactor. Some disadvantages are well known. For instance this type of systems involve an undesired thermal gradient generating hot spots through the bed which lead to poor temperature control. Tubular reactors often have high temperature limitations because of the occurrence of undesirable reactions, catalyst degradation or materials of construction. Also channeling of the gas flow may occur resulting in ineffective use of parts of the reactor bed [107].

Two reactors were used as packed bed reactors. Figures 2.17 and 2.18 show the DBD reactors used as packed bed during the catalytic screening for CeO_2 based catalysts.

2.5.2 Fluidized bed reactor

In a fluidized bed, solid particles can be mixed well with the gas acting like a fluid, which can significantly improve some physical and chemical features of the solid particles. Such gas–solid system improves the contact surface and the contact efficiency between gas flow and injected particles significantly. Therefore, fluidized bed systems are characterized by a perfect mixing of particles, a high rate of heat and mass transfer and a continuity of solid processing, in contrast to packed bed reactors. Within a fluidized bed, gas-solid reaction can be distributed in the overall working space [46]. Still, the beds are prone to erosion and particle attrition caused by constant movement and collision amongst particle and vessel walls, deterioration of the equipment by abrasion occurs and improper bed operation with large bubble sizes can drastically reduce conversion.

Despite the challenges that the fluidized bed operation represent, the advantages are incredibly attractive for processes that require efficient heat and mass transfer. The fluidization of solids was first used industrially in the gasification of coal in the early 1930s' but the application had little success. Gasoline was obtained by oil refining first straight-run distillate fraction and later by thermal cracking of heavier fractions such as gas oil. Until a french mechanical engineer Eugene Houdry, through trial and error experiments, discovered the catalytic cracking method for gasoline manufacture. The evident

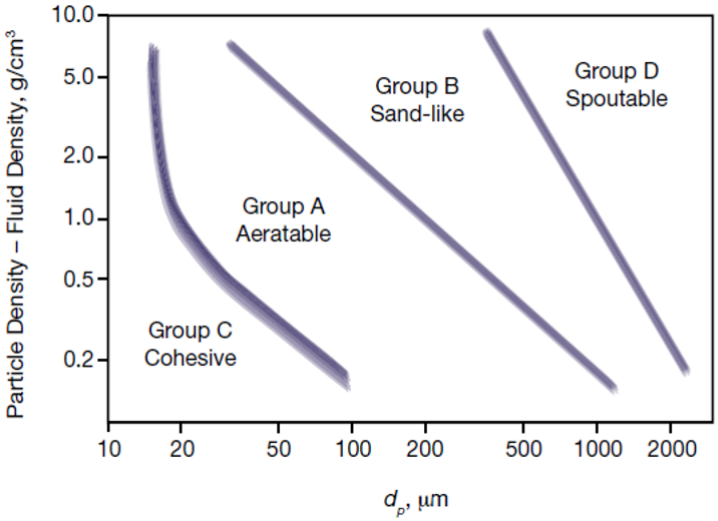

Figure 2.20: Classification of Geldart groups for powder predicted by the Sauter mean particle size and the particle density. Figure extracted from [11].

success of the Houdry process caused the world's biggest oil company, Standard Oil New Jersey (now ExxonMobil) to become interested in the process but moving away from packed bed reactors utilized in Houdry's process. Later, on 25th of May 1942, the world's first commercial fluidized catalytic cracking unit began operation at the Baton Rouge refinery in New Jersey, USA. After such success, other processes were applied to fluidized catalytic processing such as the production of phthalic anhydride by the air oxidation of coal tar-derived naphthalene. The following years, basic theoretical and experimental research into fluidization started were several theories were developed and parameters were thoroughly investigated.

Parameters of fluidized bed reactors

I. *Fluidization regimes*

In gas-solid fluidized beds, when the pressure drop across the bed exceeds the weight of the bed, the bed continues to expand with increasing gas velocity and bubble frequency increases. Bed expansion depends on the particle and fluid properties and Geldart was the first to classify powders into four categories according to their density and primarily particle size [12]. Figure 2.20 shows the Geldart clasification groups predicted by particle size and particle density.

The *minimum fluidization velocity* (u_{mf}), defined as the superficial gas velocity at which the drag force of the upward moving gas becomes equal to the weight of the particles in the bed, is one of the most important parameters associated with a fluidized bed system. Specifically, it is the point at which all the particles become suspended and are free to move. u_{mf} value is a function of the size, shape and density of the particles and the density and viscosity of the fluid.

As u_{mf} is exceeded, particles in Group A expand uniformly in the same way as a liquid-fluidized bed up to a gas velocity at which the bed collapses and voids called "bubbles" begin to form (see figure 2.21); these rise through the bed at a velocity proportional to their size and burst at the bed surface. The gas velocity at which this occurs is termed the *minimum bubbling velocity,* (u_{mb}). A typical example of a Group A powder is cracking catalyst used in the FCC process (particle size from 30 to 125 μm). Group B particles (150 up to 1000 μm particle size) such as coarse sand begin to form bubbles immediately after u exceeds u_{mf}, a type of behaviour referred to as "aggregative

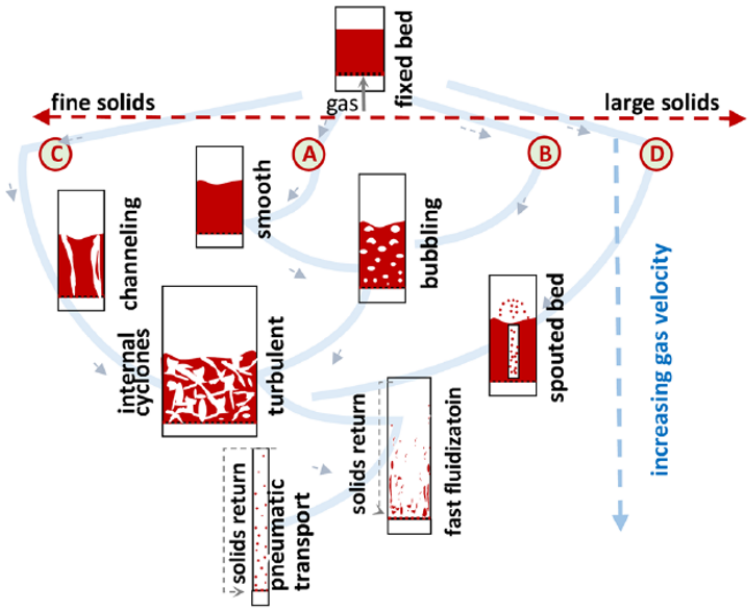

Figure 2.21: Scheme of gas velocity in different fluidization regimes. Figure extracted from [12].

fluidization". The particles in Group C (powders less than 30 μm), typically flour and cement, tend to be cohesive and are difficult to fluidize at all whereas the relatively large (around 800 to 3000 μm) and dense materials in Group D such as lead shot are prone to spouting rather than fluidizing. The great majority of fluidized-bed reactors use powders in Groups A and B.

Since 1950, researchers have developed over a hundred correlations to predict how the minimum fluidization velocity varies with particle properties, operating conditions, and reactor geometry. This property is the basis for many hydrodynamic models. Most of them are functions of the dimensionless Reynolds (Re_{mf}) and Archimedes (Ar) numbers, which are defined as:

$$Re_{mf} = \frac{\rho_g u_{mf} d_p}{\mu} \tag{2.13}$$

$$Ar = \frac{g\rho_g(\rho_p - \rho_g)d_p^3}{\mu^2} \tag{2.14}$$

where ρ_p is the particle density, d_p is the particle diameter, μ is the ambient gas viscosity, ρ_g is the density of gas, and g is the gravitational acceleration.

The Ergun equation, which has been popularly used for calculating u_{mf}, is a semi-empirical correlation accounting for the effects of particle diameter, particle density, gas density, gas viscosity, particle sphericity (ϕ), and bed voidage at minimum fluidization (ϵ_{mf})

$$Ar = \frac{1.75}{\epsilon_{mf}^3 \phi} Re_{mf} + \frac{150(1-\epsilon_{mf})}{\epsilon_{mf}^3 \phi^2} Re_{mf} \tag{2.15}$$

Since the values of ϕ and ϵ_{mf} are typically difficult to determine with precision, the previous equation can be re-expressed as follows:

$$Ar = K_1 Re_{mf}^2 + K_2 Re_{mf} \tag{2.16}$$

Wen and Yu represented one of the earliest studies on modifying the Ergun equation to calculate

u_{mf}. They found that K_2 and K_1 were invariant over a wide range of Re_{mf} of 0.001–4000, giving:

$$Re_{mf} = (33.7^2 + 0.0408Ar)^{0.5} - 33.7 \tag{2.17}$$

where $K_2/2K_1 = 33.7$ and $1/K_1 = 0.0408$. This form was adopted by numerous researchers subsequently:

$$Re_{mf} = (K_1^2 + K_2 Ar)^{0.5} - K_1 \tag{2.18}$$

Nonetheless, K_2 and K_1 can take different values depending on the bed and operating conditions. Anantharaman et al. performed a review on more than a hundred correlations on u_{mf} and Geldart powder groups published since 1950. The key conclusion stated: "the correlations available in literature for predicting u_{mf} are highly empirical and system-specific, which severely limit the utility of each to systems beyond the scope tested. However, the capacity for u_{mf} predictions based purely on first principles is not possible yet, nor is it warranted to determine a 'best' generalized correlation from those available." Additionally, the bed voidage at minimum fluidization and particle sphericity values are not typically available; these are usually subsumed into empirical constants via best-fitting of experimental data resulting in system-specific correlation under study [108].

The experimental measurement is simpler and less subject to variations due to differences of reactors or instruments or analysis methods, since it is generally accepted as the superficial gas velocity at which the pressure drop across the particle bed plateaus or the expanded bed height starts increasing significantly. The standard procedure for experimentally determining u_{mf} is described in ASTM D7743 – 12.

II. *Powder characterization*

Certain characterization parameters of the powder used are also required to have a complete picture of the beds. Bulk density (ρ_b) defines how much solids will fit into a given volume and particle density, (ρ_p) is the basis of correlations to characterize fluidized bed hydrodynamics, including bed void fraction (ϵ_v, ϵ_{mf}) and u_{mf}. The particle density is:

$$\rho_p = \frac{\rho_b}{1 - \epsilon_v} \tag{2.19}$$

Particle size and distribution are parameters equally important as density to classify powders. Catalytic reactors operate best with a wide particle size distribution and as much as 35 % fines. Sphericity is a coefficient of a particle diameter that represents how much its geometry deviates from a perfect sphere: $\phi = 1$ for spheres and $\phi = 0.84$ for cubes.

Experimental reactors

Two types of fluidized bed (FB) reactors were used in this work: FB-glow discharge and FB-DBD.

FB-glow discharge is a 2 cm diameter glass tube with two electrodes separate by 23 cm. A porous glass disk is embedded across the tube at approximately 6 cm from the lower electrode where the particles are placed. A cyclone with a glass wool cap was placed above the plasma discharge zone to let the particles fall back into the reactor and prevent the exit of the particles from the reactor into the gas line. See figure 2.14.

The FB-DBD is a coaxial double layer DBD with a 1 cm inner diameter glass tube. In the upper part, it has a small cyclone. The HV electrode has a 0.4 cm outer diameter. The section area results in 0.6594 cm^2. More details are described in section 2.4.2.

2.6 Summary

A description of the characterization techniques I personally performed was given in this chapter and each one is listed in table 2.1 along with the measurements and the institution where they were taken. Only FTIR spectroscopy was used for two purposes: gas phase characterization and surface/plasma characterization.

The SEM-EDX analysis was performed by Nuria Ferrer at the Instituto de Carboquimica (ICB) in Zaragoza, Spain. The objective is to obtain imaging on the materials used in fluidized bed - DC glow discharge as well to obtain information on the bulk composition and impurities that might be present before and after plasma reaction. The XPS analysis was performed by Laura Abramiuc in the National Institute of Materials Physics in Măgurele, Romania. The purpose is to elucidate a permanent change on the oxidation state of CeO_2 used on *in situ* experiments for DRM plasma reaction.

Technique	**Measurement**	**Institution**
FTIR spectroscopy	$[CO_2]$, $[CO]$, $[CH_4]$, $[H_2O]$, $[C_2H_x]$ surface adsorbed species	LPP
Mass Spectrometry	$[O_2]$ and $[H_2]$ $[CO_2]$ and $[CH_4]$	LPP University of Bucharest
OES	Relative O concentration (777 and 844 nm) Relative H concentration (656 nm) Relative CO concentration (3PS and Angstrom band) T_{rot}	LPP
DRIFTS	Surface adsorption species	University of Bucharest
XRD	Crystalline structure	University of Bucharest
BET	Surface area and pore size	University of Bucharest

Table 2.1: Summary of characterization techniques used to analyze plasma, gas and catalytic materials.

Several reactors were used in this thesis for different purposes and applications and they are summarized in table 2.2. All the plasma experiments were performed in LPP and one part was performed in University of Bucharest using the packed bed-DBD for the ceria-based catalysts screening.

Reactor	**Experiment**	**Purpose**
DC Glow discharge	Downstream gas characterization	Description of gas composition
Cross shape DC glow discharge	*in situ* FTIR transmission Downstream gas FTIR transmission Adsorption test	Study plasma-surface interaction Study the effect of gas composition in a catalytic surface Study adsorption bands through time
Fluidized bed - DC glow discharge (FB-glow)	Downstream gas characterization Plasma characterization	Study the effect of catalyst in the plasma Comparison with literature
Packed bed - DBD (PB-DBD)	Catalyst screening	Comparison with literature
Fluidized bed - DBD (FB-DBD)	Catalyst screening	Comparison with literature

Table 2.2: Summary of plasma/chemical reactors used in this work and the purpose for the utilization of each one of them.

Chapter 3

Downstream gas and surface adsorption characterization

Contents

3.1 Introduction

The purpose of this chapter is to demonstrate the validity of the results derived from *in situ* FTIR transmission experiments in part II. Therefore, the two main objectives in this chapter is to establish the general gas composition of CO_2-CH_4 plasmas used later to expose the catalytic materials and to properly assign the adsorption bands onto CeO_2 surface as well as the standard deviation of the time evolution upon CO_2-CH_4 plasma exposure.

First of all, it is important to know the composition of the CO_2-CH_4 plasmas used throughout all the experiments here reported. The gas characterization is done using FTIR spectroscopy and Mass spectrometry to determine the densities of CO_2, CH_4, CO, H_2, H_2O, O_2, C_2 hydrocarbons and other molecules. The influence of pressure, initial concentration of CO_2, total flow rate, and presence of sample holders in the plasma region are evaluated. Afterwards, a discussion is done along with a comparison to the literature and the detailed work reported in [87]. The characterization of pure CO_2 plasma under several conditions has already been reported before by Ana Sofia Morillo Candas in her PhD thesis [16]. Therefore, hereinafter only CO_2-CH_4 plasma is reported.

Second, the CeO_2 surface is tested in the form of a pellet in transmission mode using the FTIR spectrometer. The adsorption bands observed in the IR spectra are evaluated in a *clean* surface and upon CO_2 and CO_2-CH_4 plasma exposure.

3.2 Downstream gas characterization

The characterization of the downstream gas of CO_2-CH_4 plasma reaction provides a reference of the composition to which the catalytic surface is exposed under plasma conditions. The main products of DRM reaction are carbon monoxide and hydrogen. However, other minor products can be formed and it is crucial to know their concentrations that could have an effect on the surface reactions during plasma-surface interactions in CeO_2.

Figure 3.1 shows a schematic of the setup used for the characterization of the downstream gas coming from CO_2-CH_4 plasma under different conditions. Pressure, initial concentration of CO_2, total flow rate and the effect of sample holder in the plasma region are tested. The initial gas mixture is sent to the glow discharge and the resulting gas is sent to the measuring cell in the path of the IR beam for analysis of CO_2, CH_4, CO, H_2O, C_2 hydrocarbons and $C_xH_yO_z$ molecules densities by FTIR spectroscopy. The exit of the IR cell is connected to a quadrupole MS for analysis of non-infrared active molecules (O_2 and H_2 densities).

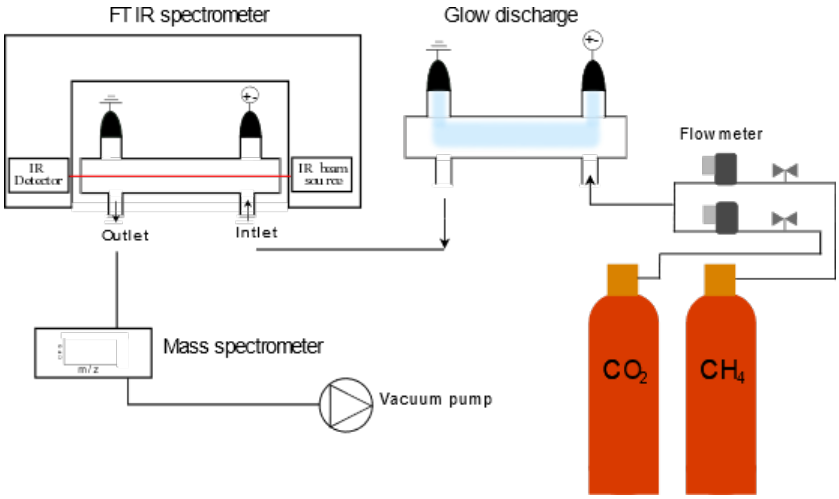

Figure 3.1: Schematic of the setup used for the characterization of gas from CO_2-CH_4 plasma reaction.

3.2.1 Initial concentration of CO_2

The effect of initial concentration of CO_2, hence the initial concentration of CH_4 as well, is evaluated on the final concentrations of the main reactants at different pressures. The initial concentrations of CO_2 tested range from 90% to 50% which correspond to 0.9 to 0.5 fraction of the total gas density. The rest of the gas corresponds to methane fraction. The total gas flow is kept constant at 7.4 sccm. Figure 3.2 shows the final concentrations of CO_2 and CH_4 in % as a function of the initial concentration of CO_2 for 0.65, 1, 3, 5 and 7 Torr at 10 mA and 50 mA plasma current. As observed, the final concentration of CO_2 decays after the plasma reaction, specially at 50 mA in comparison to 10 mA (figure 3.2a and b). Although we can notice that at low pressure (0.65 and 1 Torr) the final concentration is slightly lower in comparison to when pressure is higher (more than 3 Torr) for both currents. The same trend is observed for the final concentration of CH_4 (figure 3.2c and d) under the same conditions. It is noteworthy to point that the conversion of CO_2 does not significantly increase beyond 3 Torr for all given concentrations when compared 10 and 50 mA but it does for CH_4 conversion. For example, at 50% initial concentration of CO_2 and CH_4 at 50 mA, the final percentage of CH_4 is around 10% while for CO_2 is around 20%. This means that more CH_4 is decomposed in comparison to CO_2. A temperature driven back reaction to CO_2 is debatable given that the temperature is lower when a significant amount of H species are present

in the gas mixture as will be shown later.

CO and H_2 are the main products of the reaction of CO_2 and CH_4. Figure 3.3 displays the concentration in % of CO and H_2 as a function of the initial concentration of CO_2 for 0.65, 1, 3, 5 and 7 Torr at 10 mA and 50 mA plasma current.

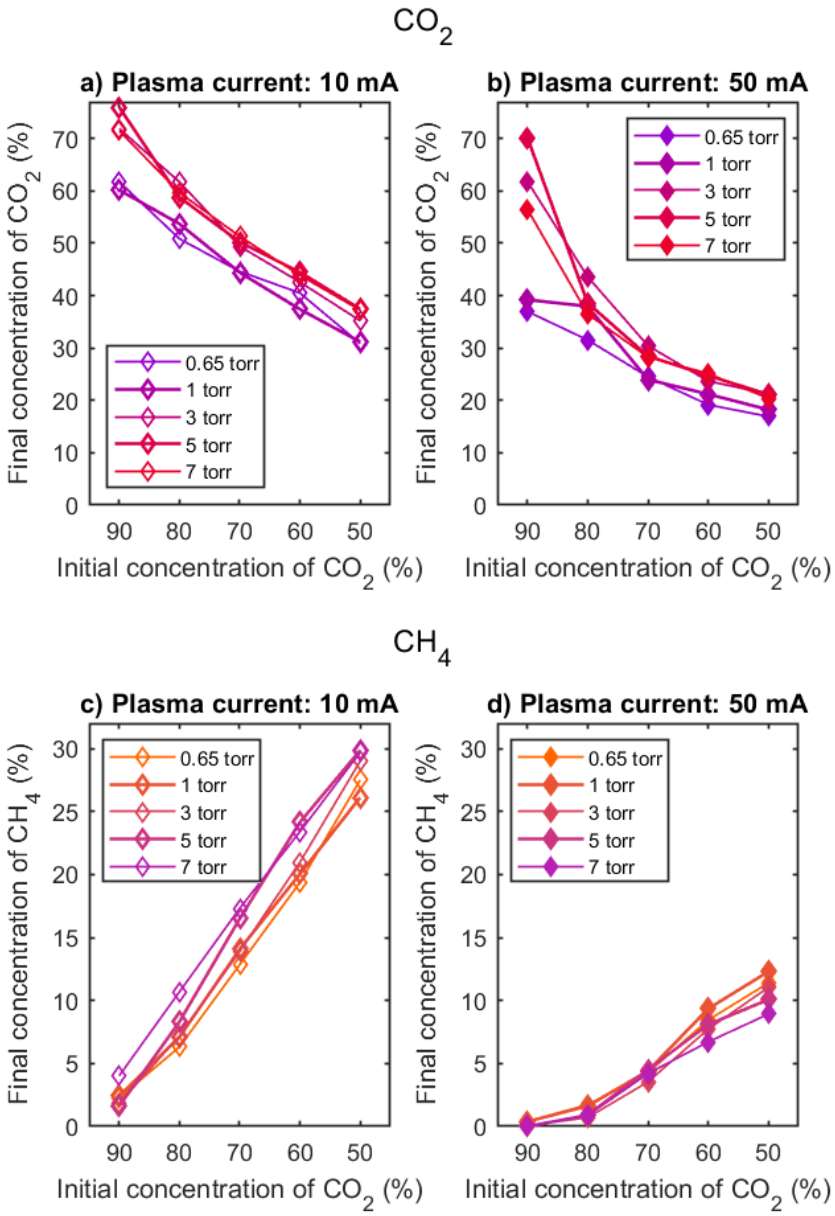

Figure 3.2: Final concentrations of the main reactants CO_2 and CH_4 in % as a function of the initial concentration of CO_2 for 0.65, 1, 3, 5 and 7 Torr at a,c) 10 mA and b,d) 50 mA plasma current. Total flow rate: 7.4 sccm.

CO is the major product of DRM plasma reaction in the initial concentrations tested here. At low current (10 mA) the concentration range 10 - 20% but when the current increases (50 mA) the concentration range 20 - 40% across all the pressures presented. In both cases, the maximum in CO concentration is reached when the initial concentration of CO_2 is 80 and 70% . Eventually the concentration decays as the initial concentration of CO_2 decreases. This is not the case for H_2 concentration as seen in figure 3.3c and d. For 80 and 90% initial concentration of CO_2, the H_2 concentration is low (less than 15%

at 50 mA). The maximum concentration is reached at 70% initial concentration of CO_2 and remains constant despite the increasing initial concentration of methane (initial concentration of CO_2 decreases). H_2 comes necessarily from CH_4 decomposition, however the final methane concentration does not stay constant as H_2 concentration. This indicates that the reaction is not entirely selective to H_2 formation and another product(s) are also formed. Figure 3.4 show minor products as O_2 and H_2O and figure 3.5 displays C_2 hydrocarbons trace concentration.

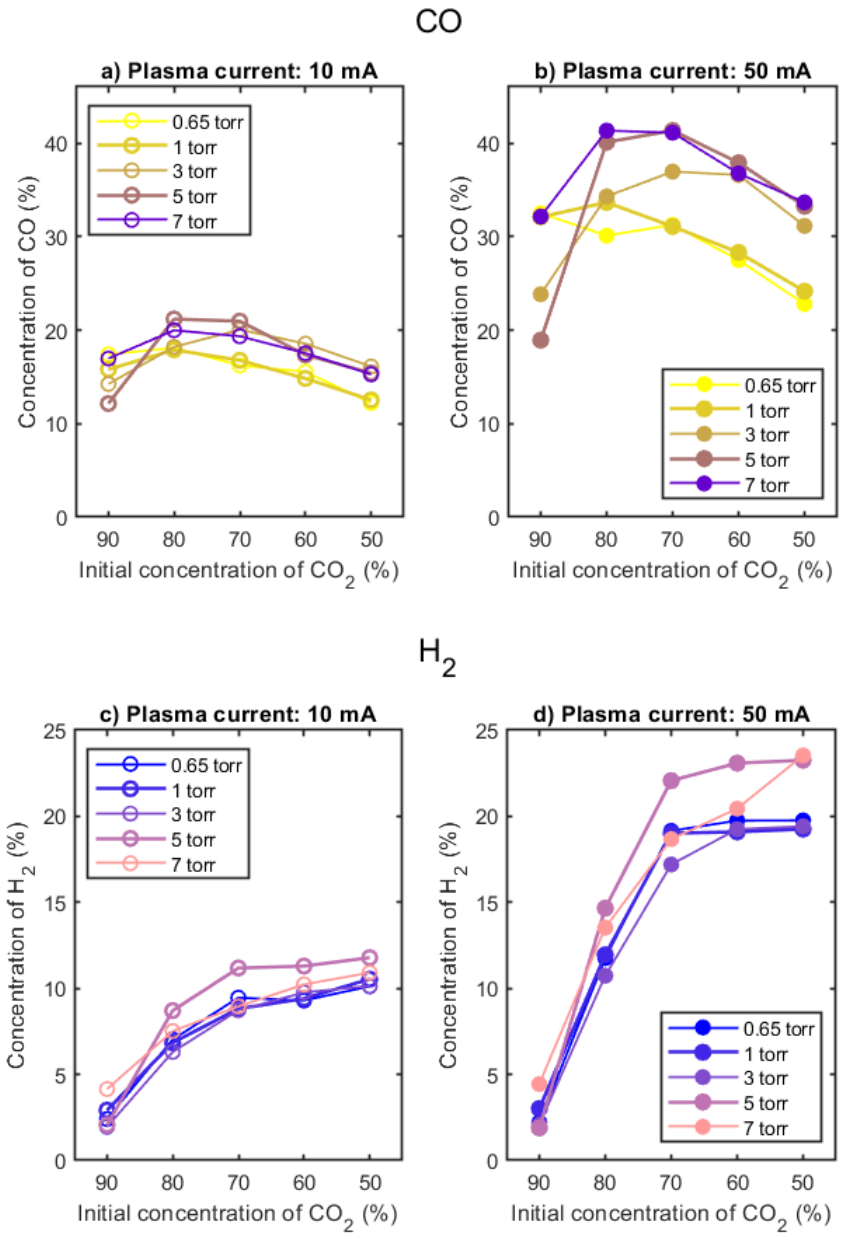

Figure 3.3: Concentrations of the main products CO and H_2 in % as a function of the initial concentration of CO_2 for 0.65, 1, 3, 5 and 7 Torr at a,c) 10 mA and b,d) 50 mA plasma current. Total flow rate: 7.4 sccm. H_2 concentration measured by mass spectrometry.

The first noticeable feature of this figure is the clear difference between O_2 concentration at low pressure (0.65 and 1 Torr) and high pressure (3, 5 and 7 Torr) for both currents. For example, at 50 mA with 0.65 and 1 Torr the O_2 concentration is around 12% when the initial concentration of CO_2 is

90 and 80% but decreases to 3% with decreasing initial concentration of CO_2. But at 5 and 7 Torr, the O_2 concentration remains constant through all the initial concentrations of CO_2, even at 10 mA plasma current. O_2 is one of the dissociation product of CO_2 while oxidation of CH_4 is expected to favour reactions leading to H_2O. The trends are not straightforward in the case of H_2O but we can notice that at 10 mA the concentration of water decreases as the initial concentration of CO_2 decreases. For 50 mA plasma current, the same trend as at 10 mA is observed but at 7 Torr the water concentration shows the highest and decrease as the pressure decreases.

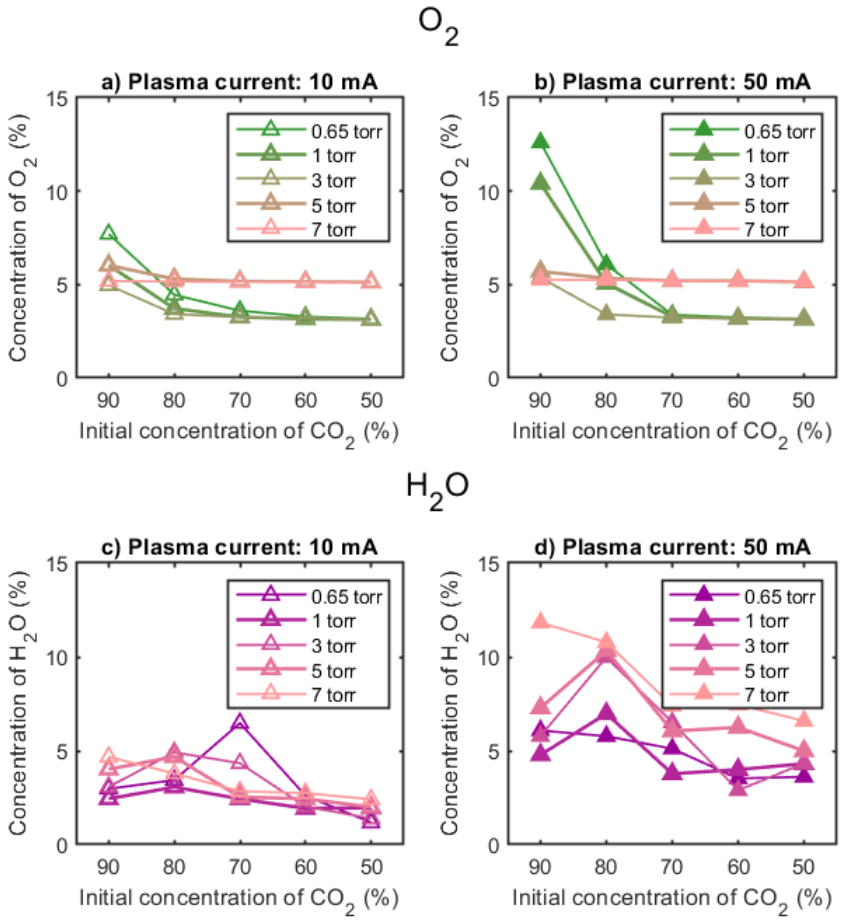

Figure 3.4: Concentrations of the O_2 and H_2O in % as a function of the initial concentration of CO_2 for 0.65, 1, 3, 5 and 7 Torr at a,c) 10 mA and b,d) 50 mA plasma current. Total flow rate: 7.4 sccm. O_2 concentration measured by mass spectrometry.

Water could explain the missing H fraction but the concentration is much lower at 50% of initial concentration of CO_2 than at 90% as seen in figure 3.4c and d. Water formation can proceed from reverse water-gas-shift reaction where CO_2 and H_2 lead to CO and H_2O. Other molecules could explain the missing fraction of hydrogen. Figure 3.5 displays C_2 hydrocarbons trace concentration. From now on, 1 and 5 Torr pressures are shown for simplicity of the figures representing low and high pressure, respectively. As noticed, 90 and 80% initial concentration of CO_2 results in basically no C_2 hydrocarbons at both currents. Ethane is the short hydrocarbon present in a more significant amount in comparison to ethylene and acetylene. C_2H_6 concentration increases as the initial concentration of CO_2 decreases meanwhile, CH_4 concentration increases. High plasma current also increases the concentration of C_2H_6 resulted from methane decomposition. For ethylene, the amount detected is very low, around 0.2% in the

case of initial concentration of CO_2 of 50% at 50 mA. In the case of acetylene, the concentrations follow a similar trend as ethane but reaches a maximum of concentration of 0.8% with initial concentration of CO_2 at 50 mA.

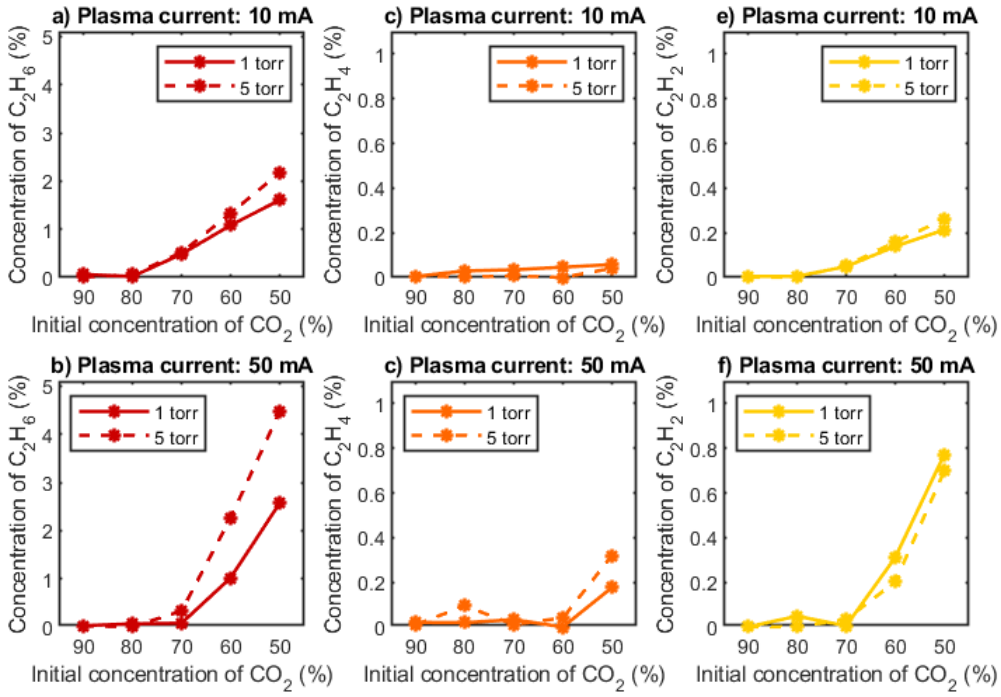

Figure 3.5: Concentrations of a,b) C_2H_6, c,d) C_2H_4 and e,f) C_2H_2 in % as a function of the initial concentration of CO_2 for 1 and 5 Torr at 10 mA and 50 mA plasma current. Total flow rate: 7.4 sccm. Solid line: 1 Torr, dashed line: 5 Torr.

The mere presence of C_2 hydrocarbons in the FTIR spectroscopy measurements reported here seems debatable given that results obtained in similar setup by Edmond Baratte were not showing any [87]. A possible explanation of this difference could be the time in post-discharge and the surfaces in contact with the gas. Here a metallic tube of ∼30 cm is connecting the exit of the plasma reactor to the measurement cell in the FTIR while only a few cm of glass tube were separating the plasma from the measurement point in Edmond's Baratte measurements. The results obtained here by Mass spectrometry support the existence in trace amount in the downstream gas of CO_2-CH_4 plasmas. Figure 3.6 shows the ion current signal of mass 30 and 26 as a function of the initial concentration of CO_2 for 1 and 5 Torr at 10 and 50 mA.

As observed in figure 3.5, ion current for mass 30 and 26 increases when the initial concentration of CO_2 decreases. This increase is attributed to ethane and not to formaldehyde given the lack of evidence from FTIR spectroscopy measurements. Mass 26 is attributed to acetylene. The mass of ethylene overlaps with CO mass which corresponds to 28 and it is not shown here. However, the presence of traces amounts of ethane and acetylene does not justify the missing H atom from H_2 densities. Therefore, the calibration of H_2 in MS could be the source of mismatch. Although, at low concentrations of H_2 the relationship between H_2 fraction in the gas mixture and the ion current signal is linear, at higher concentrations such linearity disappears displaying a higher degree polynomial fit. Nonetheless, the increase in the ion current at mass 26 and 30 strongly suggest the minor presence of C_2 hydrocarbons.

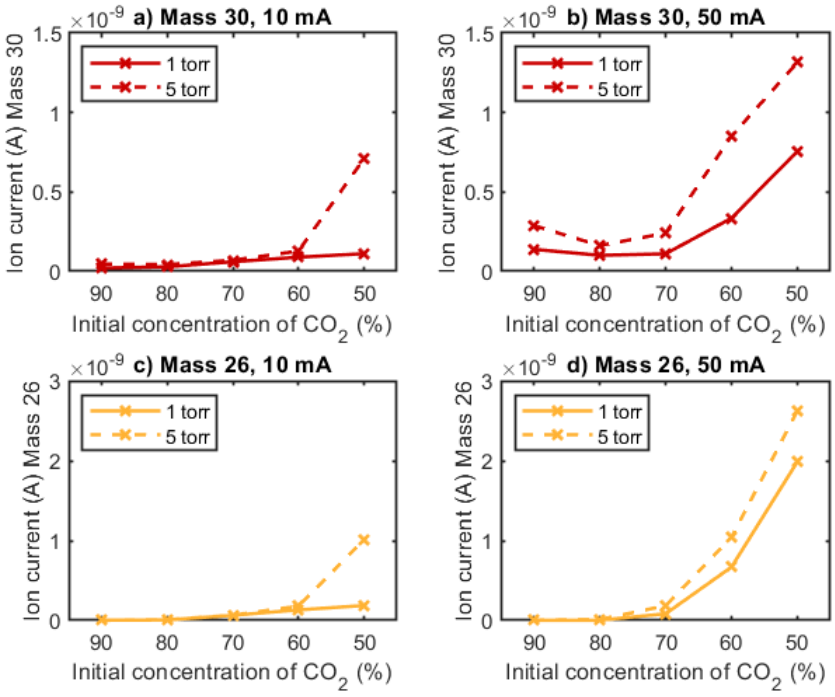

Figure 3.6: Ion current signal (A) of mass 30 and 26 as a function of the initial concentration of CO_2 for 1 and 5 Torr at a,c) 10 mA and b,d) 50 mA. Total flow rate: 7.4 sccm.

3.2.2 Flow rate

The total flow rate ($\phi_{(sccm)}$) has a direct influence on the residence time of the gas in the plasma region. The total flow rate is tested at 7.4, 6, 5, 4, 3 and 2 sccm maintaining the initial gas mixture constant with 70%CO_2-30%CH_4. The corresponding residence time is shown in table 3.1 according to the gas temperature (T_{gas}) and pressure (P) in the plasma region as calculated from equation 3.1. T^o and P^o correspond to standard conditions of temperature and pressure.

$$\tau_{res} = \frac{PV/KT_{gas}}{\phi_{(sccm)} * (P^oV^o/KT^o)} \tag{3.1}$$

Current/Flow rate	7.4 sccm	6 sccm	5 sccm	4 sccm	3 sccm	2 sccm
10 mA	0.32 s	0.39 s	0.47 s	0.59 s	0.79 s	1.19 s
50 mA	0.26 s	0.33 s	0.39 s	0.49 s	0.66 s	0.99 s

Table 3.1: Residence time (τ_{res}) calculated in s for the flow rates tested and corrected by the gas temperature and pressure for initial gas mixture 70%CO_2-30%CH_4 at 10 and 50 mA. Pressure: 1 Torr. Gas temperature was obtained as described in section 2.2.2.

Figure 3.7 shows the final concentration of CO_2, CH_4, CO and H_2 as a function of the total flow rate at 1 and 5 Torr for 10 mA and 50 mA. Both reactants, CO_2 and CH_4 have decreasing final concentration as the total flow rate decreases. Inversely, CO and H_2 concentration increases as the total flow rate decreases. This is consistent with an extended residence time and therefore a higher specific energy input at constant current. As seen in figure 3.2, CO_2 and CH_4 concentrations are much reduced at high current (50 mA), although there is no difference in concentration for CH_4 at 1 and 5 Torr.

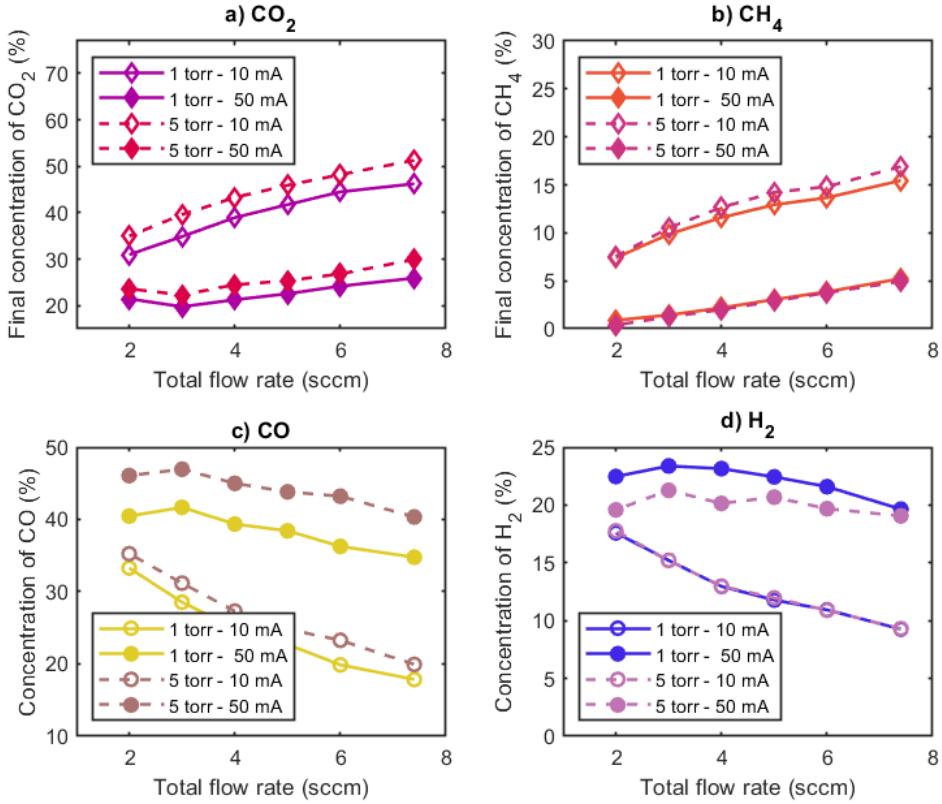

Figure 3.7: Concentrations of a) CO_2 and b) CH_4 and main products c) CO and d) H_2 in % at 1 and 5 Torr for 10 mA and 50 mA as a function of the total flow rate. Initial concentration: 70%CO_2-30%CH_4. Solid line: 1 Torr, dashed line: 5 Torr. Empty marker: 10 mA, filled marker: 50 mA.

Not only the main products follow the same trend but the minor species like O_2 and H_2O. Figure 3.8 shows the concentrations of O_2, H_2O, C_2H_6 and C_2H_2 in % at 1 and 5 Torr for 10 mA and 50 mA as a function of the total flow rate. O_2 and H_2O concentrations increase with reduced flow rate. However, ethane and acetylene follow the opposite pattern: they decrease in concentration as the total flow rate decreases. This inverse behaviour could indicate that they are intermediate species in the decomposition to H_2.

Pan et al. tested the effect of total gas flow rate from 40 to 120 ml/min in a DBD reactor [109]. They observed the same trend as in figure 3.7 for lower flow rate (*i.e.* larger residence time) with an increase of CO_2 and CH_4 conversions. This also reflects on the CO and H_2 concentrations. This effect is widely reported in other plasma sources as spark, Nanosecond Repetitively Pulsed (NRP) discharges, DBD and corona discharges for CO_2 conversion in DRM reaction [110–113].

Overall, the decrease in the total flow rate (and increase on residence time) lead to a increase on the conversion CO_2 and CH_4 while the concentrations of CO, H_2, O_2, and H_2O increase.

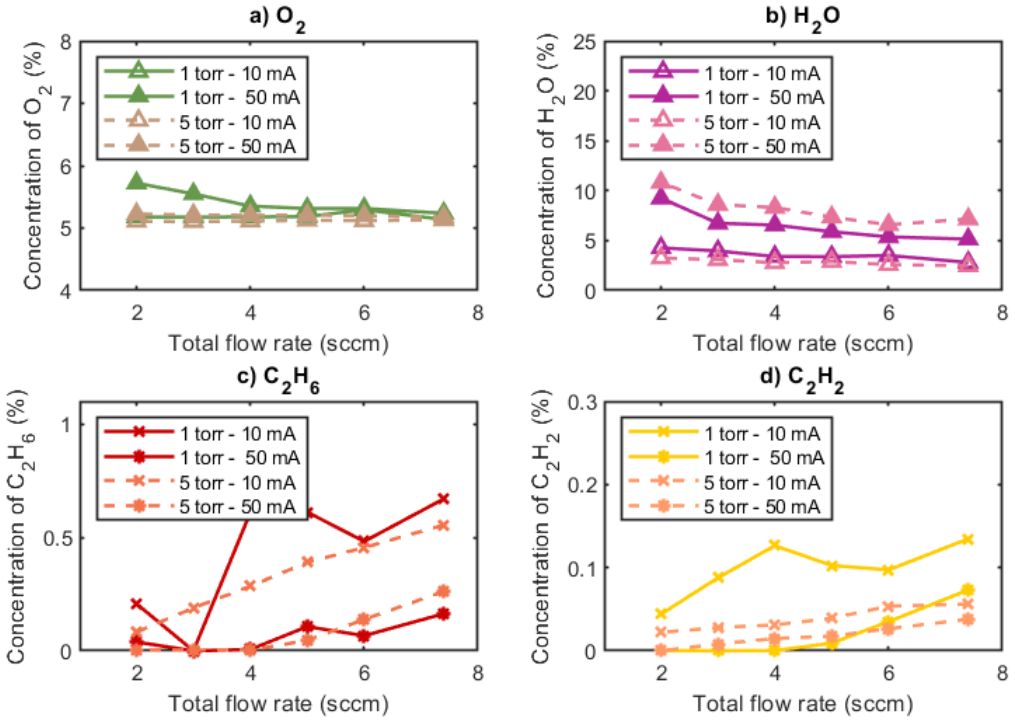

Figure 3.8: Concentrations of a) O_2, b) H_2O, c) C_2H_6 and d) C_2H_2 in % at 1 and 5 Torr for 10 mA and 50 mA as a function of the total flow rate. Initial concentration: 70%-30%CO_2-CH_4. Solid line: 1 Torr, dashed line: 5 Torr. Empty marker: 10 mA, filled marker: 50 mA.

3.2.3 Effect of sample holder with CeO_2 on plasma composition

Before testing the plasma-surface interaction by *in situ* experiments with the ceria pellet in the plasma region of DC glow discharge, we assess that the plasma characteristics, mainly the composition and therefore, the other properties like temperature, reduced electric field (E/N), residence time, etc. remain unaltered in the presence of such CeO_2 pellet. Hence, the position of the CeO_2 pellet with the glass sample holder in the plasma zone is tested here. Figure 3.9 shows a picture of the sample holder used to hold CeO_2 pellets in part II and that is exposed to DC glow discharge plasma conditions. To go a bit further in this testing, a cuvette made of glass was used to hold ∼0.15 g of powder ceria (the same CeO_2 used to prepare the pellets). The cuvette is around 5 cm long with 1 cm diameter resembling a tube cut axially in half. The idea is to expose loose ceria powder to plasma increasing the contact area instead of only testing it in a compressed form as in a pellet. The experiments were carried out varying the initial concentration of CO_2 and CH_4 at constant total flow rate of 7.4 sccm at 1 Torr for 10 and 50 mA. The results were compared with only plasma (no sample holder in the discharge zone).

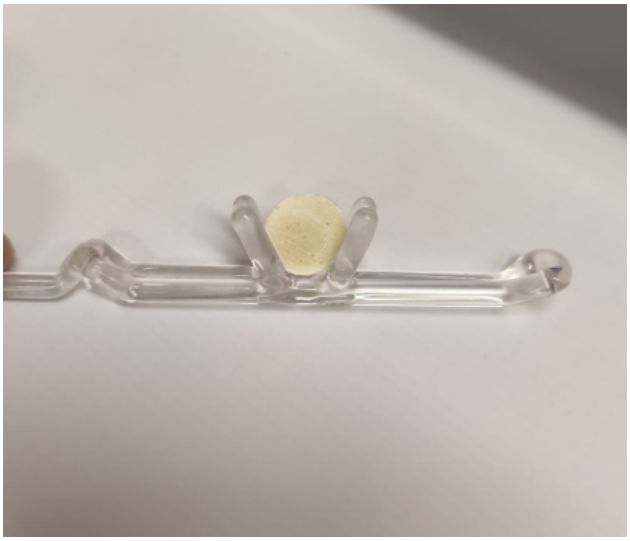

Figure 3.9: Picture of the glass sample holder used to support the ceria pellets used for the *in situ* FTIR transmission experiments reported in part II.

Figure 3.10 shows the comparison of CO_2, CH_4, CO, H_2, O_2 and H_2O concentrations as a function of initial concentration of CO_2 for only plasma, plasma/CeO_2 pellet and plasma/CeO_2 powder experiments at 1 Torr.

At simple sight, the trends for the concentrations of CO_2, CH_4, CO, H_2, O_2 and H_2O are the same as in section 3.2.1 proving the consistency of the results previously presented. In addition, the variance among the results for the three experiments is very low. This could be due to the minimum amount of sample used compared to the large plasma region. However, the surface area provided by the glass sample holder could have an impact on the plasma but it seems to be insignificant. In other *in situ* experiments, this effect is not tested because DRIFTS allows to utilise samples in powder form on a sample holder that is part of the configuration for analysis [72, 73]. The flexibility in our setup give us the chance to show that in our conditions the impact of pellets and powders on the plasma properties is minimal. In turn this means that species on the catalyst can be studied while having a good knowledge of the conditions to which the surface is exposed.

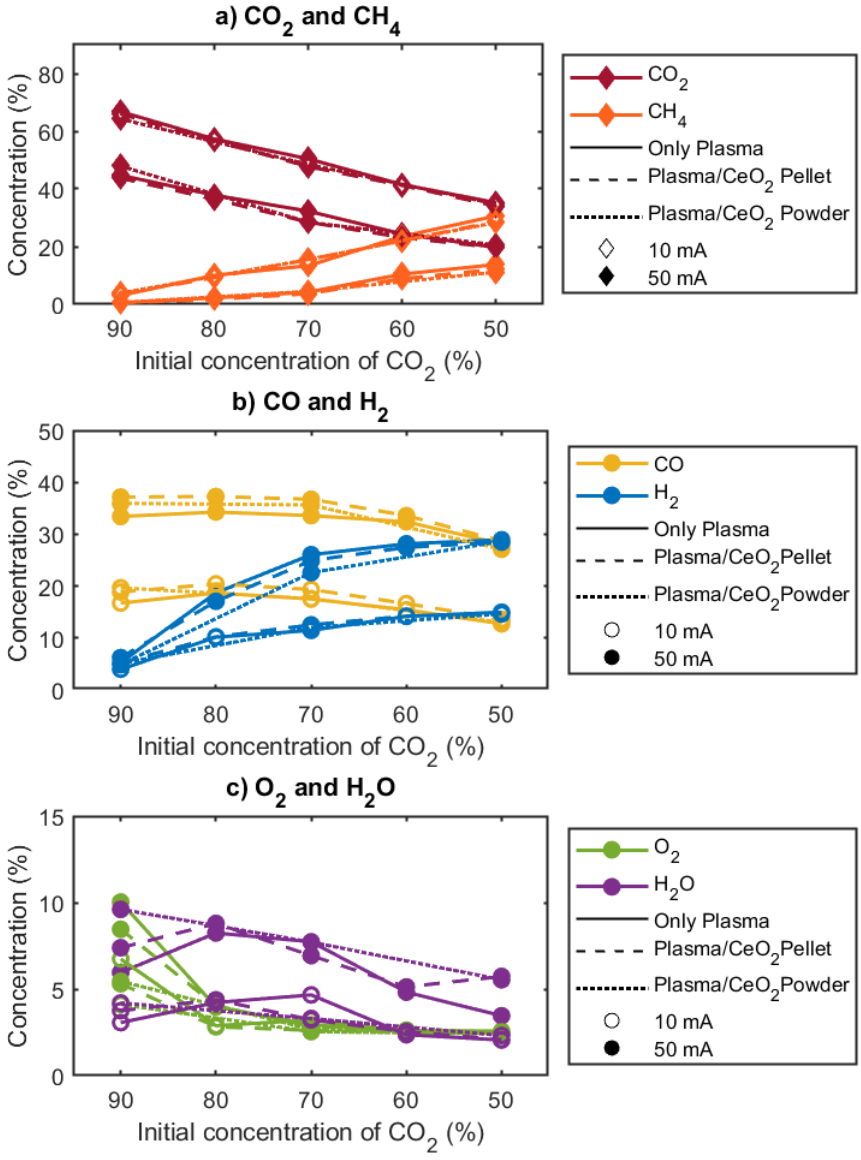

Figure 3.10: Concentrations of a) CO_2 and CH_4, b) CO and H_2, and c) O_2 and H_2O, in % at 1 Torr for 10 mA and 50 mA as a function of the initial concentration of CO_2. Initial concentration: 70%CO_2-30%CH_4. Total flow rate: 7.4 sccm. Solid line: Only plasma, dashed line: Plasma/CeO_2 pellet, dotted line: Plasma/CeO_2 powder. Empty marker: 10 mA, filled marker: 50 mA.

3.3 Surface adsorption bands in CeO_2

CeO_2 is known to adsorb CO_2 in the surface and form carbonate species. However, we need to know what bands are expected to appear or disappear from the IR spectra. The goal of this section is to identify the main absorption bands observed in the IR spectra from transmission experiments through CeO_2 pellets. The species identification and comparison with the literature help us to analyse in detail in the following chapters the effect of CO_2 only and CO_2-CH_4 plasmas on the adsorbates. Before performing FTIR transmission experiments with a ceria pellet, the surface should be clear of adsorbates that might block

surface reactions and let only CO_2 adsorb and other intermediates to form. Then, a simple procedure with consecutive steps of gas and plasmas is followed to observe possibly new absorption bands.

Experimental procedure

CeO_2 powder was pelletized under 2 tons of pressure into self-supported wafers and placed carefully in a glass holder. The ceria pellet has a diameter of approximately 1 cm. Then, the sample was placed inside the cross DC glow discharge (figure 2.13). The experimental setup (figure 3.11) consists of a cross DC glow discharge plasma reactor (as in figure 2.13) made of a Pyrex tube with a cylindrical shape with a 2 cm inner diameter placed in the path of infrared beam in the FTIR spectrometer.

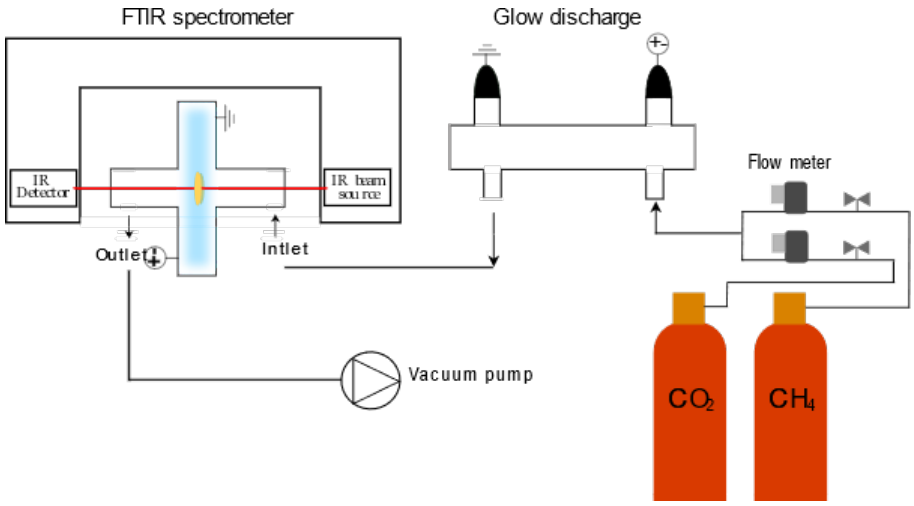

Figure 3.11: Schematic of set up for *in situ* FTIR transmission through CeO_2 pellet in a cross shaped glow discharge reactor.

For the *in situ* FTIR transmission experiments, the pellet is placed in the path of the infrared beam inside the glow discharge plasma reactor as illustrated in figure 3.11. The total flow rate is set to 5.4 sccm. Due to the difference in the distance between the electrodes, the discharge volume is reduced and consequently the total flow rate has to be reduced to maintain the same residence time as in downstream gas experiments of the previous section. For each experiment, a sequence of 6 consecutive steps lasting 10 min each is followed (figure 3.12): (1) the appropriate gas mixture (CO_2 only or CO_2-CH_4) is sent to the reactor (Before plasma) in order to follow the adsorption of initial molecules on the catalyst surface and to observe what species are formed. During step (2), a plasma at low current (10 mA) is ignited keeping the gas temperature and the dissociation of feeding gas relatively low, then during step (3) plasma current is increased to 50 mA to monitor the effect of a more intense plasma exposure and surely an increase in the gas temperature. During step (4) plasma was switched off but the same gas mixture as during step (1) is still flowing allowing to check if the adsorption of the feed gas molecules remains unchanged or to observe if there is any change after plasma treatment. O_2 gas is sent to the reactor for step (5) to exhibit any possible reversible adsorption from species observed during step (4), and finally during step (6) O_2 plasma at 30 mA is ignited to observe the oxidation of species remaining on the surface.

In the case of investigating the pristine (no plasma treatment, the material as it is) ceria surface and the cleaning procedure, single spectrum is taken and shown in transmittance. The IR spectra for *in situ* transmission experiments are taken in rapid scan mode meaning that around every 8 seconds a spectra was recorded resulting in 74 spectra taken in a span of 10 min (the duration of one step). The spectra are saved in transmittance and then converted to absorbance for ease of area calculation of the peaks.

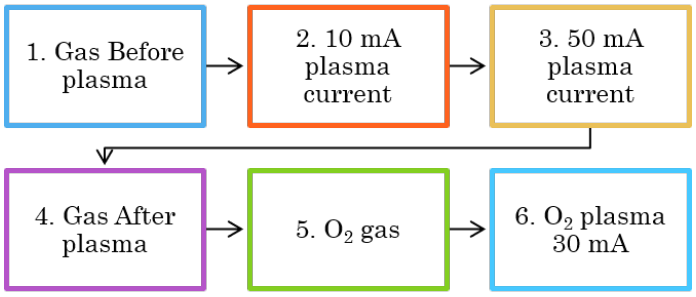

Figure 3.12: Experimental sequence of steps followed during *in situ* FTIR transmission experiments in the set up shown in figure 3.11. Details are provided in the text.

3.3.1 Clean surface

To ensure the maximum adsorption of CO_2 into CeO_2 surface and obtain reliable assignment of bands, a clean surface of ceria is needed. O_2 plasma can provide enough gas temperature and/or ion bombardment to aid in the removal of adsorbed species from ambient atmosphere (mainly from CO_2 and water). Meanwhile, it can provide O atoms to fill the surface oxygen vacancies, if needed. A simple procedure was tested: O_2 plasma at 30 mA 1 Torr for 10 min and subsequently, O_2 plasma 30 mA 5 Torr for 40 min. Figure 3.13 shows the resulting raw IR spectra of pristine ceria and after both steps under O_2 plasma treatment.

Pristine ceria pellet IR spectra shows broad bands in the region centered at 1304 and 1570 cm^{-1} which can be attributed to CO stretching vibrations of carbonates [114]. The broad band in the region from 2590 to 3700 cm^{-1} is attributed to stretching vibration of OH from water adsorption [115]. A band of weak intensity at 1180 cm^{-1} is observed which corresponds to the overtone of the longitudinal optical (LO) mode located at 595 cm^{-1} (not observed in the IR spectra) [116]. This weak peak is observed even after O_2 plasma (and in all conditions tested throughout this work) indicating that this band is not from an absorbed species but from the bulk material.

When O_2 plasma is ignited at 30 mA and 1 Torr for 10 mins the main broad bands at 1304, 1570 and 3000 cm^{-1} are very much reduced. Some new bands are observed around 2850 and 2930 cm^{-1} attributed to ν(CH) vibrations. These bands could be formed during removal of water and carbonates species from the surface. But these CH stretching vibrations are significantly reduced after 40 min of O_2 plasma 30 mA at 5 Torr. Meanwhile, some bands appear more clear at 1353, 1460 and 1515 cm^{-1}. The first two are correlated to core carbonates inaccessible to remove with our cleaning conditions that could come from residuals of chemical precursors [115]. The band at 1515 cm^{-1} (along with the shoulder next at 1550 cm^{-1}) were attributed to polycarbonates [117]. Another band observed at 1263 cm^{-1} could be attributed to a carbonates species however the correct attribution remains unknown. It is worth noting that the broad band in the range 2500 to 3500 cm^{-1} is attributed to water adsorbed and hydroxyl groups. This is significantly reduced during the first 10 minutes of O_2 plasma indicating a rapid desorption of such species from the surface.

During cleaning, most of the broad bands are cleared out except for few that are around 1200 to 1550 cm^{-1} which could be attributed to polydentate carbonates. They could remain even beyond 700 K [114]. Such high temperature cannot be reached by O_2 plasma in our conditions and other effects induced by plasma such as ion bombardment or O atoms flux to the surface do not seem to be sufficient either. In our glow discharge conditions, O_2 plasma 30 mA at 5 Torr can reach up to 580 K [118, 119]. More details on the effect of O_2 plasma on carbonates species is discussed in the following chapter. Nonetheless, extending the time under O_2 plasma conditions does not reduce the intensity of the bands

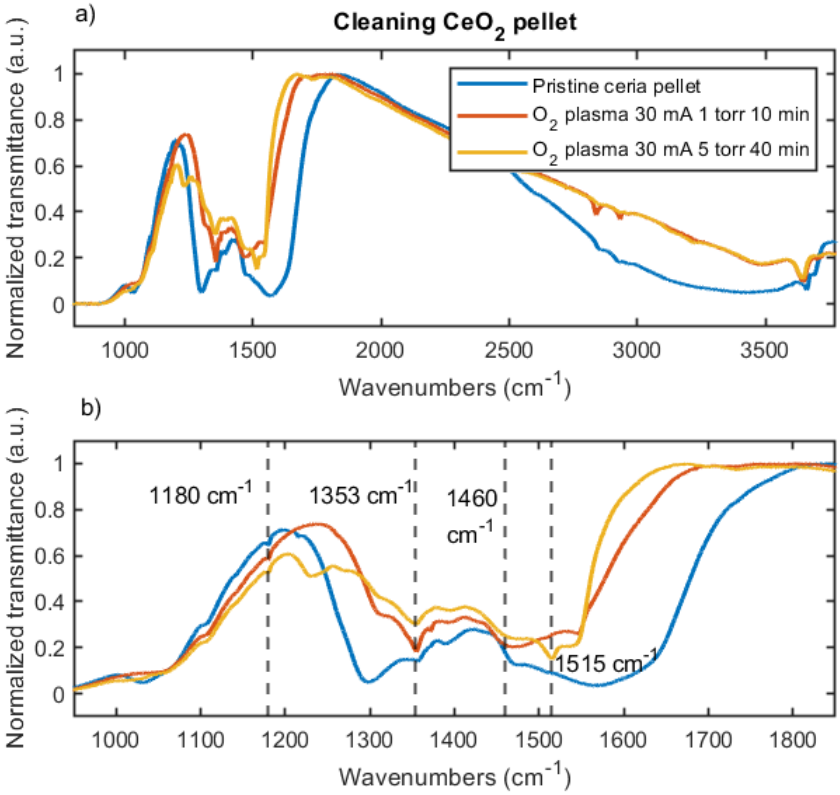

Figure 3.13: IR spectra of normalized transmittance in the region a) 800 - 3800 cm^{-1} and b) 950 - 1850 cm^{-1} of pristine ceria pellet, after O_2 plasma 30 mA 1 Torr for 10 min and after O_2 plasma 30 mA 5 Torr for 40 min. The bands at 1180, 1353, 1460 and 1515 cm^{-1} marked by vertical dash lines in b) are described in the text.

previously mentioned. Therefore, the standard procedure for subsequent experiments with CeO_2 pellets remains as: O_2 plasma 1) 30 mA 1 Torr for 10 min and 2) 30 mA 5 Torr for 40 min. The interest of applying O_2 plasma at two different pressures is that O atoms recombine less at lower pressure but the gas temperature is lower than at higher pressure [95]. Combining both conditions can therefore clean the surface in different manner.

O_2 plasma seems enough to remove most of the adsorbed species on CeO_2 surface allowing to observe clearly the adsorption of CO_2 and formation of hydrogenated species as discussed in the following sections.

3.3.2 Assignment of absorption bands in CO_2 plasma

Ceria pellet was firstly tested with pure CO_2 plasma at 1 Torr following the experimental sequence shown in figure 3.12. Figure 3.14 displays the final spectra at the end of the 10 min of each step from before plasma (1) until O_2 plasma (6) steps. In the step (1) before plasma, CO_2 is adsorbed on ceria surface displaying different bands primarily in the 1100 – 1700 cm^{-1} region. The bands with maximum intensity at 1025, 1294 and 1569 cm^{-1} are associated to ν(CO) vibrations in tridentate carbonate (written 'TC' in the following) species [117]. The bands located in the 1218, 1396 and 3618 cm^{-1} were assigned to vibrations of δ(COH), ν(CO) and ν(OH), respectively. These bands were assigned to hydrogen carbonates (written 'HC' in the following) species (also known as bicarbonates) [117].

No new bands were observed in plasma steps (2 and 3) but just a significant reduction on the intensity of the bands assigned to TC and HC. During step (4) after plasma, these bands regain the intensity they

had during step (1) before plasma. When the flowing gas is changed to O_2 (step (5)), TC and HC are only slightly reduced but when O_2 plasma is ignited at 30 mA (step (6)), all the bands are strongly reduced in intensity, almost disappearing from the spectrum. More details are given in chapter 4.

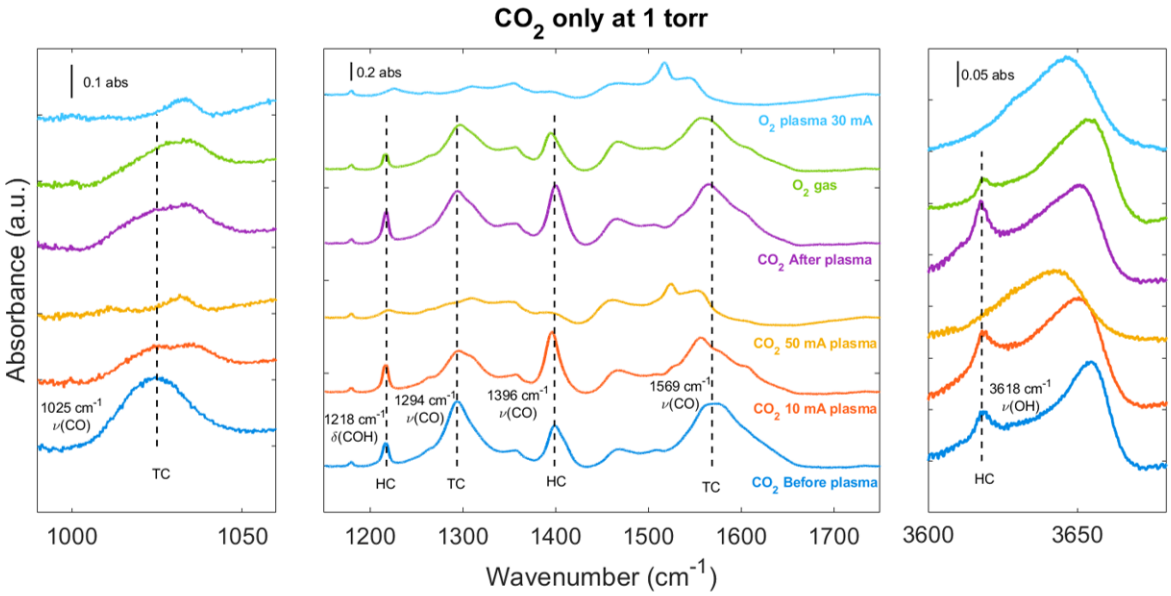

Figure 3.14: *In situ* FTIR transmission spectra of CO_2 adsorbed as carbonates species during CO_2 only experiments in ceria surface at 1 Torr in the cross DC glow discharge plasma reactor through the experimental sequence. TC: Tridentate carbonates, HC: Hydrogen carbonates. The spectra displayed corresponds to the final spectrum taken at the end of each step from the experimental sequence. Spectra are offset for clarity.

In order to understand better the evolution of carbonates species as a function of time, the area of each of these bands is determined by integrating the area under the curve defined by a range in wavenumbers and subtracting a linear baseline as shown in figure 3.15. The range was selected based on the minimum points around the peak. However, the range could fall within a range that affects the calculated area over the spectra through time. Figure 3.15 shows the sensitivity of the calculated area to the choice of wavenumber range boundaries. As an example, 3 different ranges used to extract the band HC at 1396 cm^{-1} are shown in 3.15 a_1), a_2) and a_3) and the resulting time evolution in CO_2 only at 1 Torr in 3.15 b). As observed, the small variation in the ranges do not affect significantly the area as a function of time and the trend across the three ranges is maintained. It is assumed that the same is expected in the case of the other bands assigned to TC and HC species.

Based on the bands observed here we are able to assume the presence of tridentate carbonates and hydrogen carbonates upon CO_2 adsorption from the gas phase (1). Figure 3.16 displays a simple schematic of TC and HC formation. More details are given in chapter 4.

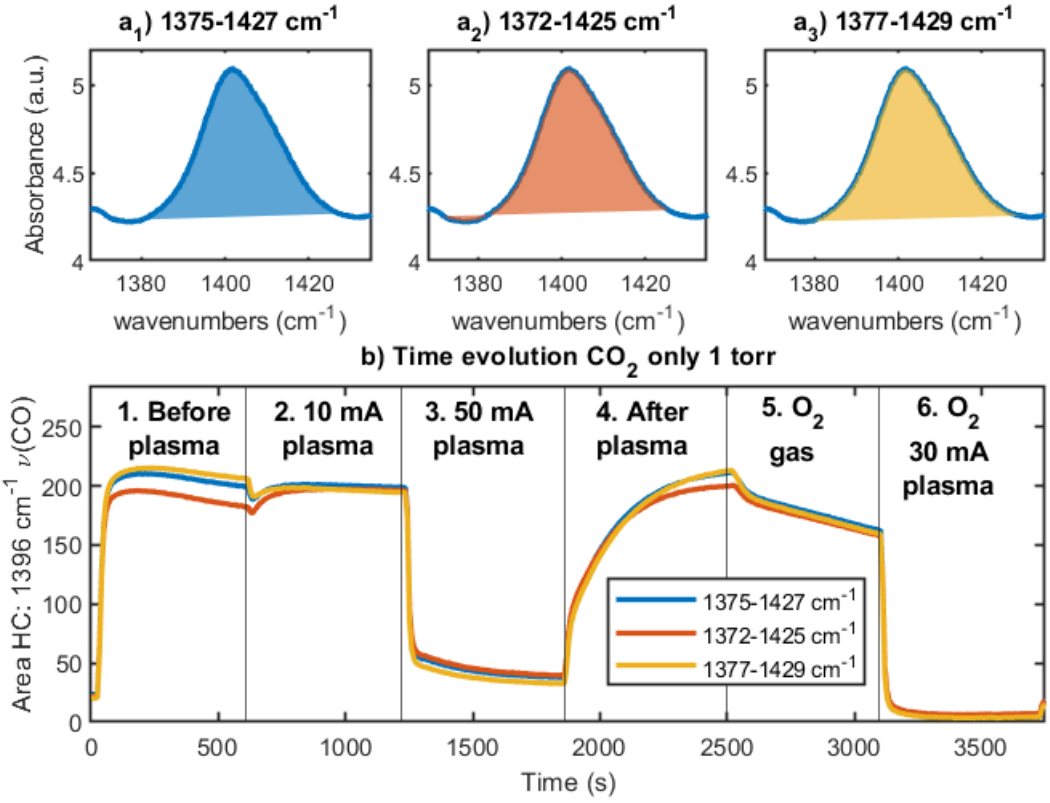

Figure 3.15: Example of area calculated for HC at the end of Before plasma (1) step for 1396 cm^{-1} ν(CO) using different ranges a_1) 1375 - 1427 cm^{-1}, a_2) 1372 - 1425 cm^{-1} and a_3) 1377 - 1429 cm^{-1} and the time evolution of each range throughout the experimental sequence. CO_2 only at 1 Torr.

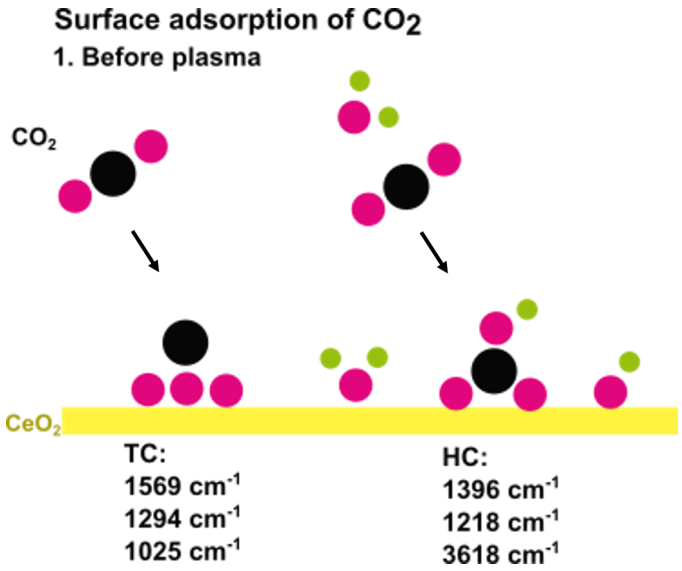

Figure 3.16: Scheme of CO_2 adsorption in CeO_2 adsorption during before plasma step based on the band observed corresponding to TC and HC species.

3.3.3 Assignment of absorption bands in CO_2-CH_4 plasma

Adding methane to the initial gas mixture for DRM reaction changes the plasma composition and therefore, the species that can be formed in surface. Figure 3.17 shows the final spectra for each step in *in situ* FTIR transmission spectra of 70%CO_2-30%CH_4 plasma at 1 Torr and 10 and 50 mA in the regions 1000 - 1100 cm^{-1}, 1200 - 1700 cm^{-1} and 2700 - 3000 cm^{-1}.

The same bands as in the previous section attributed to TC and HC during before plasma (1) step appear in the spectra, they are indicated under the peak on figure 3.17 and they are discussed in part II. New bands that were not seen in pure CO_2 now appear during CO_2-CH_4 plasma steps (2 and 3) at 10 and 50 mA and they are marked by vertical dashed lines. In particular, six bands (1358, 1370, 1545, 2722, 2845 and 2933 cm^{-1}) clearly appear during steps (2) and (3) but not in (6). In the literature these bands are consistently assigned to formates species [117, 120–123]. The bands at 1358 cm^{-1} (and 1545 cm^{-1}) correspond to symmetric and asymmetric ν(CO) vibration in formates species, respectively. The bands located at 1370 and 2845 cm^{-1} correspond to δ(OCH) and ν(CH) vibrations, respectively [120]. The bands at 2722 and 2933 cm^{-1} are attributed to a combination of asymmetric ν(CO) and δ(CH) vibrations [117, 120]. These bands are indicated by 'F' in 3.17 and in subsequent figures.

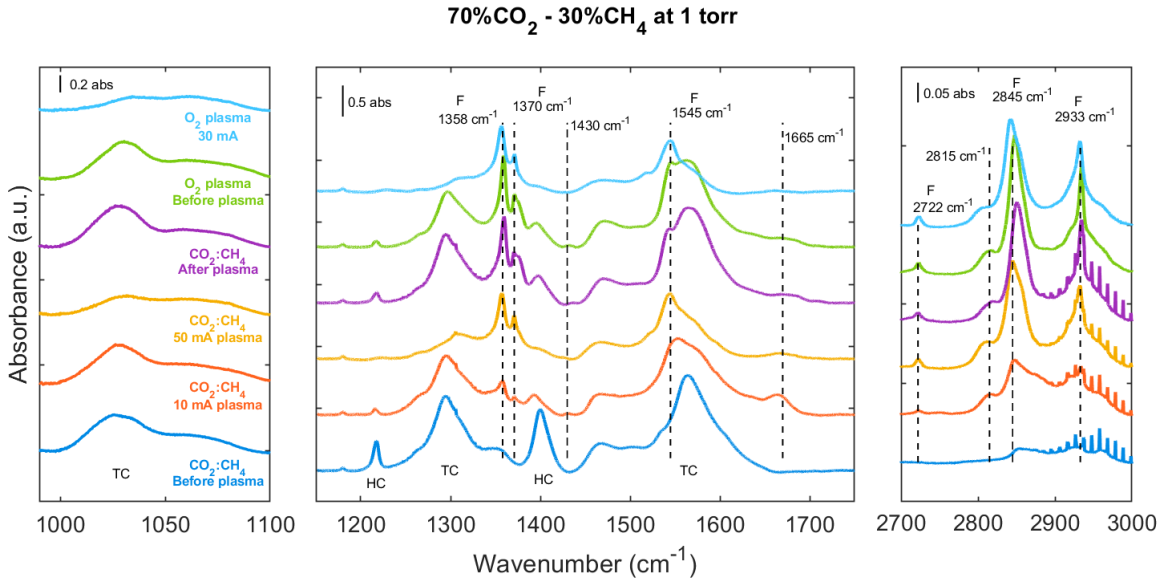

Figure 3.17: *In situ* FTIR transmission spectra of 70%CO_2-30%CH_4 plasma at 1 Torr and 10 and 50 mA in the DC glow discharge plasma reactor through the experimental sequence. The spectra shown correspond to the final spectra for each step. Spectra are offset for clarity.

Other bands that were not observed with pure CO_2 plasma are also appearing at 1430, 1665, 2170 and 2815 cm^{-1} but their assignment remain uncertain. The band at 1665 cm^{-1} is sometimes associated to a C=O bond in literature which can be tentatively related to CH_2O adsorption as a monodentate formate structure [120]. These additional bands are discussed in more detail in section 5.4.

When the plasma is off (4), the bands that appear during plasma step (formates and other bands) remain while TC specie reappear on the spectra. HC bands do not regain the intensity from step (1). This effect is discussed in more detail in chapter 4. The change to O_2 gas does not affect significantly the bands until O_2 plasma is ignited. TC and HC species then disappear from the spectra but the bands attributed to formates do stay.

To see how the bands of this particular species behaves as a function of time, the area is calculated in the same way as TC and HC in the previous section. Figure 3.18 shows an example of the effect of

the area calculated based on three different ranges used to extract the band F: 1360 cm^{-1} ν(CO) (shown in a_1), a_2) and a_3)) and the resulting b) time evolution in 70% CO_2-30% CH_4 at 1 Torr. Similarly as in carbonate species bands, the small variation in the ranges tested do not affect significantly the trend across the time evolution. It is assumed that the same is expected in the case of the other bands assigned to formates species.

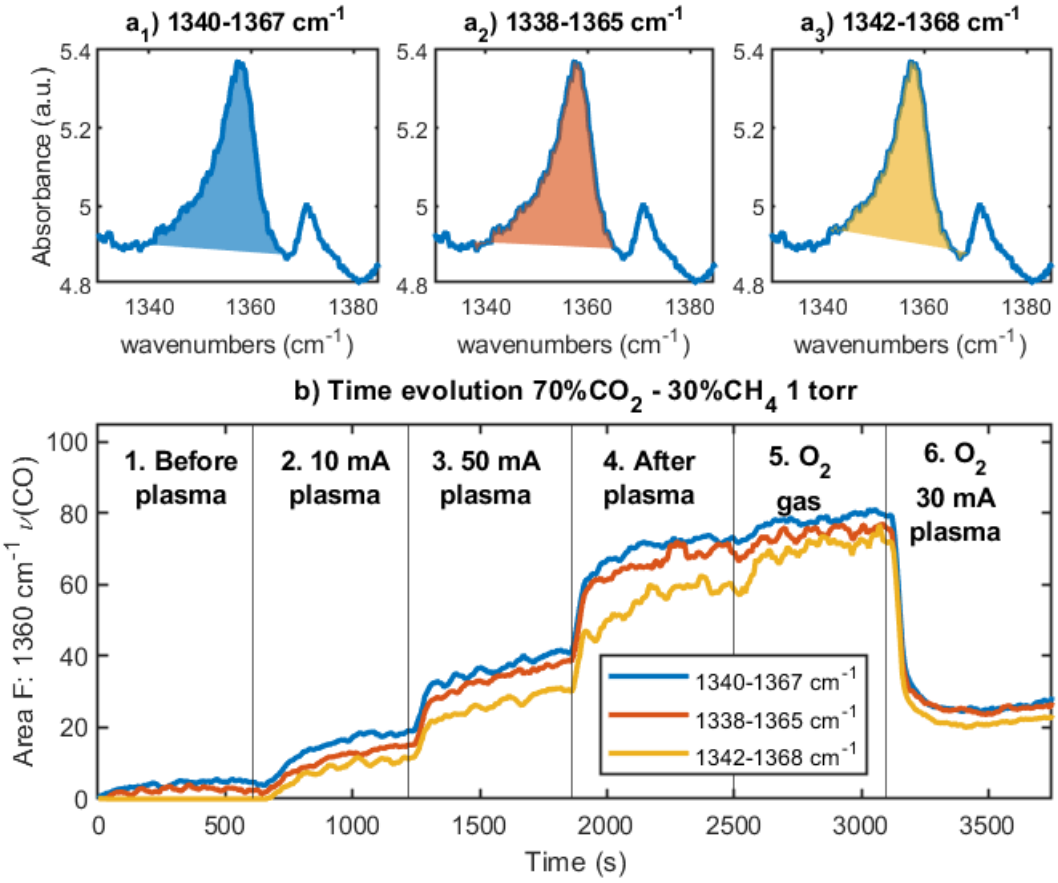

Figure 3.18: Example of area calculated at the end of 10 mA plasma (2) step for F: 1360 cm^{-1} ν(CO) using different ranges a_1) 1340 - 1367 cm^{-1}, a_2) 1338 - 1365 cm^{-1} and a_3) 1342 - 1368 cm^{-1} and b) the time evolution of each range throughout the experimental sequence. 70% CO_2-30% CH_4 at 1 Torr.

In order to confirm the assignment of these bands to formates in our case, the area of one band has been plotted as a function of the area of another band during a given plasma step. Figure 3.19 shows the correlation of 5 bands attributed to Formates at 1 and 5 Torr during steps (2),(3) and (6). The linearity obtained in these graphs with coefficient of determination $R^2 > 0.9$ confirm that these bands can belong to the same specie for 1 Torr (a_1, b_1 and c_1) and 5 Torr (a_2, b_2 and c_2). This seem to confirm the assignment of these five bands to formates specie. Nevertheless, a few inconsistencies in their time behaviour will be discussed in chapter 5. They could be due to the coexistence of different type of formates, as it has been observed with 3 different formates during methanol decomposition by Lustemberge et al. [123].

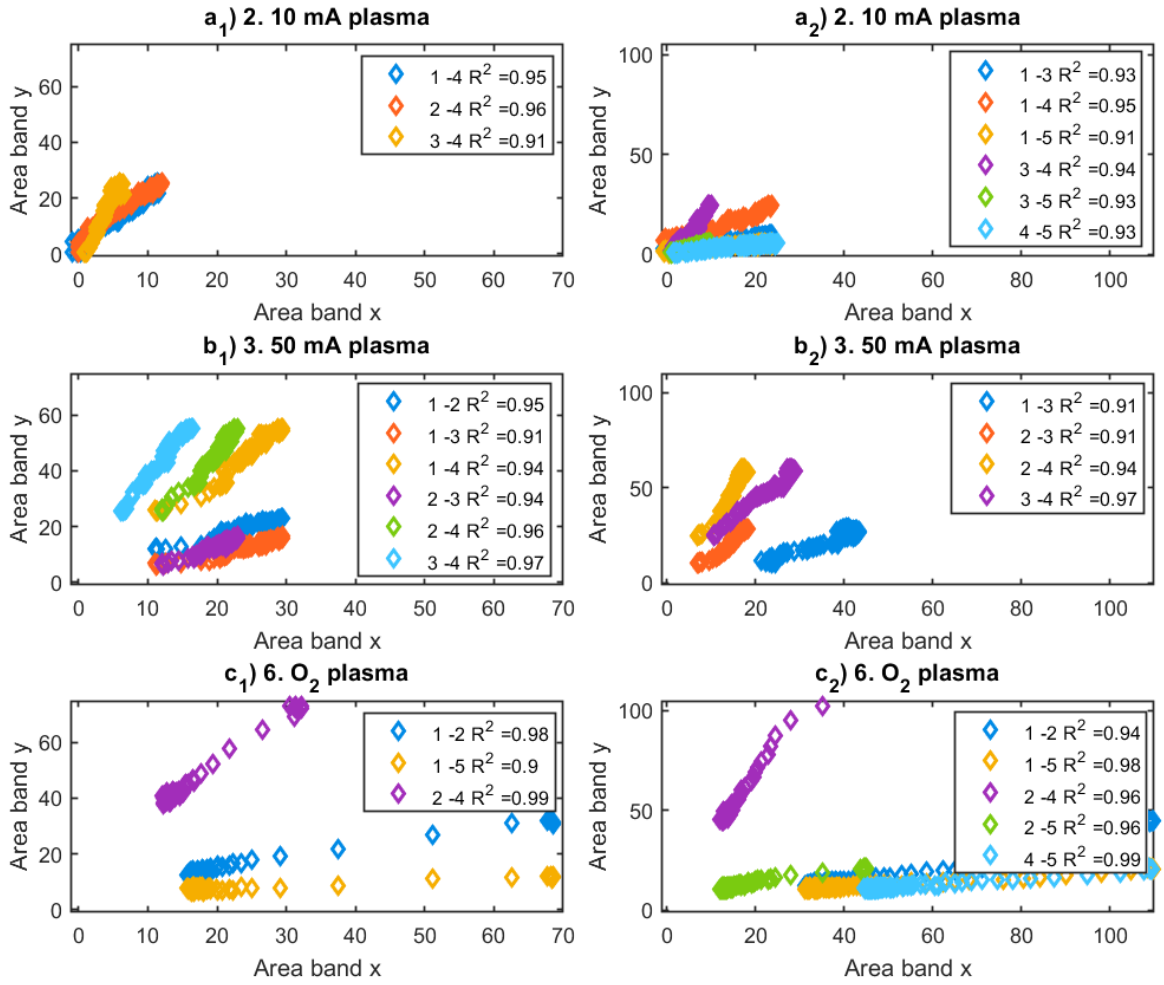

Figure 3.19: Correlation of bands x vs y during *in situ* transmission experiments for 70%CO_2-30%CH_4 at 1 Torr (a_1, b_1 and c_1) and 5 Torr (a_2, b_2 and c_2). Numbers are assigned to a specific band: 1 = 1358 cm^{-1}, 2 = 1370 cm^{-1}, 3 = 2722 cm^{-1}, 4 = 2845 cm^{-1} and 5 = 2933 cm^{-1}. Coefficient of determination R^2 is shown for every band correlated with more than 0.9.

CO_2-CH_4 plasmas can lead mainly to the formation of formates in the surface of CeO_2. Figure 3.20 shows a simplified scheme of the formation of formates species during CO_2-CH_4 plasma. Nonetheless, the mechanisms involved are described in detail in the following chapters by *in situ* FTIR transmission experiments through CeO_2 pellet.

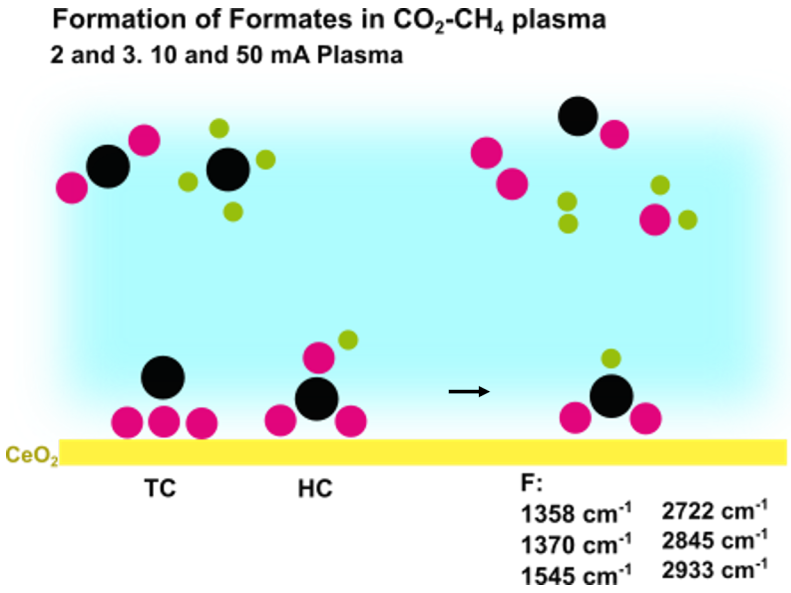

Figure 3.20: Scheme of formate formation in CeO_2 surface during CO_2-CH_4 plasma steps (2 and 3) based on the bands observed corresponding formates.

3.4 Conclusions

The downstream gas from CO_2-CH_4 plasmas is characterized by FTIR spectroscopy and Mass spectrometry through different conditions (initial concentrations, current, pressures and flow rates). The final concentration of CO_2 and CH_4 decreases with current and pressure. The concentration of CO and H_2 shows a maximum with 70%CO_2-30%CH_4 initial gas mixture. This gas mixture is used frequently throughout this thesis work. Actually from 70%CO_2-30%CH_4 initial gas mixture we began to observe traces attributed to C_2 hydrocarbons by IR and MS. These traces grow with increasing CH_4 concentration in the initial gas mixture. The variation of the total flow rate and in consequence the residence time has a marked effect on the conversions of CO_2 and CH_4 and in the final concentration of the products. The presence of the glass sampler holder with CeO_2 pellet does not change significantly the gas composition. Therefore, we can assume that the gas composition (and also the gas temperature, E/N, etc.) of the plasma tested here is the same as the plasma used during the *in situ* FTIR transmission experiments through the ceria pellet. This allowed us to confidently study the absorption bands observed in the IR spectra from CeO_2 pellet. O_2 plasma was efficient in removing a great part of adsorbates from pristine ceria. This allowed to identify tridentate carbonates and hydrogen carbonates upon CO_2 adsorption. Also, formates species were observed during CO_2-CH_4 plasma exposure. These results pave the way for subsequent experiments in part II dedicated to the detail description of adsorbates formed during CO_2 and CO_2-CH_4 plasmas by FTIR transmission experiments through a catalytic surface as CeO_2.

Part II

In situ FTIR transmission experiments

Chapter 4

CO_2 plasma interacting with CeO_2 surface

Contents

4.1 Introduction

The aim of this chapter is to bring valuable insights about the adsorbed species during pure CO_2 plasma in catalytic surface as CeO_2 and the behaviour of such species during gas and plasma conditions. Therefore, *in situ* experiments were performed at 1 and 5 Torr with 10 and 50 mA plasma current. The evolution of the carbonate bands are followed as a function of time throughout the experimental sequence (figure 3.12). Adsorption tests and downstream gas experiments are presented as well to complement the discussion from the information extracted during *in situ* experiments.

4.2 Experimental procedure

The CeO_2 powder was pelletized into self-supported wafers and placed carefully in a glass holder inside the DC glow discharge. The experimental setup is already presented in chapter 2 and 3 in figure 3.11. It consists of a cross shaped DC glow discharge plasma reactor made of glass placed in the path of infrared beam in the FTIR spectrometer. Each individual pellet was used for maximum 3 experimental sequences. Before any experimental sequence, the ceria pellet was cleaned *in situ* with O_2 plasma at 30 mA current for 50 minutes at 5 Torr with 5.4 sccm of O_2 as discussed in chapter 3. All the *in situ* experiments were carried out under flowing conditions at constant flow of 5.4 sccm (unless specified otherwise) maintaining 0.3-1 s of residence time. The experiments were performed at 1 and 5 Torr and plasma current of 10–50 mA. The gas mixture used here is CO_2 only.

For *in situ* FTIR transmission experiments, the pellet was placed in the path of the infrared beam inside the glow discharge plasma reactor as in figure 3.11. As described in the previous section, for each experiment a sequence of 6 steps lasting 10 min each was followed: (1) CO_2 was sent to the reactor (Before plasma) in order to follow the adsorption of initial molecules on the catalyst surface. During step (2), a plasma at low current (10 mA) was ignited keeping the gas temperature and the dissociation of feeding gas relatively low, then during step (3) plasma current was increased to 50 mA to monitor the effect of a more intense plasma exposure. During step (4) plasma was switched off but the same gas mixture as during step (1) is still flowing allowing to check if the adsorption of the feed gas molecules remains unchanged. O_2 gas was sent to the reactor for step (5) to exhibit any possible reversible adsorption from species observed during step (4), and finally during step (6) O_2 plasma at 30 mA was ignited to observe the oxidation of species remaining on the surface (see flowchart on figure 3.12 in chapter 3).

Two additional types of complementary experiments have also been performed to help understanding the results from *in situ* measurements. FTIR transmission experiments were performed by placing the pellet downstream the plasma ignited in an identical DC glow discharge reactor located before the FTIR spectrometer in the gas line. The steps (2) and (3) of plasma at 10 mA and 50 mA were then producing the same species as for *in situ* measurements but only the stable molecules at room temperature could reach the pellet surface. Only the step (6) of O_2 plasma was performed *in situ* in order to still have an efficient oxidation of remaining surface species. These measurements called 'downstream gas' in the following, allow to compare the evolution of surface species *in situ* and downstream by keeping the same gas composition but with or without the effects electric field, ion bombardment, rise in temperature, etc. So called 'adsorption tests' were also performed in the same reactor and gas line but without any plasma, only flowing various gas mixtures at room temperature to monitor only the adsorption of stable molecules on the pellet over long duration.

4.3 Time evolution in CO_2 plasma

Ceria pellet was firstly tested with pure CO_2 plasma at 1 Torr. As discussed in section 3.3.2, 6 bands were identified and attributed to carbonates. The bands located in the 1218, 1396 and 3618 cm^{-1} were assigned to vibrations of δ(COH), ν(CO) and ν(OH), respectively and assigned to hydrogen carbonates (HC) species (also known as bicarbonates) [117]. The bands with maximum intensity at 1025, 1294 and 1569 cm^{-1} are associated to ν(CO) vibrations in tridentate carbonate (TC) species [117]. In order to understand better the evolution of carbonates species, the area of each of these bands is followed as function of time through several steps as described in section 3.3.2. Figure 4.1 depicts the evolution of the area of the carbonates bands as a function of time on the CeO_2 pellet during all 6 steps with pure CO_2 at 1 and 5 Torr. The solid line represents an average of 3 consecutive experiments along with the shaded area illustrating the standard deviation within the same pellet.

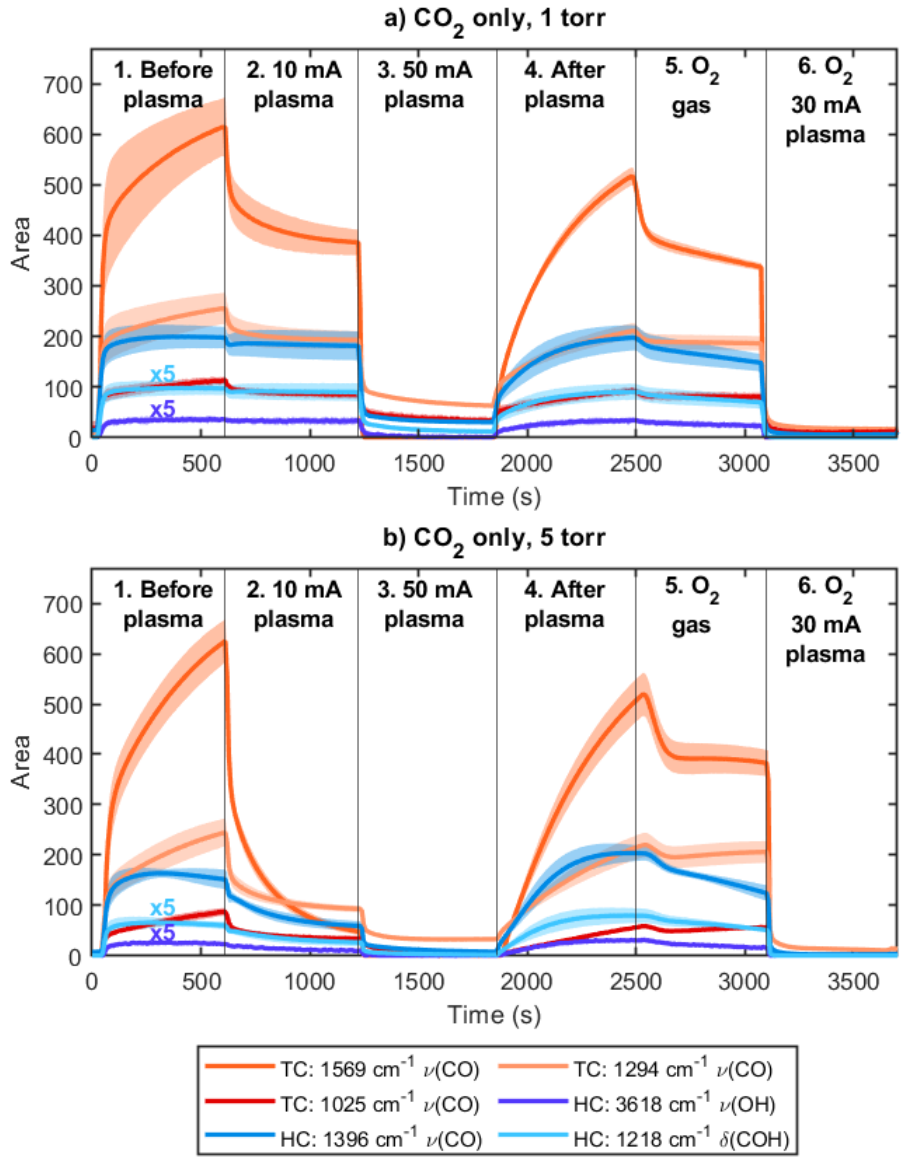

Figure 4.1: Area evolution of TC and HC bands as a function of time in pure CO_2 at 1 Torr (a) and 5 Torr (b) in *in situ* experiments. Solid line represents the average of three consecutive experiments (including cleaning with O_2 plasma in between) in the same pellet and shaded area represents the standard deviation. TC: Tridentate Carbonates; HC: Hydrogen Carbonates.

In general at 1 Torr, (figure 4.1a)) and 5 Torr (figure 4.1b)), both TC and HC tend to increase under CO_2 gas flow and decrease under CO_2 or O_2 plasma exposure. It is worth noting that standard deviation is larger during step (1) (initial CO_2 adsorption) than during any of the other steps of the sequence. This suggests that long O_2 plasma exposure (the 'pre-cleaning' with O_2 plasma is lasting 50 minutes) can affect the surface states and the surface density of adsorption sites for carbonates. However these surface modifications seems to be quickly restored under CO_2 plasma even for low current (step (2) at 10 mA) which shows already very good reproducibility for all consecutive measurements. The time evolution of TC and HC are discussed separately in the following sections.

4.3.1 Tridentate carbonates

The formation of carbonates (TC and HC) is expected given the adsorption of CO_2 onto the surface of CeO_2. Tridentate carbonates on CeO_2 are very stable species according to studies performed by Vayssilov et al [117]. The adsorption of TC during step (1) seems to proceed with two very different slopes both at 1 and 5 Torr. This adsorption slopes are significantly slower during the adsorption of TC after the CO_2 plasma (step (4)). This suggests that CO_2 plasma can modify the TC adsorption sites. However the reproducibility over the 3 successive measurement sequences on the same pellet (illustrated by the shaded coloured area) shows that these modifications are reversible after O_2 plasma cleaning. Whatever the modification of TC adsorption sites is (whether it is a change in oxidation state of the surface, some broken bounds or accumulation of other adsorbed species for instance) a strongly oxidizing plasma is restoring the TC adsorption sites. In both steps (1) and (4), the TC adsorption is not saturated after 10 minutes. This is consistent with the 'adsorption' measurements over longer time scale that will be discussed in section 4.3.2 showing a saturation only for duration longer than ∼2000 s for which an equilibrium between tridentate carbonates and CO_2 is maintained as described in [124]. During plasma steps (2) and (3), TC bands (orange and red bands on figure 4.1) first decrease rapidly and then tend to stabilize between 10 to 30% of their initial intensity depending on pressure and current. The decay of TC on the surface of CeO_2 under CO_2 plasma exposure could be due to 3 main effects:

1. An enhanced desorption due to surface heating
2. A change in partial pressure of the adsorbing specie
3. Plasma assisted desorption

In order to give insight on the relative importance of these possible contributions to the disappearance of TC, the table 4.1 shows the main parameters of the plasma measured in the same conditions to which the CeO_2 pellets is exposed on figure 4.1. It is important to remember here that adding the catalyst pellet in the plasma do not significantly affect the behaviour of the plasma in our conditions as seen in section 3.2, therefore measurements performed in the plasma without catalyst are still relevant when adding the pellet.

Pressure (Torr)	Gas	Current (mA)	E/N (Td)	T_g (K)	[CO]/N	[O]/N
1	CO_2	10	74	374	0.21	0.03
1	CO_2	50	83	550	0.31	0.13
1	O_2	30	50	370	-	0.24
5	CO_2	10	45	590	0.23	0.01
5	CO_2	50	58	840	0.35	0.05
5	O_2	30	45	580	-	0.085

Table 4.1: Values of main plasma parameters taken from [82, 125] and confirmed by measurements done for pure CO_2 [87], and from [118, 119] for O_2 in the conditions from figure 4.1.

As can be seen from table 4.1, the glow discharge used for this study can significantly heat the surface of the catalyst by several hundred degrees. As the pellet is very thin, it can be assumed that the material is thermalized with the gas temperature during the 10 minutes of each plasma step. At 1 Torr and 10 mA, TC bands decrease only to ∼2/3 of their maximum intensity while the gas temperature remains relatively low at 374 K. At 1 Torr 50 mA, and at 5 Torr 10 mA the gas temperature is similar (respectively 580 K and 550 K), and the TC bands decrease to ∼10% of their intensity at the end of step (1). TC bands are the weakest at 5 Torr and 50 mA when the gas temperature is 840 K. This suggests that thermal desorption could explain the disappearance of TC as it has already been observed in the literature [67, 117]. However, there are two observations which show that the gas temperature is not the

only parameter responsible for TC disappearance: (i) simply flowing pure O_2 gas (step (5)) is already sufficient to make 20% of the TC bands disappear at both 1 Torr and 5 Torr showing that lower partial pressure of CO_2 also contributes to TC disappearance, and (ii) a pure O_2 plasma at 30 mA makes all traces of TC disappear in a few tens of seconds, whereas the gas temperature at 1 Torr is only 374 K in this plasma.

The decay of CO_2 partial pressure could be important for the decay of TC bands even during steps (2) and (3) with CO_2 plasma because TC are formed only from CO_2, and not from CO. This is shown more in detail in section 4.3.2 with the results of adsorption experiments. The TC decay observed while flowing O_2 gas (step (5)) shows that part of TC are probably weakly bond to the surface at room temperature and their surface density depends on the partial pressure of CO_2 above the surface. The very fast decay under pure O_2 plasma would suggest another mechanism of sometimes called 'plasma assisted desorption'.

Plasma-assisted desorption process is a broad term that is used in the literature to explain the desorption from a catalytic surface of adsorbed species by ions bombardment and excited species [34, 126]. In our conditions the main ion specie both in pure CO_2 and O_2 plasma is O_2^+ even at 10 mA. The electric field and electron density are not significantly different between CO_2 and O_2 plasmas [119, 125]. Therefore the efficiency of the ion bombardment on the CeO_2 surface in our CO_2 or O_2 plasma is not expected to be very different (especially since the sheaths are collisional at the pressures studied). The faster decay of TC under the pure O_2 plasma could therefore either be the result of the O_2^+ ion bombardment combined with the absence of CO_2 in the gas phase to renew the carbonates on the surface, or it could be due to O atoms and/or excited electronic states of oxygen capable of removing TC. The O atoms density is about twice larger in the pure O_2 plasma at 30 mA than in the pure CO_2 plasma even at 50 mA as shown on table 4.1 [82, 125]. The density of other energetic electronic states such as $O(^1D)$ or $O_2(a^1\Delta)$ carrying energies of several eV will also be higher in the pure O_2 case and therefore could contribute to the faster decay of TC as well.

As a conclusion, if the effect of gas temperature on TC desorption is important, it seems that the role of excited oxygen species is also non-negligible in accelerating TC desorption, even at low gas temperature.

4.3.2 Hydrogen carbonates

In the presence of OH groups, CO_2 can react with OH generating hydrogen carbonates [117, 127]. The formation of HC shown on figure 4.1 is therefore probably a consequence of water impurities in the gas bottles. The water impurity level from the gas bottles used for these measurements is <50 ppm in CO_2 bottle, <3 ppm in O_2, and <50 ppm in CO bottle (used for adsorption tests). Despite the low level of water impurities, water could accumulate onto CeO_2 surface, and HC can be formed. Possible mechanism of formation will be discussed in the following.

HC are characterized by the bands located in the 1218, 1396 and 3618 cm^{-1} assigned to δ(COH), ν(CO) and ν(OH), respectively (see figure 3.14). Such bands increase very rapidly and reach a maximum around 140 seconds and slowly decay during step (1) on figure 4.1. They behave similarly as TC bands: they grow during CO_2 gas steps (before (1) and after plasma (4) steps) and they are reduced during CO_2 plasma steps (10 and 50 mA steps). After CO_2 plasma (step (4)), like for TC, they are formed at a slower rate than during step (1) but their maximum intensity remain the same at 1 Torr. At 5 Torr, the intensity of HC bands grows slightly higher in after plasma step (4) in comparison to before plasma

(1). A slow decay of HC is observed when flowing O_2 gas (step (5)) but less pronounced than for TC. O_2 plasma is removing HC as efficiently as TC (step (6)).

To further investigate the effect of water and OH on the formation of HC, we look at the time evolution of OH groups bands from the region 3000 - 3700 cm^{-1} (figure 4.2).

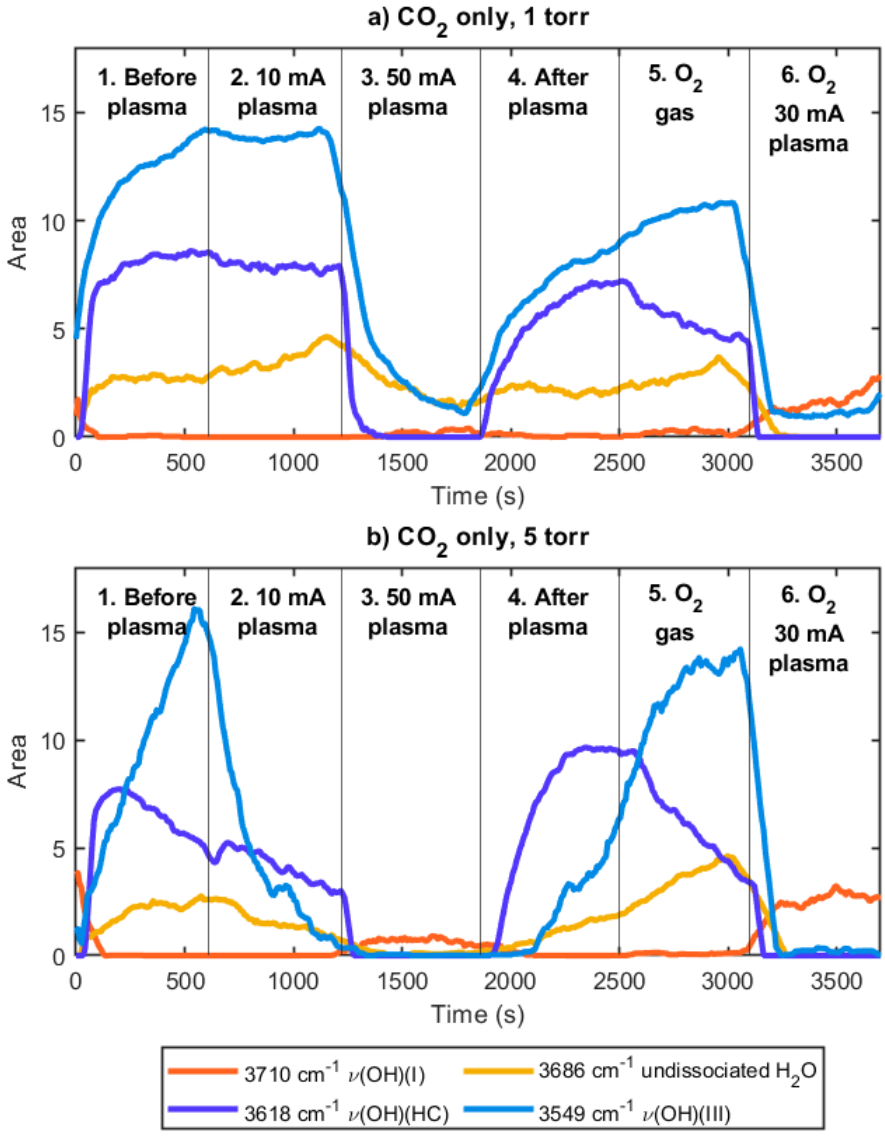

Figure 4.2: Area evolution of IR adsorption bands of 3549 cm^{-1} ν(OH)(III), 3686 cm^{-1} undissociated water, 3618 cm^{-1} ν(OH)(HC) and 3710 cm^{-1} ν(OH)(I) as a function of time in pure CO_2 at a) 1 Torr and b) 5 Torr in *in situ* experiments.

Upon CO_2 adsorption, several bands are observed at 3549 and 3686 cm^{-1} corresponding to ν(OH)(III) and undissociated water, respectively [128, 129]. On the contrary, the band at 3710 cm^{-1} attributed to ν(OH)(I) is reduced in area and disappears while carbonates bands and other OH bands grow. During CO_2 plasma at 50 mA (step (3)) and O_2 plasma (step (6)) at 1 and 5 Torr, the bands 3549 and 3686 cm^{-1} quickly decay (in a similar manner as TC and HC) indicating a desorption by rise on temperature and/or ion bombardment (O_2^+). However, plasma does not seem to prevent the reappearance of the 3710 cm^{-1} (ν(OH)(I)) as seen in figure 4.2. We could hypothesize that the presence of carbonate species

disturbs the existence of OH(I). Perhaps, during O_2 and CO_2 plasma ((3) and (6) steps), O atoms are provided to the surface structure which allows monodentate OH groups. Regarding the band at 3686 cm^{-1} attributed to undissociated H_2O, it accumulates during CO_2 gas steps (step (1)) and seems to give rise to OH(III) (3549 cm^{-1}), possibly during HC formation. During CO_2 10 mA plasma step at 1 Torr, the 3686 cm^{-1} band slightly increase while ν(OH)(III) (3549 cm^{-1}) and ν(OH)(HC) remain constant. This could indicate that under low plasma current, undissociated water can adsorb in the surface without forming new HC species. Contrary to CO_2 10 mA at 1 Torr, the bands at 3549, 3618 and 3686 cm^{-1} decay at 5 Torr 10 mA, suggesting that the increase in temperature (590 K instead of 374 K) plays an important role on the adsorption of OH species.

However, the band at 3549 cm^{-1} (ν(OH)(III)) although less intense after CO_2 plasma, continues growing even on O_2 gas at 1 and 5 Torr. The band at 3686 cm^{-1} (undissociated H_2O) seems to grow to almost the same intensity during after plasma step (4) as in before plasma step (1) but at slower rate. We can notice a difference between 1 and 5 Torr experiments during step (4): at 5 Torr, the adsorption of undissociated water is lower during step (4) than during step (1) but more HC are formed, while at 1 Torr the same amount of undissociated water is present both during step (1) and (4) and HC are formed in the same amount. When flowing of O_2 gas (step (5)), the undissociated water and OH(III) continue growing while HC are diminishing onto the surface. It seems therefore that a link exists between the amount of undissociated water in the surface and the amount of CO_2 density interacting with the surface that leads to the formation of HC. As proposed for other materials such as TiO_2, OH formed during homolytic dissociation of water, reacts with CO_2 by proton transfer or nucleophilic attack on CO_2 by nearby OH species forming a bidentate structure like HC and leaving a hydroxyl group on the surface [130, 131]. In Al_2O_3, bicarbonate formation is proposed to occur via an hydroxy group transfer to CO_2 molecule [132].

In summary, OH(I) groups are disturbed by the presence of TC and HC species and they can reappear under CO_2 and O_2 plasma conditions. The presence of undissociated water is key in the formation of HC species however, the evidence points that a too large amount (or surface density) of undissociated H_2O can hinder the reaction of CO_2 to generate HC.

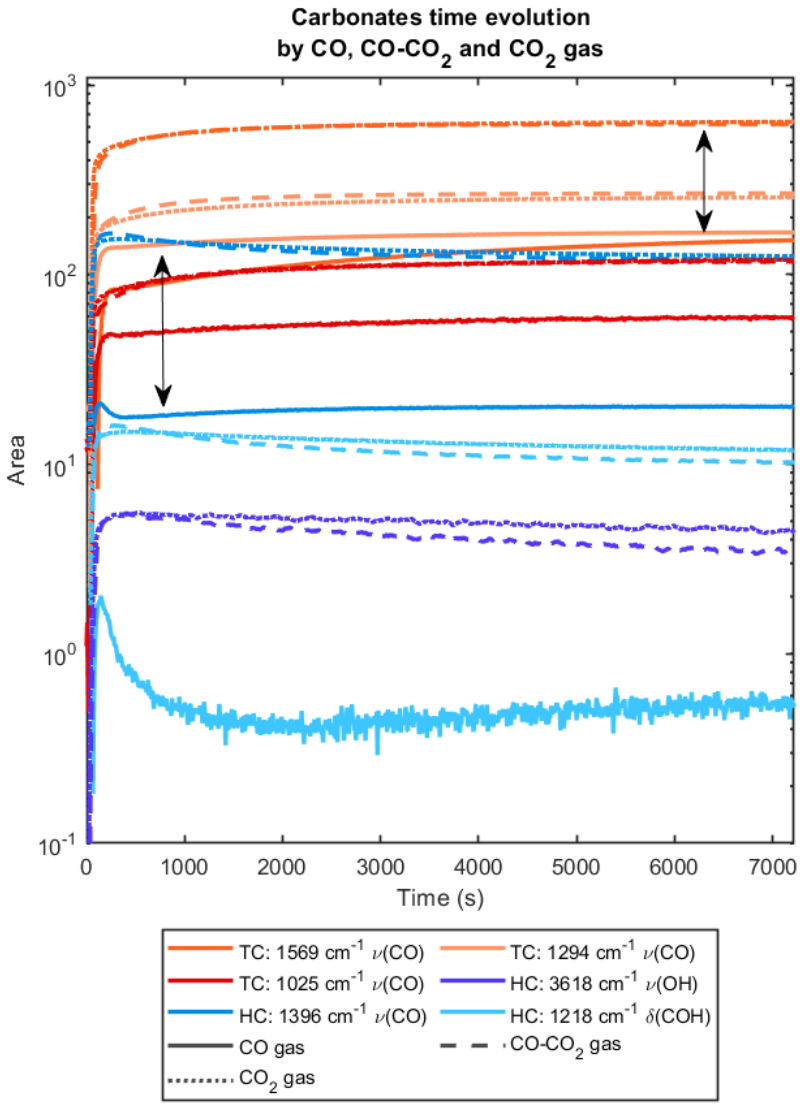

Figure 4.3: Area evolution of carbonate bands for CO, CO-CO_2 and CO_2 adsorption as a function of time for 7200 seconds at 1 Torr using the same ceria pellet. Solid line: CO; Dashed line: CO-CO_2; Dotted line: CO_2. The proportion of CO/CO_2 gas mixture is 1/1. The arrows show the difference in area compared from CO and CO_2 adsorption. Same ceria pellet used for the 3 experiments displayed here.

4.3.3 OH related bands

If large amounts of water can interfere with the formation of HC species, it is interesting to look at the adsorption of CO_2 and H_2O impurities for long periods of time. In addition, one of the main products from CO_2 dissociation, carbon monoxide, could also throw insights on the formation of HC. Figure 4.3 shows the time evolution of the areas of TC and HC bands during CO_2, CO_2-CO and CO adsorption. Figure 4.4 shows the OH groups bands from the same experiment. As mentioned before, TC bands are formed and reach a steady state stable throughout the whole experiment during CO_2 and CO_2-CO flow. HC bands appear very quick and slowly decay as long as CO_2 and CO_2-CO are flown. However when only CO is interacting with the CeO_2 surface, only weak bands of TC and HC appear. The dilution

CO_2 with CO gas seems to not have a visible effect on the adsorption rate of CO_2 nor in the formation of carbonate species. As it has been previously reported, CO interacts weakly with the CeO_2 surface resulting in less tridentate carbonates and hydrogen carbonates species [77, 124]. This low formation of carbonate species affects also the OH region as seen in figure 4.4. For this figure, as the amount of HC is so low in CO only experiment that the band 3618 cm^{-1} (ν(OH)) of HC is no longer observed, the band at 1218 cm^{-1} (δ(COH)) is used for comparison.

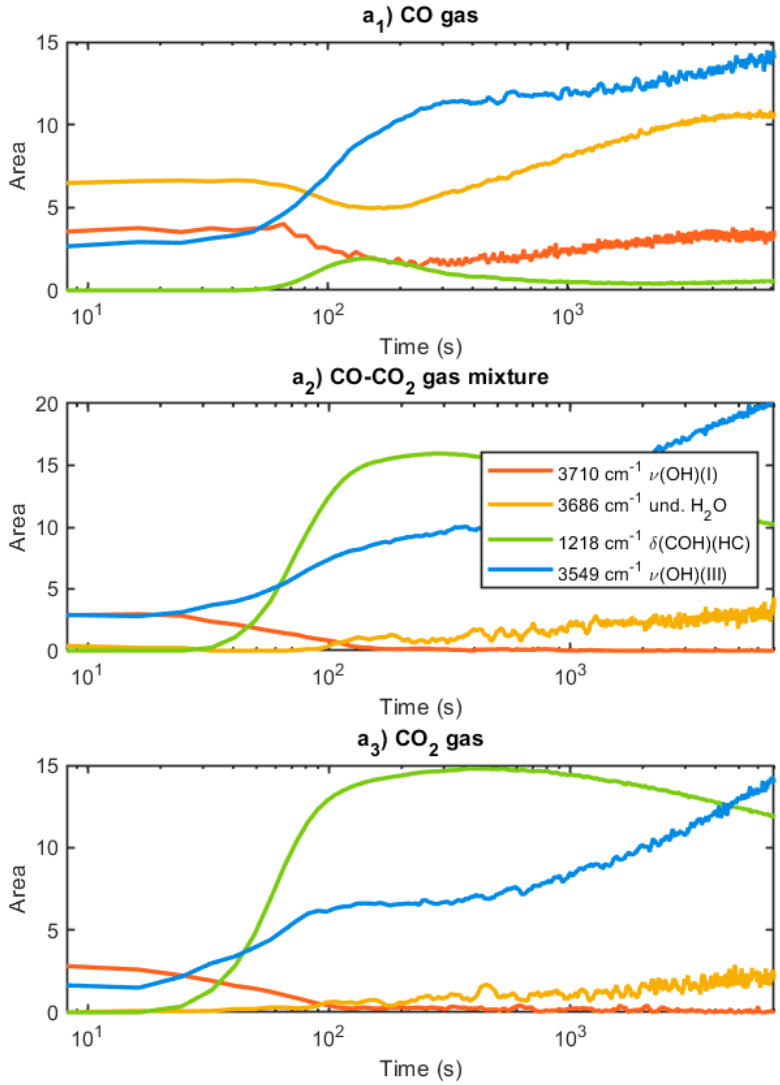

Figure 4.4: Area evolution of OH group bands for a_1) CO, a_2) CO-CO_2 and a_3) CO_2 adsorption as a function of time for 7200 seconds at 1 Torr. Same ceria pellet used for the 3 experiments displayed here.

Several things can be noticed on figure 4.4:

1. OH(I) groups (3710 cm^{-1}) are momentarily disturbed when HC appear in CO adsorption. Eventually, they reappear as HC are disappearing from the surface. TC seem to not affect OH(I) groups.

2. Undissociated water (3686 cm^{-1}) is reacting with CO to generate HC. Once the few species of HC

are formed, the undissociated water continues accumulating while the HC decrease in the surface. It should be recalled that water impurities exist in the gas bottles and can accumulate in the surface of the gas lines.

3. OH(III) groups (3549 cm^{-1}) grow simultaneously as the band δ(COH) from HC (1218 cm^{-1}). However, it is not clear if they are a side product from the reaction of water with CO_2 leaving OH groups on the surface as they continue growing even after no more HC are formed in the surface.

This shows that undissociated water (3686 cm^{-1}) is the main source of OH for the formation of HC and not hydroxyl groups already adsorbed in the surface as has been proposed in [130,131]. Also, water can accumulate on the surface and possibly hinder HC formation. A balance between CO_2 and H_2O molecules should be considered. Finally, CO does not compete with CO_2 as cannot adsorb in CeO_2 to form carbonates on the surface.

To complete these observations, measurement with the CeO_2 pellet downstream the plasma are performed. In this case the exact same gas composition produced by CO_2 plasma arrives onto the surface but without any excited states or short lived radicals, and without other effects induced by the plasma (heating, electric field, etc.). Downstream a pure CO_2 plasma, it means that a mixture of CO_2, CO and O_2 interacts with the CeO_2 pellet. Figure 4.5 show the area evolution as a function of time of a) TC and HC and b) OH groups in downstream gas experiment performed in CO_2 only at 1 Torr. Similarly as in adsorption tests from figure 4.3, TC grow rapidly in (1) and continue increasing until (4) and reach a maximum at 2500 s despite interacting with a gas mixture of CO_2, CO and molecular oxygen. In the meantime, HC reach a maximum in intensity around 300 s and decay slowly. Interestingly, the saturation of TC is $\sim$ 500 s later than during adsorption tests from figure 4.3. This could be due to the shorter residence time of the gas interacting with the surface. The flow rate was adjusted to the glow discharge reactor upstream in the gas line to 7.4 sccm to meet similar residence time as in the glow discharge located in the path of the IR beam in the FTIR spectrometer. The intensity of TC and HC decrease with the change of gas to O_2 (5) due to the change of partial pressure of CO_2 as in *in situ* experiments (figure 4.1). Still at this step, OH(III) groups (3549 cm^{-1}) reach a steady state while HC decrease and undissociated water (3686 cm^{-1}) increase. This unrelated behaviour might suggest that OH(III) groups are mere spectators or a transition state which quickly results into undissociated water from HC decomposition. In (6), the O_2 plasma reduces the bands of all bands except 3710 cm^{-1} OH(I).

Another interesting behaviour worth noting is the change in the area attributed to carbonates especially to TC species. Following the band at 1569 cm^{-1}, there is a small decrease in the area during plasma steps 2 and 3 upstream which can be attributed to the difference in partial pressure of CO_2 in the gas. Now CO and O_2 are present in the gas mixture affecting the adsorption of CO_2 and formation of carbonates, mainly TC, but not significantly. During these plasma steps (2 and 3), the OH related groups are not affected given that the H_2O impurities do not vary throughout the experiment and seem to accumulate in the surface of CeO_2 pellet.

In summary, a brief proposed mechanism is represented in the scheme from figure 4.6 where the caption describes each step followed through the experimental sequence from figure 3.12 in pure CO_2.

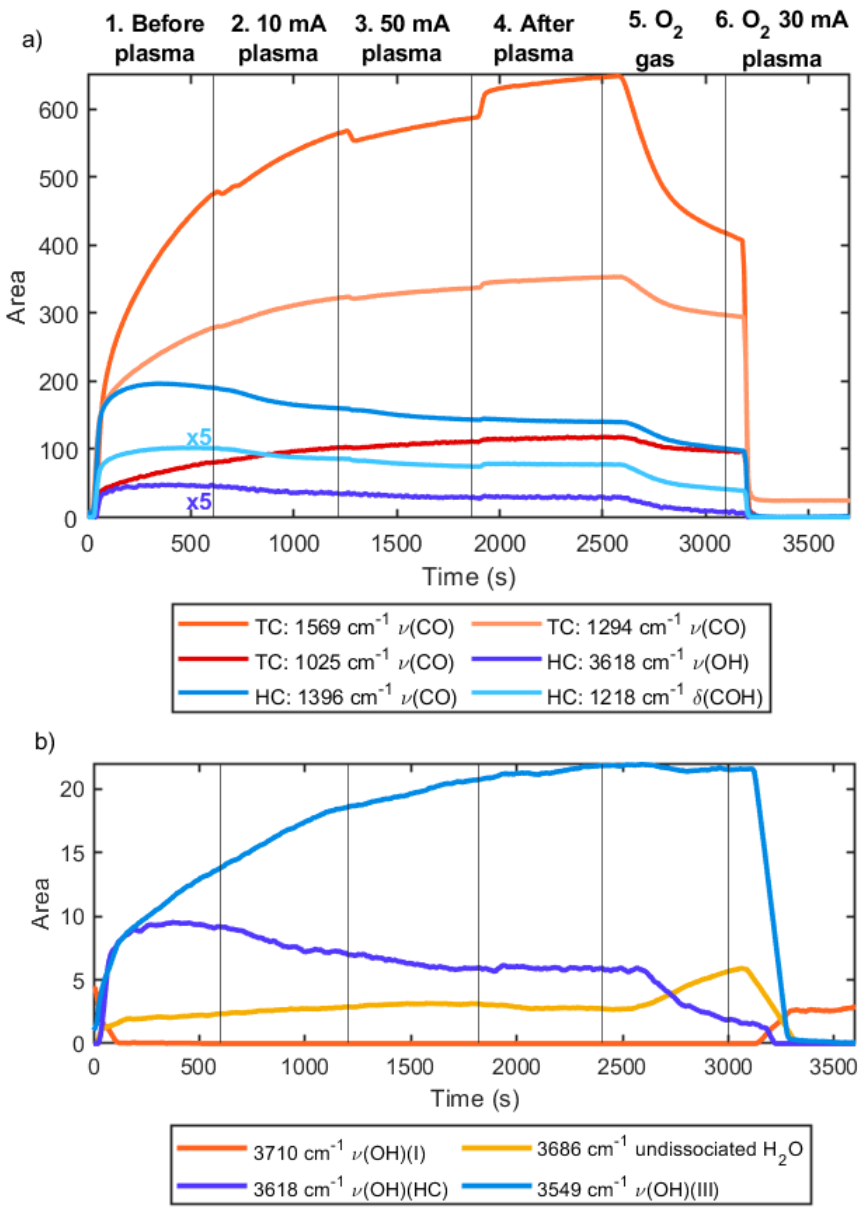

Figure 4.5: Area evolution of IR adsorption bands in Downstream gas experiments of a) TC and HC species and b) OH groups as a function of time in CO_2 only at 1 Torr. Step 6. O_2 30 mA plasma is performed *in situ* where the pellet is located. Total flowrate: 7.4 sccm.

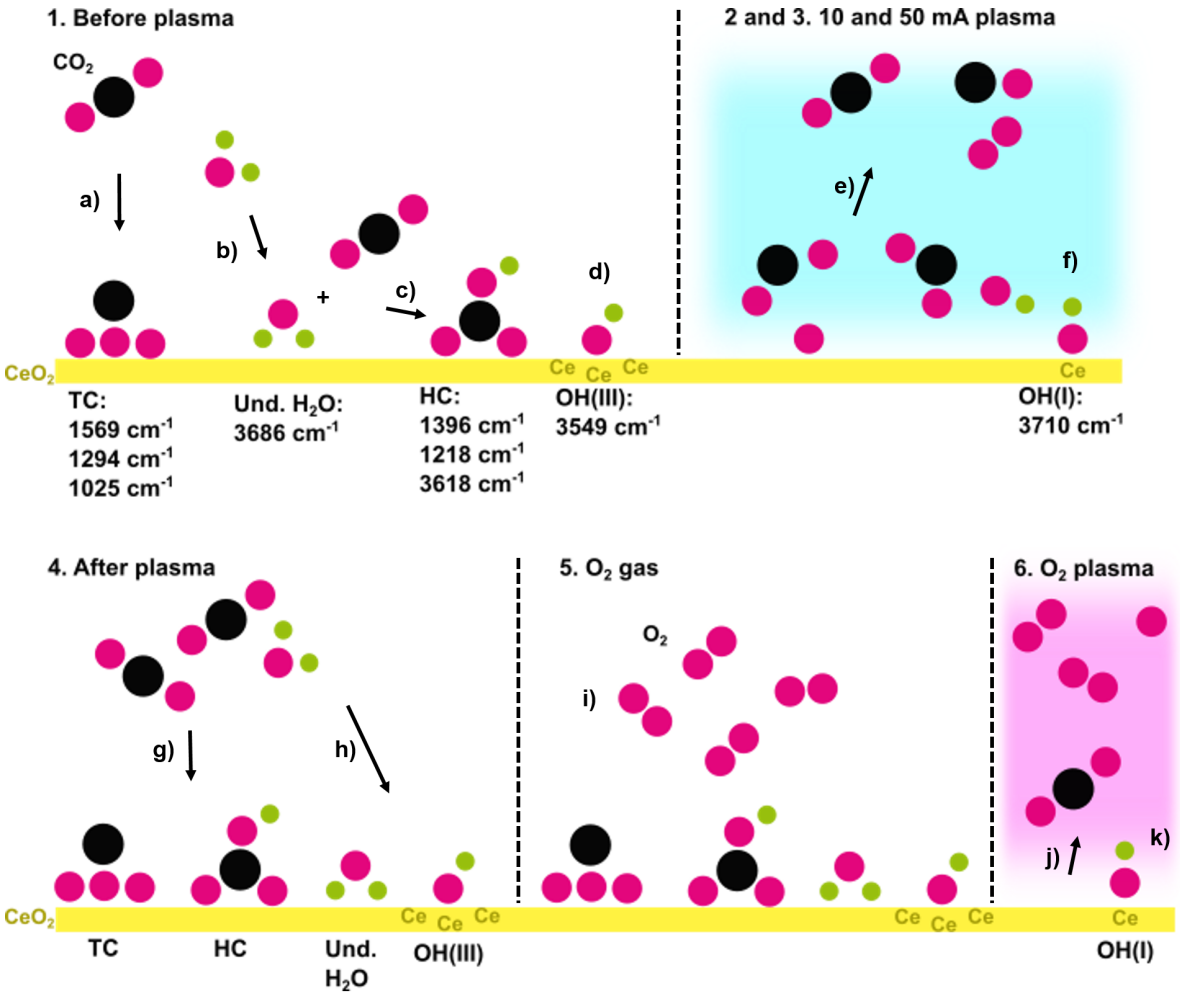

Figure 4.6: Scheme of the proposed mechanism occurring on CO_2 plasma through steps (1) to (6) in CeO_2 surface. 1. Before plasma: a) adsorption of CO_2 forming TC, b) water traces are adsorbed in the surface c) further reacting with CO_2 to form HC, d) OH(III) are simultaneously formed on the surface. 2. and 3. 10 and 50 mA plasma: e) carbonates are desorbed from the surface by increase in temperature, change in partial pressure of CO_2 and ion bombardment/excited O atoms while f) OH(I) groups reappear on the surface. 4. After plasma: g) TC and HC appear in the surface again and h) water traces are adsorbed again resulting in undissociated water and OH(III) groups. 5. O_2 gas: i) O_2 gas removes the weakly adsorbed CO_2 molecules. 6. O_2 plasma: j) the surface carbonates are removed from the surface mostly by ion bombardment/excited O atoms k) allowing OH(I) groups to form again.

4.4 Conclusions

Tridentate carbonates and hydrogen carbonates were followed as a function of time by *in situ* FTIR transmission during CO_2 only experiments using CeO_2 as catalytic surface. The saturation of tridentate carbonates on the surface depends on time of exposure reaching a maximum at 2500 s. On the other hand, hydrogen carbonates are formed by a reaction between CO_2 molecules and OH group from undissociated water (3686 cm^{-1}). Hydrogen carbonates quickly reach a maximum at 300 s and decay due to the adsorption of water impurities coming from the gas line. Despite undissociated water being the source of OH for HC formation, accumulation of too much water seems to influence HC stability in the surface as it is discussed in detail in section 5.2.2. OH(I) groups are mainly perturbed by HC species on the

surface. OH(III) groups seem to behave as spectators or a transitory state in water dissociation.

The combination of temperature, change in the partial pressure of CO_2 and ion bombardment or incoming O atoms has a role not only on CO_2 plasma steps but also during O_2 plasma affecting the TC and HC formation and desorption from CeO_2 surface. These results show from direct measurements of adsorbed species that the effect of the plasma in this case is not limited to just surface heating.

Chapter 5

CO_2-CH_4 plasma interacting with CeO_2 surface

Contents

5.1 Introduction

After studying the effect of pure CO_2 plasma on cerium oxide in the previous Chapter, CH_4 was added to the initial gas mixture at concentrations of 70%CO_2-30%CH_4. This gas mixture was selected given the maximum H_2 and CO densities produced by the plasma (see Chapter 3) while maintaining a relatively low carbon deposition. With CH_4 in the initial gas mixture, CO and H_2 are the main products. The table 5.1 reminds the main parameters of the plasma phase as measured in measurements from Chapter 3 and confirmed by measurements from [87]. It is worth noting that the gas temperature here has been obtained from the fitting of the rotational temperature of the CO Angström band as explained in chapter 2.

P (Torr)	I (mA)	E/N (Td)	T_g (K)	$[CO_2]/N$	$[CH_4]/N$	$[CO]/N$	$[H_2]/N$	$[H_2O]/N$
1	10	64.30	327	0.46	0.12	0.15	0.11	0.04
1	40	71.37	427	0.30	0.04	0.3	0.29	0.07
1	50	72.13	452	0.23	0.03	0.34	0.3	0.07
5	10	48.03	595	0.48	0.14	0.21	0.18	0.03
5	40	63.14	669	0.31	0.05	0.37	0.30	0.05
5	50	63.84	701	0.27	0.04	0.41	0.36	0.06

Table 5.1: Values of main plasma parameters in CO_2-CH_4 plasma measured by FTIR and confirmed by Mass spectrometry measurements performed in the same conditions for all the conditions used in this chapter.

An important difference with the pure CO_2 plasma is that H_2O is also formed representing up to 7% of the gas, while only traces of O_2 are detected. Indeed a kinetic model developed in the thesis of Edmond Baratte in collaboration with the group of V. Guerra from IST Lisbon has shown that in our condition, already with 10%CH_4 in the mixture, almost all O atoms are consumed by oxidation reactions of CH_x compounds. Traces of ethane, acetylene and ethylene have been detected but their absolute density do not exceed 1% of the total gas mixture for the 70% CO_2 and 30% CH_4 used here (see figure 3.5 in chapter 3). The gas composition is not changing significantly in the post-discharge compared to the *in situ* composition except for the recombination of H atoms into H_2 and the fast reactions involving CH_2O producing eventually small addition of CO and H_2. Therefore the downstream gas composition is almost the same as the composition of the plasma itself. Moreover measurements with both FTIR and mass spectrometer performed downstream the plasma reactor with and without CeO_2 pellets have shown that the amount of catalyst introduced with the pellet is small enough to not affect molecules formed in the gas phase (see figure 3.10 in chapter 3). All the plasma parameters measured with plasma only correspond therefore to the conditions to which the CeO_2 is being exposed. It is worth noting also that gas temperature is lower in CO_2-CH_4 plasma compared to CO_2. For 10 mA plasma reaches 327 K but at 50 mA only 452 K, which is ∼100 K less than in pure CO_2 at 1 Torr. At 5 Torr and 50 mA, T_g is ∼140 K colder in CO_2-CH_4. This is a consequence of the formation of high amounts of H_2 leading to a more efficient heat transfer to the walls of the reactor, especially at high plasma current.

The electric field is similar in CO_2 and CO_2-CH_4, however as T_g is increasing less with pressure in CO_2-CH_4, the reduced electric field E/N is almost constant from 1 to 5 Torr and is slightly lower than in pure CO_2 at 1 Torr, and a bit higher at 5 Torr.

The similar electric field and electron density for both CO_2 and CO_2-CH_4 is not expected to change significantly the surface species on CeO_2 between the two cases. However, the gas temperature as well as the presence of water even in small quantity has been shown to play a key role on the surface species discussed in the previous chapter. Therefore lower T_g and higher H_2O fraction in CO_2 / CH_4 plasma will probably affect the adsorbed species.

The procedure followed is the same as in chapter 4 except that the gas mixture in this chapter is 70%CO_2-30%CH_4 (unless stated otherwise for a few exceptions).

In the following sections, we will discuss the results from *in situ* experiments in combination with downstream experiments (section 5.3). As explained already, the aim of the downstream experiments is to submit the CeO_2 pellet to the gas composition of the CO_2-CH_4 plasma without the inherent effects of plasma as ion bombardment, electric field, rise in temperature, etc. The fractions indicated in table 5.1 can be considered to be the gas composition in contact with the CeO_2 pellet in both *in situ* and downstream cases. The last section presents the results from the characterization of CeO_2 pellet with XRD, SEM-EDX, XPS and surface area by N_2 physisorption (using BET theory) to discuss the effect of the CO_2-CH_4 glow discharge on the properties of the CeO_2 surface.

5.2 Time evolution in CO_2-CH_4 plasmas

Carbonates are the main precursors for formate species in DRM reaction, either in thermal catalysis or plasma-catalysis [67, 69, 72, 73]. However, the type of carbonates is not always clear. For that reason, TC and HC species are followed as a function of time during *in situ* experiments in 70%CO_2-30%CH_4 plasma.

5.2.1 Tridentate carbonates

Figure 5.1 shows the time evolution of tridentate carbonate bands (1294 and 1025 cm^{-1}) at a) 1 Torr and b) 5 Torr. The band at 1569 cm^{-1} was not added due to overlap of other contributions like the band 1545 cm^{-1} which corresponds to asymmetric ν(CO) of formates species.

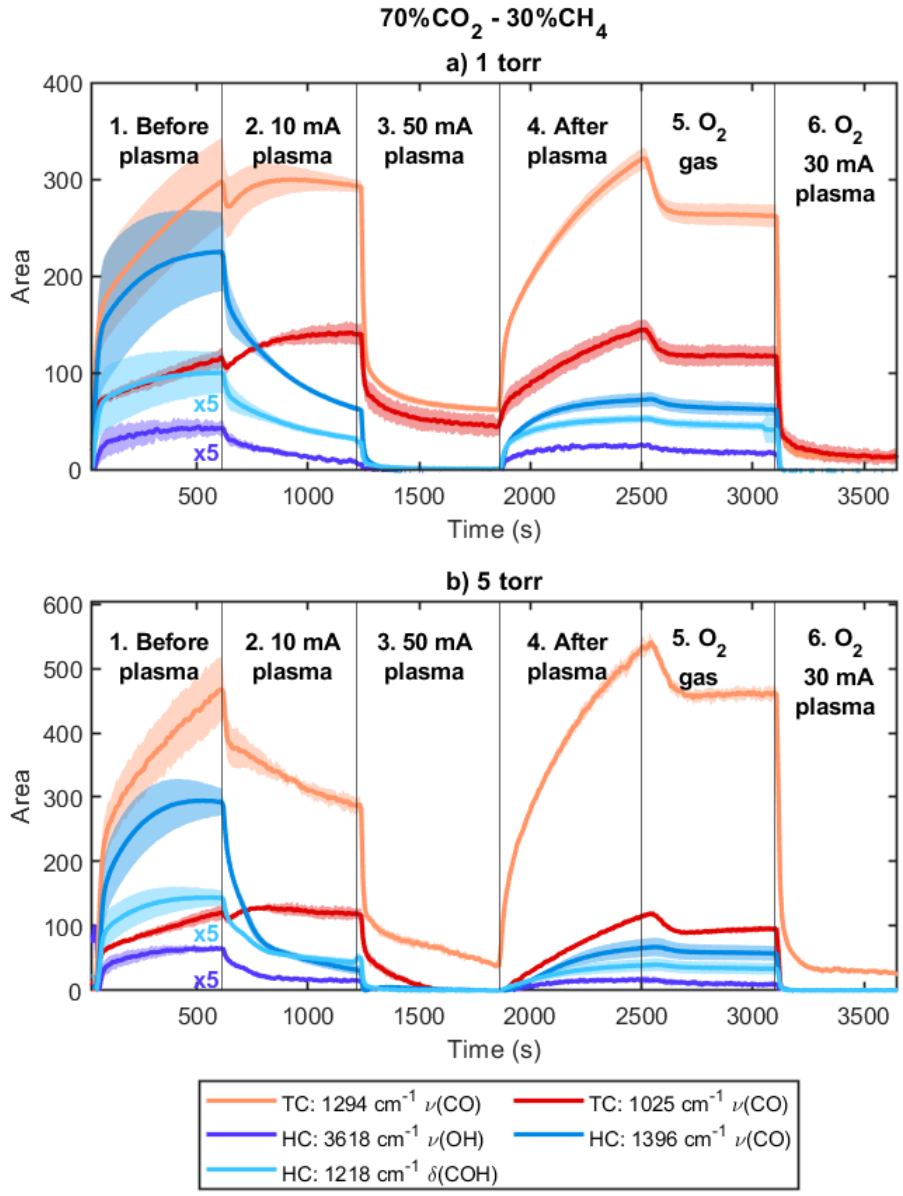

Figure 5.1: Area evolution of TC and HC bands during *in situ* 70%CO_2-30%CH_4 plasma experiment as a function of time at a) 1 torr and b) 5 Torr . Solid line represents the average of three consecutive experiments (including cleaning with O_2 plasma in between) in the same pellet and shaded area represents the standard deviation. TC: Tridentate Carbonates; HC: Hydrogen Carbonates.

In general, 1294 and 1025 cm^{-1} (ν(CO)) bands grow during (1) before plasma step indicating the formation of TC by adsorption of CO_2 as already observed in chapter 4. During steps 2 and 5, they decrease in intensity as during CO_2 only plasma experiments (figure 4.1 in chapter 4). The same occurs

under O_2 plasma (6). When plasma is off (4) and only CO_2 and CH_4 are flowing through the system, TC bands grow again indicating the re-adsorption of CO_2.

It has been shown in the pure CO_2 case, that TC disappear under plasma exposure because of the combined effect of gas temperature and oxygenated species. In CO_2-CH_4 plasma at 50 mA, for both 1 and 5 Torr, TC disappear nearly as much than in pure CO_2. However at 10 mA, TC bands are decreasing significantly less than in pure CO_2 case. At 1 Torr 10 mA it even increases slightly. The gas temperature is lower in CO_2-CH_4 (452 K instead of 550 K at 50 mA) but this can not be the explanation for a lower TC desorption at 1 Torr since the gas heating is anyway very small at 1 Torr and 10 mA even in the pure CO_2 case. Another difference in CO_2-CH_4 plasma is that O atoms are strongly consumed by oxidation reactions with CH_4 and its dissociation products. The lack of oxygenated species in the CO_2/CH_4 case is therefore likely to explain the less efficient removal of TC from the surface at 10 mA. However it should be noted that the band at 1025 cm^{-1} could be convoluted with a contribution from another species (probably formates) [117]. This could explain the inconsistency between the band at 1294 cm^{-1} which is relatively stable at 10 mA and 1 Torr while the band at 1025 cm^{-1} seem to increase.

5.2.2 Hydrogen carbonates

Figure 5.1 also shows the area evolution of HC bands (1218, 1396 and 3618 cm^{-1}) at 1 and 5 Torr for *in situ* CO_2-CH_4 plasma experiments. Like for TC, the adsorption of HC before plasma (step (1)) is evolving exactly the same as in the pure CO_2 case, showing that CH_4 in the gas mixture is not interfering with the adsorption of carbonates. During steps (2) and (3) HC are also decaying in CO_2-CH_4 plasma similarly to what was observed in CO_2 plasma. However the decay of HC is much more pronounced at 10 mA than it was in pure CO_2 plasma. Another difference is that when the plasma is off (step (4)), the HC bands do not regain the same intensity as at the end of step (1). HC bands loose about 2/3 of the area between steps (4) and (1) , contrary to TC that are reaching back the same intensity. We can therefore assume that HC formation on the surface is partially hindered under CO_2-CH_4 plasma exposure, possibly because the adsorption sites for HC are occupied by another specie.

As we have seen in section 4.3.2, hydrogen carbonates are formed by the reaction of CO_2 and undissociated water, but the results obtained at 5 Torr in CO_2 plasma seemed already to suggest a detrimental effect of a too large quantity of water molecules adsorbed on the surface. The amount of water produced by CO_2-CH_4 plasma is more than 1000 times larger than the water impurity level from the gas bottles present in the pure CO_2 measurements. It would therefore be reasonable to assume that a lot more water is adsorbed on CeO_2 in CO_2-CH_4 plasma leading to a limitation of HC formation. To confirm this hypothesis, Figure 5.2 is giving the area evolution of 3549 cm^{-1} ν(OH)(III), 3686 cm^{-1} undissociated water, 3618 cm^{-1} ν(OH)(HC) and 3710 cm^{-1} ν(OH)(I) during *in situ* 70%CO_2-30%CH_4 plasma experiments at a) 1 Torr and b) 5 Torr.

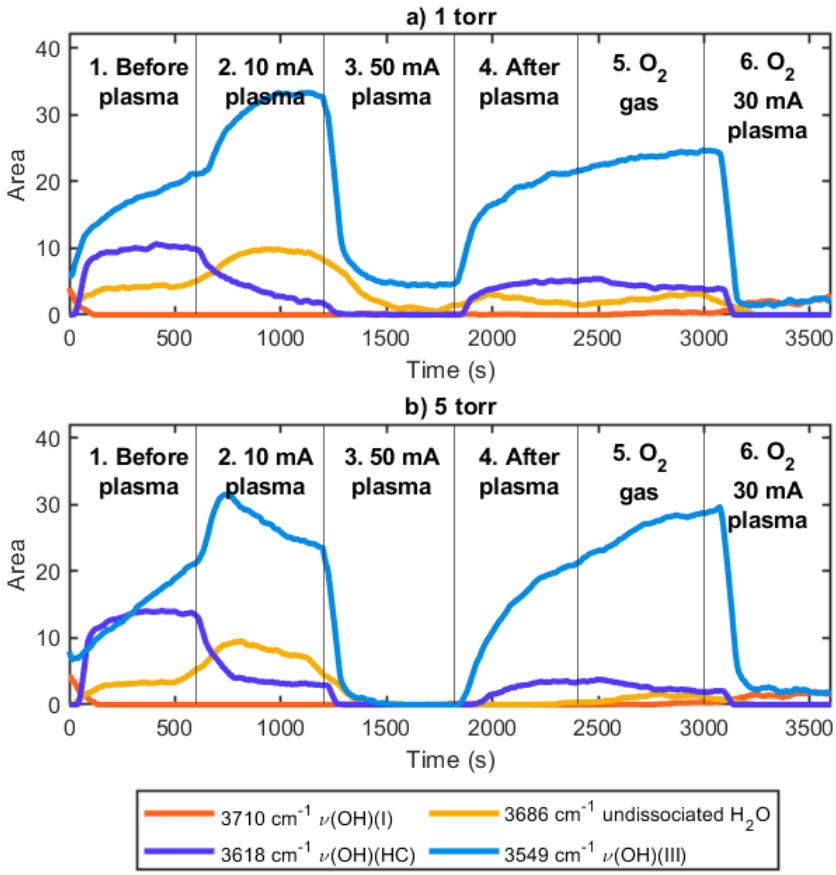

Figure 5.2: Area evolution of IR adsorption bands area of 3549 cm^{-1} ν(OH)(III), 3686 cm^{-1} undissociated water, 3618 cm^{-1} ν(OH)(HC) and 3710 cm^{-1} ν(OH)(I) during *in situ* 70%CO_2-30%CH_4 plasma experiments at a) 1 Torr and b) 5 Torr.

The general trend for these 4 bands are very similar for both pressures throughout all the steps. Parallel to the decay of HC, an increase of OH groups and undissociated water is observed. The area of OH(III) (3549 cm^{-1}) and undissociated water (3686 cm^{-1}) bands grow with 10 mA plasma (2). This demonstrate that water and/or OH radicals that are being formed by the plasma (H_2O can reach 7% as shown in table 5.1) can be adsorbed in the surface. The formation of hydroxyls and water directly on the surface due to the flux of H atoms or excited H_2 for instance could also happen. In any case, it appears that the gas temperature for 10 mA at 1 Torr (1) is not high enough (327 K) to desorb OH or to prevent its adsorption. On the contrary, when increasing the current to 50 mA during step (3), the OH(III) groups and undissociated water decrease. This corresponds either to simple desorption at higher temperature, or possibly to surface reaction generating formates.

The accumulation of OH(III) and undissociated water during step (2) seem to confirm the detrimental effect of a too large amount of water on HC appearance. However during step (3) at 50 mA, the temperature seems to be high enough to remove all these species from the surface. The smaller re-formation of HC during step (4) should therefore be explained by the presence of another specie, which could be the formates.

5.2.3 Formates

Formates are generally formed by the reaction of CO with OH groups at high temperatures (~800 K) [67]. Although, it has been reported to be formed also at room temperature on reduced ceria [133]. In the pure CO_2 case, despite the OH groups that have been observed because of water impurities from the gas bottle, no formates were detected on CeO_2 during plasma. However, when CH_4 is added to the initial gas mixture, CO_2-CH_4 plasma does generate formate species in the surface as seen on figure 3.17 with the new bands at 1358, 1370, 2722, 2845 and 2933 cm^{-1} formed during steps (2) and (3).

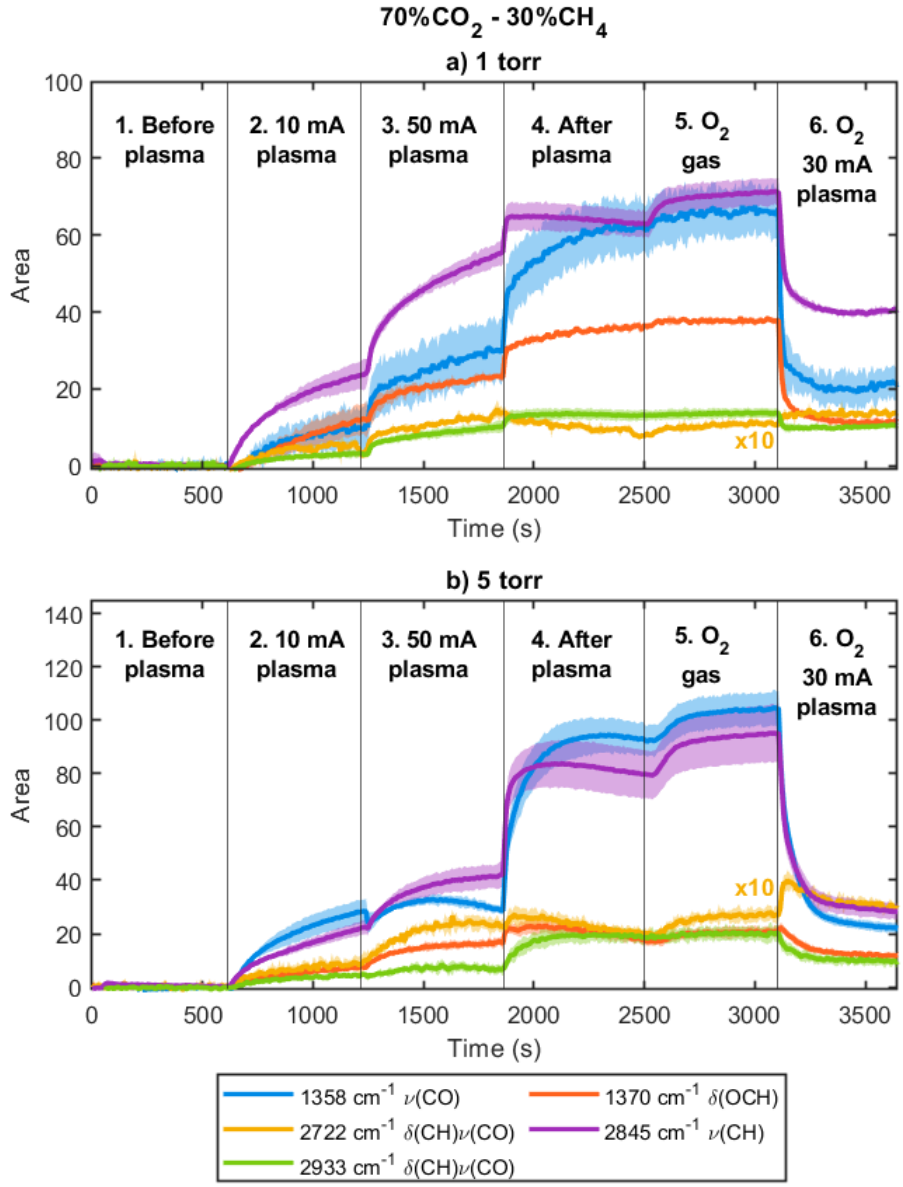

Figure 5.3: Area evolution of formate bands from 70%CO_2-30%CH_4 plasma *in situ* experiments as a function of time at a) 1 Torr and b) 5 Torr. Solid line represents the average of three consecutive experiments (including cleaning with O_2 plasma in between experimental sequences) in the same pellet. Shaded area represents the standard deviation. Band 2722 cm^{-1} was multiplied by 10 for better visibility.

The area of these five bands as a function of time through the experimental sequence is shown on figure 5.3 at 1 and 5 Torr. The solid line represents the average of three consecutive experiments (including cleaning with O_2 plasma in between experimental sequences) within the same pellet and the shaded area represents the standard deviation.

All five bands keeps growing in area during all step (2) and increase further through step (3). A fast increase is even observed at the beginning of step (4) when the plasma is off and only CO_2 and CH_4 gases are flowing through the reactor. A minor increase is observed also during step (5). The bands are reduced in intensity only during O_2 plasma step (6), but do not disappear and tend to stabilize at a constant level (figure 3.17).

All these bands are ascribed to formate species based on the literature, however, it is evident that some follow a slightly different behaviour as seen in figure 5.3. The different behavior through time indicates that possibly different types of formates (near an oxygen vacancy or at a regular site for instance) are being formed under plasma exposure and right after. It is however difficult to assign properly each band to a specific formate group, even by using the area correlation plot shown in figure 3.19. For example, for (2) step at 1 Torr (figure 3.19a_1), 3 bands among 5 are well correlated while band number 5 corresponding to 2933 cm^{-1} (ν(CO)δ(CH)) is not correlated to any of the others. However, at 5 Torr (2) (figure 3.19a_2), all 5 bands seem related to each other. In consequence, it is difficult to assign them to a specific formate group type. This could be due to the convolution of several formates types within certain bands observed, or to a baseline subtraction too rough to have enough accuracy in the area of all five bands.

In any case, contrary to TC and HC, formates do not appear before plasma exposure (step (1)) while they are quickly produced with the same gas flow composition right after switching off the plasma (step (4)). They are therefore being formed on the surface with species only produced by the plasma. The usual formation mechanisms found in literature involving CO and OH groups at high temperature should not happen at 10 mA since the temperature remains low, nor during step (4). The quick rise of formates bands at the beginning of after plasma step could correspond to the characteristic time for cooling the surface of the pellet, or to the life time of the specie responsible for formates production. One possibility given in the literature is the adsorption of formaldehyde (CH_2O) which can produce formates on metal oxides [120]. CH_2O can reach a maximum of 1% of the total gas density in our plasma but it dissociates into CO and H_2 via reactions making HCO as intermediary product (results from gas phase kinetic model). The density of CH_2O is therefore very small in post-discharge. In order to identify if the specie leading to formates is a short or a long live specie, the comparison is made between *in situ* and downstream measurement in the next section.

5.3 Comparison *in situ* vs downstream gas plasma

To investigate further the effect of plasma, the downstream gas experiments were performed to observe the effect of gas composition only. Figure 5.4 shows the spectra during downstream gas experiments at 1 Torr.

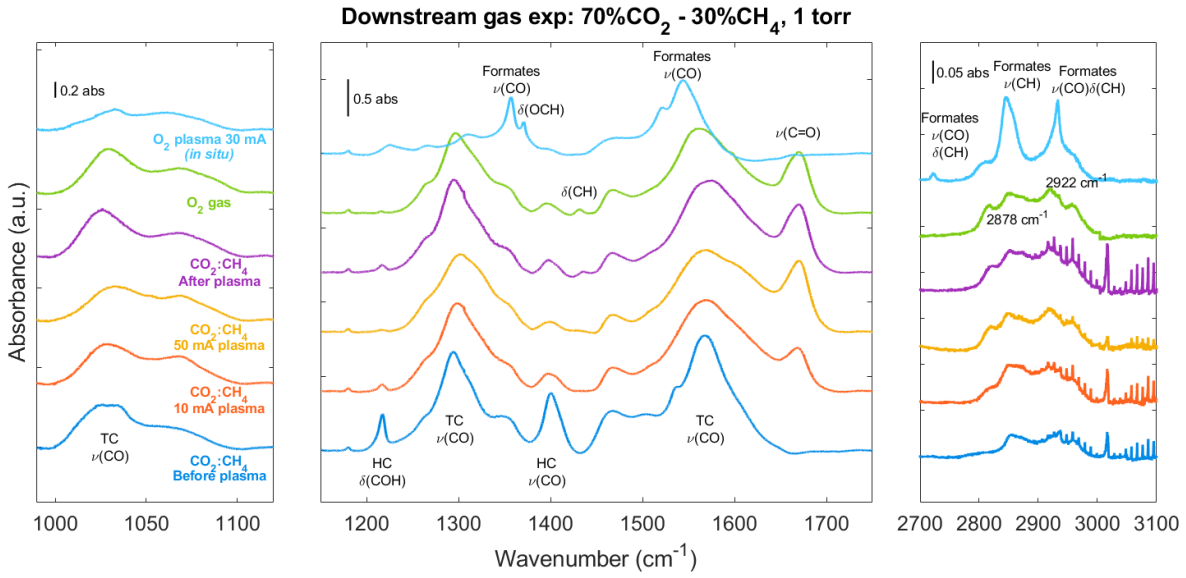

Figure 5.4: Downstream gas FTIR transmission spectra of 70%CO_2-30%CH_4 plasma at 1 Torr in the glow discharge plasma reactor through the experimental sequence. Only O_2 plasma was performed *in situ*. Spectra are offset for clarity.

The bands of TC and HC previously observed during *in situ* experiments are also detected in downstream. However formates bands seem to become prominent only during the O_2 plasma which is the only step for which the plasma is in direct contact with CeO_2 in the downstream experiment procedure. The bands attributed to TC (1025, 1294 and 1569 cm^{-1}) seem to remain intense through all the steps until O_2 plasma (*in situ*) (6)). The band at 1665 cm^{-1} for which the assignment remain uncertain appears when CO_2-CH_4 plasma is ignited and then remain until the cleaning with O_2 plasma.

The differences between *in situ* and downstream gas experiments are better seen when plotting the time evolution of the bands (see figure 5.5). The area of the bands was normalized with the largest area throughout the whole experiment sequence to facilitate the comparison.

The step (1) before plasma confirms the reproducibility of adsorption of TC and HC since this step is exactly the same during *in situ* and downstream experiment. For 10 mA plasma (step (2)), both TC and HC behaves similarly during *in situ* and downstream experiment. Carbonates are therefore removed from the surface because of lower partial pressure of CO_2 and/or competitive adsorption or reaction with stable byproducts from CO_2-CH_4 plasma such as water for instance. It confirms that the gas heating, which is anyway minimal at 10 mA, was not responsible for TC disappearance during step (2) in the *in situ* experiment. At the same time (during step (2)) formates corresponding to bands at 1370 cm^{-1} and 2845 cm^{-1} are observed only for *in situ* experiment. The gas temperature remains close to room temperature at 10 mA, but formates nevertheless needs direct plasma exposure to be formed on the surface of CeO_2. In the CO_2-CH_4 kinetic model, the fraction of CH_2O at 1 Torr for mixture of 70%CO_2-30%CH_4 has been shown to reach about 0.5% [87]. It has also been shown that eventually CH_2O will lead to the formation of CO and H_2 which would explain its absence in the post-discharge. The production of formates based on adsorption of CH_2O on CeO_2 reported in [120] could therefore explain the difference observed here between the downstream and the *in situ* experiment. During step (3), TC and HC decrease further in downstream experiment, but less than for *in situ*. The gas temperature in CO_2-CH_4 plasma reaches 650 K (see table 5.1). The decay observed in downstream could be due again to the decrease of CO_2 partial pressure as observed for 10 mA (the fraction of CO_2 is 0.46 in step (2)) and 0.23 in step (3)), but the higher gas temperature is probably enhancing the carbonates desorption

for the *in situ* case. After plasma (step (4)), a quick re-adsoprtion occur over few tens of seconds which could corresponds to the cooling of the pellet surface, followed by slower re-adsorption of TC and HC. Both TC and HC bands reach similar intensity at the end of step 4 for downstream and *in situ*. However, while TC recover the same intensity as during step (1), HC saturates at a much lower level (roughly 30% of the maximum intensity of step (1)). As already discussed in section 4.3.2, if too much water is accumulating on the surface, this can hinder the formation of HC. At 1 Torr and 50 mA in the CO_2-CH_4 plasma the fraction of H_2O produced is about 6%, which could accumulate more on the surface in the downstream experiment, explaining the lower HC formation after plasma. The O_2 gas flow, and O_2 plasma (performed *in situ* on the CeO_2 pellet in order to clean it), are inducing similar decay of TC and HC as observed in the pure CO_2 case. It is however interesting to note that formates bands that were increasing only for *in situ* experiment during steps (2) to (5) are partially decreasing under pure O_2 plasma exposure. On the contrary, for downstream experiment, formates are not detected during steps (2) to (5), but when O_2 plasma is ignited, formates species appear suddenly in the surface displaying the bands already reported in the literature (1358, 1370, 2722, 2845 and 2933 cm^{-1}) [117, 120, 129].

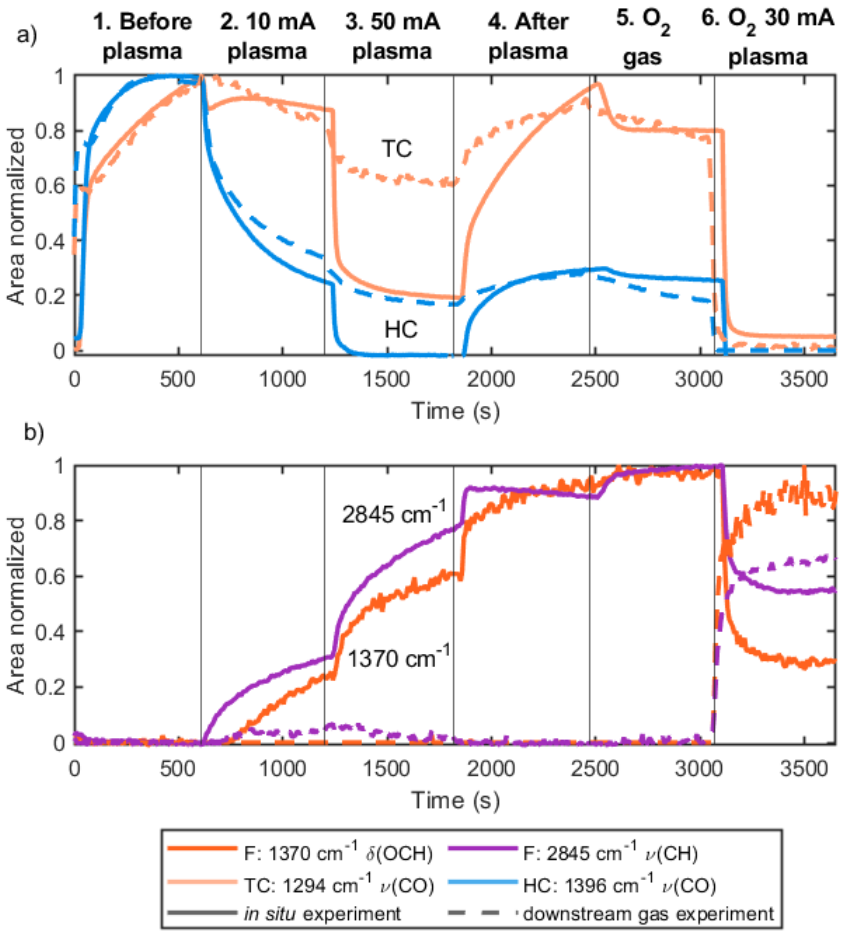

Figure 5.5: Comparison of area normalized evolution of 1294 cm^{-1} from TC, 1396 cm^{-1} from HC (a) and 1370 and 2845 cm^{-1} from formates (b) species bands during *in situ* (solid line) and downstream gas (dashed line) experiments for 70%CO_2-30%CH_4 as a function of time at 1 torr. The area of the bands was normalized with the largest area for the given band throughout the whole experiment to facilitate the comparison among different experiment O_2 plasma was the only plasma step performed in the pellet during the downstream gas experiments.

The adsorption of CH_2O could explain that CeO_2 has to be under direct exposure of the CO_2-CH_4 plasma to observe formates. Indeed CH_2O can reach about 0.5% of the gas phase in the plasma but it is dissociating into CO and H_2 downstream the plasma so that its concentration falls under the FTIR detection limit with our optical path length. Traces of CH_2O have been detected only with the mass spectrometer. In any case, even if CH_2O is involved in formates production, it can not account for the production of formates when CeO_2 is exposed to an O_2 plasma after having adsorbed the molecules coming out of a CO_2-CH_4 plasma. This is direct evidence of a purely surface-based formate production process, induced by oxygen excited species in the O_2 plasma, and/or due to plasma-induced heating of previously adsorbed molecules.

The role of water could be important on the evolution of TC, HC and Formates even downstream. To investigate further the possible formation mechanisms of these species, it is therefore interesting to look at OH and water bands in downstream experiments. Figure 5.6 displays the IR spectra in the region from 2800 - 3000 cm^{-1} for *in situ* (a) and downstream gas (b) experiment.

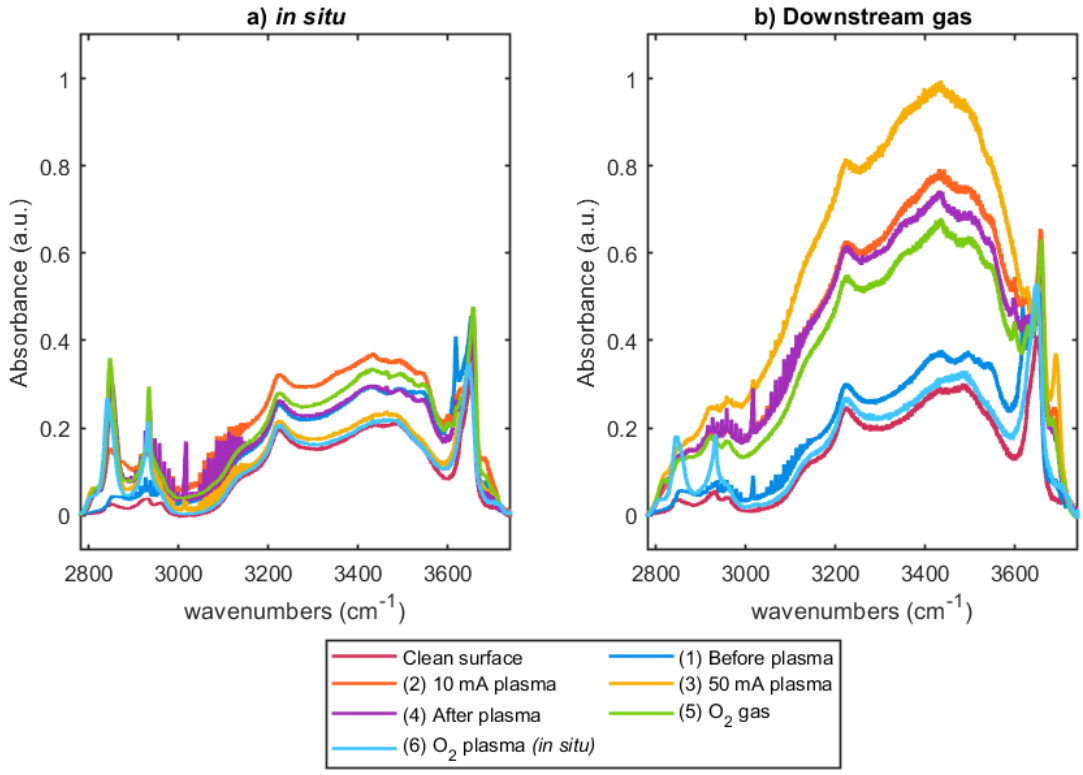

Figure 5.6: FTIR transmission spectra of 70%CO_2-30%CH_4 plasma at 1 torr in the region 2800 - 3700 cm^{-1} typical of OH groups for *in situ* experiments (a) and downstream gas experiments (b). Each spectrum is the final spectrum taken after each step from the experimental sequence.

Looking at the figure 5.6b, we can see a broad band attributed to hydrogen bonded hydroxyls [134]. The increase of the broad band in this region is assumed to result from the few percent of water contained in the gas exiting the plasma at 50mA (step (3)) which accumulates onto the surface. In addition, the undissociated water band (3686 cm^{-1}), which is supposed to be responsible on the HC formation during CO_2 plasma only, reaches a maximum during step (3). However, the band 3549 cm^{-1} (OH(III)) in (4) on *in situ* experiments (figure 5.2) is the highest among all and the area normalized of 1396 cm^{-1} during the same step in downstream gas experiments reach almost the same proportion in area as on *in situ* experiments. We can assume that OH(III) species prevent the formation of HC species.

Such phenomenon has already been reported in the literature. Agarwal et al. reported that hydrogen carbonates are preferably formed on octahedra nanoceria than in cubes or wires. They attribute this to the relatively high reactivity of OH groups on (111) planes. However, they notice how HC dissapeared upon exposure to water [134]. The mechanism is not explained but we can assume some steric effect that could block the reaction of HC formation, or that OH groups are in competition for the adsorption on active sites [133, 135]. The dissociative adsorption of H_2O into an oxygen vacancy has been calculated to be a strongly exothermic process (-2.04 eV) [78]. In contrast, HC formation has been calculated to be slightly exothermic (-0.63 eV) [117]. This enable us to suggest that traces of water promote the formation of HC and on excess surface hydroxyls hinder CO_2 from being adsorbed as HC. Additionally, HC could have a limited role on the formation of formate species under CO_2-CH_4 plasma.

The amount of water accumulating onto the surface is a key parameter to understand the type of specie appearing on CeO_2. As already mentioned, the broad band seen on figure 5.6 and attributed to hydrogen bonded hydroxyls is a good indication of the water surface coverage [134]. Figure 5.7 shows the time evolution of the area of this broadband for *in situ* and downstream experiments in pure CO_2 and CO_2-CH_4 plasma at 1 Torr. The curves have been normalized to 1 at the end of step (1) in order to better compare different CeO_2 pellets adsorbing slightly different amount of water.

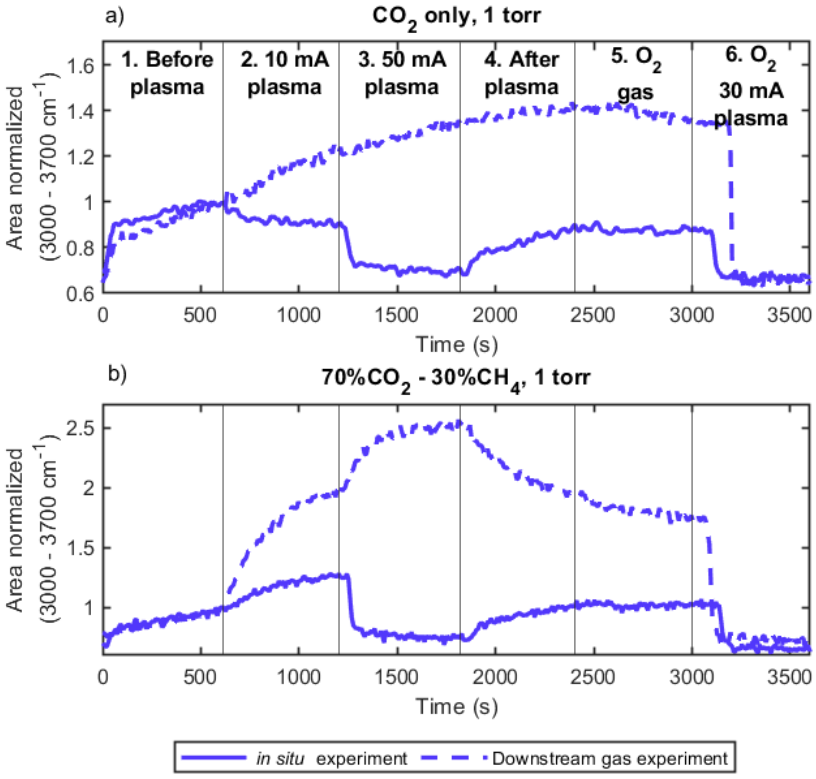

Figure 5.7: Time evolution of normalized area of the broad band in the region 3000 - 3700 cm^{-1} in a) CO_2 only at 1 Torr and b) 70% CO_2-30% CH_4 1 Torr initial gas mixtures for *in situ* (solid line) and downstream gas experiments (dashed line).

The dashed curve for the pure CO_2 case shows that across steps (1) to (5), the low level of water impurities contained in the different gas bottles (around ~50 ppm) is slowly accumulating water on CeO_2 over 3000 s. When the O_2 plasma is used for cleaning the surface (step (6)), the water desorb very quickly

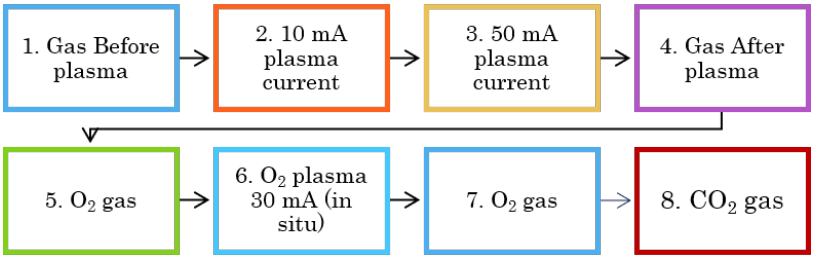

Figure 5.8: Experimental sequence of steps followed during downstream gas FTIR transmission experiments.

even though the gas temperature is only of 370 K (see table 4.1). For the *in situ* case in pure CO_2, the desorption of water is observed already during steps (2) and (3) for which the gas temperature reaches 374 and 550 K respectively. The small decay of water for CO_2 plasma at 10 mA despite the similar gas temperature as the pure O_2 plasma at 30 mA illustrates that oxygenated species are largely enhancing the water desorption. During step (4) and (5), water impurities from the gas bottles are re-adsorbing slowly like in the downstream experiment. The behaviour is very different for the CO_2-CH_4 plasma case. During steps (2) and (3) a much faster adsorption of water is observed in downstream experiment which correspond to the accumulation on the surface of water produced by the plasma (around 6% of the gas in these conditions, see table 5.1). After switching off the plasma, the partial pressure of water in the downstream gas goes back to the impurity level, and water starts to desorb slowly from the surface during steps (4) and (5). For the *in situ* experiment, the adsorbed water increases during the CO_2-CH_4 plasma at 10 mA contrary to the pure CO_2 case. At 50 mA, the direct plasma exposure and the gas temperature around 452 K is sufficient to remove the adsorbed water despite the large amount produced in the gas phase. Similarly to the broadband associated to hydrogen bonded hydroxyls, the bands at 3549 cm^{-1} (OH(III)) and at 3686 cm^{-1} (undissociated water) also increases under 10 mA CO_2-CH_4 direct plasma exposure but disappear at 50 mA.

As discussed earlier, CH_2O could be partly responsible for formates appearance but at the end of step (5) in downstream experiment, only TC and water remain in large quantity on CeO_2 surface. Even HC are present in much lower quantity than at the end of step (1). The appearance of formates bands at 1370 and 2845 cm^{-1} growing under O_2 plasma exposure (figure 5.5b) is therefore likely to results from a reaction involving TC in presence of water. TC and OH groups could react to generate formates in the surface with atomic oxygen, the O_2 excited species or simply gas heating providing the energy to adsorbates and promoting formates production. It is not clear if the CH bond from formates is formed by proton transfer from the surface OH to the C atom (Langmuir-Hishelwood mechanism) or the H atom is briefly on the gas phase reacting with the carbonate (Eley–Rideal mechanism) but based on the literature, it seems to be the first case [135]. Nonetheless, it is clear that plasma is the driving force that assist on the reaction of TC and OH groups in the formation of formate species.

At the end of (6) only formates species are expected to be present in the surface. Water and carbonates have already reacted under O_2 plasma, therefore, HC should be able to form again. To test this, two additional extra steps where performed to the downstream gas experiment: O_2 gas (step (7)) and CO_2 gas (step (8)). Figure 5.9 displays the time evolution of carbonate species through the experimental sequence shown in figure 5.8 with 70%CO_2- 30%CH_4 plasma at 1 Torr. Step (1) and (4) to (8) are shown here.

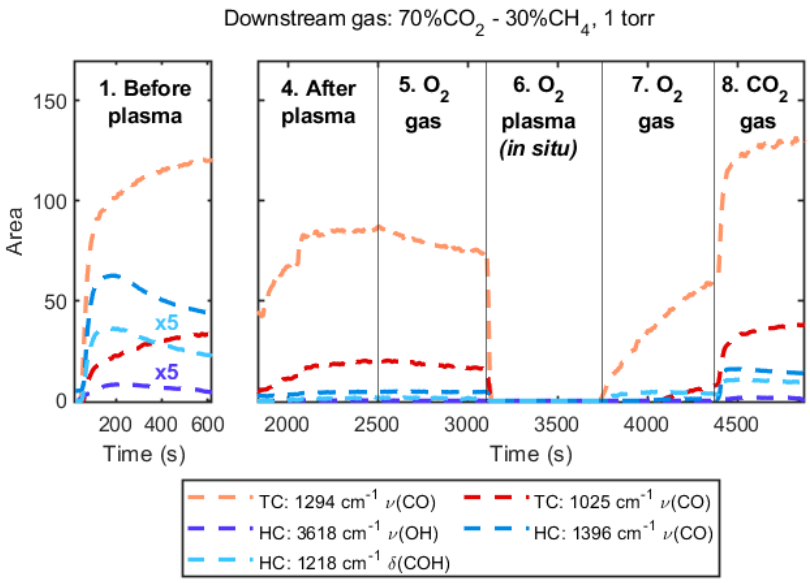

Figure 5.9: Time evolution of TC and HC in downstream gas FTIR transmission experiments with 70%CO_2-30%CH_4 plasma at 1 Torr in the glow discharge plasma reactor through the experimental sequence from figure 5.9. Step (1) and (4) through (8) are shown here. Only O_2 plasma was performed *in situ*.

Similarly as in figure 5.5, TC and HC formed quickly in (1) upon CO_2 adsorption and follow the same trend up to (6). In (7), 1294 cm^{-1} band grows indicating some TC species formed in the surface, perhaps from residuals CO_2 from the reactor or surface. However, when CO_2 gas is sent to the reactor, TC bands increase as much as in (1) while HC bands barely increase 1/3 of the area that it had at the end of (1). We have to recall that Formate species are formed in (6) and remain stable afterward. The residual water from the gas bottles should not affect much the formation of HC on the surface. Hence, the generation of HC could be hindered by the presence of formates. Both species have a bidentate structure with a difference in the hydrogen (C-OH for HC and C-H for formates) and could share the same adsorption sites. It is clear now that TC, HC and Formates have specific adsorption sites in CeO_2 surface.

5.4 Unknown species and other bands in CO_2-CH_4 plasma

As it was mentioned in the beginning of CO_2-CH_4 plasma section and shown in figure 3.17, some bands appear in the spectra which are not assigned yet to a specific species and they are worth discussing. Four bands are observed: 1430, 1665, 2170 and 2815 cm^{-1}.

Firstly, the growing band at 1665 cm^{-1} during 10 mA plasma could be attributed to ν(C=O) [136]. Subsequently, the band decrease in (3) with higher plasma current. Again, we compare with the downstream gas experiments in figure 5.4 and the band 1665 cm^{-1} seems to grow more and stay for the rest of the experiments. The existence of this band may suggest the formation of a monodentate species that could hold a carbonyl group C=O stabilized by hydrogen bonded species (most likely other bidentate formates and/or OH groups) [123]. Although, Lustermberg et al. did not report such band during methanol decomposition to formate species. If it does not belong to a carbonyl vibration, the second assumption could be that it is assigned to surface bonded water. If it grows similarly as the broad band in the

3000 - 3700 cm^{-1} region, it could be related to water bending mode [137]. The band 1665 cm^{-1} reaches a maximum absorbance during 50 mA plasma gas and stabilized until step (6) in 70%CO_2-30%CH_4. While in the case of the OH broad band (figure 5.7b) reaches a maximum absorbance also during 50 mA plasma gas but decays through (4) and (5). Unfortunately, 1665 cm^{-1} and OH broad band evolution do not follow the same trend.

The weak band at 1430 cm^{-1} could be ascribed to a δ(CH) vibration [136]. However, it is very weak to make a proper assignment or try to relate it to another band. The shoulder at 2815 cm^{-1} could be assigned to ν(CH) given the location in the spectra and it is still observed even during downstream gas experiments before and during O_2 plasma. These bands do not behave as other formates bands. This could be due to the adsorption of accumulated minor traces of formaldehyde as reported in the kinetic model [87]. Although, formaldehyde when adsorbs in CeO_2 form bands like formate species as reported in [120]. Moreover, when different initial concentration of CO_2 during downstream experiments are tested, we can observe that the CH region varies.

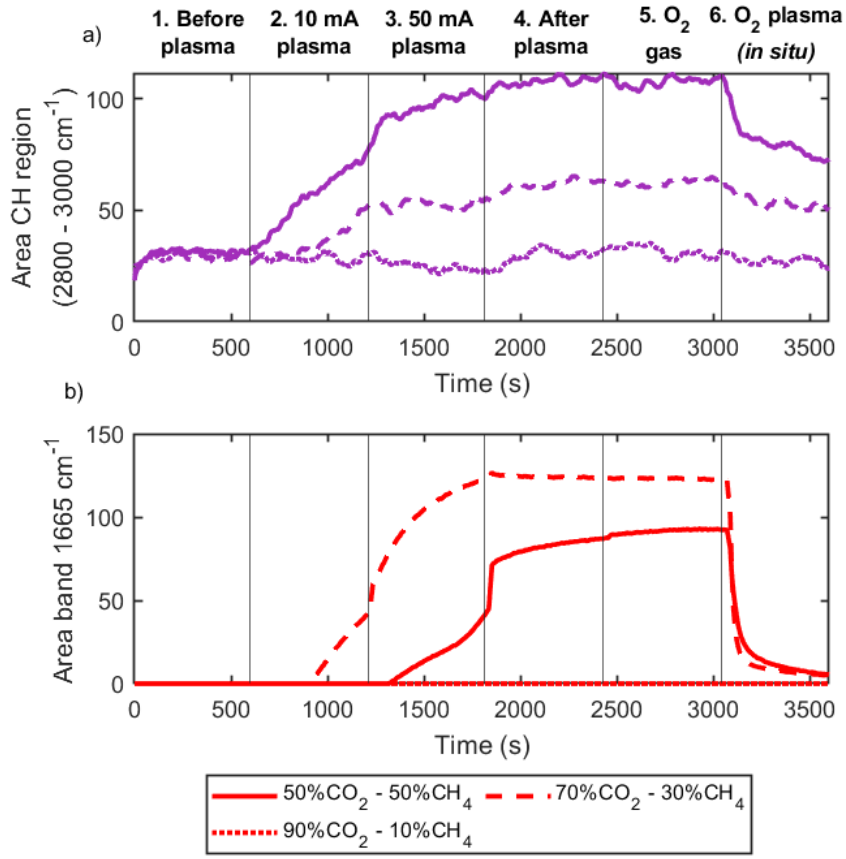

Figure 5.10: Area evolution of CH broad band area of from the region 2800 - 3000 cm^{-1} (top) and 1665 cm^{-1} band (bottom) during downstream gas experiments for different initial concentrations of CO_2-CH_4 at 1 Torr. Solid line: 50%, dashed line: 70% and dotted line: 90%.

In an attempt to correlate these bands, the time evolution of the band at 1665 cm^{-1} and the broad band of the region 2800 - 3000 cm^{-1} are compared in figure 5.10. If both bands belong to the same species (perhaps from formaldehyde or formic acid traces), by increasing the initial methane concentration more traces of CH_2O would be interacting with the surface, and we could expect that the area would be higher for both bands at 50%CO_2. As seen in figure 5.10, it is not the the case. The highest intensity for 1665 cm^{-1} band is seen for 70%CO_2 while for the broad band 2800 - 3000 cm^{-1} it is for 50%CO_2. Clearly, none of these features are related to each other or neither to formaldehyde or formic acid molecules.

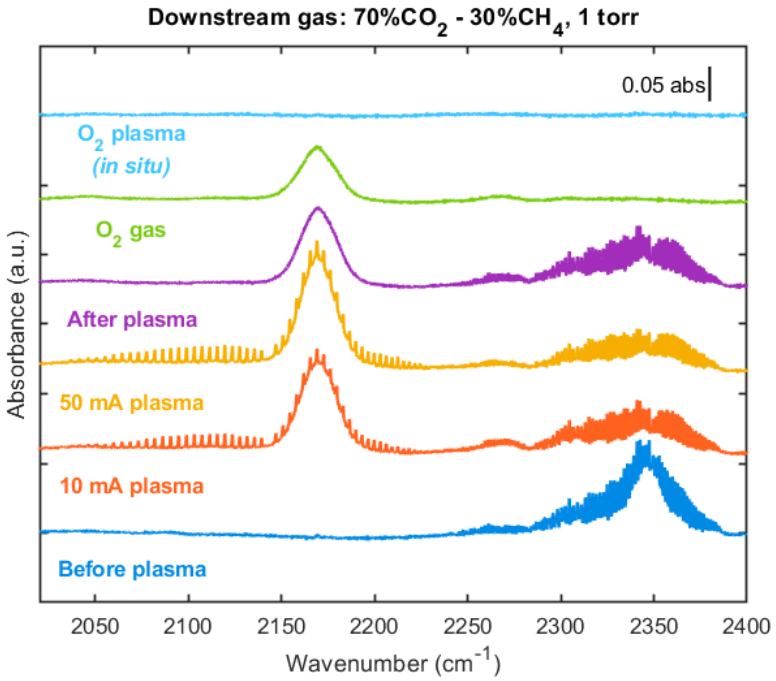

Figure 5.11: Region 2050 - 2400 cm^{-1} FTIR spectra showing CO and CO_2 gas phase bands from downstream gas of 70%CO_2- 30%CH_4 plasma experiments at 1 Torr. Spectra are offset for clarity.

In addition, in the region of CO gas phase, another adsorption band at 2170 cm^{-1} appeared (figure 5.11) attributed to a linearly adsorbed CO on unsaturated coordinated Ce^{4+} cations. Its shift from the gas phase value is a measure of the Lewis acid strength [138]. This band is visible on *in situ* experiments (not shown here) only during 10 mA plasma step on CO_2-CH_4 plasma and weakly during 50 mA plasma but still remained strong during the downstream gas from 50 mA plasma step and onward. It is worth mentioning that CO interaction during adsorption tests of figure 4.3 does not reveal this band, therefore, the presence is due to interaction with another molecule. The presence of water adsorbed in the surface seems to be in contradiction to this band at 2170 cm^{-1} attributed to CO on Ce^{4+} cations with unsaturated co-ordination [138]. Surface oxidation is expected from water adsorption preventing the CO adsorption on unsaturated Ce^{4+} cations. Such unsaturation of the surface Ce^{4+} cations could lead to some homolytic H_2 dissociation forming OH species but the dissociation of H_2 at room temperature is not stated in the literature yet possible on *in situ* plasma. The appearance of this band on downstream gas experiments suggest unequivocally the change in the saturation of the surface by mere interaction of the gas without the effect of the plasma which ultimately helps on the catalysis for surface intermediates (as formates).

When the initial concentrations of CO_2-CH_4 plasmas are varied during downstream gas experiments, we observe that in the first experiment (with the same pellet) the 2170 cm^{-1} is very strong but for the subsequent experiments it becomes weaker (figure 5.12). During the repetition of the same conditions after three experiments,the band remain weak. This effect could be due a coverage of those sites that do not allow again the CO to interact with the unsaturated Ce^{4+} cations. This suggest that the surface is altered during each experiment that even O_2 plasma cleaning procedure cannot fully renew it. Further studies are needed to elucidate the presence of this band.

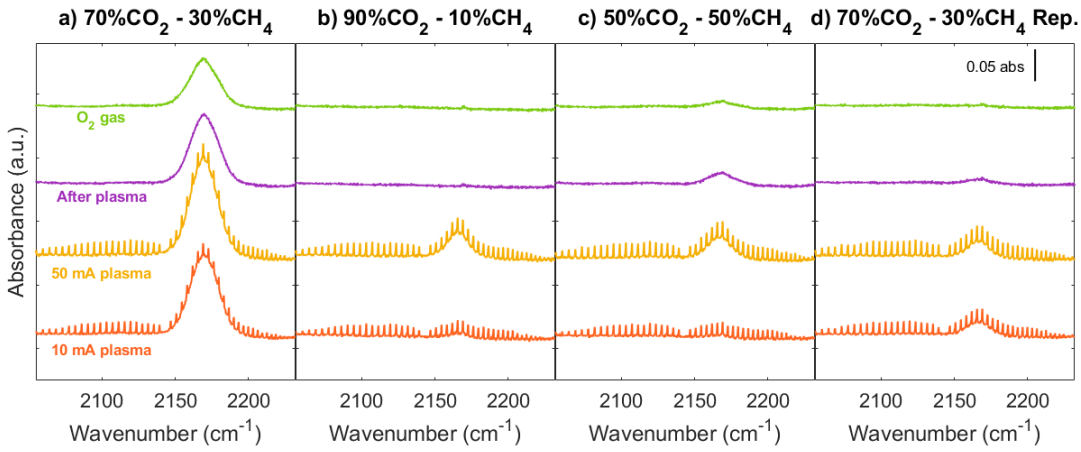

Figure 5.12: Region 2050 - 2250 cm^{-1} FTIR spectra showing CO phase bands from downstream gas experiments for different initial concentrations of a) 70%CO_2-30%CH_4, b) 90%CO_2-10%CH_4, c) 50%CO_2-50%CH_4 and 70%CO_2-30%CH_4 repetition at 1 torr. Only resulting spectra from step (2) through (5) is shown. Same ceria pellet was used for the 4 different experimental results shown here. Spectra are offset for clarity.

Nevertheless, these results indicate that a change is produced in the material that could be reversible or not on the long term. We have to keep in mind that the main products of CO_2-CH_4 plasma are CO and H_2 which are known to be reducing agents [114]. The presence of these species in the plasma/gas phase could not be neglected despite performing the fundamental studies in under several mbar of pressure. If a change in the CeO_2 pellet is in fact occurring, it should be observed by other means either in the bulk structure or solely on the surface. In order to elucidate the effect of the plasma, several characterization techniques were used to test the ceria before (pristine ceria) and after plasma exposure. The comparison between the pristine CeO_2 and the CeO_2 pellet after CO_2-CH_4 plasmas is crucial for the understanding on the effect of the plasma on the surface material as described in the following section.

5.5 Ceria characterization

Before any characterization, the CeO_2 pellets were visually inspected after a set of experiments and this were compared with a pristine CeO_2 pellet. Figure 5.13 shows two pellets before and after CO_2-CH_4 plasma exposure at 1 Torr.

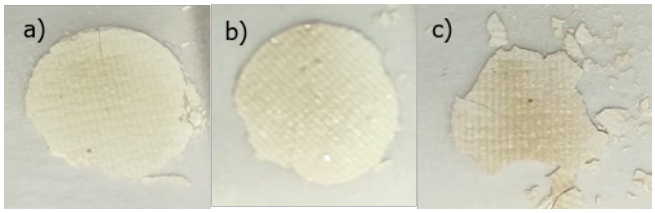

Figure 5.13: Pictures of two CeO_2 pellets a) before plasma exposure, b) after 70%CO_2-30%CH_4 plasma exposure (step 1 to 6 from experimental sequence in figure 3.12) c) after 50%CO_2-50%CH_4 plasma exposure (step 1 to 4).

However, plasma exposure did not always induce a change in color. It could give a hint whether color modification is due to a change in the oxidation state or carbon deposition. The presence of CH_4 in the

gas/plasma mixture can be sufficient to produce coke on the surface as it was explained in [87]. On the other hand, H_2 formed can be enough to reduce the surface of CeO_2. Hence, characterization techniques are needed to elucidate what can occur in the surface of the ceria. X-ray Photoelectron Spectroscopy (XPS) can provide information regarding the oxidation state of ions on the material surface. Figure 5.14 shows the deconvolution bands of XPS spectra of Ce 3d of a) ceria pellet used on 70%CO_2-30%CH_4 plasma that changed color and b) pristine ceria.

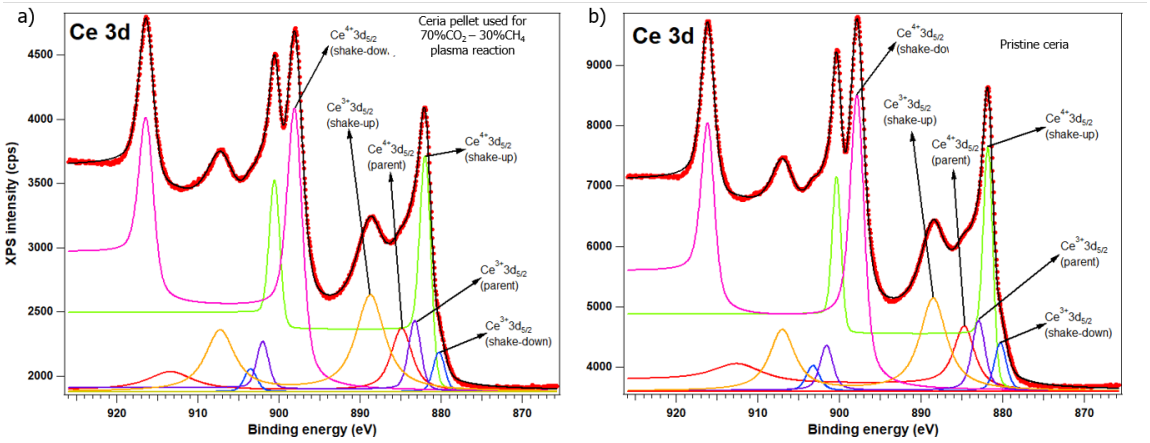

Figure 5.14: XPS spectra of Ce 3d of a) ceria pellet used on CO_2-CH_4 plasma that changed color and b) pristine ceria. Analysis performed by L. Abramiuc in Măgurele, Romania based on [13].

Sample	Ceria pellet	Pristine ceria
Ce^{3+}/Ce^{4+}	0.6419	0.6403

Table 5.2: Ratio of Ce^{3+}/Ce^{4+} ions of a) ceria pellet used on 50%CO_2-50%CH_4 plasma that changed color and b) pristine ceria from XPS analysis

The Ce^{3+}/Ce^{4+} ion ratio from table 5.2 show that there is no significant difference between the pristine ceria and the ceria pellet used under CO_2-CH_4 plasma. This could be due to the rapid reoxidation of the surface of CeO_2 when it is exposed to ambient air. Also, XPS is a surface analysis that relies on the first layers of atoms on the metal oxide structure. For bulk analysis, X-Ray diffraction was used to evaluate a change in the crystalline phase and compare pristine ceria (non-treated with plasma or any other process) and ceria exposed to plasma in our conditions (CO_2-CH_4 plasmas at 1 torr per the experimental sequence described in section 4.2). Figure 5.15 displays the normalized intensity vs 2θ angle from the X-ray diffraction pattern of pristine ceria, ceria under plasma exposure that remained yellow and ceria under plasma exposure that changed color. The peaks identified at 28.6, 33.1, 47.5, 56.4, 59.1, 69.4, 76.7 and 79.1° correspond to *hkl* reflections (111), (200), (220), (311), (222), (400), (331) and (420), respectively.

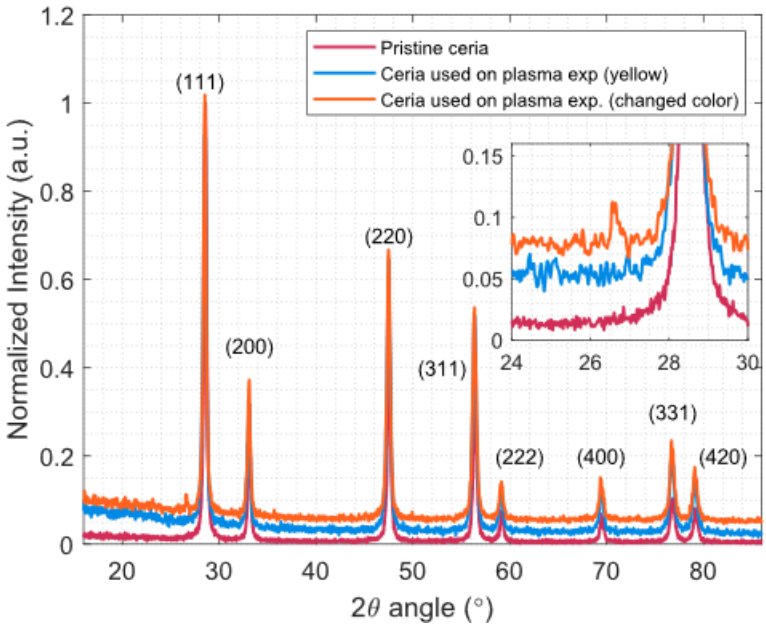

Figure 5.15: X-ray diffraction pattern of pristine ceria, ceria under plasma that remained yellow and ceria that changed color under plasma exposure. Patterns are offset for clarity.

A small peak is present at 26.5° which seems to be above noise level. No evidence of *hkl* reflections corresponding to Ce_2O_3 are observed and assuming that carbon could be the source of such peak, the pattern was compared with CeC_2 and graphite [139]. Figure 5.16 shows the normalized intensity as a function of 2θ angle from 15 to 40 ° of ceria used on plasma experiments that changed color and CeC_2 and graphite. It could possibly meet the assignment to a carbon structure formed in surface.

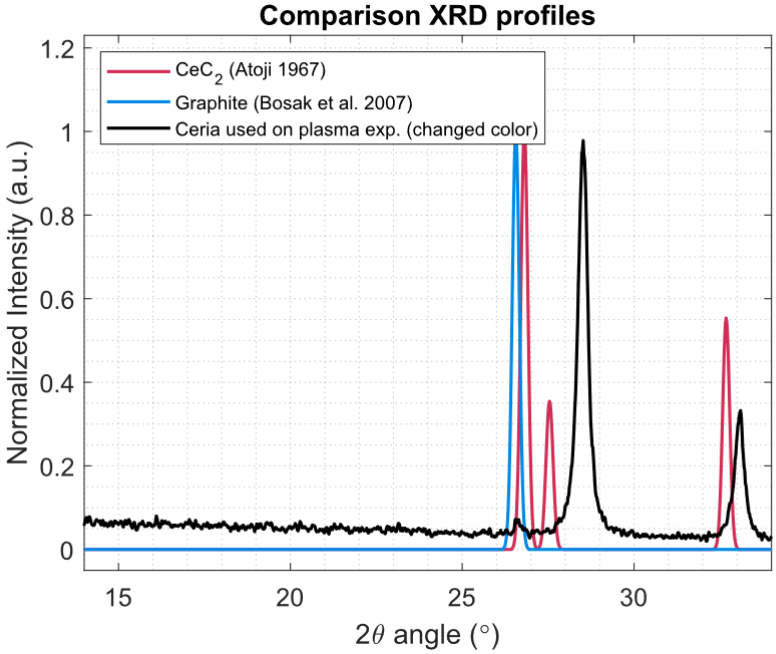

Figure 5.16: X-ray diffraction pattern of ceria that changed color under CO_2-CH_4 plasma exposure, CeC_2 and graphite [14, 15].

Carbon deposition is expected given the decomposition of CH_4 in plasma and reported in the literature [140–142]. However, Derivative Thermogravimetry (DTG) analysis could provide more information regarding coke formation on the surface of CeO_2 pellet [143].

To conclude, SEM-EDX analysis was performed on pristine ceria and ceria pellet exposed to CO_2-CH_4 plasma and the results are shown in figure 5.17.

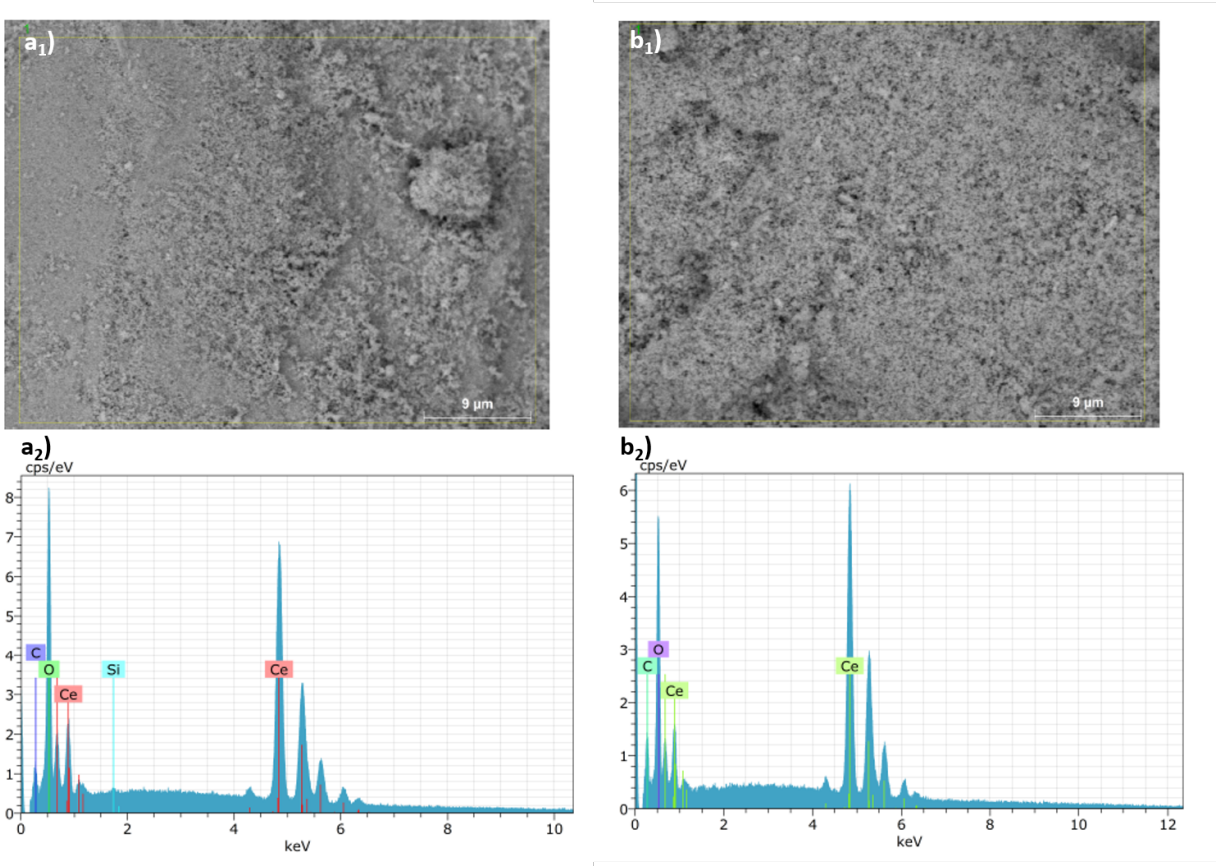

Figure 5.17: SEM image from a_1) pristine ceria and a_2) ceria exposed to CO_2-CH_4 plasma with their respective EDX spectra (b_1 and b_2). Analysis carried out by Instituto de Carboquimica, Zaragoza, Spain.

The commercial ceria used here is in the nanoscale size (<50 nm) and it was challenging to obtain a defined pictures of the particles. However, with EDX analysis it was able to give information on the composition of the material (figure 5.17a_2 and b_2). Ce and O atoms compose the material with 80 and 12 wt%, respectively. C atoms were found in both samples from around 3.5 wt%. In addition, a small speak was found in ceria exposed to plasma which seems to correspond to Si atom but the concentration is weight is 0.17%. This could be explained by some sputtering of Si atoms from the reactor walls after prolonged exposure to plasma conditions.

In summary, the experimental sequence followed throughout this chapter at low pressure seems to have a very little effect on the CeO_2 structure and resulting, if any, low carbon deposition.

5.6 Conclusions

Tridentate carbonates and hydrogen carbonates are adsorbed in the surface despite a dilution of CO_2 gas molecules with CH_4. During *in situ* experiments, when plasma is ignited, formates species are formed while TC and HC disappear. The comparison of *in situ* and downstream experiment suggest that the presence of formates results from TC reacting with OH groups, although the adsorption of intermediary CH_2O is not ruled out. Water adsorption or formation from side reaction during CO_2-CH_4 plasma seems to be detrimental in the HC formation after plasma (step 4) as it was suggested in chapter 4. The adsorption sites of formates and HC could be the same. The exposure of the CeO_2 pellets during these experiments does not result in a permanent change to the metal oxide structure and at most some carbon deposition could be observed.

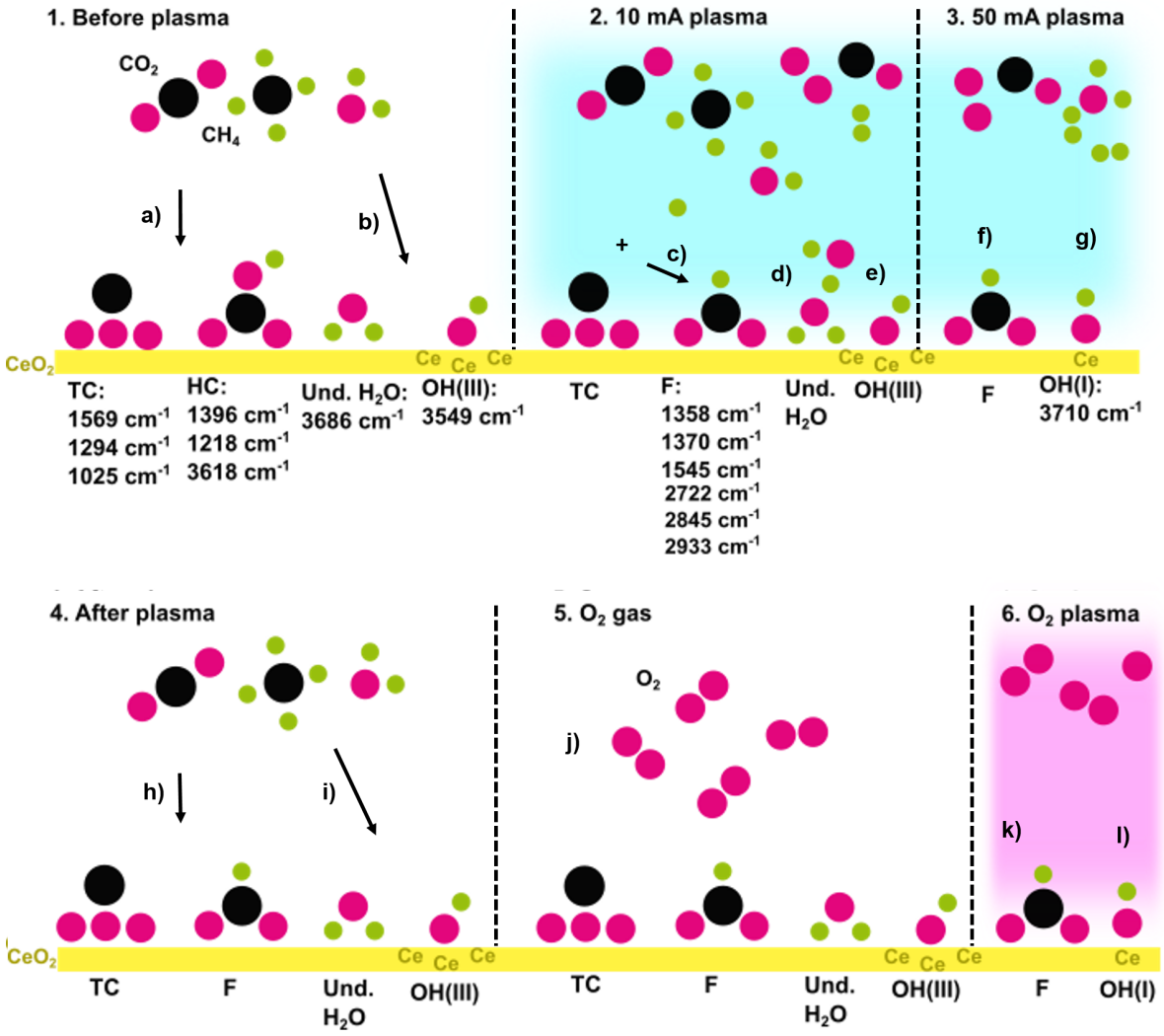

Figure 5.18: Scheme of the proposed mechanism occurring on CO_2-CH_4 plasma through steps (1) to (6) in CeO_2 surface. 1. Before plasma: a) adsorption of CO_2 forming TC and HC along with b) undissociated water from water traces in the gas bottles forming OH(III) groups simultaneously. 2. 10 mA plasma: c) TC species react with H atoms forming formates, d) water is formed in the gas/plasma phase and adsorbed in the surface e) forming also OH(III) groups. 3. 50 mA plasma: f) formates continue forming in the surface and g) OH(I) reappear in the surface. 4. After plasma: h) TC species are formed in the surface again, HC is barely present due to the presence of formates in conjunction to the i) water previously formed as side product resulting in undissociated water and OH(III) groups. 5. O_2 gas: j) O_2 gas removes the weakly adsorbed CO_2 molecules, formates and H_2O/OH species remain. 6. O_2 plasma: k) TC react with the remaining H atoms available in the surface forming formates simultaneously as some formates are being removed, l) OH(I) groups reappear again.

Chapter 6

Glow discharge with other gas mixtures interacting with CeO_2 surface

Contents

6.1 Introduction

The aim of this chapter is to complement the findings from chapter 4 and 5, by investigating the reactivity of surface intermediates in CeO_2 with other gases namely N_2, Ar and He. *in situ* FTIR transmission experiments are performed here as well but instead of using O_2 as oxidizing agent, N_2, Ar and He are tested here in steps (5), (6) and an additional step (7) consisting in just flushing with the new gas.

In addition, O_2-CH_4 plasmas are investigated to try to elucidate the tentatively assigned bands observed during CO_2-CH_4 plasmas experiments.

6.2 N_2 plasma interacting with Carbonates

N_2 plasma is tested because N_2 is present in air and in gas exhausts therefore, it is important to evaluate the effect of N_2 and atomic N on the carbonates formed on CeO_2. The procedure followed is the same as in chapter 4 except that O_2 is replaced by N_2 in steps 5 and 6. Figure 6.1 shows the final spectra of each step for CO_2 only experiments with N_2 gas and plasma. The spectra overall looks practically the same as in figure 3.14 in chapter 3 when CO_2 only and O_2 was used to remove the carbonates from the surface. The bands with maximum intensity at 1025, 1294 and 1569 cm^{-1} are associated to TC species. The bands located in the 1218, 1396 and 3618 cm^{-1} are assigned to HC species [117]. No new bands were observed with just N_2 gas flow step (5). Under N_2 plasma exposure no new bands were observed

either so that it can be assumed that no new species with N atoms were formed but some of the bands from previous steps are removed.

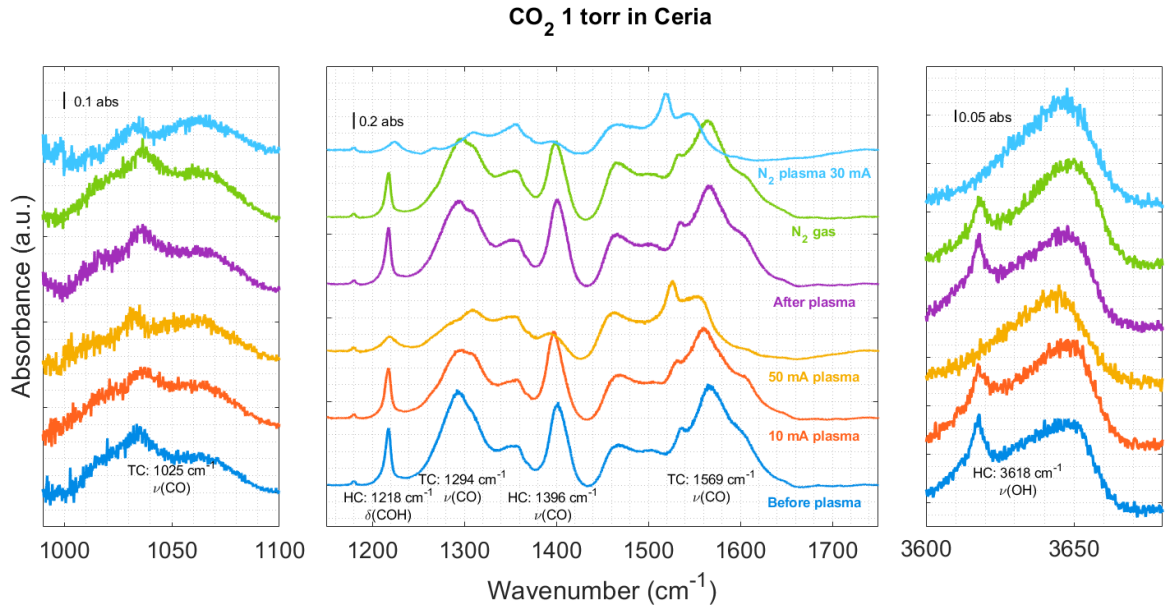

Figure 6.1: *In situ* FTIR transmission spectra of CO_2 adsorbed as carbonates species during CO_2 only experiments with N_2 gas/plasma in the final steps in ceria surface at 1 Torr. TC: Tridentate carbonates, HC: Hydrogen carbonates. The spectra displayed corresponds to the final spectrum taken at the end of each step from the experimental sequence. Spectra are offset for clarity.

Figure 6.2 shows the evolution of carbonates and OH species bands as a function of time. As expected the trends are the same during the 4 first steps as what was observed in figure 4.1 in chapter 4. TC, HC, OH(III) and undissociated water grow with CO_2 gas before plasma (1), the bands are reduced in area with 10 mA plasma (2) and almost disappear with 50 mA plasma current (3). Only OH(I) reappears in the absence of HC. The bands reappear in (4) indicating that TC and HC are formed again in the surface. During (5) the bands attributed to TC and HC decrease in area because N_2 gas removes the physisorbed CO_2 molecules while also changing the partial pressure of CO_2 interacting with the CeO_2 surface. In step (6), all the bands disappear quite fast (except the one attributed to OH(I)), indicating a strong desorption.

N_2 plasma is capable of removing carbonate species, OH(III) and undissociated water from the surface (6). Temperatures of pure N_2 plasma in a glow discharge can range 500-700 K at 5 Torr [144]. It has been measured in a glow discharge in a glass tube of 15mm diameter for various pressures and current in [145]. From this work and the modelling work from [146], it can be extrapolated that the gas temperature in our N_2 plasma at 1 Torr and 30 mA is about 450 K. T_{gas} is therefore higher in N_2 than in pure O_2 plasma (table 4.1) which could explain the fast desorption observed. The dominant excited electronic states in N_2 plasma include N(4S), N_2(A) and vibrationally excited N_2 which can carry a lot of energy and contribute to the desorption of species.

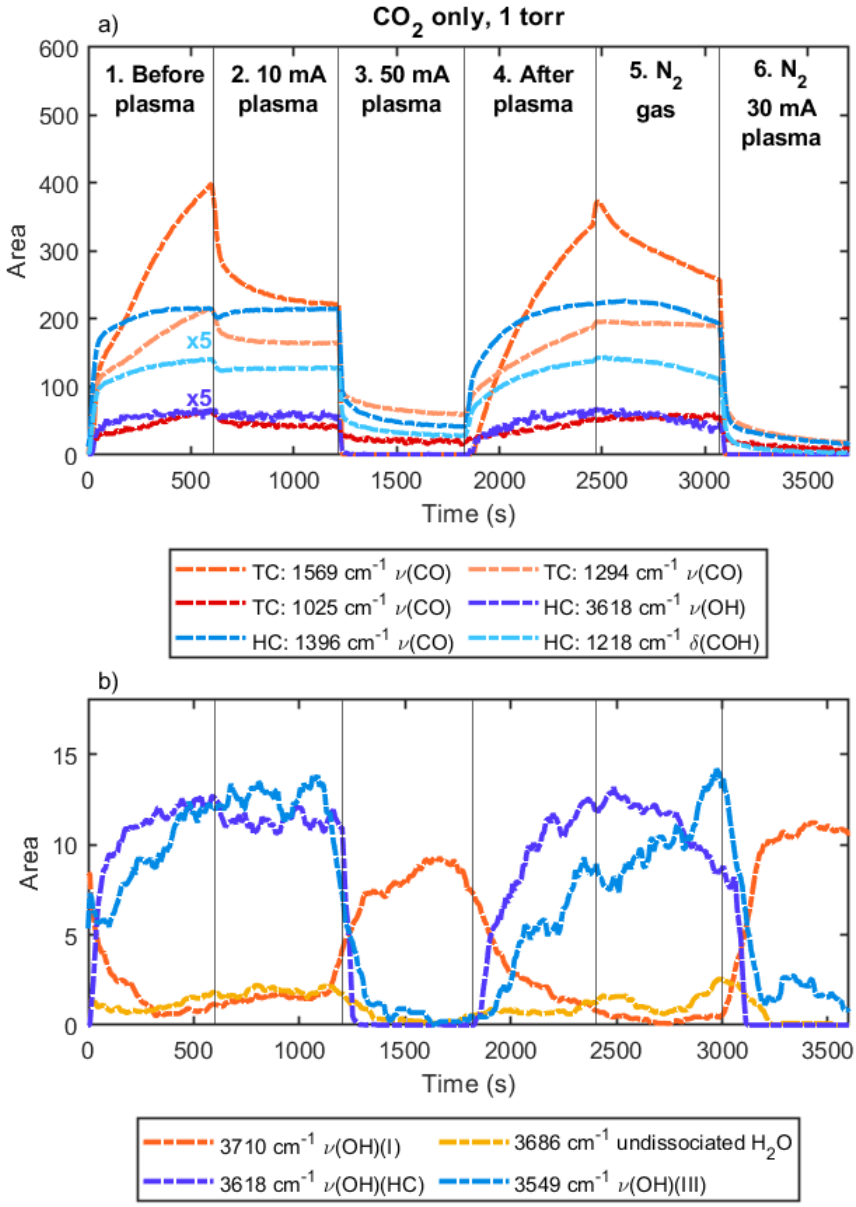

Figure 6.2: Time evolution of the area corresponding to a) TC and HC bands and b) OH group bands for CO_2 only at 1 Torr using N_2 for step 5 and 6.

6.3 Comparison with Ar, He or N_2-H_2 plasma after CO_2-CH_4

Argon and Helium are noble gases often used in non thermal plasmas including in glow discharge [147, 148]. The procedure followed is the same as in chapter 5 except the gas used after CO_2-CH_4 plasma steps. The sequence is slightly modified as seen in figure 6.3. In the case of Argon, the Ar plasma step will not be shown because the infrared emission of Ar plasma is too strong and the spectra were too noisy to be exploited. On figure 6.4 the spectra at the end of each step is shown for the Argon case after 70%CO_2-30%CH_4 plasma. The step (6) is not shown because of the noise but step (7) is shown last.

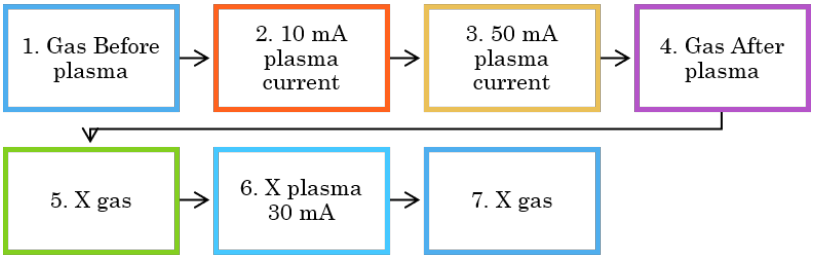

Figure 6.3: Experimental sequence of steps followed during *in situ* FTIR transmission experiments in the set up shown in figure 3.11 for testing different gases in steps 5, 6 and 7. X means Ar, He, in this section and O_2 or 5%H_2-N_2 in the following ones.

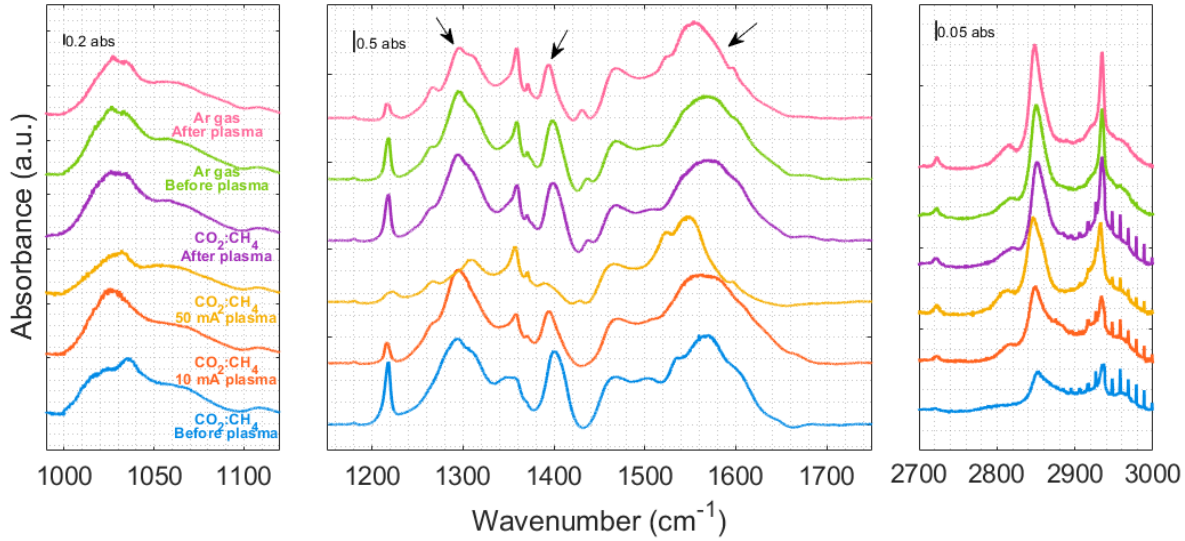

Figure 6.4: *In situ* FTIR transmission spectra during 70%CO_2-30%CH_4 plasma experiments with Ar gas/plasma in the final steps in ceria surface at 1 Torr. The spectra displayed corresponds to the final spectrum taken at the end of each step from the experimental sequence. Ar 30 mA plasma step (6) is not shown but step (7) is shown instead. Spectra are offset for clarity.

The IR spectra from (1) to (4) are similar to the results shown in chapter 3 and 5. Carbonates species are formed in (1), formates appear in (2) and grow in (3). In step (4), TC and HC species appear again in the spectra. The spectra looks very similar in subsequent steps (5 and 7). The arrows in the final spectrum (step (7) in pink) point to the bands assigned to 1294, 1569 (TC) and 1396 cm^{-1} (HC) which are still present after Ar plasma. This indicates that contrary to N_2 plasma, Ar plasma does not provide temperature high enough and/or excited species with enough energy to desorb carbonates form the surface. The gas temperature is unknown in our Argon glow discharge but according to literature, it is not necessarily lower than in pure N_2 [149]. In fact, when a small percentage of N_2 is added in an Argon glow discharge the gas temperature can even be lowered because of the lowering of the electric field [150]. The change in partial pressure (removal of CO_2 from the gas phase) is the same for both Ar and N_2 plasma and in the case of Ar it seems to not be enough to reduce significantly the area of the bands attributed to carbonates. Therefore the difference between Ar and N_2 plasma in carbonates removal during step (6) would be due to the excited states formed in the N_2 plasma that are more efficient for removing the carbonates, like the excited species in O_2 plasma.

To compare better this behaviour with other gases in the final steps, Ar, He, 5%H_2-N_2 are tested and

compared with O_2 (from chapter 5) at 1 Torr. The areas are normalized by the largest area obtained through steps (4) and (7) and plotted as a function of time. Figure 6.5 shows the bands 1294 cm^{-1} (TC) and 1218 cm^{-1} (HC) as a function of time from step (4) to (7).

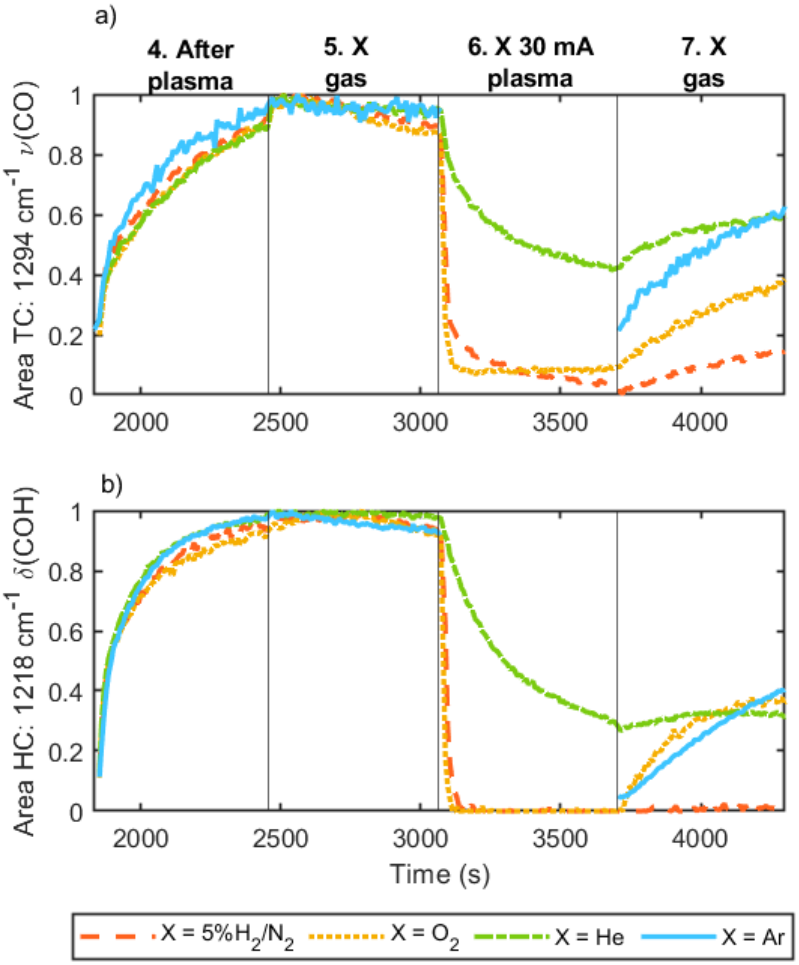

Figure 6.5: Normalized area of bands at a) TC: 1294 cm^{-1} and b) HC: 1218 cm^{-1}, as a function of time for 70%CO_2-30%CH_4 plasma at 1 Torr in CeO_2 surface for X = Ar, He, O_2 or 5%H_2-N_2.

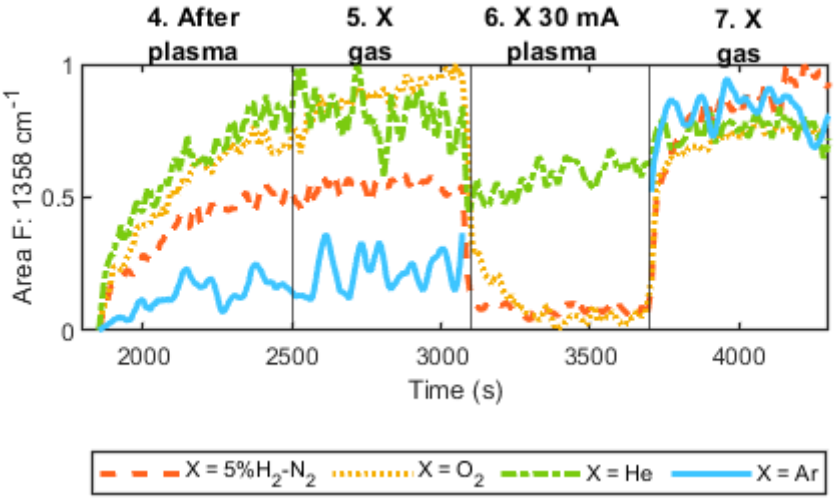

Figure 6.6: Normalized area of Formate bands at F: 1358 cm^{-1} as a function of time for 70%CO_2-30%CH_4 plasma at 1 Torr in CeO_2 surface for X = Ar, He, O_2 or 5%H_2-N_2.

The most efficient plasma to remove TC and HC from the CeO_2 surface is H_2-N_2 plasma. This mixture is even more efficient than pure O_2 plasma for the same current (30 mA) and pressure (1 Torr). After a 'cleaning' by a H_2-N_2 plasma, the HC do not reform contrary to what is observed after an O_2 or Ar plasma. The small size of the H_2 molecule is not *a priori* crucial in the cleaning efficiency since the helium plasma is the one that removes the least carbonates from the surface. The helium plasma is also the one for which the gas temperature is the lowest although at 1 Torr the gas temperatures are not very high anyway whatever the gas considered.

The cleaning of the carbonates does not occur by simply circulating the different gases above the surface of CeO_2 (step (5)). The intervention of excited species from the different plasmas is necessary to remove the carbonates. At 1 Torr in our conditions, the sheaths forming above the surfaces are *a priori* sufficiently collisional so that the average energy of the ions impacting the surface does not change much from one gas to another, which seems to exclude the effect of simple ion bombardment. Further studies would be necessary to really pinpoint the species responsible for the desorption and/or destruction of carbonates from the CeO_2 surface but all these measurements seem to show that it is not simply an effect of temperature nor of lower partial pressure of CO_2 above the surface. Excited electronic or vibrational states, or radicals formed in the plasma seem to be responsible for the removal of carbonates.

6.4 O_2-CH_4 plasmas

In order to elucidate the unknown species from the tentatively assigned bands in CO_2-CH_4 plasma experiments, O_2-CH_4 plasma is investigated during the interaction with CeO_2 surface. Using pure molecular oxygen for combustion of methane, CO_2 and water are the main products:

$$CH_4 + 2\,O_2 \longrightarrow CO_2 + 2\,H_2O \qquad \Delta H_{298K} = -\,890.7 \text{ kJ/mol}$$

However, incomplete oxidation of methane leads to CO formation. It should be noted that a detailed and extensive description on the plasma phase kinetics was not performed for this particular gas mixture in our research group as it has been done and reported in [87]. Nonetheless, some measurements were performed for 54%O_2-46%CH_4 plasma following the same procedure as described in chapter 3. The table 6.1 compiles these results along with fractions in CO_2-CH_4 for comparison.

Gas mixture	I (mA)	$[CO_2]/N$	$[CH_4]/N$	$[CO]/N$	$[H_2]/N$	$[H_2O]/N$	$[O_2]/N$
70%CO_2-30%CH_4	10	0.46	0.12	0.15	0.11	0.04	0.02
	50	0.23	0.03	0.34	0.3	0.07	0.02
54%O_2-46%CH_4	10	0.05	0.2	0.03	0.11	0.11	0.28
	50	0.19	0.12	0.04	0.22	0.15	0.15

Table 6.1: Values of main plasma parameters in CO_2-CH_4 plasma and O_2-CH_4 plasma at 1 Torr measured by FTIR and complemented by Mass spectrometry measurements for O_2 and H_2.

As reported on the table, the plasma products of both initial gas mixtures is the same. For example, at 50 mA plasma, the resulting CO_2 fraction is 0.25 and 0.19, for CO_2-CH_4 and O_2-CH_4, respectively. As for the other components, the fractions differ. For example, the fractions of water are higher in O_2-CH_4 plasma than in CO_2-CH_4.

For O_2-CH_4 plasma experiments, we performed the same procedure described in chapter 5 but starting with 70%O_2-30%CH_4 initial gas mixture at 1 Torr. Tests with a rich O environment as a first step to elucidate the source of unknown species without creating significant carbon deposition that could damage the glow discharge reactor. Figure 6.7 shows the IR spectra at the end of each step for 70%O_2-30%CH_4 following the experimental step sequence.

In step (1), no carbonate bands were observed as no CO_2 is sent to the reactor but only O_2 and CH_4. However, we can notice the gas phase absorption bands corresponding to methane in the region 2700 - 3000 cm^{-1}. When plasma is ignited (step 2), bands corresponding to TC are observed at 1025, 1294 and 1569 cm^{-1}. HC bands are not clearly observed at this stage. Bands at 1358, 1370, 1545, 2722, 2845 and 2933 cm^{-1} appear in the spectra which are assigned to formate species. By step (3), the bands attributed to TC species disappear indicating that TC are not being formed in the surface. However, formate bands seem to increase in intensity. No bands are observed at 1430, 1665 and 2818 cm^{-1} with 70%O_2-30%CH_4 plasma which were tentatively assigned to δ(CH), ν(C=O) and ν(CH), respectively. No new bands were observed in the IR spectra throughout the whole experimental sequence. With a large excess of oxygen, the bands with uncertain assignment are not appearing.

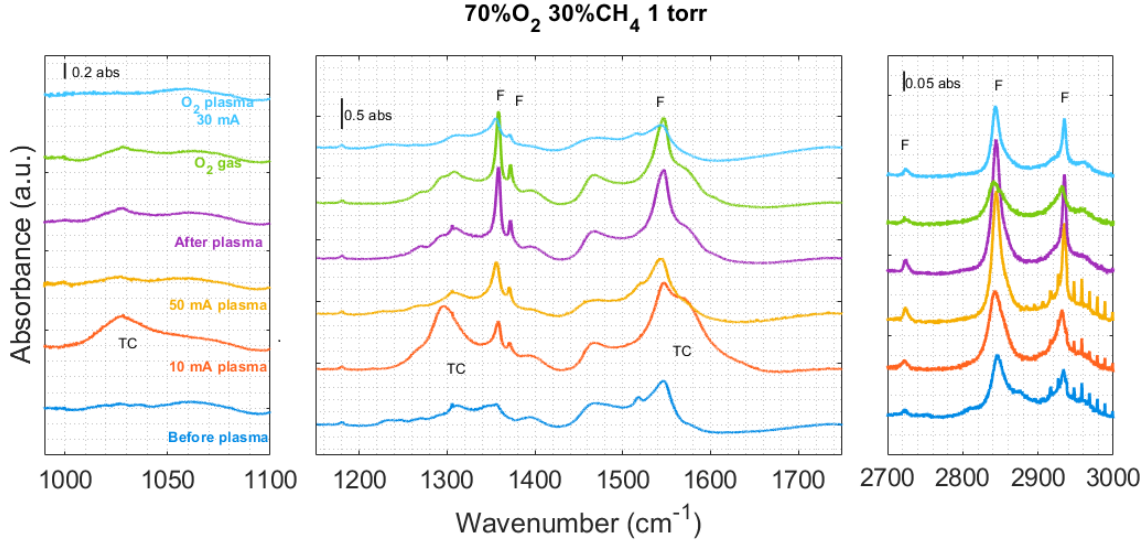

Figure 6.7: *In situ* FTIR transmission spectra of 70%O_2-30%CH_4 initial gas mixture at 1 Torr in CeO_2 surface in the cross DC glow discharge plasma reactor through the experimental sequence. TC: Tridentate carbonates, HC: Hydrogen carbonates, F: Formates. The spectra displayed corresponds to the final spectrum taken at the end of each step from the experimental sequence. Spectra are offset for clarity.

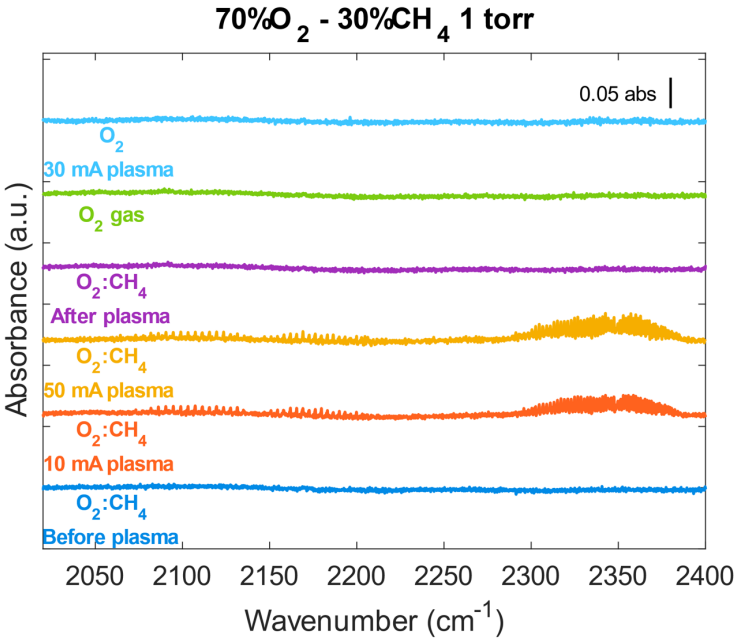

Figure 6.8: Region 2050 - 2400 cm^{-1} FTIR spectra showing CO and CO_2 gas phase bands from *in situ* experiments of 70%O_2-30%CH_4 plasma at 1 Torr. Spectra are offset for clarity.

To follow better the behaviour of the bands observed, area is obtained and followed as function of time. Figure 6.9 shows the carbonates bands and OH bands. Following the band 1294 cm^{-1} (attributed to TC), it appears to grow very quickly as soon as the plasma is ignited. In (5), the TC bands are reduced indicating that TC species are desorbed from the surface and no new TC can be formed again. Similar effect is observed in CO_2 only and CO_2-CH_4 plasma. When the plasma is off, the bands 1294 and 1025 cm^{-1} grow back but with less intensity probably from CO_2 leftover traces formed during O_2-CH_4 plasma (as CO_2 is observed in figure 6.8). The areas remain constant throughout O_2 gas step. Subsequently, during O_2 plasma, the area of the bands is drastically reduced.

Regarding HC, the band at 1396 cm^{-1} grows weakly in (2). The bands 3618 and 1218 cm^{-1} are not observed at all indicating that HC species are barely formed on the surface despite having undissociated water (3686 cm^{-1}) still at 10 mA plasma current. In (3), the 1396 cm^{-1} band is drastically reduced as TC bands. The band grows again in (4) but the others remain absent from the spectra. The area remains constant in (5) and is reduced again with O_2 plasma (step 6).

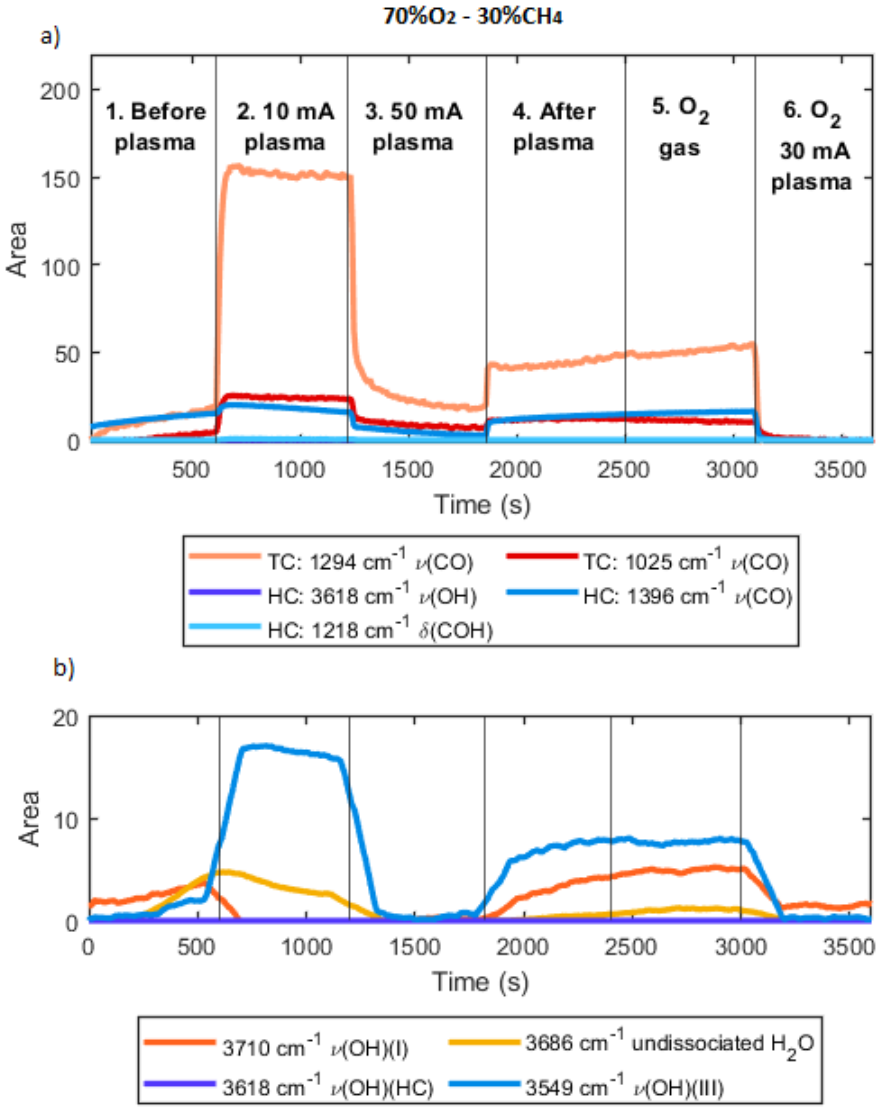

Figure 6.9: Time evolution of the area corresponding to a) TC and HC bands and b) OH group bands for 70%O_2-30%CH_4 plasma at 1 Torr during *in situ* FTIR transmission experiments.

The band at 3710 cm^{-1} (OH(I)) grows in (1) when no carbonates bands are present. When the plasma is on, the band disappears but the band at 3549 cm^{-1} (OH(III)) grows significantly. All OH bands disappear at 50 mA plasma but they grow once the plasma is off (4). The areas remain constant through (5) and even the O_2 plasma managed to decrease the bands at 3549 cm^{-1} (OH(III)) and 3686 cm^{-1} (undissociated water).

Formates bands evolution with time are shown in figure 6.9. Formates bands grow during (2), (3) and (4) in a similar way as in CO_2-CH_4 plasma despite that plasma is off in (4). This behaviour is still unclear. The area of all bands remain constant through O_2 gas. The area is reduced when the O_2 plasma is ignited.

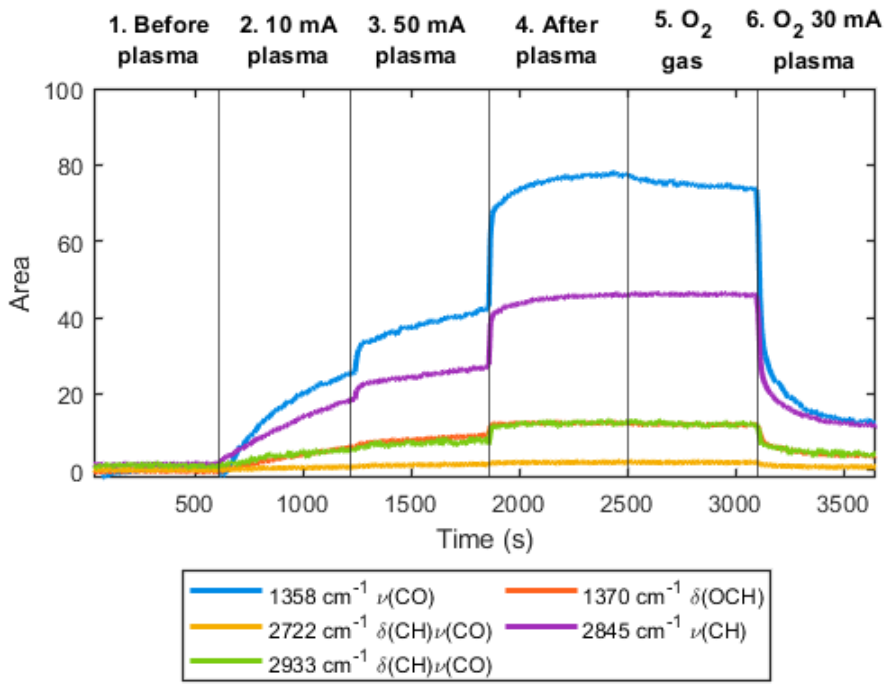

Figure 6.10: Time evolution of the area corresponding to Formate species in 70%O_2-30%CH_4 plasma at 1 Torr during *in situ* FTIR transmission experiments.

Based on what has been described, it seems that tridentate carbonates are the main carbonates species formed as soon as CO_2 is being formed during 10 mA plasma. HC are not formed with enough quantity to be relevant in this discussion. This is probably due to the larger water fraction at 10 mA O_2-CH_4 plasma than in CO_2-CH_4 plasma. In the meantime, formates species began to form while undissociated water reacts with carbonates. OH(III) species are formed greatly at this step. Carbonates and OH species disappear from the surface mostly by reaction leading to formates as they continue increasing. When the plasma is off, some carbonates are formed from CO_2 traces in the reactor. OH bands are adsorbed again in the surface while some formates continue forming on the surface. O_2 gas flowing seems to not remove any physisorbed molecules as the area of the bands remain quite stable. At O_2 plasma step, all the species are desorbed except formate species which are still present on the surface.

6.4.1 Variation of CH_4

For further investigation, 35%O_2-65%CH_4 plasma is tested to compare with 70%O_2-30%CH_4. Figure 6.11 displays the IR spectra at the end of each step for 35%O_2-65%CH_4 at 1 Torr following the experimental step sequence.

At simple sight, TC bands (1025, 1294 and 1569 cm^{-1}) appear when the plasma is ignited (2). HC bands are not clearly observed at this stage either. Bands at 1358, 1370, 1545, 2722 2850 and 2933 cm^{-1} appear in the spectra which are assigned to Formate species. The bands attributed to TC species disappear in (3) indicating that TC are not being formed in the surface. However, formate bands seem to increase in intensity. No bands are observed at 1665 cm^{-1} (tentatively assigned to ν(C=O)) or 1430 cm^{-1} (tentatively assigned to δ(CH)) at this step but the band at 2818 cm^{-1} does appear in the IR spectra. This band is tentatively assigned to ν(CH) in CO_2-CH_4 plasma. No other bands were observed in the IR spectra throughout all the experimental sequence.

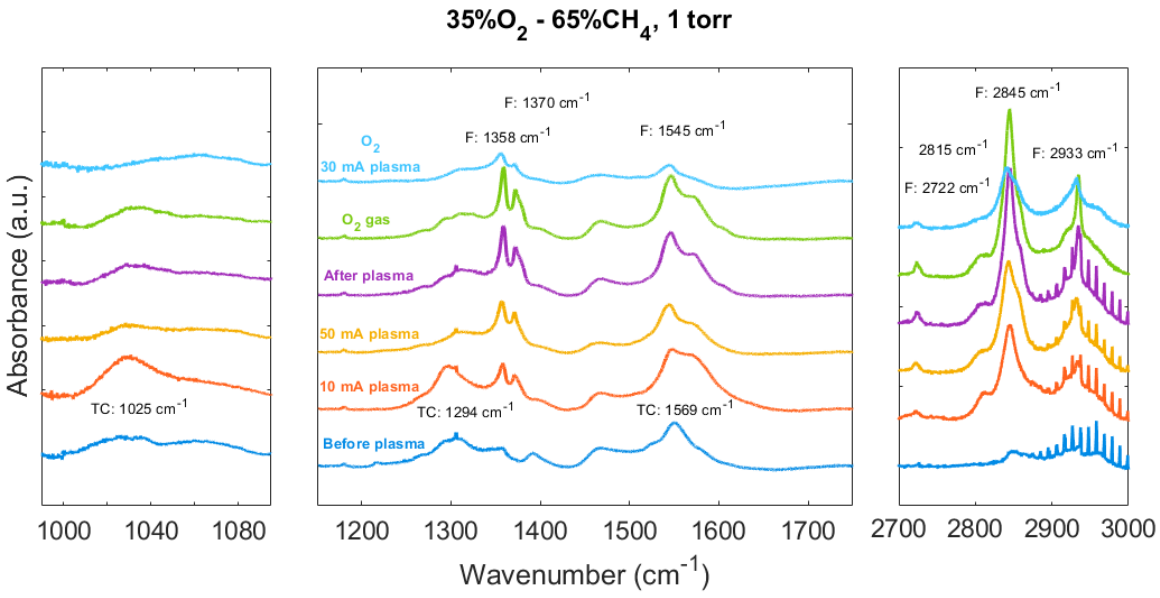

Figure 6.11: emphin situ FTIR transmission spectra of 35%O_2-65%CH_4 initial gas mixture at 1 Torr in CeO_2 surface in the cross DC glow discharge plasma reactor through the experimental sequence. TC: Tridentate carbonates, HC: Hydrogen carbonates, F: Formates. The spectra displayed corresponds to the final spectrum taken at the end of each step from the experimental sequence. Spectra are offset for clarity. IR spectra at the end of each step for

For both initial concentrations of CO_2 and CH_4, the area of the bands is extracted from the IR spectra and normalized with the largest area for the given band throughout the whole experiment to facilitate the comparison. The time evolution of the bands attributed to carbonates, formates and OH species are shown in figure 6.12. In figure 6.12b, formate bands grow during plasma (steps 2 and 3) and after plasma (4) and remain stable during O_2 gas. The area is reduced during step (6). On the other hand, TC (1294 cm^{-1}) and HC (1396 cm^{-1}) bands (in figure 6.12a) quickly grow during 10 mA plasma. Both TC bands are relatively stable with both O_2-CH_4 concentrations. The areas are reduced but do not disappear completely during 50 mA plasma. Both TC bands regain 1/3 of the maxima area for both concentrations O_2-CH_4 in (4 until 5). During O_2 plasma both bands decrease in area. HC bands followed different trends:

- HC band in 70%O_2-30%CH_4 initial gas mixture behave in a similar matter as TC through all the experimental steps.
- However, HC band in 35%O_2-65%CH_4 initial gas mixture rises very quickly and area decreases to zero in 400 seconds. This is an unusual behaviour and not observed in other experiments. The band does not appear again in the whole experiment.

We recall that undissociated water band (3686 cm^{-1}) is still present in the 70%O_2-30%CH_4 experiment (figure 6.9). However, for 35%O_2-65%CH_4, undissociated water does not grow back after plasma (4) in figure 6.12c. When HC trend is compared with the area of undissociated water (3686 cm^{-1}) we noticed that both seem to follow a similar behaviour in (4) until (6). This is consistent with the conclusions of chapter 5 that undissociated water is necessary to react with CO_2 to form hydrogen carbonates.

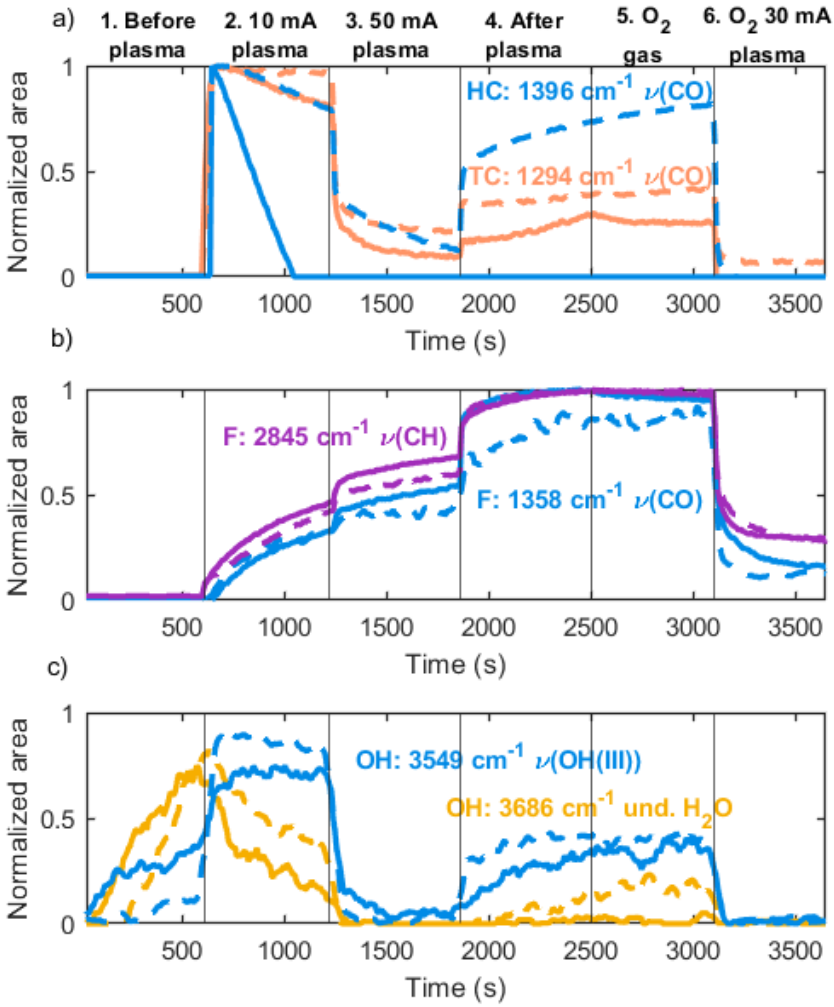

Figure 6.12: Normalized area of bands at a) TC: 1294 cm^{-1} and HC: 1396 cm^{-1}, b) F: 2845 and 1358 cm^{-1} and c) 3549 and 3686 cm^{-1} as a function of time for 35%O_2-65%CH_4 (solid line) and 70%O_2-30%CH_4 (dashed line) plasma at 1 Torr in CeO_2 surface.

These experiments show that the main surface adsorbates are the same in O_2-CH_4 and CO_2-CH_4 plasmas in CeO_2 surface. The order of appearance in the surface is different depending on the gas mixtures. Carbonates species just appear when CO_2 is formed in O_2-CH_4 plasma.

However, these experiments with O_2-CH_4 plasma does not give us any information on the unknown bands at 1430 cm^{-1}, 1665cm^{-1} and 2818 cm^{-1}. Only when 100%CH_4 plasma was performed following the same procedure as above, the bands at 1430 and 1665 cm^{-1} were finally observed in the IR spectra. This means that they are related to CH_4 decomposition products only. The area of the bands was extracted and plotted as a function of time. Figure 6.13 shows the time evolution of 1430, 1665 and 2818 cm^{-1} for pure CH_4 plasma and 35%O_2-65%CH_4.

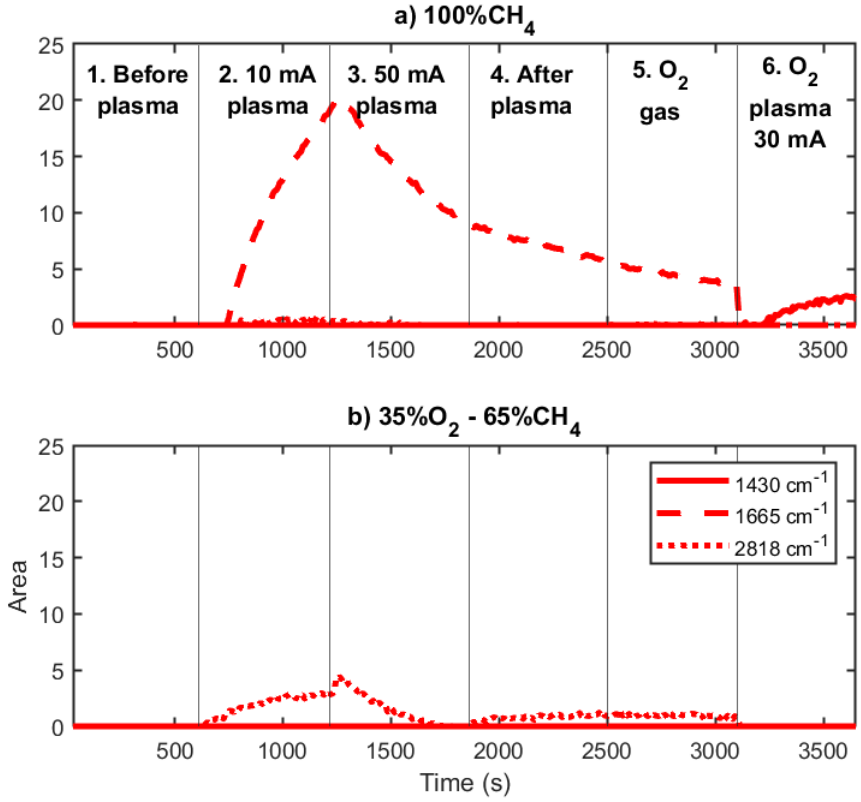

Figure 6.13: Time evolution of the area corresponding to 1430 cm^{-1} (solid line), 1665 cm^{-1} (dashed line) and 2818 cm^{-1} (dotted line) bands for a) 100%CH_4 plasma and b) 35%O_2-65%CH_4 plasma at 1 Torr during *in situ* FTIR transmission experiments.

The band at 1665 cm^{-1} appears during 10 mA plasma step (2) and decrease in intensity when the plasma current is increased to 50 mA (3). The band continues decreasing after plasma (4) and during O_2 gas (5). It is rapidly decreasing in O_2 plasma (6). Shortly after, the band at 1430 cm^{-1} appears and starts growing during O_2 plasma.

This trend could indicate that species attributed to 1665 cm^{-1} give rise to the other species from 1430 cm^{-1}. Every paper consulted during this thesis work involving CeO_2, formaldehyde, formic acid, formates, carbonates and water species does not mention a band that appears in the IR spectra at 1665 cm^{-1}. The closest band is 1640 cm^{-1} attributed to δ(HOH) but this possible assignment was discarded in section 5.4 in chapter 5 as it is not related to the behaviour of OH groups or undissociated water. If the band is not attributed to C=O of unidentate formates, formaldehyde or water, then it could have another origin.

We know that methane conversion in low temperature plasma results mainly in the formation of acetylene, a C_2 hydrocarbon besides H_2 [151]. Also, it is known that polymerization of CH_4 can occur in low temperature plasmas [152]. Many of the products are aliphatic chains with saturated and unsaturated units. Even though these groups were not observed in the gas phase during CO_2-CH_4 and O_2-CH_4 plasmas, they could still be formed below the detection limit of the instrument or formed and quickly decomposed under plasma. In addition, it should be reminded that carbon deposition was observed in the HV electrode of the DC glow discharge reactor during plasma kinetic studies for CO_2-CH_4 plasmas as reported in [87]. Only when CH_4 is used alone in plasma, no O atoms are present in the plasma phase that could oxidize and decompose such species.

If we assume that the band 1665 cm^{-1} is attributed to carbon-carbon bonds, it could not entirely explain the appearance of such band on downstream gas experiments in chapter 5. Unless we assume that such species can be formed in trace quantities and accumulate in the surface of the ceria pellet. However, aliphatic compounds are not known to adsorb in a metal oxide surfaces as methane in gaseous form does not adsorb in CeO_2. An hypothesis would be to assume that the aliphatic chains have endings with O atoms like ketones or carboxylic groups that could help to interact with OH groups in the surface or possibly fill an oxygen vacancy in the unsaturated CeO_2 surface. In such case, then a C=O could also be attributed to this particular band. Such attribution could occur only if we assume that O atoms are extracted from the surface of CeO_2 in pure CH_4 plasma and linked to C atom. This structure has not been reported in the literature concerning CeO_2 and C. The closest structures could be carboxylates or carbonite but Vayssilov et al. discarded that such species could be stable enough to be formed and observed by IR spectroscopy [117]. Actually, carbonite structure was studied by Binet et al. [153]. They found that defects formed in the surface can lead to carbonite at high temperatures but none of the bands proposed fitted our case.

At this point we can assume that the unknown species has a C-C due to the aliphatic groups. Then, when O_2 plasma is ignited, the band at 1430 cm^{-1} appears indicating that the species attributed to this particular band can be formed only when O atoms are present. This band is not observed in CO_2 plasma alone and it is weakly observed in CO_2-CH_4 plasma experiments. In section 5.4 in chapter 5, it was attributed to δ(CH). However, it is not observed during CH_4 plasma alone in (2) and (3), therefore it can not be a CH group. Based on the location, it is likely to be attributed to C-O bond. Li et al. studied CO and CO_2 adsorption on CeO_2 and they identified unidentate carbonate with bands located at 1454, 1354 1045 and 856 cm^{-1} [133]. Again, Vayssilov et al. found them unlikely to be observed in the IR spectra [117]. Tabakova et al. [154] report a band at 1430 cm^{-1} (along with bands at 1340 and 1050 cm^{-1} in their work) observed in ceria during thermal water-gas-shit reaction and assigned to carbonates. No more information is given regarding the nature of such carbonate but we know that it can be formed in particular conditions. If this band is not observed during CO_2 only and O_2-CH_4 plasma experiments but it is observed in CO_2-CH_4 and CH_4 plasma, we can assume that only it is formed only by pyrolisis of CH_4 in plasma. Perhaps, the environment rich in H atoms could be necessary to create the sites to form such particular carbonates. Although work on nanostructured ceria interacting with CO suggest a shift on carbonates bands and the possible formation of polydentate carbonates depending on the defects created by the shape and reduction of the surface [155]. Probably, a thermal reduction of the CeO_2 material used in our lab before the subsequent interaction with CO or CO_2 gas could provide more information regarding the observation of new or shifted carbonate bands in IR spectra.

The band at 2818 cm^{-1} appears mostly in 35%O_2-65%CH_4 plasma experiments in step (3) and decays through (3). The band seems visible during (4) and (5) and disappears in (6). This behaviour does not fit the trend of any other unassigned band. In pure CH_4 plasma, a weak shoulder is observed in (2) but quickly disappears in (3). Given the location of the band, it is still attributed to CH group although the intensity was expected to be higher in pure CH_4 plasma experiment.

It is clear that the discussion done here has not resolved the identification of such bands but has lead to several hypothesis and to new ideas that can help to investigate further. It would be interesting to carry out a downstream gas experiment where the gas product of CH_4 plasma is sent to the ceria pellet and see the absorption bands from CeO_2 without the effect of temperature, electric field, ion bombardment, etc. as done in section 5.3 in chapter 5.

6.5 Conclusions

N_2 plasma at 30 mA has a T_{gas} higher (around 80 K) than O_2 plasma in the same conditions. The dominant excited electronic states in N_2 plasma include N(4S), N_2(A) and vibrationally excited N_2 can carry energy to contribute on the desorption of adsorbed species. In the case of Ar plasma, desorption of carbonates or formates from CeO_2 surface is not achieved. Ar does not provide enough temperature and/or excited species to efficiently remove adsorbates as N_2 or O_2 plasmas. When He plasma is tested, the desorption is improved compared to Ar plasma but still performs lower than N_2 and H_2 plasmas. The presence of H_2 in N_2 plasma seems to improve the desorption capability of pure N_2 plasma as HC are not observed anymore in (7) compared to H_2 plasma. However, it is clearly noted that at 1 Torr, ion bombdament, change in partial pressure and temperature are not the only factors playing a role in the desorption of Carbonates and Formates. More work has to be done to elucidate which electronically or vibrationally excited species could be behind the desorption process.

O_2-CH_4 plasmas experiments confirmed once more that TC species are the main carbonates species involved in the formation of formates during plasma. The study of O_2-CH_4 plasmas gave several clues in an attempt to elucidate the origin of bands at 1430, 1665 and 2818 cm^{-1}. The band at 1430 cm^{-1} is suspected to belong to a carbonate species formed under specific conditions. The band at 1665 cm^{-1} is still tentatively attributed to C=O or to C-C (either saturated or unsaturated) bond. The band at 2818 cm^{-1} is still not clear what could be true nature of this particular vibration. Indeed, work still needed as it is not clear yet the species behind those IR bands.

Part III

Innovative routes for CO_2 conversion by plasma-catalysis

Chapter 7

CO_2 plasmas in Fluidized bed - DC glow discharge reactor

Contents

7.1 Introduction

A fluidized bed consists of a mixture of fluid and solid particulate submitted to appropriate conditions that lead the solid to behave as a fluid. Particles become fluidized when an upward-flowing gas imposes a high enough drag force to overcome the downward force of gravity. When the gas velocity is high enough that the drag force on the particles equals the weight of the particles, the bed becomes fluidized. This process is called *Fluidization* and it involves the injection of a fluid into a bed of particles, which enable the bed of particles to move with the injected fluid in a fluid state manner.

The fluidization of solid particles improves the contact surface area with the gas phase resulting in a high rate of heat and mass transfer. As mentioned in the introduction section 1.3, fluidized bed - plasma

reactors coupled with non-equilibrium plasmas could bring these advantages and improve the overall conversion of CO_2. In conventional fluidized thermal catalytic reactors, the catalytic material is crucial on the performance, however, in plasma reactors the mere presence of such materials could also imply a different effect in the excited species and other parameters. In addition, the fluidization is expected to provide a significant advantage working at low pressure. The mininum fluidization velocity increases as a result of increasing mean free path of molecules and decreasing gas density by decreasing the operating pressure [156].

Here, we present the results from the testing of Al_2O_3 as a fluidizing material which is known to have very little catalytic activity for CO_2 reactions, in a low pressure glow discharge similar to the one presented in previous chapters. The goal of this chapter is therefore not to achieve high chemical conversion performance but to elucidate the effect of the fluidized particles on the plasma itself.

7.2 Experimental procedure

To evaluate the CO_2 conversion and the effect of alumina particles fluidizing in the glow discharge reactor the set up was arranged as seen in figure 7.1. The fluidized bed - glow discharge (FB-GD) reactor is presented in figure 2.14. A 2 cm diameter glass tube with an embedded porous glass disk was used as Fluidized bed - glow discharge reactor. The discharge is established between two hollow cathode electrodes separated by 23 cm. The powder particles are hold inside the reactor by the porous glass disk embedded across the tube around 6.5 cm from the outer side of the bottom electrode. Above the discharge region, a cyclone is placed to allow the particles to fall back into the reactor. A pressed glass wool was installed at the exit of the FB-GD (after the cyclone) to prevent any possible particle to reach the gas line.

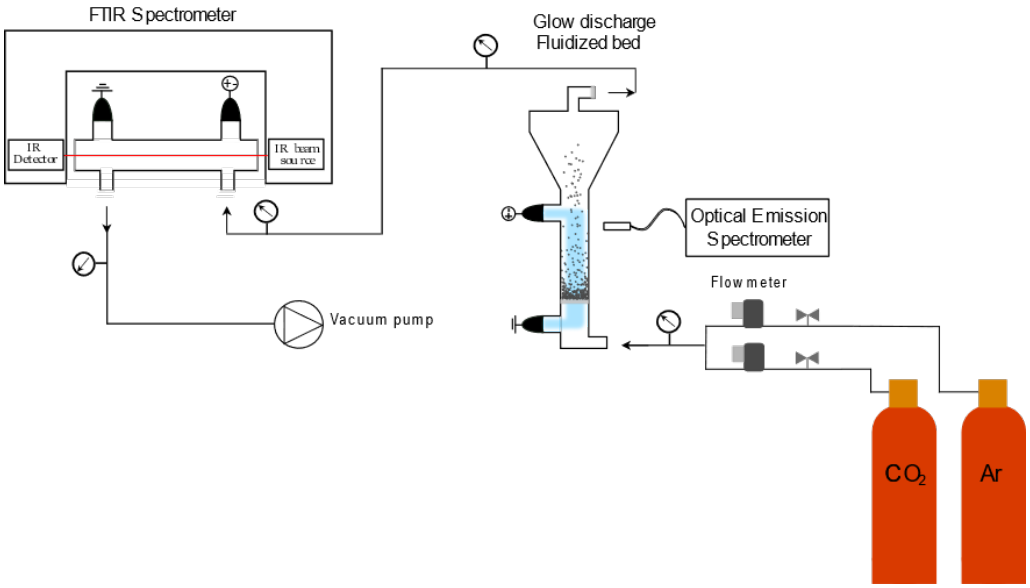

Figure 7.1: Schematic of experimental setup for CO_2 plasma in DC Glow discharge - Fluidized bed at low pressure.

γ-Al_2O_3 (known as 'alumina') was used as solid particles for fluidization. The alumina used is neutral from Sigma-Aldrich with an average size of $\sim$100 μm. No pretreatment was done before plasma experiments.

The reactor inlet was connected to 3 flowmeters for CO_2, CH_4 and Ar gases from their respective bottles. The exit of the reactor was connected by corrugated stainless steel hoses to the IR cell located

in the path of the infrared beam in the FTIR spectrometer. At the exit of the IR cell, a vacuum pump was installed to maintain low pressure in the system. The pressure is regulated manually and measured by four pressure gauge: at the entry and exit of the reactor and entry and exit of the IR cell located in the path of the FTIR spectrometer. The pressure imposed during the experiments was the pressure just after the porous glass disk which is the pressure the largest portion of the plasma region where the particles are fluidized.

An optical fibre was located normally to the reactor to measure axially in points along the plasma region using an optical emission spectrometer. The purpose is to characterize the observable species axial evolution and the gas temperature. Figure 7.2 shows a picture of the glow discharge - fluidized reactor along with red dots representing the approximate positions at 5, 6, 7, 8, 9, 11, 14, 18 and 22 cm where optical emission spectra were taken. The porous glass disk is located around 6.5 cm (transversal red dotted line) above the lower point of the electrode which is considered to be the position 'zero'.

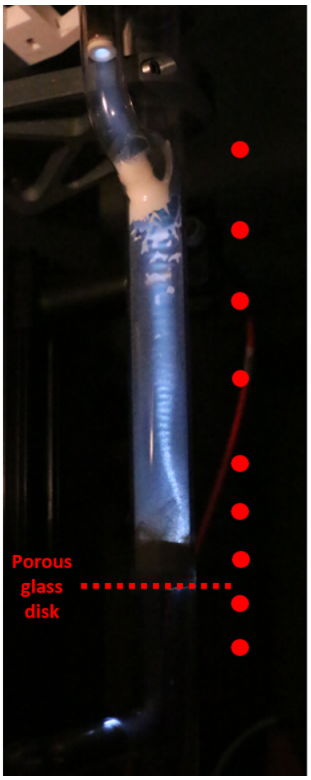

Figure 7.2: Picture of the DC glow discharge - fluidized reactor with Al_2O_3 particles along red dots representing the positions where optical emission spectra was taken. Dashed line indicates the position of the porous glass disk.

The emission from CO 3rd Positive system band 3PS ($B^3\Sigma+ \rightarrow a^3\Pi$), CO Angström band ($B^1\Sigma+ \rightarrow A^3\Pi$), two O atom emission lines at 777 nm ($^5P_{1,2,3} \rightarrow {}^3S$) and 844 nm ($^3P_{0,1,2} \rightarrow {}^5S$) and H_α atom emission line at 656 nm were evaluated (see also energy diagram on figure 2.5 from chapter 2). The intensities of O lines at 777 nm (from now on O777) and 844 nm (from now on O844), 3PS and Angström band of CO and H atom at 656 nm (from now on H656) were normalized by the intensity of Ar line at 750 nm. 3% of Ar is added into the gas mixture as it is done for actinometry measurements, in order to have a reference for the variation of electric field and electron density along the plasma. Indeed, as Ar is not reactive, its density is considered constant, and the variation of the Ar line intensity is therefore solely due to its excitation by electrons (and a bit to non radiative quenching). CO rotational temperature T_{rot} was obtained by fitting of ($\nu1$, $\nu2$) = (0,1) optical transition of CO Angström band and it is considered a good estimation of the gas temperature in our plasma [5, 16].

The downstream gas composition (reactants and products) was analysed by FTIR spectroscopy [93]. The dissociation fraction was estimated and compared to previous results from CO_2 plasmas [16, 82, 125]. In order to bring additional information on the adsorption of CO_2 onto Al_2O_3 surface, *in situ* FTIR transmission experiments were performed in the same manner as described in section 4.2. Three experimental conditions were performed three times each, and the average is presented in the following sections along with their standard deviation (+/-σ) as error bars. A summary of the parameters and conditions varied during these experiments is displayed in table 7.1.

It is important to note that the gas flow used here (20 sccm) is higher than the one used in all our previous measurements with glow discharges (7.4 sccm most of the time). A higher flow rate is indeed

Gas mixture	100%CO_2 95%CO_2-5%CH_4
Current	12, 20 and 30 mA
Pressure	1.5, 2 and 2.5 torr
Total flowrate	20 sccm
Material	Al_2O_3 (∼100 μm)
Quantity	0 (empty reactor), 1 and 4 g

Table 7.1: Parameters and conditions tested in DC Glow discharge - Fluidized bed reactor

necessary to achieve fluidization of the alumina particle bed. This also results in a higher pressure drop on both sides of the porous glass disk. These measurements are the first ever in a FB-GD at few Torr in CO_2 containing gases. The measurements were therefore first carried out in pure CO_2. The initial aim was to test with the same CO_2-CH_4 mixtures used in the previous chapters, but as will be described later, only a small percentage of 5%CH_4 could be measured here due to the clogging of the pores of the glass disk at higher CH_4 percentages.

7.3 CO_2 plasma in Fluidized Bed - Glow Discharge (FB-GD)

Before starting discussing the results from CO_2 plasmas on a complex reactor as a fluidized bed - glow discharge (FB-GD), it is important to try to understand the effect of the presence of a porous glass disk embedded in the glass reactor. Figure 7.3 shows the plasma region of the FB-GD reactor empty with CO_2 plasma only. The porous glass disk induces a bright hot spot, which can sometimes jump depending on the preferential path the plasma current is taking through the pores of the glass disk. On the left one can see the glow discharge light emission (without any particles) with the embedded disk. The plasma region looks homogeneous except at the position of the porous glass disk where high plasma current density is expected.

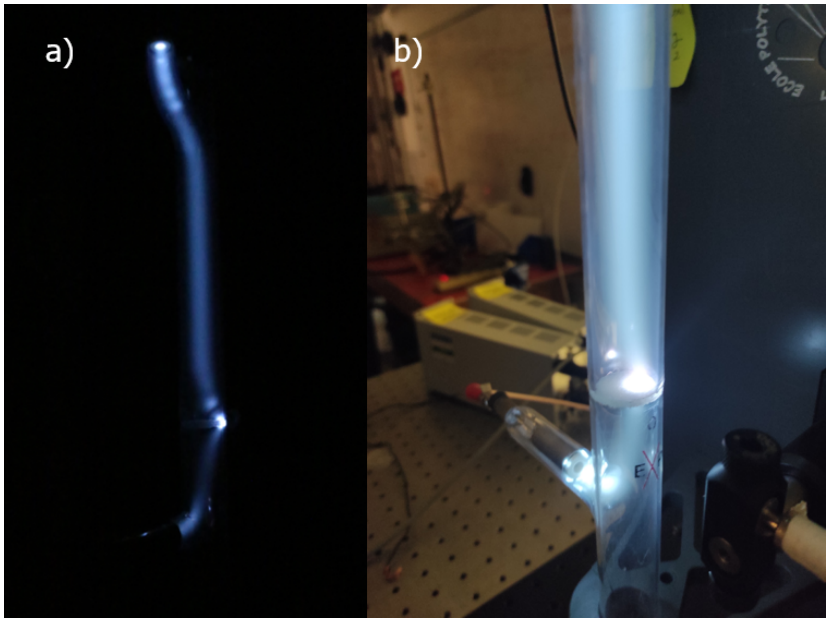

Figure 7.3: Empty glow discharge - fluidized bed reactor with CO_2 plasma showing the a) whole positive column and b) a close up picture of the bright spot in the porous glass disk at 1.5 torr and 20 mA plasma current.

The intensity of the light is different before and after the porous glass disk which could indicate a difference in the excited species in the plasma and/or difference in temperature.

7.3.1 Gas temperature

Figure 7.4 shows the gas temperatures deduced from rotational temperature of the Angström band in the empty reactor as a function of the position along the plasma region in the FB-GD at constant pressure (2 Torr).

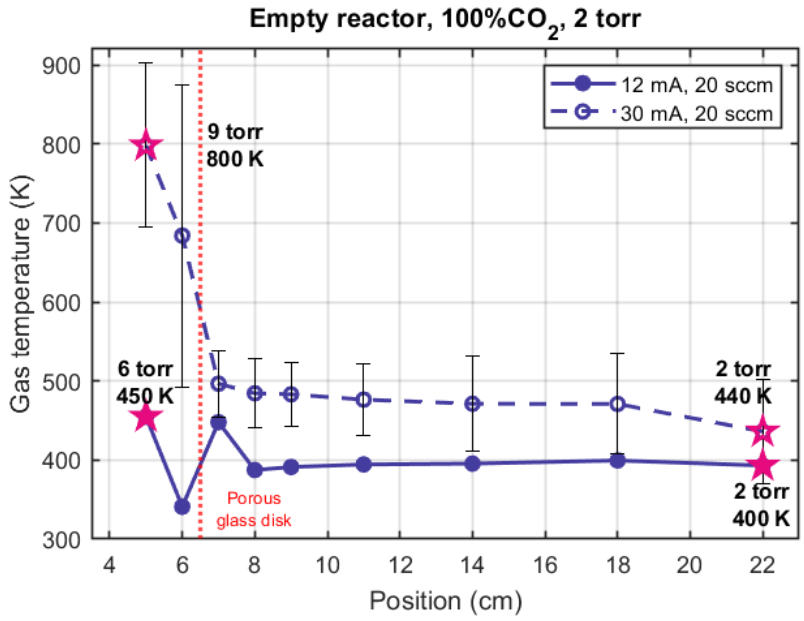

Figure 7.4: Gas temperature (T_{rot} of CO) along the plasma region in the empty FB-GD discharge reactor for 12 mA (solid line) and 30 mA (dashed line) current in 100%CO_2. Error bars correspond to the +/-σ. Pressure was set to 2 Torr after the porous glass disk. The red dotted line indicates the position of the porous glass disk. Total flow rate: 20 sccm.

Two currents are displayed: 12 and 30 mA, showing an increasing temperature with increased current, as expected. Following the temperature across the reactor, the temperature is higher before the porous glass disk than after, which can be explained by the change of pressure. Indeed the porous glass disk induce a large pressure drop which is measured with pressure gauges before and after the reactor. When 2 Torr is kept constant at 12 mA after the porous glass disk, ~6 Torr is measured before, and for 30 mA, up to ~9 Torr is measured upstream. The gas temperature is known to increase with pressure in our discharge. On figure 7.4 the gas temperature at 30 mA is around 800 K before and ~450 K far after the disk (marked by pink stars in figure 7.4). When comparing with the temperature obtained in a 'regular' glow discharge (same reactor tube without any embedded disk), the temperatures are consistent with the pressures measured upstream and downstream the glass disk in the FB-GD. Figure 7.5 shows a figure extracted from A.S. Morillo-Candas doctoral thesis comparing the values of gas temperatures obtained by two different spectroscopic techniques [16]. Taking the values at 2 Torr and roughly extrapolating at 9 Torr for 30 mA, the temperatures are 510 and 830 K, respectively (also marked by pink stars). This comparison demonstrate the consistency of gas temperatures across reactors and validates the accuracy of the estimation of rotational temperature of CO.

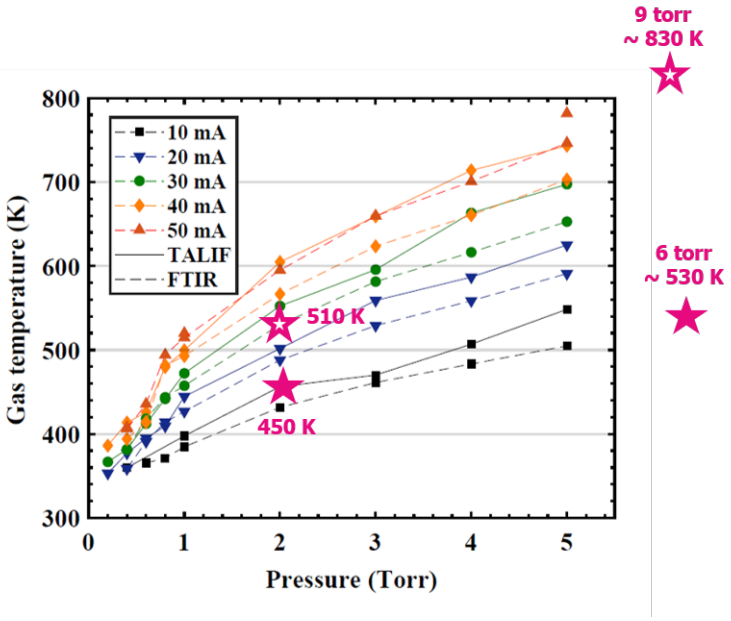

Figure 7.5: Gas temperature variation versus pressure for currents between 10 and 50 mA obtained from the FTIR spectra (rotational temperature of CO_2 and CO) and from the Doppler broadening of TALIF signal (translational temperature of O atoms) in 100%CO_2. Glow discharge reactor without embedded glass disk. Total flow rate: 7.4 sccm. Figure taken from [16].

In the following, empty reactor (0 g of Al_2O_3) is compared with different quantities of solid particles through different conditions of current and pressure. Figure 7.6a displays the effect on the gas temperature (K) of the presence of 1 and 4 g of Al_2O_3 compared with empty reactor (0 g) for 12 and 30 mA at 2 Torr. No significant difference on gas temperature is seen for 12 and 30 mA when adding Al_2O_3 particles at 2 Torr. The gas temperature just increases with current from 400 K to 520 K at the exit of the plasma between 12 and 30 mA. In figure 7.6b, a small increase in temperature is observed with pressure increasing from 1.5 to 2.5 Torr in the plasma region after the glass disk with constant current. Although, at 1.5 Torr there is almost 100 K difference between 4 g of alumina and the empty reactor. At 2 and 2.5 Torr, the temperature ranges 471-550 K with and without particles. Even so, comparing amongst pressures, the temperature remains very similar with Al_2O_3 particles. This is consistent with what was observed in the empty reactor results and with the 'regular' glow discharge data (see figure 7.5). Just a slight increase in temperature between 4 g of Al_2O_3 and empty reactor maybe exist especially towards the upper electrode (position at 22 cm).

This could be due to the contraction of the plasma region by the presence of the particles. Indeed, as seen on the picture from figure 7.7, when Al_2O_3 particles are added, the plasma column becomes narrower, probably because of electrostatic repulsion. Indeed the Al_2O_3 particles become negatively charged in the plasma. They repel each other, which contributes to changing the fluidization regime of the bed. Negatively charged particles also tend to repel electrons. Thus, the plasma finds itself having to pass through a narrower 'effective cross-section' of the tube. As the current is kept constant when comparing measurements with and without particles, this means that the current density is higher in the plasma column in the presence of Al_2O_3 particles. Therefore, one would expect the temperature measured by OES to be higher with particles (since the CO rotational temperature is obtained from emission in a region with higher current density). However, in our low pressure conditions, the cooling of the gas is dominated by heat transfer to the walls [157]. Moreover, one of the known interests of fluidized

beds is to favour the heat transfer to the walls. The fact that the measured temperature is the same with and without particles could therefore be the result of a more important heating in the narrower plasma column, compensated by a more efficient heat transfer to the walls. Such modification of the positive column can also have an impact on excited species.

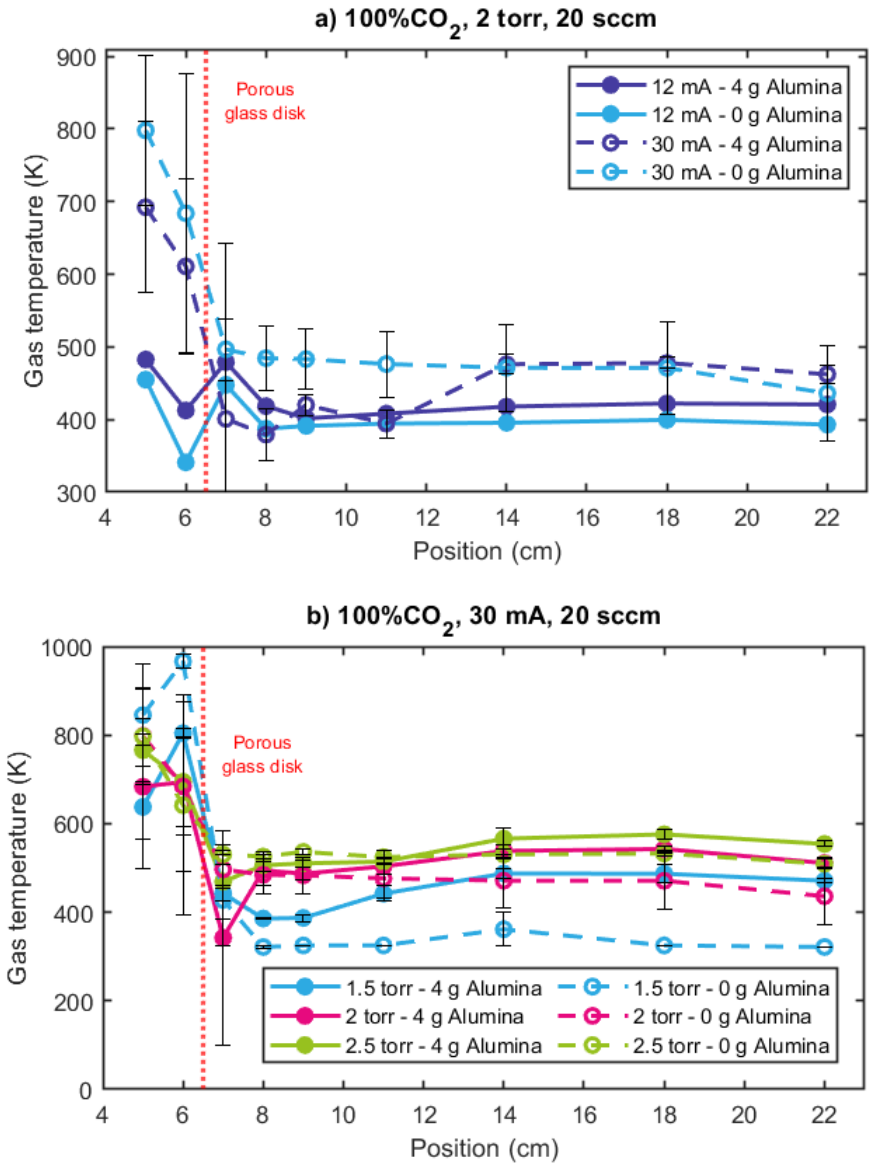

Figure 7.6: Gas temperatures in 100%CO_2 plasma *versus* position in the fluidized bed - glow discharge as a function of a) current at 2 Torr and b) pressure at 30 mA with 0 and 4 g of Al_2O_3. Total gas flow: 20 sccm.

It should be emphasized that during plasma experiments, besides the narrower plasma volume, the Al_2O_3 particles were also attaching to the walls as seen in the picture of figure 7.2. Before plasma, the flowing gas moves the particles up as they are falling down. However, the movement is restrained once the plasma is ignited. Instead of moving the majority of the particles, some remain in the bottom, some keep moving and some others stick to the reactor walls. This is attributed mostly to the electrostatic charges of the particles under plasma exposure.

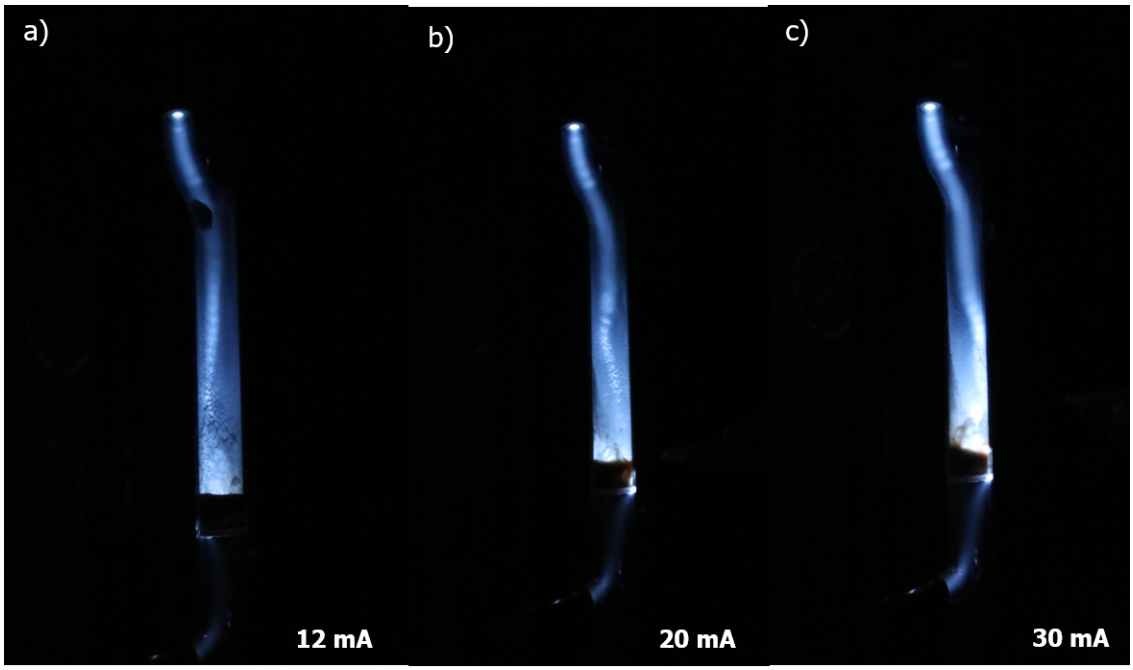

Figure 7.7: Pictures of FB-glow discharge with alumina particles at a) 12, b) 20 and c) 30 mA.

7.3.2 O atoms emission lines

To compare across different conditions, 3%Ar is added to the gas flow as a reference to take into account the influence of the variation of electron density and reduced electric field in the variation of atomic and molecular line emission. Therefore, the Ar line intensity is used to normalize the intensity of the emission lines of interest because the density of Ar is not changing (it is not chemically reactive) and its emission intensity is only affected by properties of the electron exciting the emitting level (if the non radiative quenching is neglected). The ratio I_{O777}/I_{Ar750} is often used in a technique called 'Actinometry' to determine the O atoms density from plasma emission [95]. The principle is similar to what is described in Appendix A and rely on the idea that the ratio I_{O777}/I_{Ar750} is proportional to the O atom density and the ratio of the excitation coefficient of the two emitting excited states of O and Ar (k_{Ar750}/k_{O777}), see details in [95]). The ratio of the excitation coefficients k_{Ar750}/k_{O777} is a monotonous rising function of the reduced electric field (E/N) which can be calculated when using a Boltzman solver like the code LoKI-B [158]. Therefore, if the E/N is known in the condition studied, by measuring I_{O777}/I_{Ar750}, the O atoms density could be known. Unfortunately the electric field in the FB-GD is difficult to determine, preventing us from knowing the absolute O atoms density. Nevertheless, the ratio I_{O777}/I_{Ar750} remain a marker of the evolution of both O atoms density and the ratio k_{Ar750}/k_{O777} together.

Figure 7.8 shows the normalized intensity of O777 emission line along the plasma region in empty FB-GD reactor at different plasma currents with total flow rate of 20 sccm at 1.5 Torr after the glass disk.

Four main points can be observed:

- A large drop of I_{O777}/I_{Ar750} is observed for all pressures between before and after the glass disk.
- The normalized intensity tends to slightly decrease from the glass disk to the exit of the plasma both with and without particles.
- If anything, the ratio I_{O777}/I_{Ar750} is slightly lower with particles than without above position ~10 cm.

- A small bump of I_{O777}/I_{Ar750} is seen at 1.5 and 2.5 Torr just above the glass disk with the 4 g of particles.

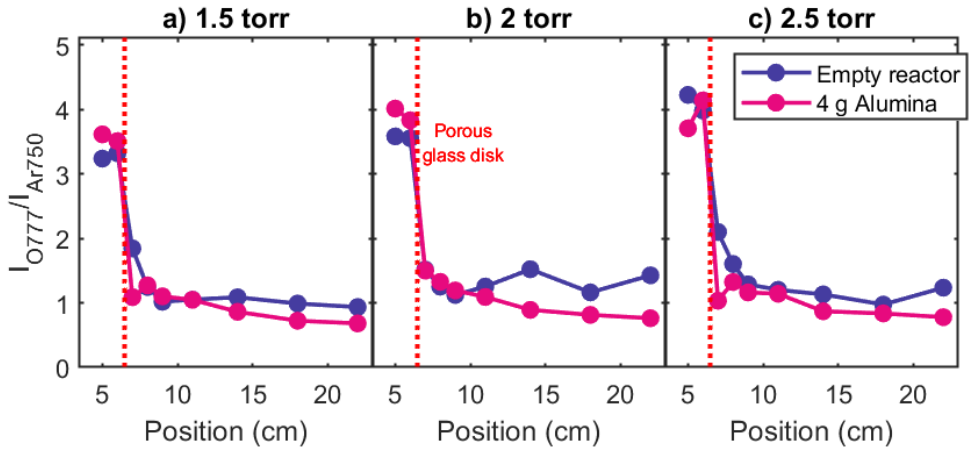

Figure 7.8: Intensity of O777 emission line normalized by Ar750 emission along the plasma region in FB-glow reactor for 30 mA at a) 1.5, b) 2 and c) 2.5 Torr. Total flow rate: 20 sccm.

In our regular glow discharge, the E/N in pure CO_2 is decreasing with pressure [95], therefore k_{Ar750}/k_{O777} should decrease as well. The large drop of I_{O777}/I_{Ar750} must then be related to a real drop of atomic oxygen between before and after the glass disk. This is surprising because the higher pressure before the glass disk should favour the recombination of O atoms into O_2 [95]. A possible explanation is that the plasma is very bright just below the glass disk because all the current is passing through a preferential path in one of the pores of the glass disk. The current density in this high pressure part is therefore very high, which could explain a high dissociation and O atoms density in this region.

The apparent diameter of the plasma column, both with and without particles is expanding from the glass disk to the exit of the plasma (see pictures 7.3 and 7.7). Again this probably reflects a variation of the current density along the plasma column, which could explain the slight decay of I_{O777}/I_{Ar750} both with and without particles.

Finally, in our pure CO_2 glow discharge the O atoms mostly recombine at the walls [95]. Adding Al_2O_3 particles is therefore expected to increase the surface available for O atoms to recombine into O_2. The small decay of I_{O777}/I_{Ar750} with the 4 g of Al_2O_3 above 10 cm could therefore reflects a stronger O atoms recombination on the particles.

A similar approach using a normalization by the Argon emission can be applied to get insight on the behaviour of other excited states.

7.3.3 CO Angström band

The intensity of CO emission lines can give us an idea of the dissociation processes occurring in the plasma and particle fluidization. Figure 7.9 shows the area of CO Angström band normalized by the intensity of the Ar750 along different positions in the plasma region in FB-GD for 100%CO_2 at a) 2.5 Torr and b) 1.5 Torr for empty reactor and 4 g of Al_2O_3. A first comment is that the normalized CO intensity is the same with and without particles before the glass disk, showing that in absence of particles, this ratio is reproducible.

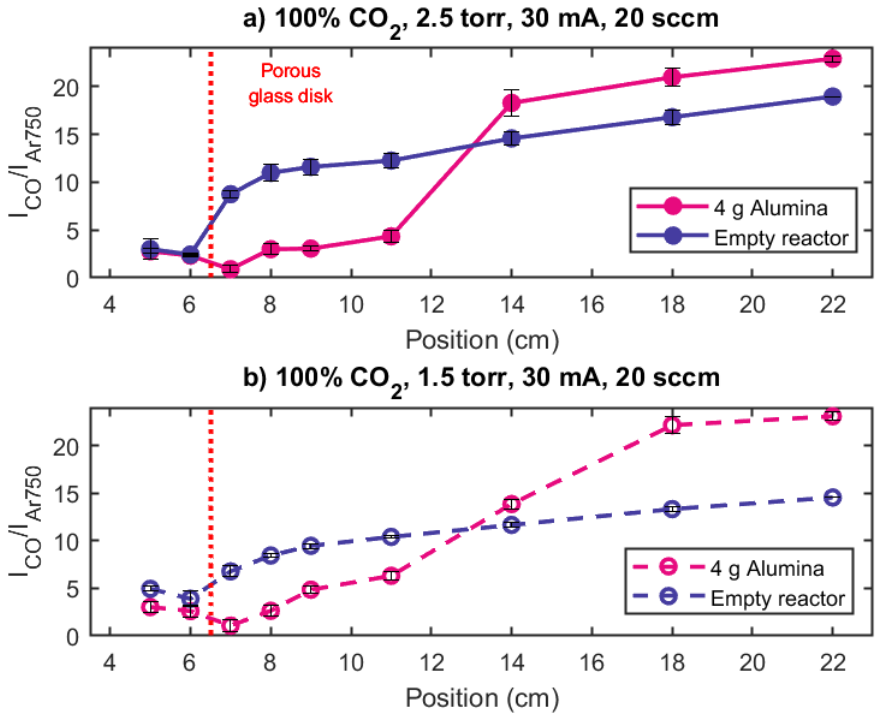

Figure 7.9: Ratio of CO Angström band normalized by the Ar750 line intensity along different positions in the plasma region in FB-Glow discharge for 100%CO_2 at a) 2.5 Torr and b) 1.5 Torr for empty reactor and 4 g of Al_2O_3. Total flow rate: 20 sccm. Current applied: 30 mA.

Above the glass disk, several points can be noticed:

- For both pressures, the normalized CO intensity (I_{CO}/I_{Ar750}) increases with distance both with and without Al_2O_3 particles.
- With 4 g of Al_2O_3, the ratio I_{CO}/I_{Ar750} is lower than in empty reactor until ~13cm above the glass disk for both pressures.
- With 4 g of Al_2O_3, the ratio I_{CO}/I_{Ar750} is higher than in empty reactor at the exit of the plasma.

Like for the O atoms in the previous section, the intensity (or area) of CO Angström band (I_{CO}) depends not only on the CO density ([CO]) but also on the electron density (n_e) and the excitation coefficient that is a function of the reduced electric field ($k(E/N)$):

$$I_{CO} \sim n_e, k(E/N), [CO] \tag{7.1}$$

Before trying to explain the observation from figure 7.9, it is therefore necessary to make an attempt to determine more accurately how the E/N is varying.

By using LoKI-B, a simulation of Electron Energy Distribution Function (EEDF) in pure CO_2 plasma for several E/N has been made (see thesis of Edmond Baratte [87]). From this EEDF, a ratio of electron impact excitation rate coefficient was calculated for the two O atoms emission lines at 777 nm and 844 nm (k_e^{O777}/k_e^{O844}). This ratio is a monotonously decaying function of the reduced electric field (see more in Appendix A). In summary we can use the ratio of the intensity of O777 and O844 as a simplified relation of E/N:

$$\frac{I_O^{777nm}}{I_O^{844nm}} \approx \frac{k_e^{O777}}{k_e^{O844}} \left(\frac{E}{N}\right) \rightarrow f\left(\frac{E}{N}\right) \tag{7.2}$$

Figure 7.10 shows E/N in Td estimated from the ratio I_O^{777nm}/I_O^{844nm} along the plasma region in the FB-GD reactor in 100%CO_2 at a) 20 and b) 30 mA for empty reactor and with 4 g of Al_2O_3. In general, the electric field is much higher below the disk which is contradictory with the fact that E/N decreases with pressure in our 'regular' pure CO_2 glow discharge [95]. A possible explanation is that the porous glass disk gets negatively charged, which creates kind of a sheath despite the fact the the discharge current can still flow through the pores but this remain unclear.

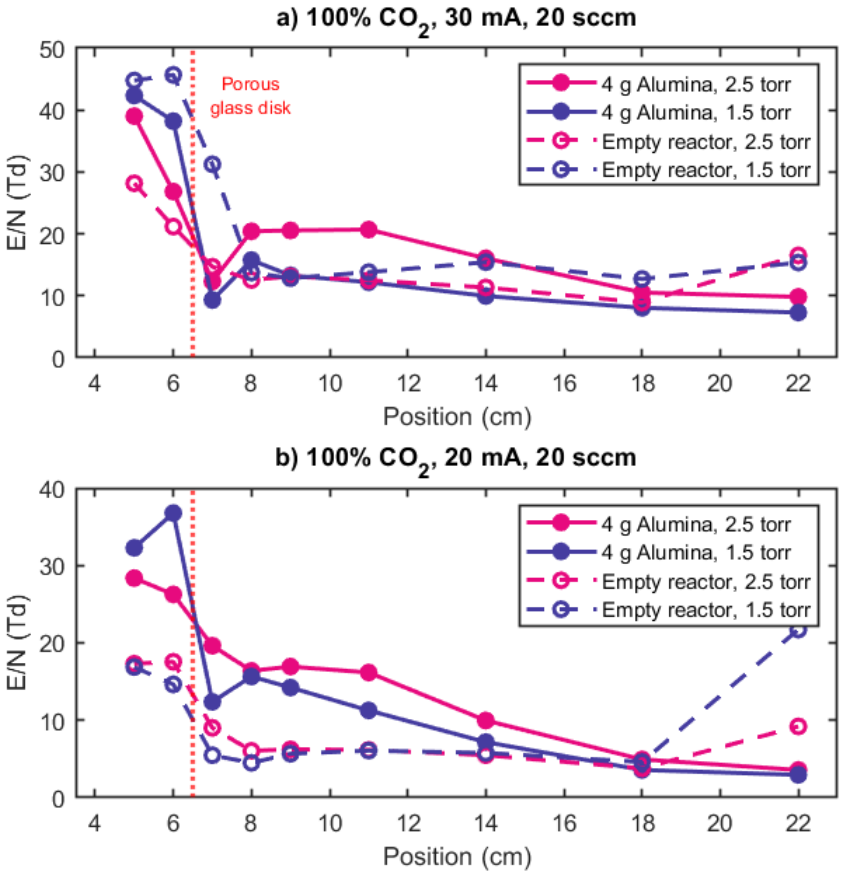

Figure 7.10: Reduced electric field alone the plasma region in the FB-GD reactor in 100%CO_2 at a) 20 and b) 30 mA for empty reactor and with 4 g of Al_2O_3. Pressure: 2.5 and 1.5 Torr (after the disk).

After the porous glass disk (position above 6.5 cm), the E/N is reduced by more than half (at 30 mA) or by a third (20 mA) in all pressures and with/without Al_2O_3 particles. The absolute values of E/N found are all between 4 and 22 Td which is way lower than the E/N measured with floating potential probe in our regular CO_2 glow discharge. Indeed, for 2 Torr and 30 mA, the E/N should be around ~65 Td. This large discrepancy on absolute values is a limitation of the line ratio method used for estimating the E/N. Indeed, the ratio k_e^{O777}/k_e^{O844} is only varying by a factor 2 when E/N varies from 20 to 200 Td. The precision on the measured ratio I_O^{777nm}/I_O^{844nm} is then not sufficient (even when taking into account the intensity calibration of the optical system) to obtain accurate absolute values. Nevertheless, the relative values are still valid. If the measured E/N is decaying, it actually correspond to a real decay.

An interesting effect occurs in the region between 8 and 14 cm along the reactor where the E/N goes from 16 Td to 6 Td with 4 g of Al_2O_3 while it remains quasi constant in the empty reactor. This is markedly observed more at 20 mA (figure 7.10b). The charge loss could be particularly strong in the lower region (below 14 cm) because of the presence of the Al_2O_3 particles. The density of Al_2O_3 particles is the highest in this region increasing the charge losses. The electric field strength must then increase to sustain the plasma. Such effect has already been reported in fluidized bed-DBD reactor with alumina powders [56]. Then, the E/N is similar in 4 g and empty reactor in the region around 14 and 18 cm where the particle density becomes small. At 22 cm the electric field in the empty reactor seems to increase which is probably due to the proximity of the electrode (the optical fiber is probably facing too much the inside of the hollow cathode), but the absence of this effect with particles remains unclear.

Despite the large uncertainty of the line ratio method to determine the E/N, these results seems to confirm an expected fact: the presence of a large density of Al_2O_3 particles tends to enhance the E/N in the lower part of the reactor. The axial profile of E/N is then decreasing with the position.

Going back to the observation made on figure 7.9, the decay of E/N should correspond to a decay of the normalized Angström band area. Indeed the ratio of the excitation rate coefficient for the $CO(B^1\Sigma^+)$ state responsible for the Angström band and the Argon line at 750 nm should increase with the E/N Therefore we can probably relate the increase in intensity of CO Angström band towards the exit of plasma region with an increase in the CO density. To confirm that CO density at the exit of the plasma is higher in presence of particles than without, FTIR measurements are performed downstream the reactor.

7.3.4 Dissociation of CO_2

The downstream gas of the plasma reaction in the fluidized bed - glow discharge was analyzed by FTIR spectroscopy and fitted to obtain CO and CO_2 fractions. The conversion of CO_2 is calculated with equation 7.3.

$$Conversion\ of\ CO_2\ (\%) = \frac{[CO_2]_{in} - [CO_2]_{out}}{[CO_2]_{in}} * 100 \tag{7.3}$$

Conversion of CO_2 is shown in figure 7.11 as a function of a) pressure and b) current for 100%CO_2 plasma with 4 g and 1 g of Al_2O_3 and the empty reactor. Generally, the dissociation of CO_2 is almost constant as function of pressure with or without particles or at least no clear trend can be seen on the limited range of pressure variation allowed by our setup. In the meantime, when the conversion is compared as a function of current, the dissociation is increased as expected. In both comparisons (as a function of pressure and current), the higher conversions are achieved with 4 g of Al_2O_3 in the FB-GD reactor with a maximum of 35% at 30 mA and the lowest at 13% in the empty reactor at 12 mA. Clearly, the more particles are added, the higher the conversion of CO_2 is for all pressures and currents. The plasma being constrained by the particles as seen in figure 7.12a), one could have thought that part of the gas would go through the reactor without seeing the plasma but the conversion seems more efficient. To check if the reduction in the volume of the plasma region can have an effect on the dissociation of CO_2, additional measurements are made in a 1 cm diameter glow discharge tube (see figure 7.12b). By reducing the inner diameter of the glow discharge tube, the current density is increased like we suppose it happens in the fluidized bed when the negatively charged particles repel the plasma.

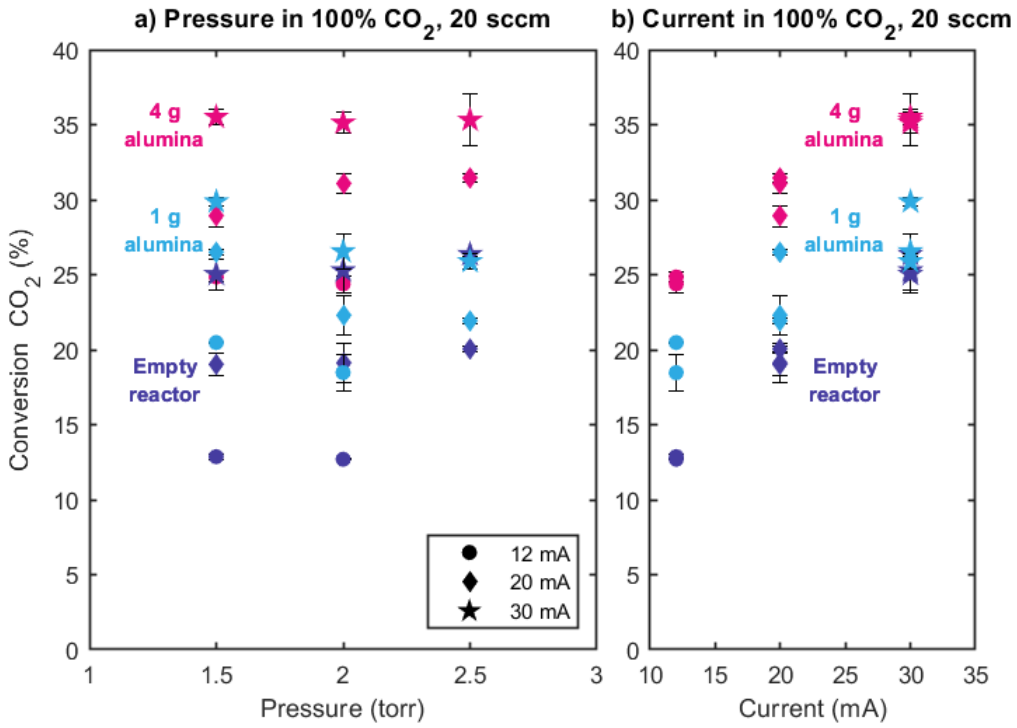

Figure 7.11: Conversion of CO_2 as a function of a) pressure and b) current for the empty reactor, 1 g of alumina and 4 g of alumina in the fluidized bed - glow discharge in 100%CO_2. Total flow rate: 20 sccm. Error bars represent the +/- standard deviation.

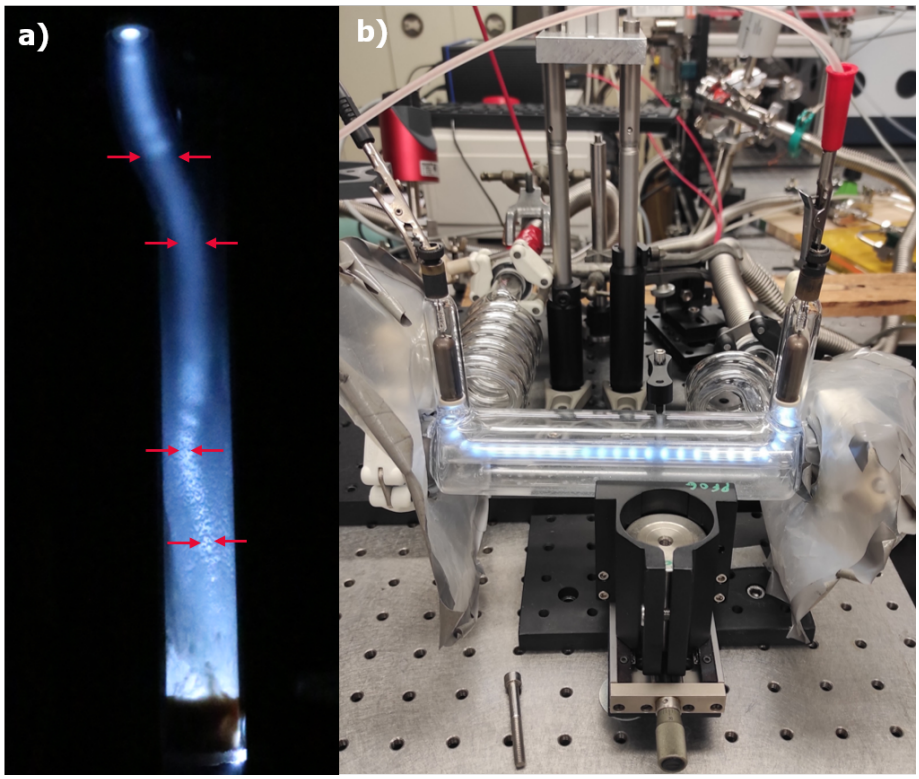

Figure 7.12: Pictures of a a) 2 cm diameter FB-GD with Al_2O_3 particles and b) 1 cm diameter regular Glow discharge.

To facilitate the comparison amongst the two reactors (FB-GD) with particles and 1 cm inner diameter regular glow discharge), the applied current was adjusted to keep similar Surface Current Density (SCD) in mA/cm^2:

$$SCD = \frac{Current\ (mA)}{Area_{reactor}\ (cm^2)} \tag{7.4}$$

With an inner diameter of 2 cm, the section of the tube in the FB-GD reactor is 3.14 cm^2 and the resulting SCD is 3.81, 6.36 and 9.54 mA/cm^2 for the 12, 20 and 30 mA currents studied. In consequence, the applied current in the 1 cm diameter glow discharge were 3, 5 and 7.5 mA to match the same SCD. Figure 7.13 shows the conversion of CO_2 as function of the surface current density for empty reactor in FB-GD of 2 cm diameter, with 1 and 4 g of Al_2O_3 in FB-Glow and 'regular' Glow discharge of 1 cm diameter.

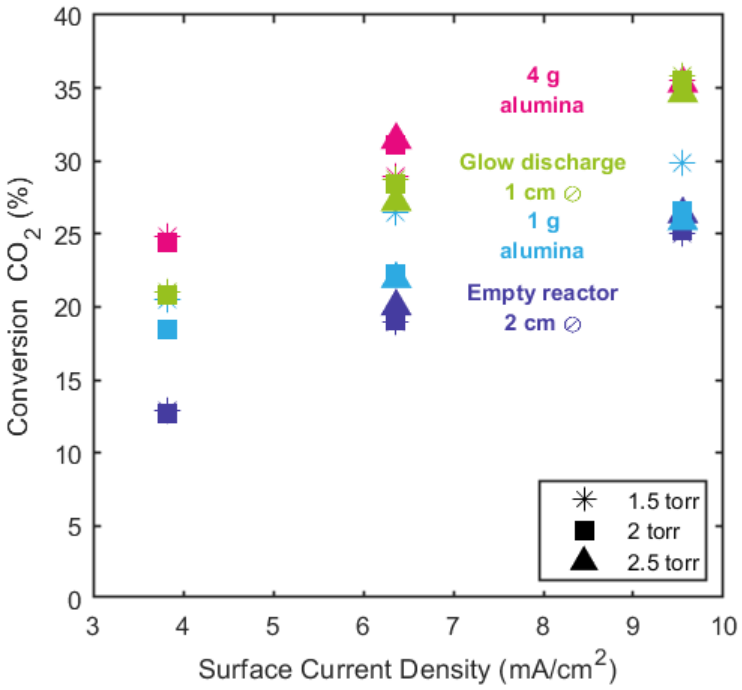

Figure 7.13: Conversion of CO_2 as a function of Surface Current Density (mA/cm^2) for FB-GD reactor of 2 cm diameter empty, with 1 or 4 g of alumina, and for empty glow discharge reactor with 1 cm diameter in 100%CO_2 plasma. Total flow rate: 20 sccm.

Similarly to what is observed in previous figures, empty FB-GD reactor results in the lowest conversion from the four cases. Following 3.8 mA/cm^2 at 2 Torr, we can observe that the conversions go from 12, 18, 20 and 24% for empty reactor, 1 g alumina, glow discharge 1 cm diameter and 4 g alumina, respectively. Although, towards 9.5 mA/cm^2, the difference amongst them becomes more clear: 4 g of alumina and glow discharge 1 cm diameter give the same conversion, ~34% while 1 g of alumina and empty reactor have around 25%. This comparison tell us that the constriction of the plasma region caused by the presence of the fluidizing Al_2O_3 particles is one of the main mechanism that enhances the conversion on the fluidized bed - glow discharge reactor given the little catalytic activity of Al_2O_3 alone. The question remains as to why a higher surface current density results in a higher conversion, when part of the gas flow is not directly in the plasma in the FB-GD case. It is not due to a higher gas temperature since in the FB-GD we have measured the same temperature with and without particles. The effect of higher

current density on the CO_2 conversion remains unclear but it is interesting to note that at atmospheric pressure, spark discharges (having a larger current density) have demonstrated higher conversion than DBD or corona in pure CO_2 despite a much higher gas temperature which should favour back reaction mechanisms [159–161].

7.3.5 Catalytic testing

Once the plasma has been studied under the interaction with an inert material as bare alumina, the FB-GD is tested with other materials with a catalytic activity. Alumina is a catalytic material tested in other fluidized bed plasma reactors for CO_2 conversion [54–56]. Commercial CeO_2 used in II has not been evaluated in this chapter because this material is in the nano scale range. When added to the reactor and flown 20 sccm of gas flow rate, channels were created and the powder was not fluidized. This material has fine solids and belongs to Geldart group C (see figure2.21 from chapter 2). Therefore, to evaluate the catalytic activity of CeO_2 in the fluidized bed, the commercial alumina tested throughout this thesis was impregnated with CeO_2. 30% wt CeO_2/Al_2O_3 was prepared at Instituto de Carboquimica in Zaragoza, Spain specifically for this work. In addition, tests where performed with commercial catalyst 10% wt Ni/Al_2O_3 (called 'IBERCAT') as this material is later tested for CO_2 methanation in FB-DBD (chapter 9). The material was tested as it was (called 'not reduced') and after a pretreatment with 25%-75% of H_2-Ar plasma with total flow rate of 57 sccm for 90 min (called 'reduced'). Figure 7.14 shows the conversion of CO_2 as a function of SCD in empty reactor, with 4 g of Al_2O_3, 10%Ni/Al_2O_3 and 30%CeO_2/Al_2O_3 in 100%CO_2 plasma.

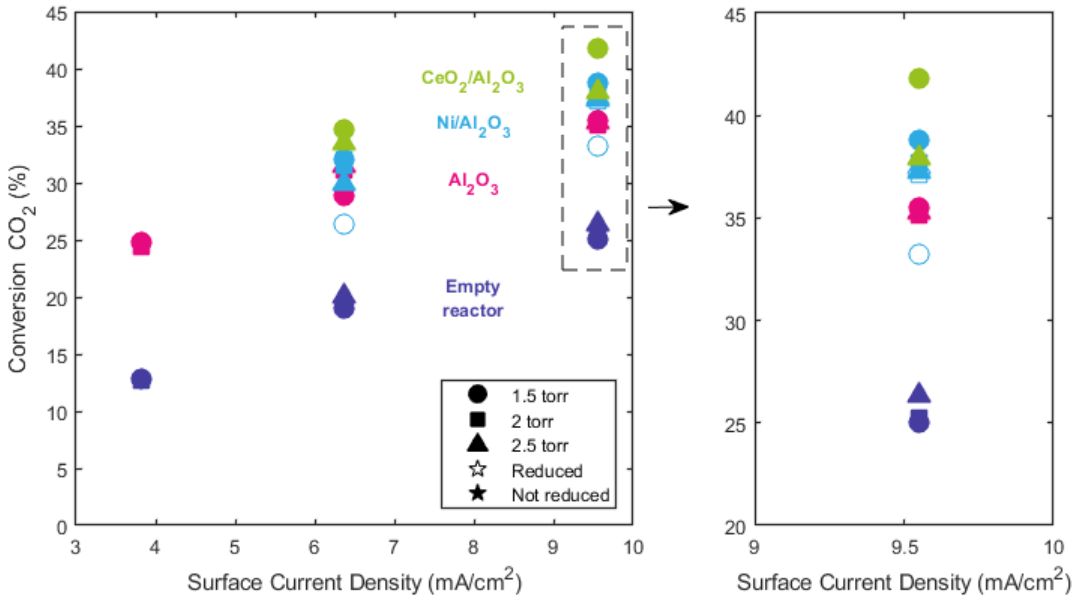

Figure 7.14: Conversion of CO_2 as a function of Surface Current Density (mA/cm^2) for FB-GD in empty reactor (dark blue), with 4 g of Al_2O_3 (pink), 10%Ni/Al_2O_3 (light blue) and 30%CeO_2/Al_2O_3 (green) in 100%CO_2 plasma at different pressures. The dashed line square represents the zoom made to the data later displayed in the right. Filled symbol: not reduced; empty symbol: reduced with H_2-Ar plasma for 90 min. Total flow rate: 20 sccm.

The order of the higher conversion goes as follows: CeO_2/Al_2O_3 > Ni/Al_2O_3 not reduced > Ni/Al_2O_3 reduced ~ Al_2O_3 > empty reactor (plasma only). CeO_2/Al_2O_3 resulted in 42% conversion of CO_2 at 1.5 torr and 30 mA plasma current. This improved conversion has been attributed to redox properties due

to oxygen mobility in ceria compared to other metal oxides as alumina [90]. It is worth to mention that Ni/Al_2O_3 not reduced gave better performance in terms of conversion in contrast to the reduced one. Perhaps the metallic Ni was deactivated during the plasma reaction and no more CO_2 was adsorbed. This remains as an hypothesis given that the material was not subsequently tested and compared before and after plasma reaction. Further studies are need to elucidate the role of Ni on the conversion of CO_2.

7.4 CO_2-CH_4 plasma in FB-GD

The goal of this section is to present results obtained by the addition of methane to the initial gas mixture as it has been done in previous chapters. The comparison helps to discuss the effect of CO_2-CH_4 plasma with fluidizing particles and viceversa. However, the same concentrations of CO_2-CH_4 tested in chapter 3 and 5 cannot be reproduced here. We attempted to realize tests using 70%CH_4-30%CH_4 plasma but we encountered several problems. Figure 7.15 shows a picture of the FB-GD during 70%CH_4-30%CH_4 plasma and after. As seen, dark spots started to appear in the porous glass disk strongly indicating carbon deposition. Also, the pressure after the disk was increasing and it was difficult to stabilize. This could be due to the high current density at the porous glass disk. Consequently, we reduced as much as possible the amount of CH_4 in the initial gas mixture to 5% without further problems. Hereinafter, 95%CO_2-5%CH_4 concentration is studied and reported here.

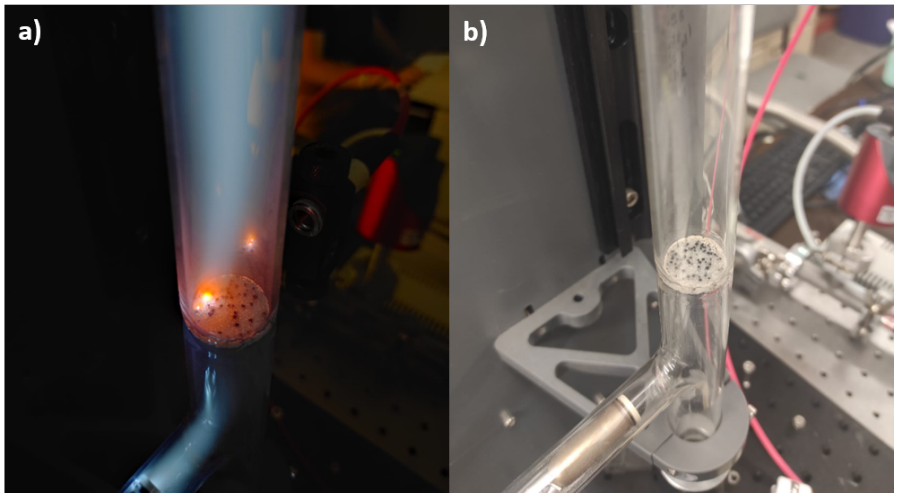

Figure 7.15: Pictures of the FB-GD a) during 70%CH_4-30%CH_4 plasma and b) after plasma.

7.4.1 Gas temperature in CO_2-CH_4 plasma

The gas temperature was estimated from the CO Angström band in the same way as done in the previous section for CO_2 plasma. Figure 7.16 shows the gas temperature across the FB-GD comparing 100%CO_2 plasma and 95%CO_2-5%CH_4 plasma for 1.5 and 2.5 Torr.

With the addition of CH_4, in the regular glow discharge, the gas temperature is lower because of higher thermal conductivity of CH_4 and mostly H_2. Here, 5%CH_4 is not enough to significantly and generally reduce the temperature.

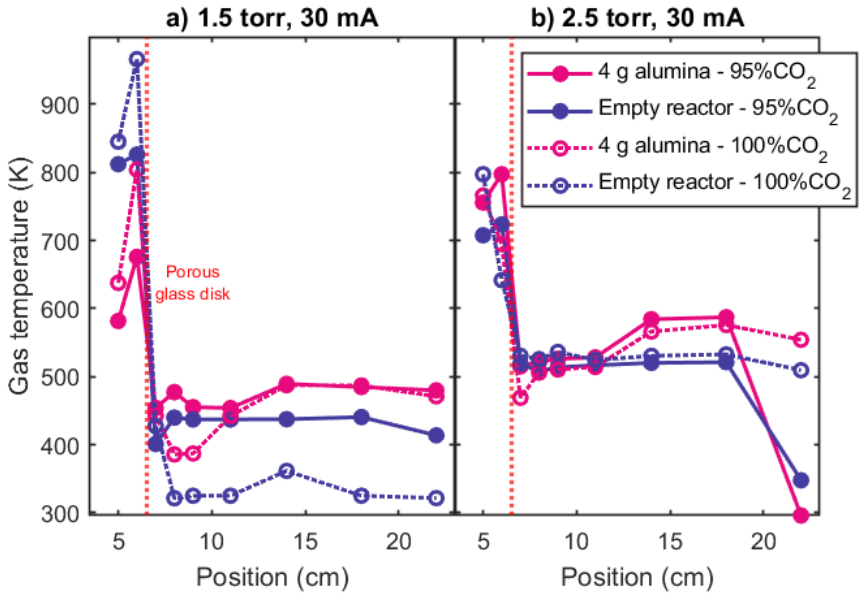

Figure 7.16: Gas temperature along the FB-glow reactor at a) 1.5 Torr and b) 2.5 Torr for 95%CO_2-5%CH_4 plasma (solid line) and 100%CO_2 plasma (dotted line). Current: 20 mA. Total flow rate: 20 sccm.

Yet, we can observe several trends:

- As expected temperature is always higher at higher pressure. This is quite evident for the empty reactor from 1.5 Torr to 2.5 Torr with the same current.
- There is no significant increase of temperature with the addition of alumina particles for both gas mixtures even with increasing pressure.
- Temperature seems stable after the porous glass disk around 9 cm and beyond. However, in the last position at 2.5 Torr, there is a significant reduction of the temperature to ∼320 K.

In case of empty reactor with 100%CO_2 and 95%CO_2, there is 100 K difference at 1.5 Torr. This difference does not persist at 2.5 Torr with the same current. The reason behind this increment is not clear but this could indicate that the pressure plays a role on the empty reactor. With 4 g of alumina, the gas temperatures remain the same.

7.4.2 H_α

The H_α line at 656 nm can help us trace the dissociation of CH_4. Figure 7.17 shows the I_{H656}/I_{Ar750} along the FB-GD reactor at 1.5 and 2.5 Torr and 30 mA plasma current.

It is interesting to observe how the I_{H656}/I_{Ar750} increases across the reactor reaching a maximum close to the upper electrode. In the case of alumina, the ratio is lower than empty reactor just after the glass disk but at 9 cm the ratio is significantly higher than empty reactor. This increase in the intensity of H emission line is probably related to an increased conversion of CH_4. The same has been observed previously for the CO Angström band and conversion of CO_2 in pure CO_2 plasma (figure 7.9). The lower H intensity just above the porous glass disk with the 4 g of alumina could be the result of a higher atoms recombination on the Al_2O_3 particles.

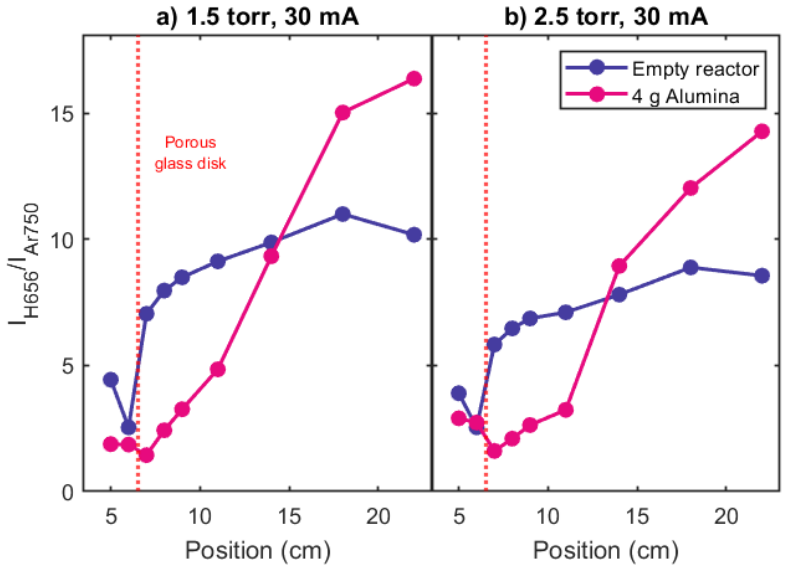

Figure 7.17: I_{H656}/I_{Ar750} along the FB-GD reactor at a) 1.5 Torr and b) 2.5 Torr for 95%CO_2- 5%CH_4 plasma at 30 mA. Total flow rate: 20 sccm.

7.4.3 CO Angström band in CO_2-CH_4 plasma

CO concentration follows the dissociation of CO_2 and the oxidation of CH_4 and byproducts in the plasma. Figure 7.18 shows the ratio of $I_{COAngström}/I_{Ar750}$ across the FB-GD for 95%CO_2-5%CH_4 plasma at 2.5 and 1.5 Torr for empty reactor and 4 g of Al_2O_3.

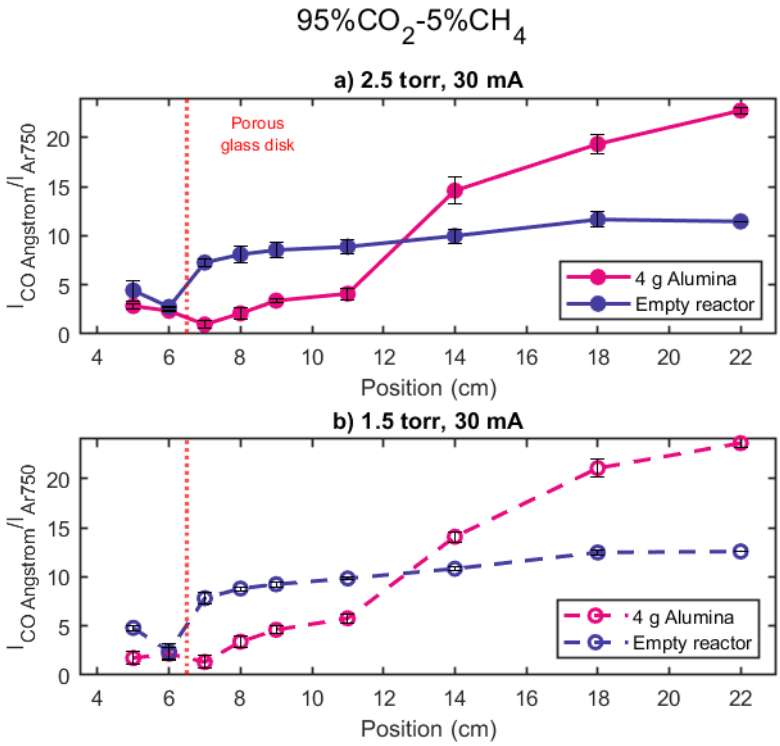

Figure 7.18: Ratio of $I_{COAngström}/I_{Ar750}$ intensity across the FB-GD for 95%CO_2-5%CH_4 plasma at a) 2.5 Torr and b) 1.5 Torr for empty reactor and 4 g of Al_2O_3. Total flow rate: 20 sccm. Current applied: 30 mA.

The trend is the same as observed for H656 in the previous subsection and as in figure 7.9 for pure CO_2 plasma. We assume a real increase in CO density enhanced by the presence of the Al_2O_3 particles in contrast to empty reactor. This is further discussed in the following section.

7.4.4 Conversion of CO_2 and CH_4

The fludization of particles increases the conversion of CO_2 either by constraining the plasma region and expanding the surface area where O atoms can recombine. The recombination of O can provide an advantage to CH_4 decomposition. 5% was added to the gas mixture and tested through different currents and pressures. Figure 7.19 shows the conversion of CO_2 and CH_4 as a function of surface current density for empty reactor and with 4 g of Al_2O_3.

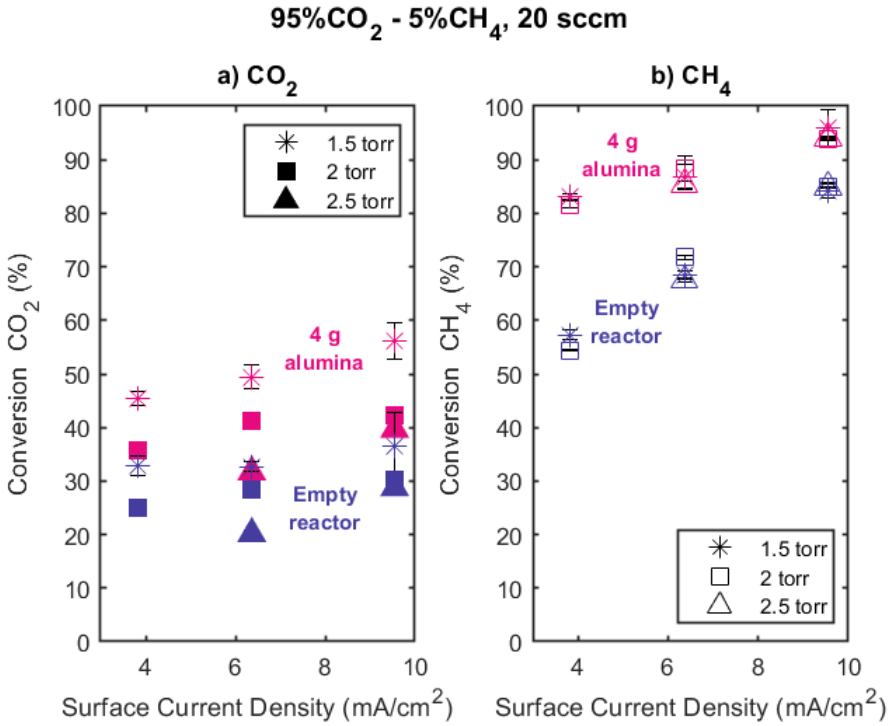

Figure 7.19: Conversion of a) CO_2 and b) CH_4 as a function of SCD in 95%CO_2-5%CH_4 plasma in FB-GD with 4 g of Al_2O_3 particles (pink) and empty reactor (dark blue) at 1.5, 2 and 2.5 Torr. Error bars represent +/- standard deviation of 3 experiments with multiple measurements.

Methane and carbon dioxide conversion are higher in the presence of 4 g of Al_2O_3 particles in comparison to the empty reactor across all conditions of pressure and current tested. Evidently, increasing current and decreasing pressure resulted in increased conversion of both reactants. However, the pressure does not seem to affect the conversion of CH_4 given that the three pressures tested give similar results (94% for 9.81 mA/cm^2 (30 mA) with 4 g of alumina). Regarding CO_2, the pressure seems to affect the most the conversion increase at 1.5 Torr with 58% and 42% for 2 and 2.5 Torr with 4 g of Al_2O_3. The variation seems larger in the case of fluidizing Al_2O_3 particles.

To continue the investigation on CO density from the CO Angström band emission line seen in previous section, the yield was calculated for CO:

$$Yield\ of\ CO\ (\%) = \frac{[CO]_{out}}{[CO_2]_{in} + [CH_4]_{in}} * 100 \tag{7.5}$$

We can see that the CO concentration follows the same trend as CO_2 and CH_4 conversion (figure 7.20):

- Final CO density in the downstream gas increases with 4 g of Al_2O_3 than plasma only.
- The concentration of CO increases with surface current density for empty reactor and 4 g of alumina.

This behaviour is consistent with the trends observed in the ratio of $I_{COAngström}/I_{Ar750}$.

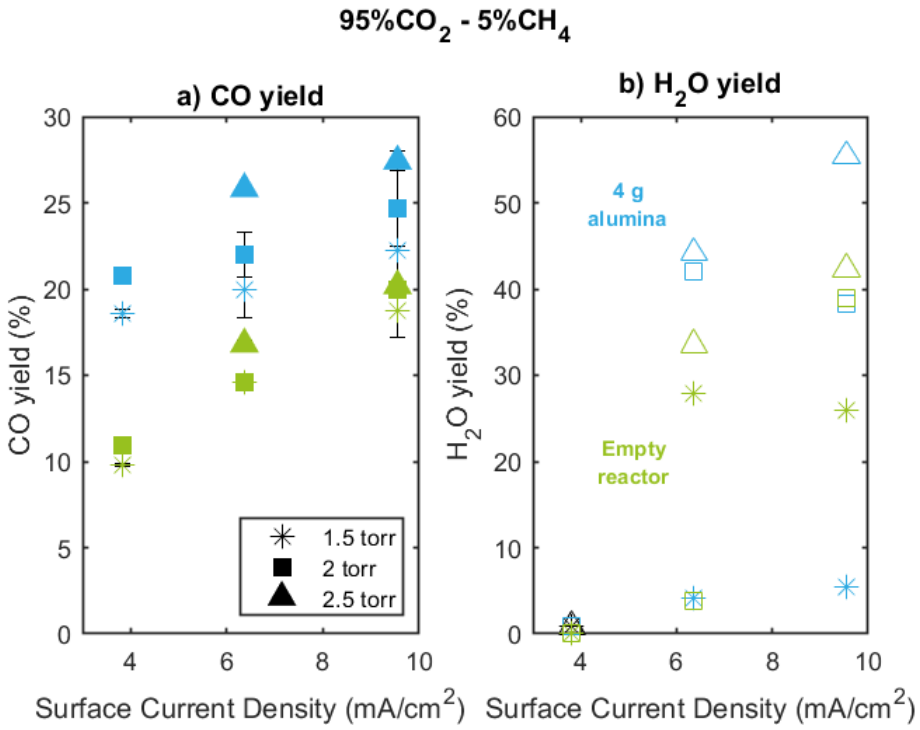

Figure 7.20: Yield of a) CO and b) H_2 as a function of SCD in 95%CO_2-5%CH_4 plasma in FB-GD with 4 g of Al_2O_3 particles (green) and empty reactor (light blue) at 1.5, 2 and 2.5 Torr. Error bars represent +/- standard deviation of 3 experiments with multiple measurements.

Water is a byproduct of the reaction but the more likely product to be formed rather than H_2 due to the low concentration of methane. C_2 molecules are not expected at such low concentration of methane. Water yield was calculated from H_2O density obtained from the IR spectra:

$$Yield\ of\ H_2O\ (\%) = \frac{2[H_2O]_{out}}{4[CH_4]_{in}} * 100 \tag{7.6}$$

Although, the trend is a bit different for water yield. Low SCD (3.82 mA/cm^2) results in almost no water. Above than that few points are noted:

- At 6.36 and 9.54 mA/cm^2, ~26% yield is obtained at 1.5 torr with empty reactor. With 4 g of Al_2O_3, the yield is around 5%.
- This trend inverts and by increasing the pressure 4 g results in higher yields than empty reactor.

This could indicate that higher pressure and in the presence of alumina particles, water formation is pushed forward, but at low pressure, the particles do not help to form water. H_2 is expected to be formed instead of water only if enough H atoms are present in the mixture.

According to the 0D model developed in [87], we can draw some hypothesis of what could be occurring at this particular gas mixture. For H_2O formation in empty reactor (plasma only), the main mechanism is:

$$CH_2O + OH \longrightarrow H_2O + HCO$$

and decreases with pressure as seen in figure D.2 from Appendix D. And the main mechanism for H_2 loss is:

$$H_2 + OH \longrightarrow H_2O + H$$

which decreases with increasing pressure (figure D.1). However, when the alumina particles are added, the contribution of surface recombination could become more predominant at 1.5 torr:

$$H + H_{ads} \longrightarrow H_2$$

along with the simultaneous loss of water:

$$O(^1D) + H_2O \longrightarrow 2OH$$

$$e^- + H_2O \longrightarrow e^- + OH + H$$

However, at 2.5 torr, the destruction of H_2 could be in competition with CH_2O:

$$H_2 + OH \longrightarrow H_2O + H$$

$$CH_2O + OH \longrightarrow H_2O + HCO$$

Again, these are hypothesis based on a model designed for plasma kinetics only and not for plasma-surface. However, it can provide some conjectures on the contribution of an extended surface available for chemical processes.

Comparison of CO_2 conversions

Interestingly, CO_2 conversion was much higher in 95%CO_2-5%CH_4 plasma in comparison to 100%CO_2 plasma. Figure 7.21 displays the difference in both cases. At 6.3 mA/cm^2 (20 mA), the conversion of CO_2 with 4 g of Al_2O_3 particles at 2.5 Torr the conversion is ~30% for both plasmas (95%CO_2-5%CH_4 and 100%CO_2). However, at 1.5 Torr with 95%CO_2-5%CH_4 the conversion results is almost 50% while in the same conditions but in pure CO_2 plasma the conversion is barely 30%. It has been shown that in our condition, the main back reaction mechanism in pure CO_2 plasma is CO($a^3\Pi$) + O_2 giving CO_2 + O(^{3}P). This mechanism could be hindered either because the CO($a^3\Pi$) state is quenched or consumed in reactions with hydrogenated species, or because the O_2 molecules are strongly reduced in presence of CH_4 as shown in chapter characterization. However with 5% CH_4, another back reaction mechanism can occur with CO + OH producing back CO_2 and H. The OH species could react on Al_2O_3 particle to produce more water as seen on figure 7.20. If the back reaction mechanism forming back CO_2 is lower, its conversion is higher.

This could also be explained by the increase in H atom density. When we look at the H atom in 4 g of alumina, the signal is larger towards the exit of the reactor in comparison to empty reactor (figure 7.17). Probably due to charge loss leading to an increase in the electric field which could give more energetic electrons for the dissociation and therefore more conversion of CO_2 and CH_4 resulting in more H atoms towards the exit of the reactor. These conjectures remain only as hypothesis and more investigations would be needed to clarify the role of H atoms and alumina particles in the increase of conversion of CO_2. Nonetheless, the addition of 5%CH_4 in the gas mixture has markedly an effect on the conversion of CO_2.

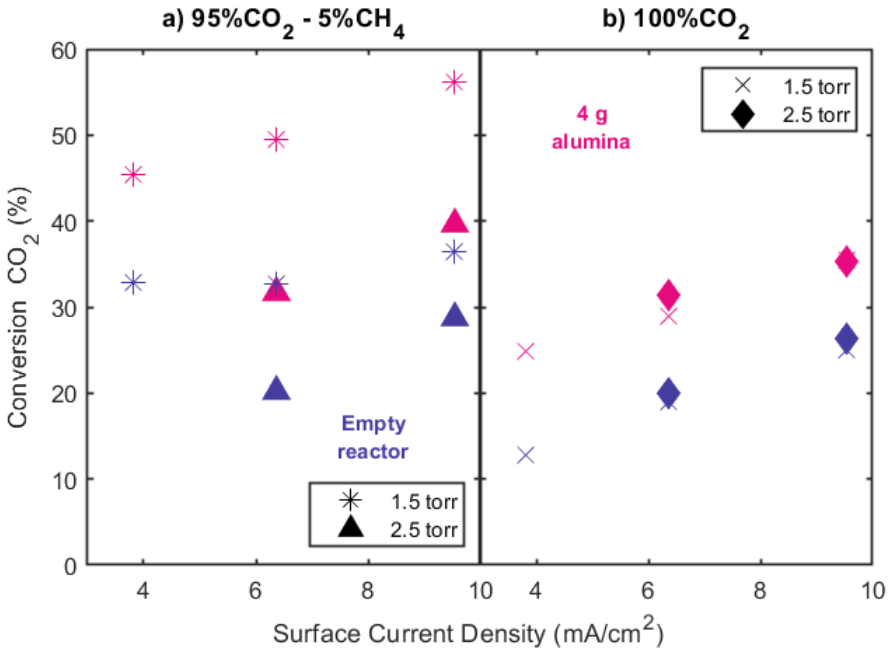

Figure 7.21: Conversion of CO_2 in a) 95%CO_2-5%CH_4 plasma and b) 100%CO_2 plasma as a function of SCD (mA/cm^2) in FB-GD reactor with 4 g of Al_2O_3 particles (pink) and empty reactor (dark blue) for 1.5 and 2.5 Torr. Total flow rate: 20 sccm.

7.5 CO_2-H_2 plasma in FB-GD

Another interesting reaction for CO_2 recycling is CO_2 methanation which is an exothermic reaction in standard conditions:

$$CO_2 + 4\,H_2 \rightleftharpoons CH_4 + 2\,H_2O \qquad \Delta H_{298K} = -165\ \text{kJ/mol}$$

15% wt Ni-30% wt CeO_2/Al_2O_3 catalyst was tested for 20%CO_2-80%H_2 plasma. The catalyst was prepared at the Instituto de Carboquimica, Zaragoza, Spain. The same procedure was followed as in previous gas mixtures. Figure 7.22 shows the gas temperature, ratio of I_{O777}/I_{Ar750}, ratio of I_{H656}/I_{Ar750} and ratio of $I_{CO\ Angström\ bands}/I_{Ar750}$ for 20%CO_2-80%H_2 plasma. Some points in the plots are missing because the data treatment was not possible in such points as the black catalyst was attached to the wall under plasma conditions. This effect prevented to obtain enough UV-Visible light emission for measurement. However, the trends are clearly observed in figure 7.22.

Several points are worth remarking:

- The gas temperature obtained by the fitting of the rotational vibration of CO for the four conditions

presented here is around 300-350 K. Very low compared to pure CO_2 plasma which is around 350-550 K (figure 7.6).

- The ratio I_{O777}/I_{Ar750} decreases after the porous glass disk as observed in previous plasma mixtures. Some increase in the ratio is observed with the empty reactor at 1.5 Torr.
- The ratio I_{H656}/I_{Ar750} is nearly zero with the catalyst.
- The ratio $I_{CO\ Angström\ bands}/I_{Ar750}$ increases along the tube similarly to previous results.

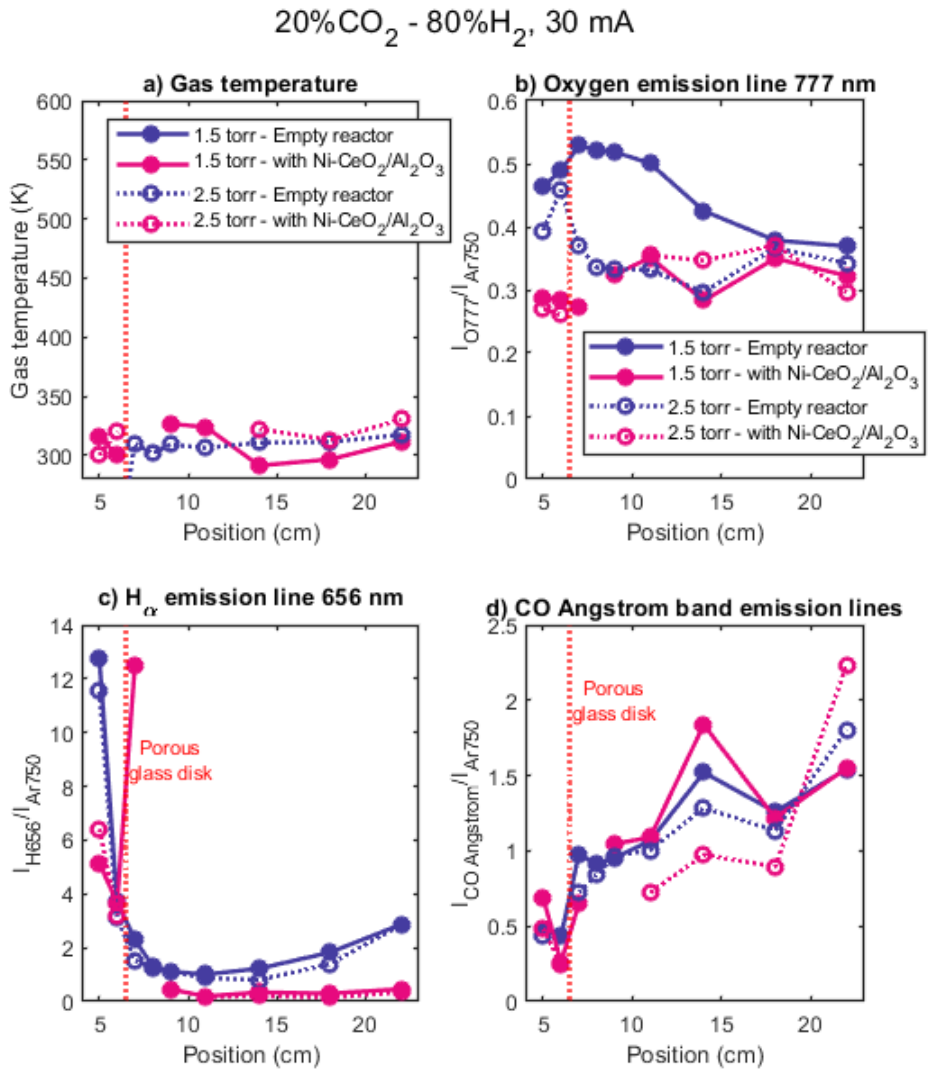

Figure 7.22: a) Gas temperature, b) ratio of I_{O777}/I_{Ar750}, c) ratio of I_{H656}/I_{Ar750} and d) ratio of $I_{CO\ Angström\ bands}/I_{Ar750}$ of 20%CO_2-80%H_2 plasma with 15%Ni-30%CeO_2/Al_2O_3 catalyst and empty reactor (plasma alone). Plasma current: 30 mA, total gas flow: 20 sccm.

The gas temperature is expected to be low due to the presence of large quantities of H/H_2 in the gas/plasma which help to dissipate the heat to the wall due to the large thermal conductivity of these species. This is aided by the fludization of the catalyst. However, CO_2 methanation is an exothermic reaction unless other reactions are taking place instead like Reverse Water-Gas-Shift (RWGS).

The downstream gas was analysed by FTIR spectroscopy to know the fractions of the main products of 20%CO_2-80%H_2 plasma reaction. The conversion of CO_2 was calculated as in previous sections. Yield of CO, CH_4 (carbon based) and H_2O (oxygen based) was calculated by the following equations:

$$Yield\ of\ CO\ (\%) = \frac{[CO]_{out}}{[CO]_{in}} * 100 \tag{7.7}$$

$$Yield\ of\ CH_4\ (\%) = \frac{[CH_4]_{out}}{[CO_2]_{in}} * 100 \tag{7.8}$$

$$Yield\ of\ H_2O\ (\%) = \frac{[H_2O]_{out}}{2[CO_2]_{in}} * 100 \tag{7.9}$$

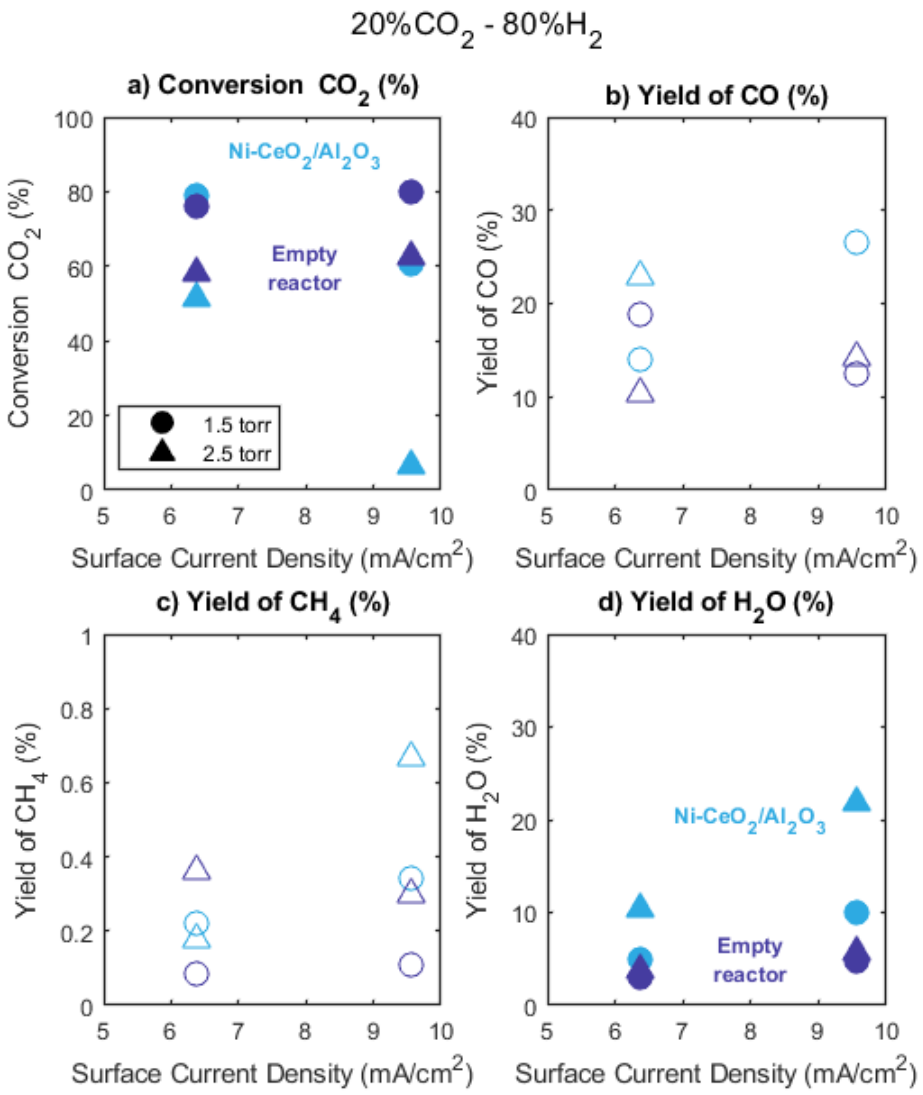

Figure 7.23: a) Conversion of CO_2, b) yield of CO, c) yield of CH_4 and, d) yield of H_2O of 20%CO_2-80%H_2 plasma with 15%Ni-30%CeO_2/Al_2O_3 catalyst and empty reactor (plasma alone) at 1.5 and 2.5 torr. Total gas flow: 20 sccm.

The results are shown in figure 7.23 as a function of surface current density to ease the comparison with the other sections.

- The conversion of CO_2 seems to be very similar in empty reactor and with 15%Ni-30%CeO_2/Al_2O_3 catalyst across the conditions tested.
- With the catalyst, the CO yield resulted slightly higher than plasma alone but besides that the yield ranges 10 - 30 % in the conditions tested.
- The absorption bands corresponding to methane were barely observed in the IR spectra. The MATLAB treatment script was able to obtain trace fractions after the background subtraction. The yield of methane is below 1% but no clear trend is observed.
- Regarding water, the yield seems higher with Ni based catalyst at 2.5 Torr.

Despite the presence of Ni based catalyst, the reaction proceeded mainly as RWGS:

$$CO_2 + H_2 \rightleftharpoons CO + H_2O \qquad \Delta H_{298K}=42.1 \text{ kJ/mol}$$

Perhaps, the fluidization of the catalyst did not help the CO_2 methanation reaction.

7.6 *In situ* experiments on Al_2O_3

Al_2O_3 is an interesting surface due to the simultaneous acidic and basic characteristics. Widely used in heterogeneous catalysis as a support and prone for strong adsorption of CO_2 and NH_3. *In situ* FTIR transmission experiments were performed in the same manner as the procedure described in section 4.2 but using Al_2O_3 powder instead to prepare a pellet. Figure 7.24 shows the final spectra after each step for CO_2 only at 1 torr.

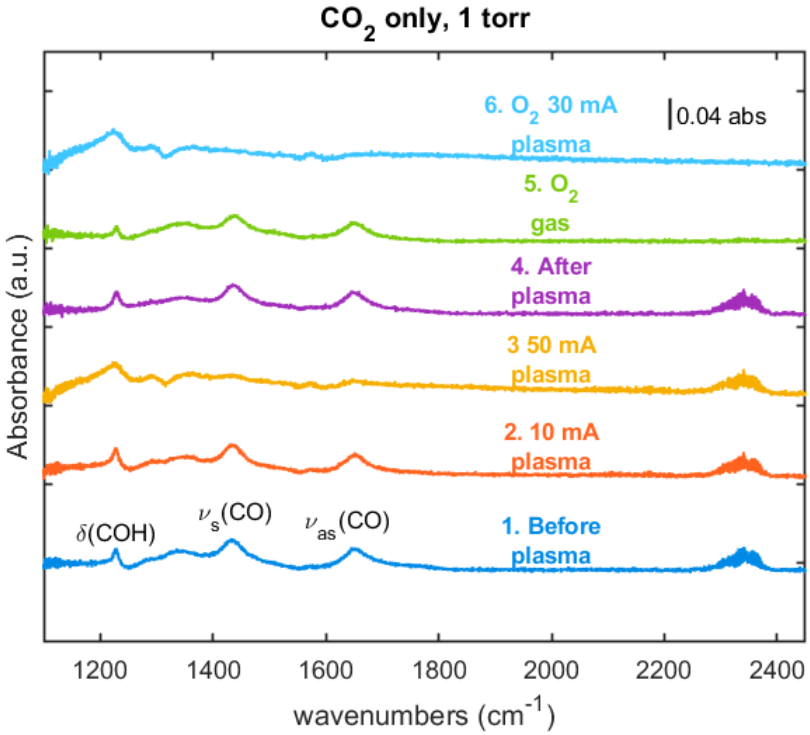

Figure 7.24: *In situ* FTIR transmission spectra of CO_2 adsorbed as bicarbonates species during CO_2 only experiments in Al_2O_3 surface at 1 Torr in the cross DC glow discharge plasma reactor through the experimental sequence (figure 3.12). The spectra displayed corresponds to the final spectrum taken at the end of each step from the experimental sequence. Spectra are offset for clarity.

Three bands were observed upon CO_2 adsorption: 1229, 1432, 1654 cm^{-1}. Looking in the literature, they are assigned to δ(COH), symmetric ν(CO) and asymmetric ν(CO) vibrations, respectively, of bicarbonate species (HC) [132]. No defined bands were observed in the 2700 - 3700 cm^{-1} region attributed to ν(CH) or to hydroxyl groups. The area of the bands assigned to bicarbonates was estimated as described in chapter 3.

These three bands were followed as a function of time for each step. Figure 7.25 shows the evolution. HC are formed quickly during CO_2 gas exposure in (1). The area is reduced slightly at (2) and significantly reduced at (3). This means that bicarbonates are desorbed from the surface during plasma exposure but they are formed again when the plasma is off (4). It seems that it follows the same mechanisms as CO_2 in CeO_2 described in chapter 4. Although, the band at 1229 cm^{-1} does not disappear entirely from the spectra but it does change shape. The band is reduced in intensity but broadens during 50 mA plasma and O_2 plasma step. We can assume that the change in shape would mean that the band does not correspond to bicarbonate species but to another species. In the literature, no specific species was attributed to this particular band but given our experience from part II, we can assume a carbonate species.

Translating these results to what happens in the fluidized bed, we assume that the CO_2 adsorbed during the fluidization of the alumina is limited. There is evidence of HC at 10 mA (∼12 mA in the FB-GD) at 1 Torr but at 20 and 30 mA, these species could be reduced in the surface. Considering that the pellet and the free particles have slightly different amount of adsorption sites available. Perhaps at atmospheric pressure, Al_2O_3 would adsorb more CO_2 in the form of bicarbonates. This same material is tested in chapter 8 and 9 for CO_2 conversion but using DBD reactors.

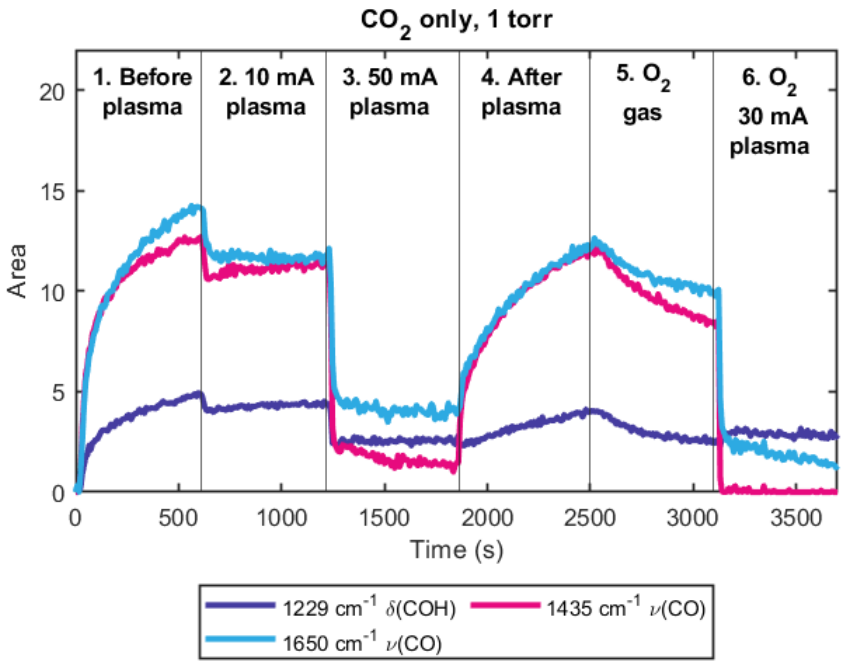

Figure 7.25: Area evolution of 1229, 1435 and 1650 cm^{-1} bands in Al_2O_3 as a function of time in pure CO_2 at 1 Torr in *in situ* FTIR transmission experiments.

7.7 Characterization of Al_2O_3

Al_2O_3 was characterized before and after the experiments performed in the FB-GD reactor. Important parameters in fluidzation are the shape (related to sphericity) and particle diameter (size). SEM analysis was performed to investigate if the particles changed appearance after the long treatment in fluidization (figure 7.26). No apparent change in appearance is observed in these pictures of Al_2O_3 particles before and after plasma.

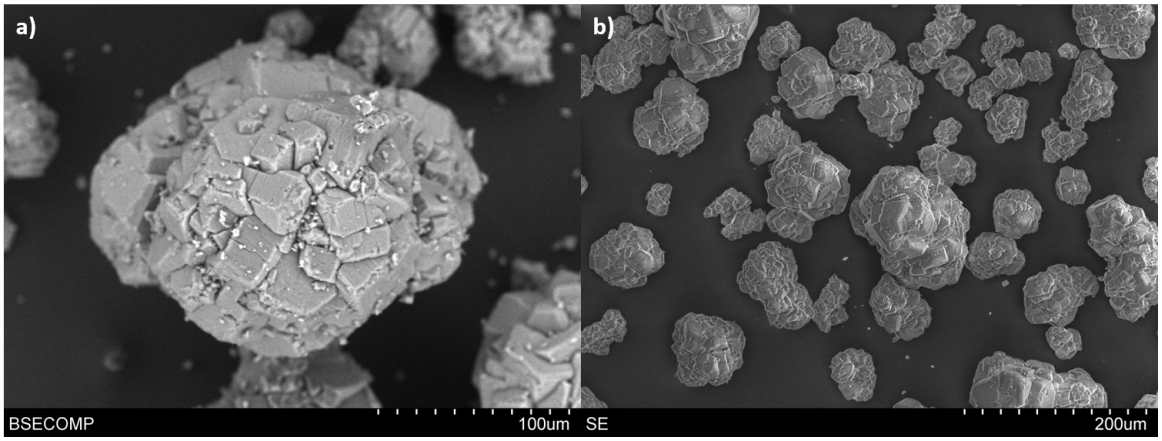

Figure 7.26: SEM analysis of Al_2O_3 a) before and b) after plasma treatment in FB-GD. Analysis carried out by Instituto de Carboquimica in Zaragoza, Spain.

However, the appearance does not rule out a change in size. The supplier of Al_2O_3 particles mentions a size of 105 μm in the specification sheet of the product. Still, the particle size was measured before and after plasma treatment in FB-GD. The particle size analysis results are shown in figure 7.27.

The results present the volume of the sample as a function of the particle diameter. The distribution of the particle diameter has a mode at 105.9 μm for the pristine Al_2O_3. For the Al_2O_3 used after FB-GD experiments, the distribution has changed and now the mode is around 37.97 μm. This reduction on the particle size is expected by attrition of the particles. Attrition refers to the breaking of the parent particle producing smaller particles often called fines (see figure 7.28).

The physical properties of the gas may remain constant in a fluidized process but those of the powder may not. If fines are produced by attrition and are not lost from the system, the fine particles will increase and the overall particle diameter decrease [162]. The fine particles are dangerous for the system as they could leave the reactor and allocate in the gas line through the setup. Nevertheless, a glass wool was installed at the exit of the reactor right after the cyclone to avoid as much as possible the way of fine particles.

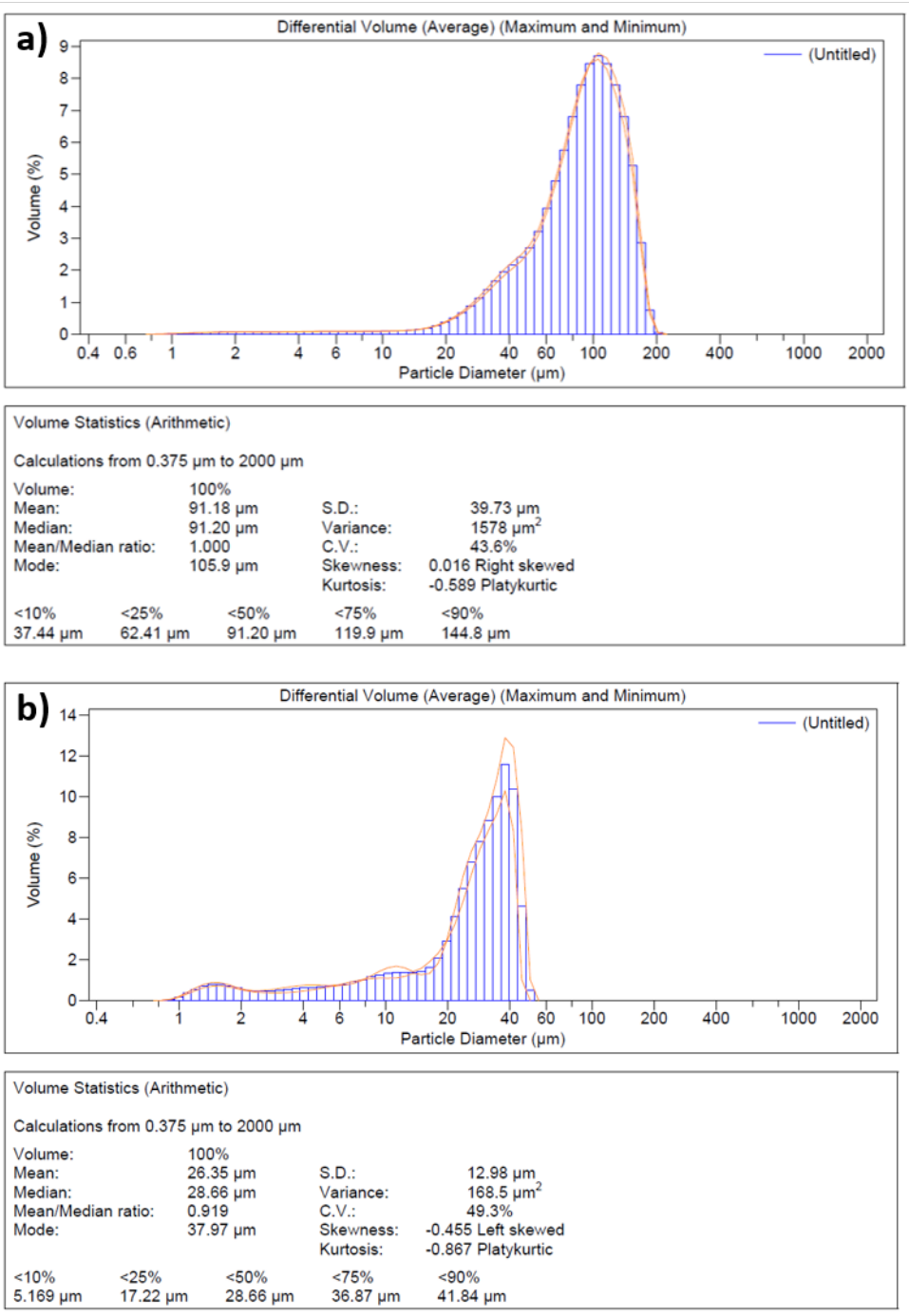

Figure 7.27: Particle size analysis of Al_2O_3 a) before and b) after plasma treatment in FB-GD. Analysis carried out by Instituto de Carboquimica in Zaragoza, Spain.

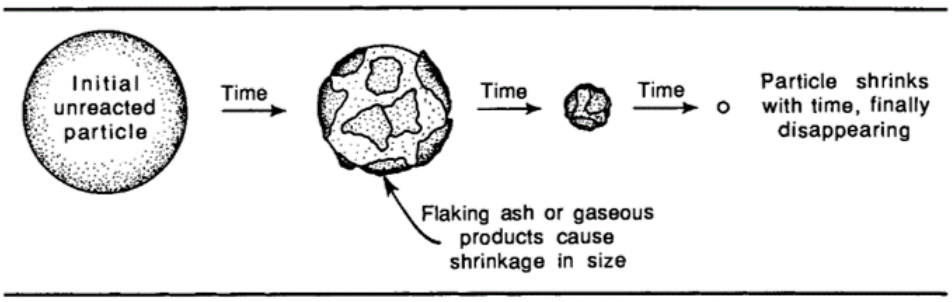

Figure 7.28: Schematic of shrinking of particles through time subjected to fluidization process. Particles shrink by formation of either gaseous product or flaky solid, or by attrition. Figure extracted from [17].

Finally, the specific surface area (SSA) was measured by N_2 physisorption using BET theory. The SSA from pristine alumina was measured to be 160.73 m^2/g and after FB-GD experiments it was reduced to 151.41 m^2/g. A reduction on the particle size should result in larger surface area exposed in equal amount of material.

7.8 Conclusions

Fluidized bed - glow discharge reactor was tested for CO_2 conversion. In pure CO_2 plasma, the gas temperature was measured in empty reactor and with 4 g of alumina and no significant increase in the temperature was observed. This was also compared to previous results obtained in pure CO_2 plasmas. The O atom density decreased simultaneously as the CO Angström band increased. The effect of the electron density and the E/N was considered but the increase in the CO Angström band was truly caused by an increase in CO density. This was later confirmed by conversion of CO_2 estimated from the downstream gas by FTIR spectroscopy. The decrease in the O atoms density in the presence of fluidizing Al_2O_3 particles in the plasma region could be due to the increment in surface area where O atoms can recombine preventing a back reaction to CO_2.

In addition, the enhanced performance of the FB-GD was mostly attributed to the constrain on the plasma volume caused by the fluidization of the alumina particles and demonstrated by testing a 1 cm diameter simple glow discharge.

Due to the high current density located at the porous glass disk, limited amount of methane was able to be added to the initial gas mixture. 95%CO_2-5%CH_4 plasma alone was tested and it resulted in similar gas temperature in the presence of Al_2O_3 particles. Also, it was observed an increase in CO_2 conversion in comparison to only CO_2 plasma. Hindering of the back reaction mechanism remains as an hypothesis and further studies should followed.

In situ FITR transmission experiments demonstrate that Al_2O_3 can absorb CO_2 in the gas phase forming bicarbonates but these are desorbed during high plasma currents. Similar behaviour is expected during experiments in the FB-GD.

Finally, the characterization of the alumina demonstrate that the fluidization of the particles during the experiments cause a shrinking of the particles modifying the physical properties of the bed over time.

Nevertheless, this fundamental study in an innovative configuration represent a step forward to application in standard conditions for CO_2 recycling.

Chapter 8

Catalytic testing of Ceria on Packed bed - DBD

Contents

8.1 Introduction

DBDs are discharges widely used in plasma and plasma-catalysis, especially for CO_2 conversion [163–167]. Plasma-catalysis has been proven to improve the dissociation in comparison to plasma alone. Figure 8.1 shows the data obtained from 74 papers for CO_2 conversion as a function of Specific Energy Input (SEI) in DBD reactors. The data were extracted using the PIONEER database tool developed within the CO_2 PIONEER project. Different CO_2 plasma reactions (CO_2 splitting, CO_2 hydrogenation, reverse water-gas-shift and dry reforming of methane) and different coupling of plasma reactor with catalysts (packed bed and fluidized bed) in DBD reactors are presented in this plot. Despite the differences in operational conditions, reactants and absence or presence of a wide variety of catalysts, it is clear that there is a significant improvement in CO_2 conversion by plasma-catalysis. In average, higher CO_2 conversion can be achieved with lower SEI values with plasma-catalysis in contrast to plasma only.

The most common configuration to test the performance in plasma-catalysis is a packed bed reactor where the catalyst usually remains fixed in the discharge zone. The presence of this catalytic bed modifies the properties of the plasma as much as the plasma modifies the reactions taking place at the surface of the catalyst and both effects must be investigated.

In part II, adsorbed species appearing during plasma-surface interactions were thoroughly described with CeO_2 in glow discharge. The catalytic activity of CeO_2 is now to be tested and compared in packed bed DBD. Two different DBD reactors configurations are used for this testing. First, the coaxial DBD

reactor designed and built in University of Bucharest was tested with CeO_2 used in *in situ* experiments along with other ceria materials synthesized at the Instituto de Carboquimica. A characterization of the materials before and after plasma was performed to evaluate any change on the surface and in the bulk. Second, another coaxial DBD reactor from LPP in Ecole polytechnique was used to study more in depth the electrical characteristics. The conversion rates in pure CO_2 are used as benchmarks to be able to compare the two reactors and ensure that the conclusions drawn from one system can be extrapolated to the other. Power and current peaks are further discussed as an alternative to optical *in situ* plasma measurements. The aim is to complement previous chapters and give results on the performance of each catalytic material tested in this thesis work.

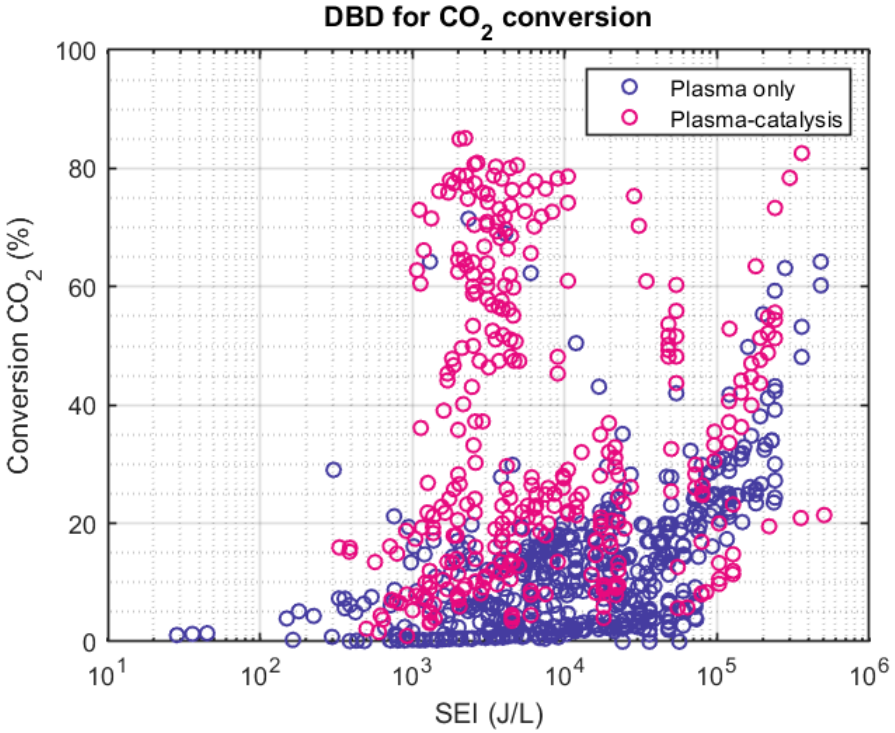

Figure 8.1: Summary of conversions of CO_2 as a function of SEI using plasma only (dark blue) and plasma-catalysis (pink) in DBD reactors. Data extracted from 74 papers using the PIONEER database tool developed within the CO_2 PIONEER project (www.db.co2pioneer.eu, date of extraction: 21/02/2023). Reactions: CO_2 splitting, CO_2 hydrogenation, Reverse water-gas-shift and Dry reforming of methane. Plasma-catalyst coupling: Packed and Fluidized bed.

8.2 Experimental procedure

Cerium oxide, compared to other metal oxides, shows a promising role on the conversion of CO_2 by plasma-catalysis [89, 90]. Different CeO_2-based materials were tested in a packed bed reactor at atmospheric pressure. The schematic of the coaxial DBD used in University of Bucharest is shown in figure 8.2. For each experiment, 0.4 g of material were added to the reactor and compared with the plasma only (no catalyst). No pretreatment was performed to CeO_2 before plasma reaction. The total flow was set to 2 sccm. The initial concentration of CO_2 and CH_4 was varied with 100, 90, 80, 70, 60 and 50% CO_2 to test the effect of carbon dioxide concentration in DBD. Also, the time evolution of species remaining adsorbed onto the surface was followed after 0, 1, 5, 10, 15 and 20 min of CO_2-CH_4 plasma exposure through DRIFTS measurements. The plasma discharge was ignited at 20 kV and 300 Hz with a ns pulsed

power supply. The downstream gas at the exit of the reactor was sent to the mass spectrometer and the measurements taken after 30 min of plasma reaction. Conversions of CO_2 and CH_4 were calculated per ion current (I) signal (a.u.) from MS before plasma (only gas) and during plasma. To avoid interference with atomic oxygen (mass 16), the mass 15 was chose to follow methane signal, therefore, mass 44 and 15 were followed for these experiments.

$$Conversion\ of\ CO_2\ (\%) = \frac{I(mass\ 44)_{gas} - I(mass\ 44)_{plasma}}{I(mass\ 44)_{gas}} * 100 \tag{8.1}$$

$$Conversion\ of\ CH_4\ (\%) = \frac{I(mass\ 15)_{gas} - I(mass\ 15)_{plasma}}{I(mass\ 15)_{gas}} * 100 \tag{8.2}$$

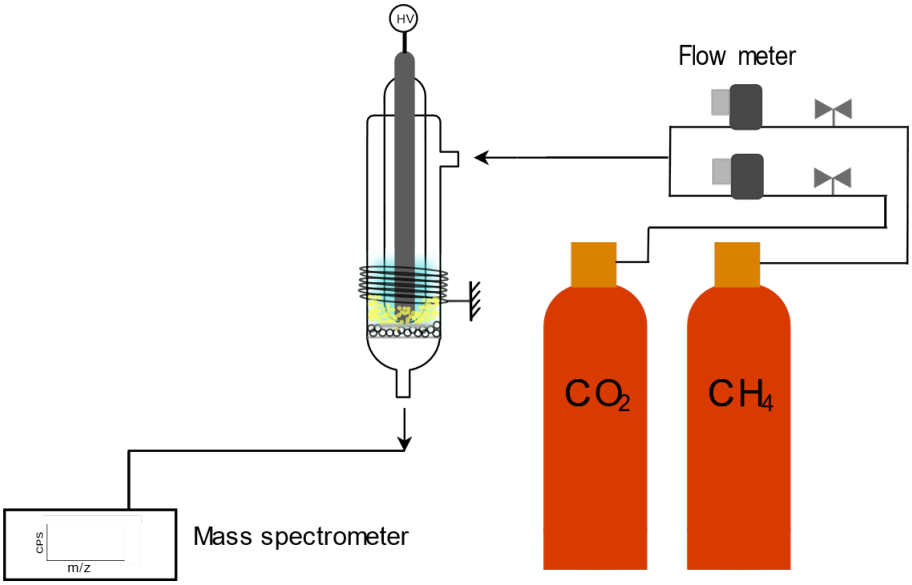

Figure 8.2: Schematic of the setup used for the catalytic testing of CeO_2 materials at atmospheric pressure and 2 sccm total flow. Tests performed in University of Bucharest, Romania.

Surface area analysis was measured by N_2 desorption and estimated by BET theory. DRIFTS, XRD and TPD-CO_2 analysis were performed to the ceria materials before and after plasma reaction. The details on the measurements methods are given in chapter 2.

A second coaxial packed bed DBD was used in Ecole polytechnique to investigate more in detail the electrical data and provide a link between the packed bed reactor from Bucharest and the fluidized bed DBD shown in the next chapter. The schematic of the coaxial DBD used as packed bed in Ecole polytechnique is shown in figure 8.3. The aim of these experiments is to relate the data on CO fraction with the input power as well as the discharge current peaks. The data obtained are compared with plasma alone (reactor empty) and with ceria (packed bed). 0.3 g of ceria powder were added to the reactor. The CO_2 and CO_2-CH_4 gas mixtures were sent to the reactor with a total flow rate of 7.4 sccm (u = 0.000123 L/s). The exit of the reactor was connected to the entrance of an IR cell to analyse the downstream gas by FTIR (ARCoptix). The CO fraction was estimated by the area of the band 2143 - 2222 cm^{-1} and extrapolated by a linear regression obtained by CO calibration in O_2 gas. Details on the calibration are described in the experimental section.

The voltage was varied from 10 to 15 kV amplitude (20 to 30 kV peak-to-peak). The schematic of the equivalent circuit of a DBD is shown in figure 8.4a as well as an ideal Lissajous figures (or charge-voltage (Q-V) diagram on figure 8.4b). This method was used to measure the average power transferred to the

gas but also to gain information about the capacitance of the system and the way charges are being transferred during each half period of the power supply. The measured capacitance can be compared with the theoretical capacitance of the reactor calculated as described in Appendix C. The measurements of the current peaks were done using a Rogowski coil between the ground electrode of the reactor and the capacitor. The envelope of the current peaks corresponds to the accumulation over 1000 periods of the maxima of current peaks. This provide a statistical distribution of the time of ignition of plasma filaments during a period of the applied voltage.

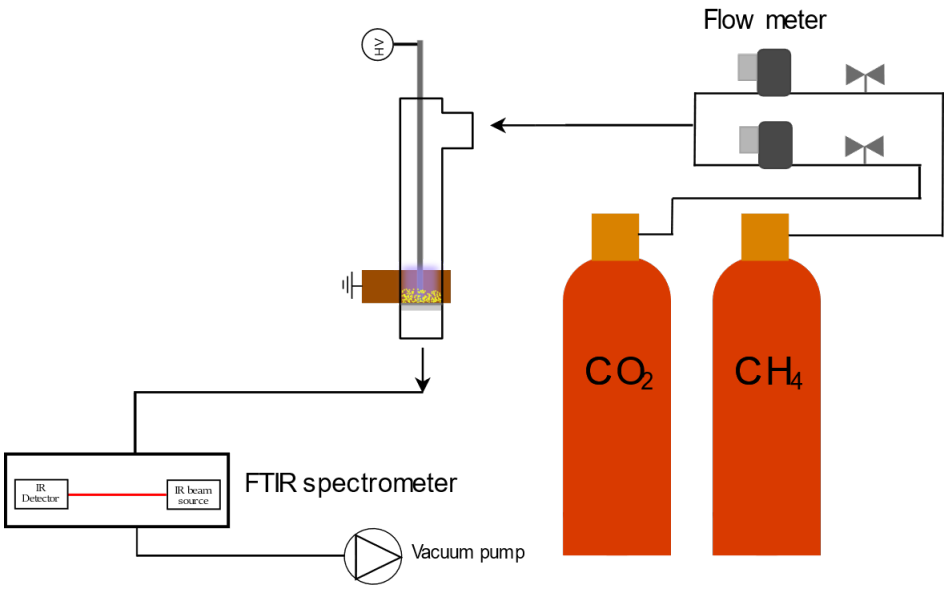

Figure 8.3: Schematic of the setup used for the catalytic testing of CeO_2 materials at atmospheric pressure and 450 torr and 7.4 sccm total flow. Tests performed in Ecole polytechnique, Palaiseau, France.

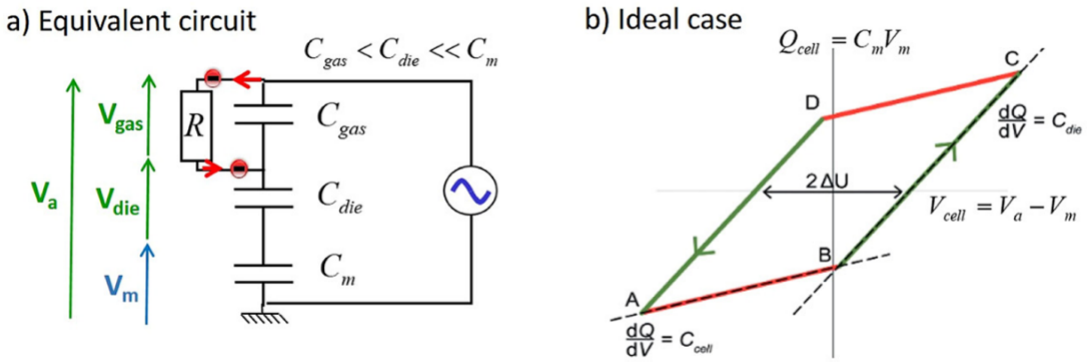

Figure 8.4: a) Schematic of equivalent electrical circuit of DBD and b) schematic of ideal Lissajous figure. Figure extracted from [18].

8.3 Initial concentration of CO_2

The first material tested with the reactor in the University of Bucharest is commercial CeO_2 nanopowder from Sigma Aldrich (previously used during *in situ* FTIR transmission experiments in part I) and here denoted as 'CeO_2 (SA)'. Figure 8.5 shows the conversion of CO_2 and CH_4 as a function of the initial concentration of CO_2 at atmospheric pressure with plasma-ceria and plasma only. 'Plasma+Ceria' results

in higher conversion than plasma alone with a maximum of 15% with initial concentration of CO_2 of 80%. Regarding CH_4 conversion, no clear trend is observed between all initial concentrations of CO_2 for plasma alone and plasma+ceria. One factor that could attribute to this enhancement is that carbon dioxide can adsorb on the surface of CeO_2 but not methane.

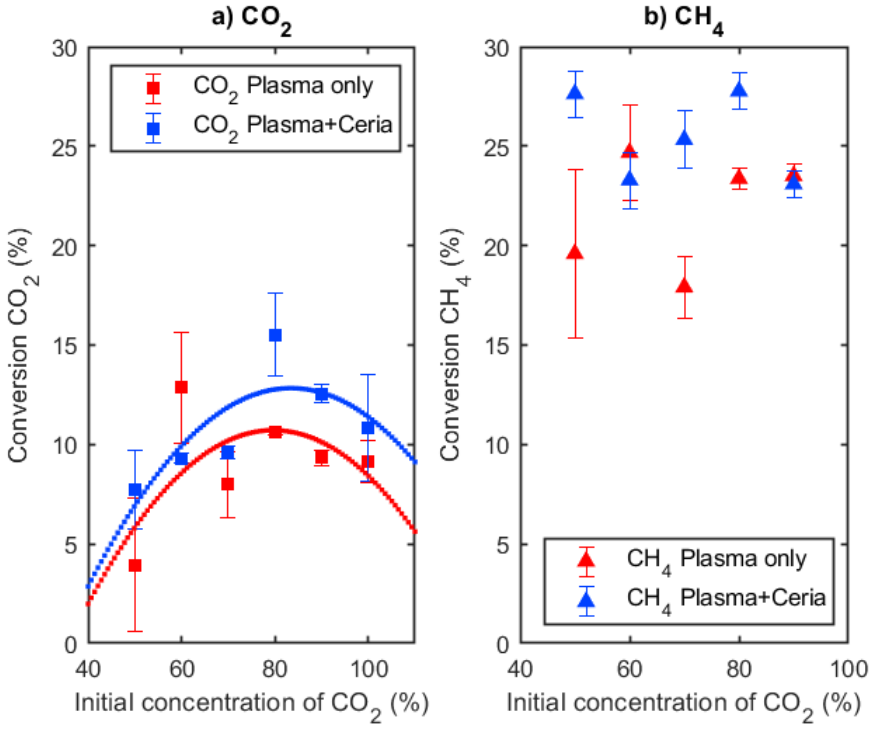

Figure 8.5: Conversion of a) CO_2 and b) CH_4 as function of the initial concentration of CO_2 using CeO_2 (SA) in Packed bed - DBD. Error bar represents +/- standard deviation from 3 experiments. Total flow rate: 2 sccm.

Looking at the surface adsorbates through DRIFTS analysis of the CeO_2 samples after DBD plasma at different initial concentrations could provide hints of what occur on the surface. Figure 8.6 shows the DRIFT spectra in Kubelka-Munk units for pristine ceria (CeO_2 (SA)) and the ceria samples after each CO_2-CH_4 plasma reaction in DBD.

Bands in the 1000 - 1800 cm^{-1} range are usually assigned to stretching vibrations (ν(CO)) in carbonates and formates species [117]. Four major peaks are identified in this region with a maxima around 1656, 1451, 1341 and 1050 cm^{-1}. The band at 1554 cm^{-1} is only observed in pristine ceria in addition to the aforementioned bands in the region 1000 - 1800 cm^{-1}. It is difficult to assign specific bands to tridentate carbonates and hydrogen carbonates as in previous chapters due to the overlap of huge peaks, hence in this chapter they will be called just 'Carbonates'. Additionally, the ν(CO) vibrations in formates species can also be overlapped with carbonates like the bands at 1358 cm^{-1} (F) and 1545 cm^{-1} (TC) (see chapter 5). The band at 1656 cm^{-1} is very close to the band 1665 cm^{-1} observed in chapter 5 (figure 5.10) which is tentatively attributed to carbonyl stretching vibration. The broad band in the range 2900 - 3750 cm^{-1} is related to stretching vibrations of OH groups on the surface or undissociated water adsorbed through H bonded hydroxyls [134]. A small defined peak is observed at 3700 cm^{-1} which is associated to OH(I) groups [134]. The assignment in pristine ceria is similar to what has been observed previously in part II.

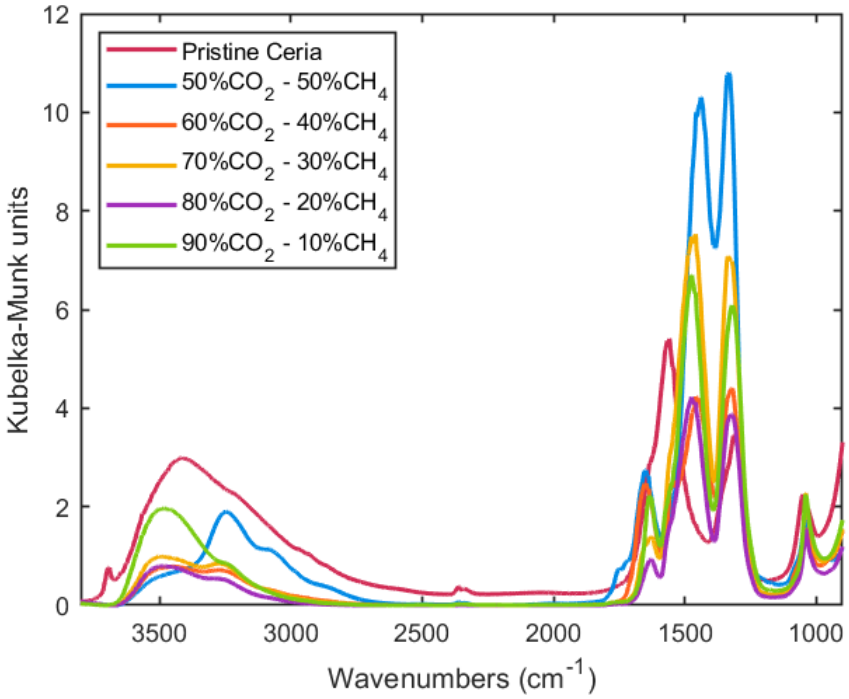

Figure 8.6: DRIFT spectra in Kubelka-Munk units for pristine ceria (CeO_2 (SA) before any plasma treatment) and for ceria used after 30 min of CO_2-CH_4 plasma reaction in DBD at different initial concentrations of CO_2.

However, there are some differences when CO_2-CH_4 plasma is applied at varying concentrations of CO_2. The band at 3700 cm^{-1} attributed to OH(I) species appears only in pristine ceria. The broad band previously mentioned at 2900 - 3750 cm^{-1} seems to split in two giving a maximum at 3240 cm^{-1} at 50% initial concentration of CO_2, and a maximum at 3490 cm^{-1} at 90% initial concentration of CO_2. For the spectra corresponding to initial concentration of CO_2 between 90 and 50%, the broad band seems to have two maxima. This could be a differentiation on the type of OH groups, either type (III) or (II) [129], although around 3200 cm^{-1} it can also correspond to stretching vibrations of CH groups.

The evolution of the ratio of bands area at 1656, 1451, 1341 cm^{-1} normalized by the band at 1050 cm^{-1} is followed as a function of initial concentration of CO_2 in CO_2-CH_4 plasma. The area was extracted as described in chapter 3, section 3.3.2. The overall intensity of the spectra obtained by DRIFT depends on the way the powder is placed in the instrument. To be able to compare the spectra between them, it is necessary to normalize the areas by the one of a peak which is stable in all the conditions. In this case, the bands are normalized by the band at 1050 cm^{-1} because this band seems relatively consistent across all samples. The results are shown in figure 8.7. We can notice the following:

- The area of the band at 3400 cm^{-1} follows a curve reaching a minimum at 70%CO_2. However the shape of the band changes when compared at time zero and 20 min which indicates a difference in OH species type adsorbed in CeO_2.
- The band at 1656 cm^{-1} slightly declines in area with increasing concentration of CO_2.
- Bands 1451 and 1341 cm^{-1} reach a maxima at 70%CO_2 and then remain similar for higher initial concentration of CO_2.

Larger areas of formate species bands would have been expected for higher concentrations of CH_4 in the initial gas mixture but it is hard to elucidate this without the presence of bands in the 2700 - 2900 cm^{-1}

region. We could think of the band at 1656 cm^{-1} but this band is not known to be attributed to formate species. Perhaps, it could correspond to formaldehyde traces but there is no conclusive evidence of it in this chapter nor in chapter 5.

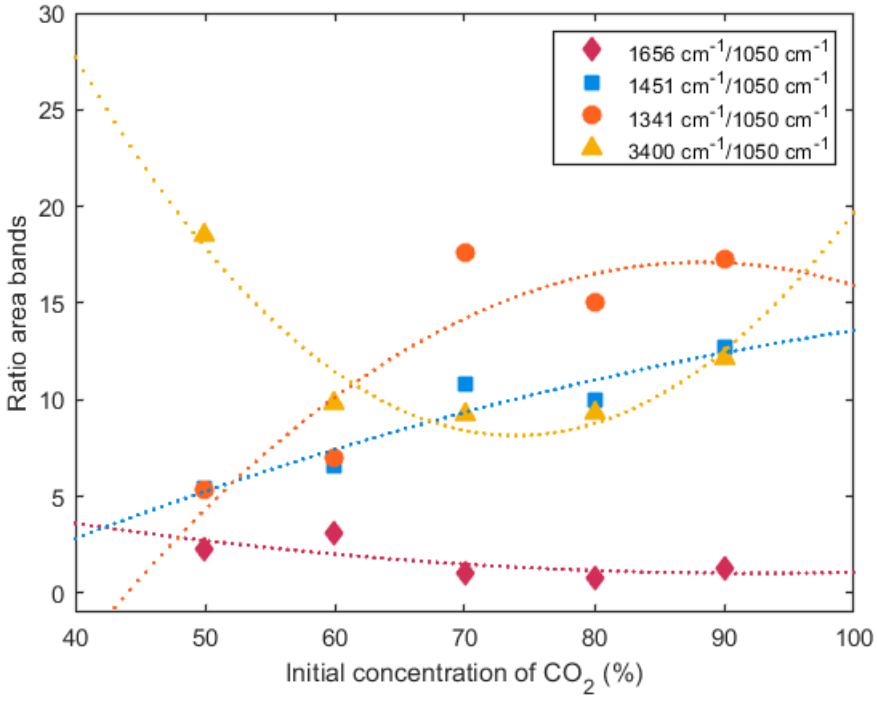

Figure 8.7: Ratio of the bands' area 1656, 1451, 1341 and 3400 cm^{-1} normalized by 1050 cm^{-1} band as a function of initial concentration of CO_2 in CO_2-CH_4 plasma reaction in DBD. The dotted line follows the general trend of the points plotted here.

In any case, no conclusive evidence of formate bands (ν(CH)) usually present between 2700 - 2950 cm^{-1} are present after 30 min of reaction in the DBD at atmospheric pressure. In addition, we must recall the absence of OH(I) species caused by the presence of carbonates adsorbed on the surface as observed in chapter 4.

8.4 Time evolution

In an attempt to understand what might occur on the surface, the ceria surface was analyzed by DRIFT spectroscopy after 1, 5, 10, 15 and 20 min of CO_2-CH_4 plasma exposure. Figure 8.6 shows the DRIFT spectra in Kubelka-Munk units after 70%CO_2-30%CH_4 plasma reaction in DBD at 0, 1, 5, 10, 15 and 20 min using CeO_2 (SA). The gas mixture was chosen for comparison with the results from chapter 5.

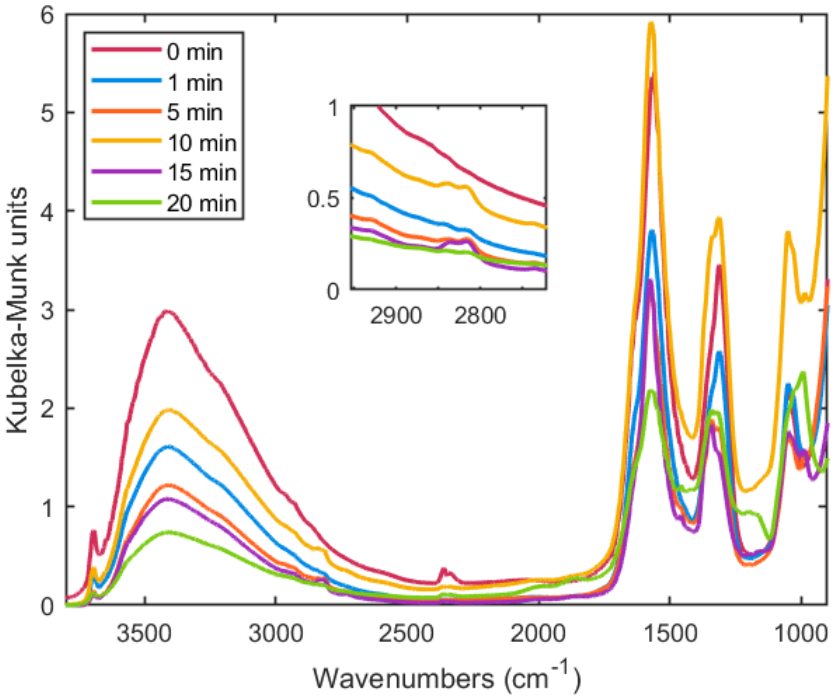

Figure 8.8: DRIFT spectra in Kubelka-Munk units after 70%CO_2-30%CH_4 plasma reaction in DBD at different times (0, 1, 5, 10, 15 and 20 min) using CeO_2 (SA) as packed material. A close view of the region 3000 - 2700 cm^{-1} is shown in a box inside the figure.

The spectra looks very similar to the spectra presented in figure 8.6 with few differences:

- The band at 3700 cm^{-1} is still present until 20 min of plasma reaction but not at 30 min as seen on figure 8.6.
- The area of the broad band at 3400 cm^{-1} seems to decrease with time but the two maxima observed on figure 8.6 are not yet visible after 20 min .
- Weak bands are observed in the region 2789 - 2862 cm^{-1} strongly suggesting ν(CH) vibrations from formate species. These bands appear at 5, 10 and 15 min spectra.
- Instead of four peaks as seen in figure 8.6, three major peaks with maxima at 1575, 1310 and 1050 cm^{-1} are observed through all times tested.

If we compare the spectrum after 20 min (green line) from figure 8.8 and the spectrum after 30 min (yellow line) from figure 8.6, both with 70%CO_2-30%CH_4 plasma, we can see a difference in the main peaks in the 1000 - 1800 cm^{-1} range. The peak at 1656 cm^{-1} is not present after 30 min reaction and the bands at 1451 and 1341 cm^{-1} are shifted to 1575 and 1310 cm^{-1}, respectively. The evolution of adsorbed species on the surface is therefore not yet reaching a steady state after 20 min of plasma exposure.

In order to follow the band evolution in a similar way as it has been done in part II, the area of the bands at 1050, 1575, 1310, 2830, 3400 and 3700 cm^{-1} were followed as a function of time. The bands 2830, 3400 and 3700 cm^{-1} are attributed to ν(CH) of formates, broad band from hydrogen bonded OH groups and ν(OH(I)), respectively. However, the bands at 1050, 1575 and 1310 cm^{-1}, are not clearly assigned yet. The ν(CO) vibration from formates can be overlapped in that region. Therefore, the areas are plotted as a function of one another as done in chapter 3 for formates bands. The coefficient of determination with more than 0.9 is indicated in the legend of the figure 8.9.

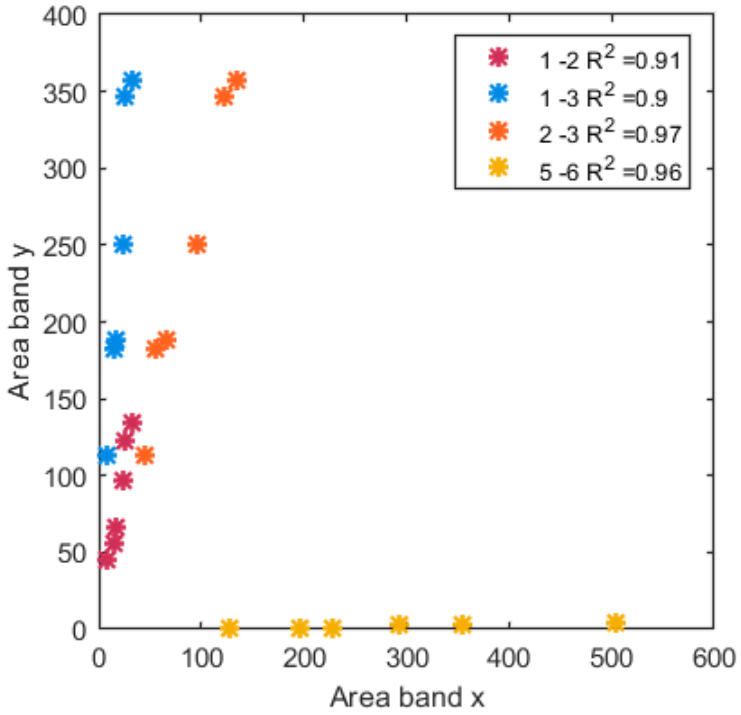

Figure 8.9: Correlation of bands x vs y during time evolution of areas by DRIFT surface analysis for 70% CO_2-30% CH_4 in PB-DBD. Numbers are assigned to a specific band: 1 = 1050 cm^{-1}, 2 = 1310 cm^{-1}, 3 = 1575 cm^{-1}, 4 = 2830 cm^{-1}, 5 = 3400 cm^{-1} and 6 = 3700 cm^{-1}. Coefficient of determination R^2 is shown for every band correlated with more than 0.9.

The bands 1050, 1575 and 1310 cm^{-1} are clearly correlated. Therefore, they are assigned to carbonates species. The ν(CO) vibration from formate species could still be present but the contribution is minimal. The bands 3400 and 3700 cm^{-1} are related. The OH groups are bonded to other OH groups on the surface through hydrogen bonding. The band at 2830 cm^{-1} is not correlated to any other band observed in the IR spectra. Thereafter, the species can be followed as a function of time. The overall intensity of the spectra obtained by DRIFT depends on the way the powder is placed in the instrument. To be able to compare the spectra between them, it is necessary to normalize the areas by the one of a peak which is stable in all the conditions. The area of the bands at 1575, 1310, 2830, 3400 and 3700 cm^{-1} were normalized by the area of bands 1050 cm^{-1}. This band is chosen for normalizing the other ones because it appears in every spectra when varying the initial concentrations of CO_2-CH_4 and during the time evolution while the other bands shift their maxima or vary with intensity depending on the condition.

Figure 8.10 shows the ratio of the area bands of 1575, 1310, 2830, 3400 and 3700 cm^{-1} normalized by 1050 cm^{-1} as a function of time.

The band at 2830 cm^{-1} assigned to formates increases from 5 to 15 min reaction and it is reduced by 20 min. Simultaneously, 1575 and 1310 cm^{-1} reach a minimum around 10 min following an opposite trend as 2830 cm^{-1}. The same occurs for 3400 cm^{-1}. The band 3700 cm^{-1} seems to decrease from time 0 to 1 min and seems keep the same relative area. We recall that OH(I) groups are perturbed by the presence of HC on the surface. In this case, carbonates are present in pristine ceria corresponding to time zero so the subsequent perturbation of such species could be due to the presence of other species as formates or increase of carbonates on the surface.

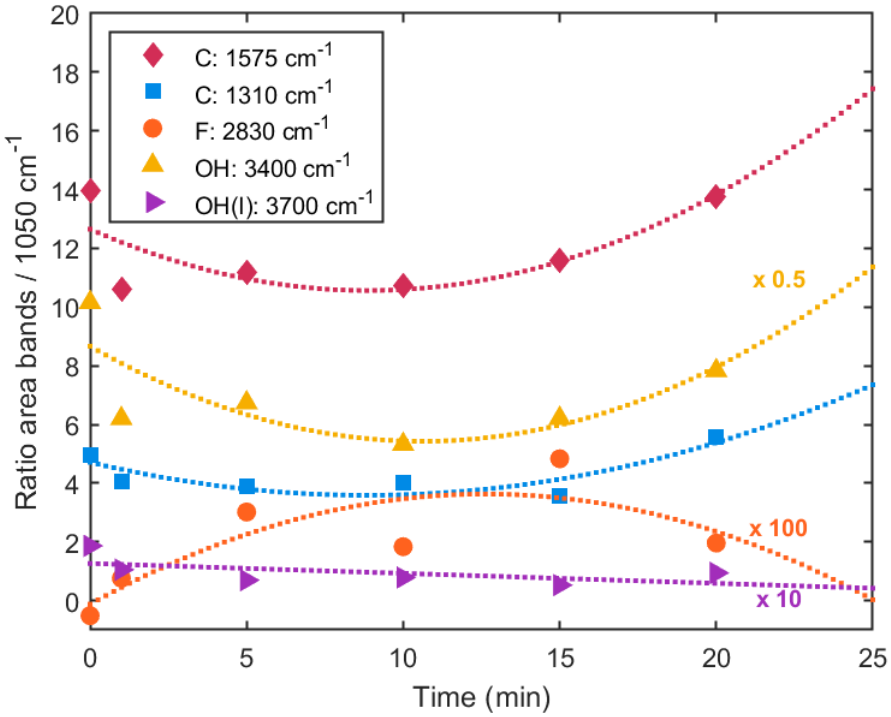

Figure 8.10: Ratio of bands at 1575, 1310, 2830, 3400 and 3700 cm^{-1} normalized by 1050 cm^{-1} as a function of time for 70%CO_2-30%CH_4 plasma reaction in PB-DBD. The dotted line follows the general trend of the data plotted. C: Carbonates, F: Formates and OH: Hydroxyl groups.

Based on the literature reviewed and the conclusions obtained in chapter 5, where carbonates (TC) react with OH species, we propose the following: Carbonates (1575 and 1310 cm^{-1}) decrease reaching a minimum at 10 min due to the reaction with OH groups or undissociated water adsorbed through H bonded hydroxyls (broad band 3400 cm^{-1}). In the meantime, Formates are formed (2830 cm^{-1}) and decays after 10 mins. No formates species are observed after 20 min but carbonates and OH species are still present on the surface. This mechanism is similar to what has been proposed in part II in the DC glow discharge at low pressure.

In contrast to the 10 min test reaction in the glow discharge, here we test up to 30 min of reaction and no formates are observed on the surface. Another process should occur in the plasma or surface that does not allow more formates to form beyond 20 mins of reaction.

Despite the difference in conditions and discharges, one at atmospheric pressure in DBD plasmas and another at low pressure in DC glow discharge plasmas, formation of formates suggest the same surface mechanisms.

8.5 Test of different Ceria materials

Subsequently, different ceria materials prepared in the Instituto de Carboquimica in Zaragoza and by myself in the University of Bucharest were evaluated in the conversion of CO_2 and CH_4. More details on the preparation of Ceria (solgel) is described in Appendix B. A summary of the ceria samples tested here is presented in table 8.1 along with the reference to the methodology followed to prepare the ceria materials.

These materials were tested with initial concentrations of 70%CO_2-30%CH_4 to compare with the results obtained in chapter 5. Figure 8.11 shows the conversion of CO_2 and CH_4. The conversion of

CO_2 results are somewhat similar around 8% for the first 6 cerias from the left part of the figure. The presence of 1%Y_2O_3 in CeO_2 does not show a markedly improvement on the conversion. CeO_2 (KIT 6-template) and $Ce_{0.5}$-$Zr_{0.5}O_2$ (Urea precipitation) result in the lowest conversions below 4%.

Composition (method of synthesis)	Ref.
CeO_2 (SA)	-
CeO_2 (solgel)	[81]
CeO_2 (Urea precipitation)	[168]
1%Y_2O_3 - CeO_2 (KIT-6 template)	[169, 170]
CeO_2 (Ce acac calcination)	-
CeO_2 (KIT-6 template)	[169, 170]
$Ce_{0.5}Zr_{0.5}O_2$ (Urea precipitation)	[168]

Table 8.1: Ceria materials tested with 70%CO_2-30%CH_4 plasma in Packed bed - DBD at atmospheric pressure along with reference to the methodology used to prepare the materials.

No clear trend is observed again for methane conversion in the first 6 samples but it is worth noting three things:

- CeO_2 (SA) resulted in the largest conversion with almost 25%.
- CeO_2 (KIT 6-template) resulted in 11% conversion of methane, still lower than the rest of the samples.
- Similarly to CO_2 conversion in $Ce_{0.5}$-$Zr_{0.5}O_2$ (Urea precipitation) samples, CH_4 conversion is around 4%.

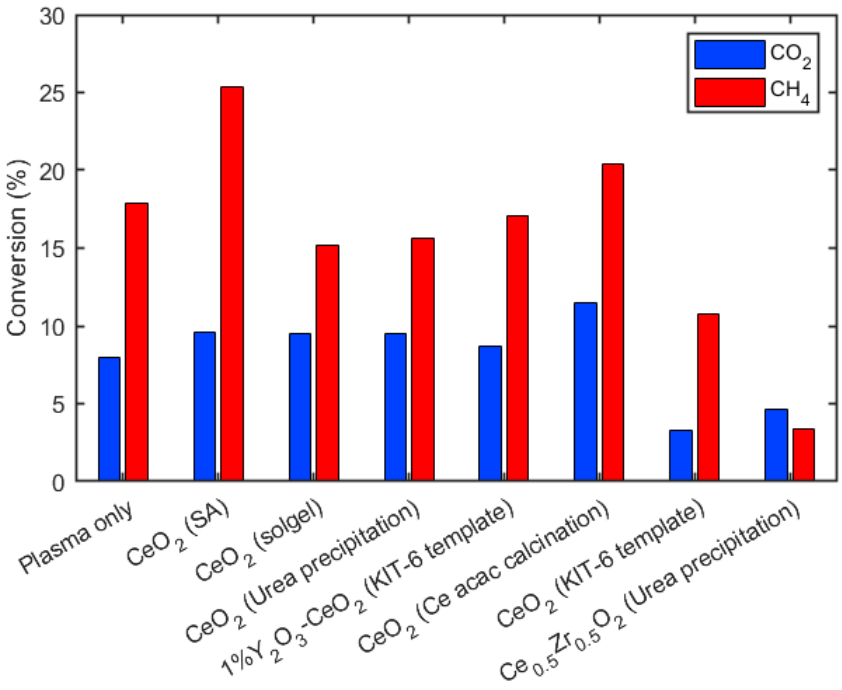

Figure 8.11: Conversion of CO_2 (blue) and CH_4 (red) for different ceria based materials with initial concentration of 70%CO_2-30%CH_4 at atmospheric pressure. The methodology followed is indicated in parenthesis. Total flow rate: 2 sccm.

This difference in CO_2 conversion can be explained by the amount of active sites where the CO_2 molecule can adsorb and dissociate. TPD-CO_2 analysis was performed in all the ceria samples (before

plasma exposure). Figure 8.12 shows the desorption of CO_2 as a function of temperature for two representative samples: CeO_2 (SA) and CeO_2 (solgel). Usually in TPD-CO_2, the strengths of basic sites are reported in terms of temperature range where the chemisorbed CO_2 on the basic sites is desorbed. A large peak is observed around 100°C and a very flat one around 350°C which are associated to weak and medium strength basic sites for CO_2, respectively.

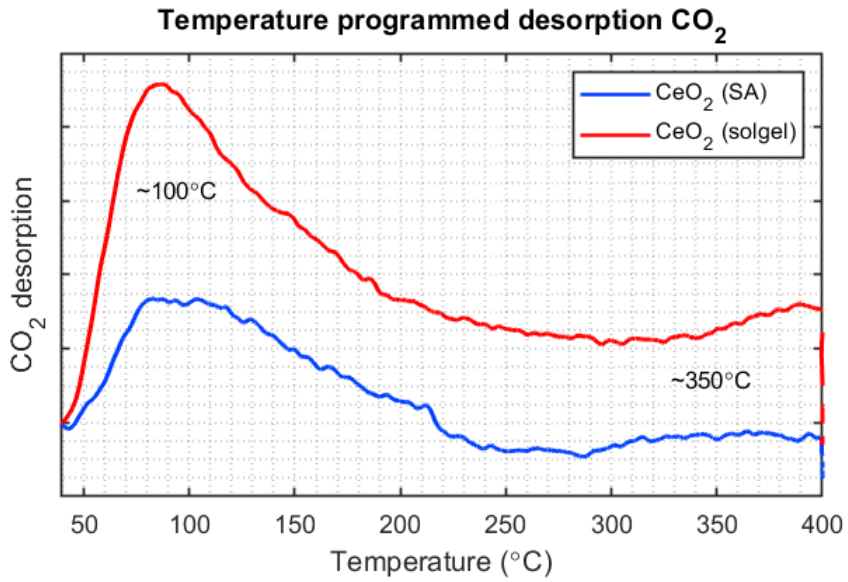

Figure 8.12: CO_2 desorption by TPD analysis of CeO_2 (SA) and CeO_2 (solgel) samples before plasma reaction (pristine samples).

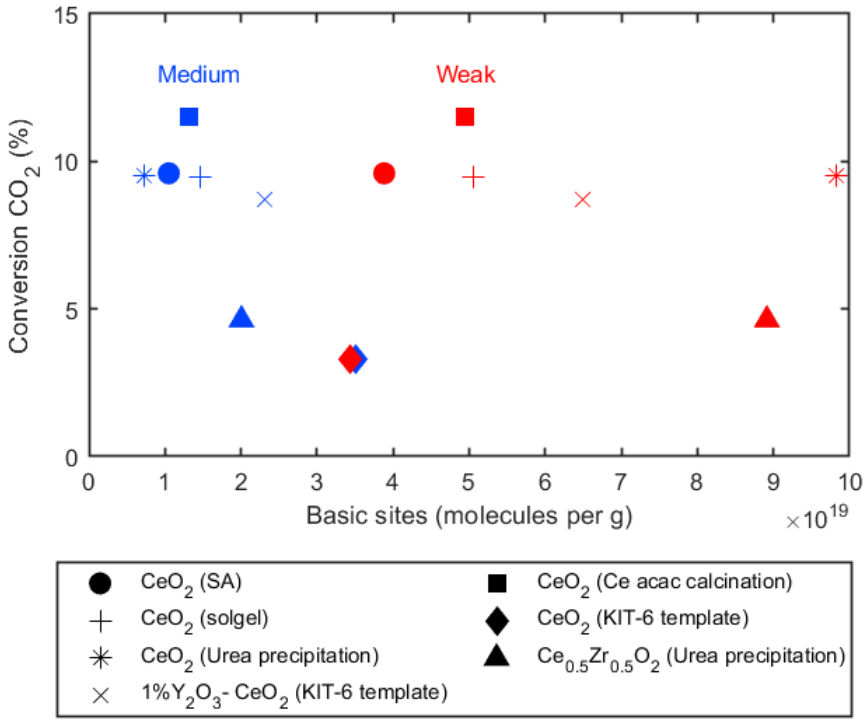

Figure 8.13: Conversion of CO_2 as a function of weak (red) and medium (blue) strength basic sites per gram of ceria before plasma.

The amount of basic sites was estimated by integration of these peak areas [171]. Figure 8.13 shows the conversion of CO_2 as a function of amount of basic sites per gram of material. The weak basic sites are scattered and no visible trend is observed. In contrast, medium basic sites seem to create a linear trend where lower conversion is observed with large amount of basic sites which correspond to CeO_2 (KIT 6-template) and $Ce_{0.5}$-$Zr_{0.5}O_2$ (Urea precipitation) samples.

We could hypothesize that this large amount of medium basic sites is impacting negatively the surface conversion of CO_2 by forming strongly bonded carbonates and saturating the adsorption sites. Such species subsequently remain on the surface blocking the formation of formates leading to a decrease in the generation of CO and H_2. Nonetheless, this assumption goes beyond a mere attribution on the amount of basic sites because the conversion with these two samples is even lower than plasma alone. The maximum for CeO_2 (solgel) seems to be shifted to higher temperatures which could create a difference in the bond energy, and therefore the basicity strength.

The presence of Zr ions in $Ce_{0.5}$-$Zr_{0.5}O_2$ (Urea precipitation) seems to not help on the surface conversion of CO_2 despite the reported improved conversion in mixed Cerium-Zirconium materials, in thermal catalysis [172, 173] and plasma-catalysis [174].

The available surface can help to clarify what could occur in these particular cases of minimal conversion. Table 8.2 shows the surface area obtained by BET method from N_2 physisorption for CeO_2 (SA), CeO_2 (solgel), CeO_2 (Urea precipitation) and CeO_2 (KIT-6 template).

Composition (method of synthesis)	BET Surface area (m^2/g)	Analysis done:
CeO_2 (SA)	14.63 (13.93 after DBD plasma)	University of Bucharest
CeO_2 (solgel)	39.48	University of Bucharest
CeO_2 (Urea precipitation)	58.8	Instituto de Carboquimica
CeO_2 (KIT-6 template)	131.05	Instituto de Carboquimica

Table 8.2: BET surface area from N_2 physisorption of ceria materials tested with 70%CO_2-30%CH_4 plasma in Packed bed - DBD at atmospheric pressure.

Firstly, we notice that CeO_2 (SA) has the lowest surface area among all the samples. However, the sample CeO_2 (KIT-6 template) has the largest surface but results in the lowest conversion of CO_2. This extended surface area seems to not contribute on the conversion of CO_2 or even to be perhaps detrimental. This could also be linked to the amount of basic sites as discussed above.

To get more hints on the real impact of the catalyst on the conversion of CO_2, the possible modification of the ceria induced by plasma has to be discussed. The surface area could be modified by the prolonged exposure to plasma but as we see here the surface area did not change in the case of CeO_2 (SA) sample. Yet, the crystalline structure should also be evaluated. XRD analysis was performed in the samples from table 8.1 before plasma and after 70%CO_2-30%CH_4 plasma in the DBD. Figure 8.14 displays the XRD profiles for the samples utilized in this section. The peaks identified at 28.6, 33.1, 47.5, 56.4, 59.1, 69.4, 76.7 and 79.1° correspond to *hkl* reflections (111), (200), (220), (311), (222), (400), (331) and (420), respectively. These peaks correspond to stoichiometric ceria. Only $Ce_{0.5}$-$Zr_{0.5}O_2$ sample shows additional peaks at 30.22 and 34.96° corresponding to a crystalline phase of ZrO_2 [175]. Either peaks attributed to graphitic structures are observed in any sample as it was observed in the ceria pellets used in chapter 5. A comment on the crystallite size could complement the discussion on the morphology that might affect the surface conversion of CO_2. However, it must be done with a complete characterization along with TEM or SEM which was not available at the moment of these experiments. Nonetheless, we can confirm that DBD plasma exposure did not change the crystalline structure as the XRD patterns seem unchanged.

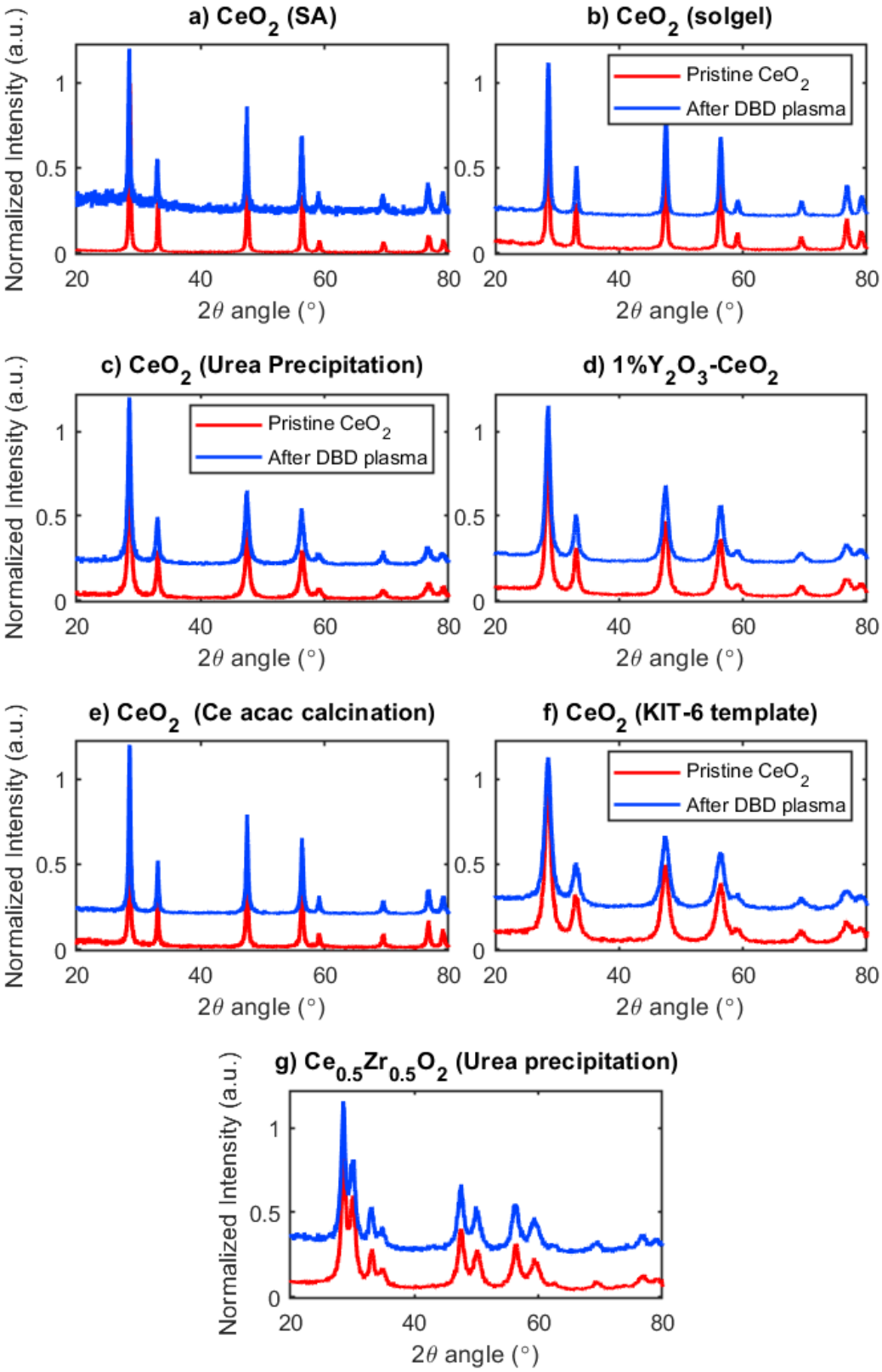

Figure 8.14: XRD profiles of a) CeO_2 (SA), b) CeO_2 (solgel), c) CeO_2 (Urea precipitation), d) $1\%Y_2O_3$ - CeO_2 (KIT-6 template), e) CeO_2 (Ce acac calcination), f) CeO_2 (KIT-6 template) and g) $Ce_{0.5}Zr_{0.5}O_2$ (Urea precipitation) pristine samples (red) and after DBD plasma (blue). The offset of the pattern is for clarity.

In summary, the effect of different CeO_2 on the conversion of CO_2 and CH_4 is not very large compared to plasma alone. Except for the CeO_2 (SA) and CeO_2 (Ce acac calcination) it would even tend to be detrimental for the conversion. The amount of medium strength basic sites and surface area seems to be important on the surface conversion of CO_2. However the fact the best conversion is obtained for CeO_2 (SA) which has the lowest BET Surface area illustrates that for plasma-catalysis coupling, the porosity at nanometric scale is not necessarily the most important one since the plasma can not develop in such small structures. Additional study dedicated to the macroscopic structure of the different CeO_2 could therefore be interesting to try to understand if the plasma can develop better because of structures at a micrometric scale. It is also important to note that the presence of Zr ions in $Ce_{0.5}$-$Zr_{0.5}O_2$ seems to not help in the performance, either. Exposing the different catalysts to plasma did not affect the crystalline structure as observed by XRD profiles. In order to gain more insight on the cause for the observed conversion with the different material, it is also necessary to analyse whether the plasma itself is developing in a similar manner or not in presence of the various materials. The specific energy input but also the maxima of current peaks is therefore studied in the following section.

8.6 CO fraction vs SEI

The energy density transferred to the gas in a plasma catalysis reactor is often expressed as the ratio of the power to the volumetric flow, usually known as Specific Energy Input (SEI). It is a useful parameter to compare the performances of very different plasma sources, but it does not account for the possible inhomogeneity of energy deposition within a given reactor. An indirect way to know the specific energy input is to extrapolate the CO density from pure CO_2 plasma without any catalyst (empty reactor) in dielectric barrier discharges. Indeed, as concluded by Brehmer et al., CO production in DBD (for pure CO_2 plasma without any catalyst) follows a single trend as a function of the specific injected energy for different conditions (thickness of dielectric, configuration, dimensions) [19]. Figure 8.15 displays a figure extracted from the aforementioned work with CO densities as a function of SEI.

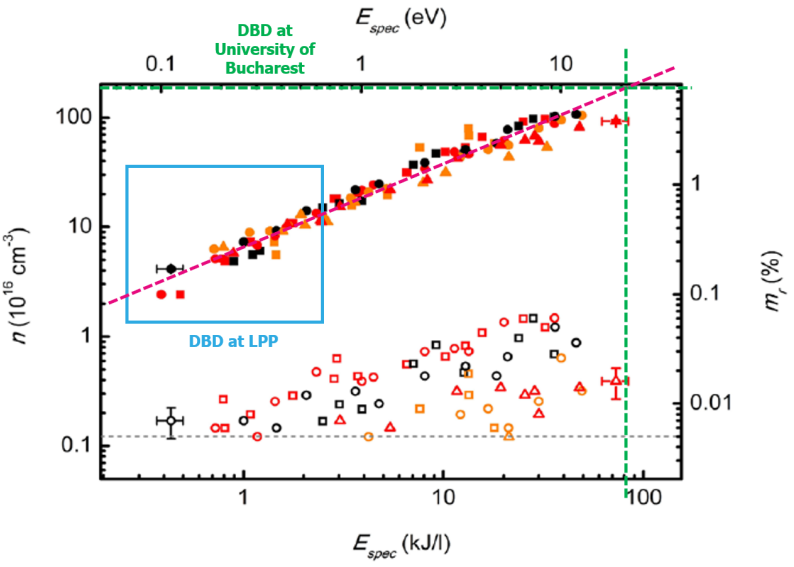

Figure 8.15: Figure extracted from [19] showing the densities of CO (full marker) as a function of specific energy input. Pink dashed line represents the trend followed by the measurements reported in the paper. Green dashed line shows the CO density and corresponding specific energy input from the results obtained by the DBD at University of Bucharest for pure CO_2 plasma. The light blue box points the region of CO density and SEI expected for the results shown in this chapter.

Considering the conversion of CO_2 in 100%CO_2 plasma only (no ceria) to be 9.2%, the CO density can be estimated to be 225 x 10^{16} cm^{-3} at atmospheric pressure. Following the trend by the CO density as a function of specific energy (pink dashed line), the corresponding SEI is around 80 kJ/L in the packed bed - DBD from Bucharest. Surely, high SEI results in high conversion of CO_2 but testing at lower SEI with a catalytic material could correspond to conditions more favourable to observe a beneficial effect of the catalytic material on the conversion. The range of SEI tested in the reactor from LPP is shown with the light blue box on figure 8.15). The measurements at LPP were using a Packed bed - DBD setup (figure 8.3) as described in the experimental section in this chapter. Table 8.3 summarized the parameters and conditions used in both sets of experiments between the DBD reactor in the University of Bucharest and LPP.

Parameters	**University of Bucharest**	**LPP**
Plasma volume	1.04 cm^3	1.38 cm^3
Amount of catalyst	0.4 g	0.3 g
Total flow rate	2 sccm	7.4 sccm
Frequency	300 Hz	1000 Hz
Voltage	pulsed 20 kV	amplitude 15 kV
Pressure	750 Torr	450 and 750 Torr
Data obtained	CO_2 and CH_4 conversion Material characterization	CO fraction Electrical data

Table 8.3: Experimental conditions of the PB-DBD used through this chapter.

To ease the comparison across different conditions and with the literature, SEI in kJ/L is calculated from the following expression:

$$SEI\left(\frac{kJ}{L}\right) = \frac{\mathbb{P}_{(J/s)} \cdot \left(\frac{PV}{KT_{gas}}\right)}{\phi_{(L/s)} \cdot \left(\frac{P^\circ V^\circ}{KT^\circ}\right)} * \frac{1}{1000} \tag{8.3}$$

$\mathbb{P}$ corresponds to power in J/s (W); P°, V° and T° correspond to standard conditions of pressure and temperature. Assuming the variance in gas temperature in plasma is negligible at low SEI $T_{gas} \approx T^\circ$ then, SEI equation can be simplified:

$$SEI = \frac{\mathbb{P}_{(J/s)} \cdot P}{\phi_{(L/s)} \cdot P^\circ} \tag{8.4}$$

Pressure has a direct impact on the number of molecules in a given space as indicated by the ideal gas equation. Therefore, pressure variation should always be considered to correct the flow rates, usually set at atmospheric pressure and not always properly considered in results reported in the literature.

8.6.1 CO_2 plasma

CO fraction measurements were performed for varying applied voltage which translates to different powers. Representative samples were used in this second round of tests in PB-DBD: CeO_2 (SA), CeO_2 (SA) no CO_2, CeO_2 (solgel) and CeO_2 (Urea precipitation). 'CeO_2 (SA) no CO_2' refers to a commercial ceria recently acquired from Sigma Aldrich brand and corresponds to the same product (ceria nanopowder <50 nm) as the ceria used in part II for *in situ* experiments. However, this sample in particular does not adsorb CO_2 at low pressure (1-5 Torr) (this particular point will be discussed later). Therefore, the ceria here is denoted as 'CeO_2 (SA) no CO_2'. Figure 8.16 presents the CO fraction as a function of SEI in the resulting gas from CO_2 only in PB-DBD for plasma only and different ceria.

First of all, the conversion values obtained in pure CO_2 with plasma only are in reasonably good agreement with the figure 8.15 with ~3.5 x 10^{17} cm^{-3} for 2.5 kJ/L. In general, a lower pressure (450 Torr) is beneficial for the conversion of CO_2 at a given specific energy. This is perhaps the result of

a larger volume of plasma since the field required to sustain the plasma is lower at reduced pressure. Concerning the different catalysts, we can notice several trends:

- The sample CeO_2 (SA) results in larger CO fraction in comparison to plasma only for both pressures.
- On the contrary the sample CeO_2 (SA) no CO_2 does not show more conversion than plasma alone even though a small effect is perhaps existing at 750 Torr.
- The CO fraction from CeO_2 (solgel) and CeO_2 (Urea precipitation) seem slightly lower (at 750 Torr) or slightly higher (at 450 Torr) than the fraction obtained by plasma only but this could fall within the experimental error.

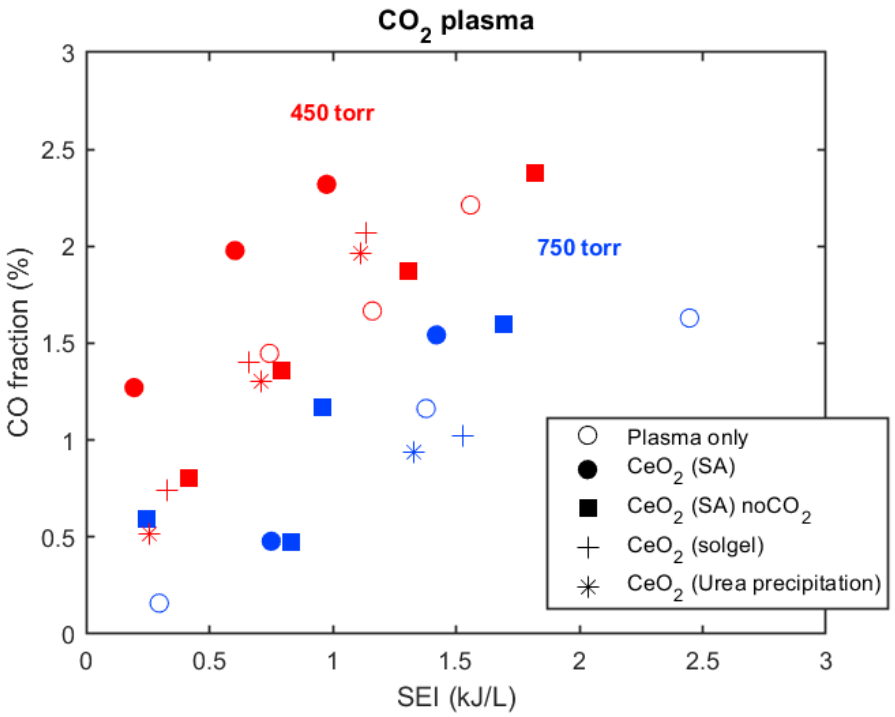

Figure 8.16: CO fraction as a function of SEI for CO_2 plasma in plasma only and packed bed mode with CeO_2 (SA), CeO_2 (SA) no CO_2, CeO_2 (solgel) and CeO_2 (Urea precipitation) at 750 Torr (blue) and 450 Torr (red). Total flow rate: 7.4 sccm.

These observation are consistent with the ones from figure 8.11 in the sense that only the CeO_2 (SA) sample provides better CO_2 conversion than plasma alone. In order to determine whether this effect is due to a real surface reactivity or to a modification of the plasma properties induced by the presence of ceria, the electrical characteristics of the discharge are analysed under the different conditions.

The Lissajous figures will be discussed in combination with the peak current envelopes. The so-called 'envelopes' are the maximum amplitudes of the current peaks accumulated over a thousand periods of voltage. They provide a statistical information about the event transferring the largest amount of charge at once which can be compared for plasma in contact with different packing materials. Figure 8.17 shows the Lissajous diagram and envelope of the current peaks from experiments with plasma only and CeO_2 (SA), CeO_2 (SA) no CO_2, CeO_2 (solgel) and CeO_2 (Urea precipitation) in pure CO_2 plasma.

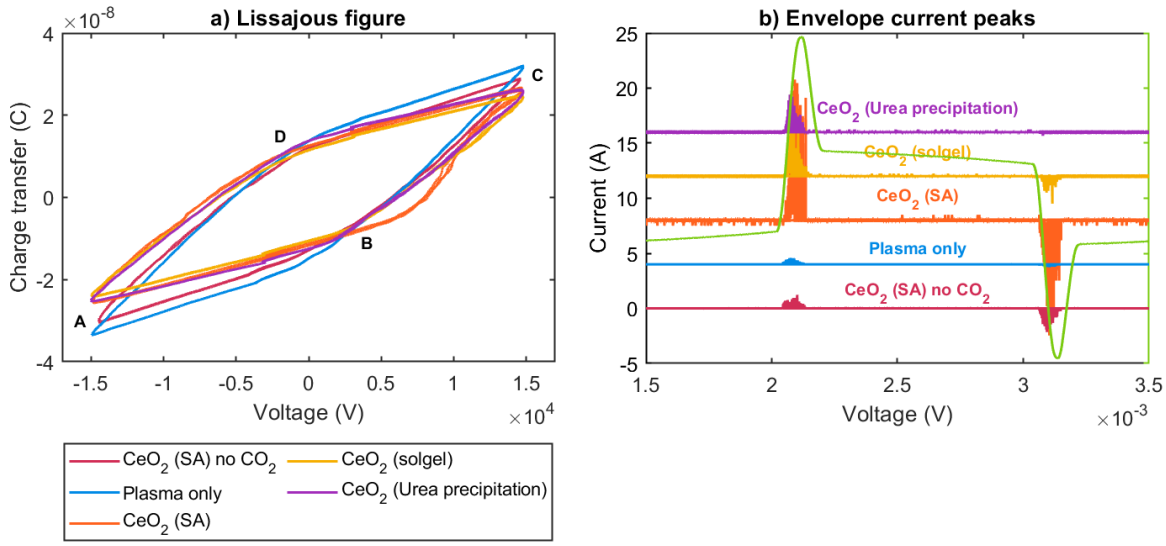

Figure 8.17: a) Lissajous figure and b) envelope of the current peaks from experiments with plasma only and CeO_2 (SA), CeO_2 (SA) no CO_2, CeO_2 (solgel) and CeO_2 (Urea precipitation) in pure CO_2 plasma PB-DBD, 15 kV amplitude (30 kV peak-to-peak), 750 Torr. The envelope corresponds to the accumulation of 1000 periods. An offset of 4 A is added between envelopes of different conditions for clarity. One voltage cycle (green) is overlaid to show the timing of current peaks with respect to the voltage.

The Lissajous figure shape can tell us more than just the average power. We will refer to the figure 8.4 for the further discussion on the following Lissajous figures. From figure 8.17a, we can note the following:

1. The slope from A to B (and from C to D) that corresponds to the capacitance of the reactor is the same for almost all the CeO_2 sample but is larger for plasma only and CeO_2 (SA) no CO_2
2. The corner of the parallelogram at point B happens at higher applied voltage with CeO_2 (SA) and CeO_2 (solgel), especially during positive half period. These two cases also shows the largest maxima of current peaks on the envelope signals.
3. The difference in height from point B to C (or D to A), ΔQ, is larger for the empty reactor than for the packed bed with ceria materials. The only exception is again the CeO_2 (SA) no CO_2 which shows a ΔQ almost as large as for Plasma only. the two cases CeO_2 (SA) no CO_2 and Plasma only are also the ones showing the lowest amplitude on the envelopes despite a larger ΔQ.

Concerning the first point (1), the slope (Q/V) during segments A-B and C-D is related to the capacitance of the reactor during plasma OFF phase (C_{cell}). This capacitance can be estimated just from the dimension of the reactor considering the reactor as 3 cylindrical capacitances in serie namely the capacitance of the inner glass tube covering the high voltage electrode (C_{die1}), the capacitance of the gas gap (C_{gas}), and the capacitance of the outer glass tube (C_{die2}). Therefore the reactor capacitance is given by

$$C_{cell} = \frac{1}{\frac{1}{C_{die1}} + \frac{1}{C_{gas}} + \frac{1}{C_{die2}}} \tag{8.5}$$

The value of a cylindrical capacitance is given by the following equation:

$$C_{cylinder} = \frac{2\pi\epsilon_0\epsilon_r L}{ln(b/a)} \tag{8.6}$$

where ϵ_0 is the vacuum permittivity, ϵ_r the relative permittivity of the considered material, $L = 2.1\ cm$ the length of the ground electrode, and a, b the inner and outer radius respectively of the cylindrical capacitance. Taking $\epsilon_r = 4.5$ for the glass, the calculated value of capacitance for the empty reactor is about 1 pF in very good agreement with the value deduced from the slope of the Lissajous plot during plasma OFF phase (see table 8.6).

$$slope\ (m) = \frac{Q}{V} = C_{cell} \tag{8.7}$$

When the reactor is filled with CeO_2 powder, the value of C_{gas} should be increased by the presence of a high permittivity material in the gap resulting in an increased C_{cell} given by equation 8.5. The dielectric permittivity of CeO_2, especially in form of a powder, is difficult to determine accurately. The dielectric properties can be influenced by the morphology, grain size, grain boundaries, cation distribution, frequency of applied field, temperature, etc. [176]. Nevertheless a typical value of ϵ_r for CeO_2 is around 23 [177]. If the whole gas gap would be filled by a solid cylinder of CeO_2, the value of C_{cell} would increase to 4.9 pF (see calculated value in table 8.6). However the capacitance measured from the Lissajous is on the contrary lower than for the empty reactor (between 0.83 and 1.14 for the various packing materials, see table 8.6). A possible explanation for this apparent contradiction is related to the 'effective' volume in which the plasma filaments can actually initiate under the different conditions. Indeed a decrease of C_{cell} when adding powder of a high dielectric permittivity material in the gas gap could be explained by a shorter effective length of the ground electrode (shorter L in equation 8.6). The plasma filaments needs typically a few tens of microns at atmospheric pressure to develop. If a powder bed is too dense, the filament ignition will be more difficult. In presence of CeO_2 powder, plasma is probably igniting only in a part of the catalytic bed and the resulting charge deposition on the surface of the inner and outer glass tube is happening only on a shorter length than L in equation 8.6. It is difficult to estimate the height over which the plasma is effectively igniting in each condition. Moreover, as it will be shown later, the particles when being charged tends to be electrostatically expelled from the electrode region. Nevertheless the values of C_{cell} measured from Lissajous slopes and given in table 8.6 would corresponds to a decrease of about 15% of the effective length of the ground electrode compared to the empty reactor. However this decrease of effective length should be even larger to compensate for the presence of a high dielectric permittivity material in the gas gap.

Conditions	**calculated C_{cell} (pF)**	**C_{cell} from Lissajous (pF)**
Empty reactor	1.05	1.14
Reactor filled with CeO_2 (SA) no CO_2	~4.9	1.14
Reactor filled with CeO_2 (SA)	~4.9	0.95
Reactor filled with CeO_2 (solgel)	~4.9	0.85
Reactor filled with CeO_2 (Urea precipitation)	~4.9	0.83

Table 8.4: Reactor capacitance values calculated with reactor dimensions and obtained from Lissajous slope (m) during plasma OFF phase (using a linear fit from point A to B where the slope is obtained from $y = mx + b$) in CO_2 plasma in PB-DBD.

The difficulty of plasma filaments initiation in the presence of CeO_2 powder is also visible with points 2 and 3 listed above in the observations of figure 8.17. Although the peak amplitude of the applied voltage is the same for all conditions, corner B of the Lissajous figures shows that the plasma initiation starts at higher applied voltage in the presence of CeO_2 (SA) and solgel. This also corresponds to higher maximum amplitudes of current peaks. The measured amplitudes of several amperes (the samples CeO_2 (SA) and CeO_2 (solgel) showed amplitudes way larger than the rest of the samples, 12.96 and 5.96 A, respectively) are much larger than the peak currents of a single individual streamer over a gap of a few mm. These large amplitude are the result of either simultaneous ignition of several streamers synchronized within a few nanoseconds, or due to one intense filament crossing the gas gap after collecting charges on a large

surface of the dielectric barrier by surface discharges. The beginning of the current peaks start also later in times during the rise of the applied voltage. Figure 8.18 shows a zoom of the envelope of the current peaks from figure 8.17 during positive half period of the voltage.

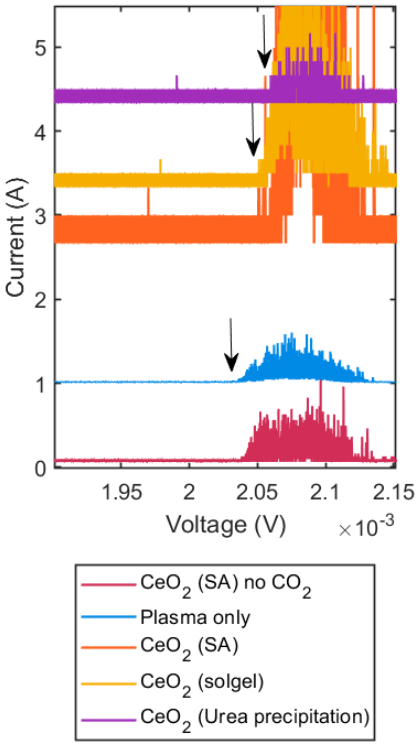

Figure 8.18: Zoom in view of the envelope of the current peaks from figure 8.17. The envelope is offset for clarity.

The arrows points the time (*i.e.* the applied voltage) at which the peaks starts being ignited. In plasma only and CeO_2 (SA) no CO_2 they start at 2.02 mV, followed by CeO_2 (SA) and CeO_2 (solgel) and finally in CeO_2 (Urea precipitation). This could be due a higher potential required to start the discharge, or difference in accumulated charge from previous voltage cycles.

It has been shown in [178] that envelopes signals shows large current amplitudes when the experimental conditions make difficult the accumulation seed electrons necessary to initiate streamer breakdown. The electrical data from figure 8.17 therefore shows that streamer breakdown is more difficult in the presence of CeO_2 (SA) and CeO_2 (solgel), than in the empty reactor. As a result, although the amount of total charge transferred is somewhat smaller, the charges are transferred during a smaller number of 'events' (a total number of filament initiation), and therefore each initiation induces a larger peak current.

More investigation would need to be done to identify the reason for this change in plasma filament ignition behaviour. It could be a consequence of different energy of adsorption of charges on the surface of the different CeO_2 materials. It is however surprising that the CeO_2 (SA) no CO_2 behaves so similarly to the empty reactor. It could be that the density of particle in the powder bed is making the difference from one condition to another. The macroscopic size of the particles could matters, but also the electrostatic repulsion between the particles which can spread them more or less in the reactor. Other works have already shown that metal oxides in the discharge region decreases the transferred charge per half-cycle. The accumulation of charge on the surface of non-conductive packing materials could inhibit the charge transfer between the electrodes because too large amount of charge per unit of length of the streamer need to be deposited on the catalyst [179]. It is also interesting to note that the materials influencing the most plasma ignition (CeO_2 (SA) and CeO_2 (solgel)) are the ones with the smallest BET surface area (see table 8.2). Perhaps this relatively small BET surface influence the charge adsorption on the outer surface of the particles.

In any case, the only material showing a clear increase of CO_2 conversion both in the DBD reactor from Bucharest and in the one from Ecole polytechnique is also the one showing the most influence on the plasma filament ignition. The higher conversion observed with CeO_2 (SA) could therefore be a consequence of its influence on the plasma properties more than its surface reactivity.

Comparison with Al_2O_3

To understand what occurs with other materials in the packed bed configuration, 0.3 g of Al_2O_3 was tested in the same reactor. The tests are being performed with two gas flows at 7.4 sccm and 42.9 sccm. The higher gas flow is the one that will be used for the fluidized bed configuration in the next chapter

but here the gas flow is injected from the top of the reactor so that the gas flow itself is not putting the particles into motion.

Figure 8.19 shows the CO fraction as a function of SEI for plasma only, CeO_2 and Al_2O_3 at 7.4 sccm and plasma only and Al_2O_3 at 42.9 sccm in pure CO_2 plasma in packed Bed - DBD.

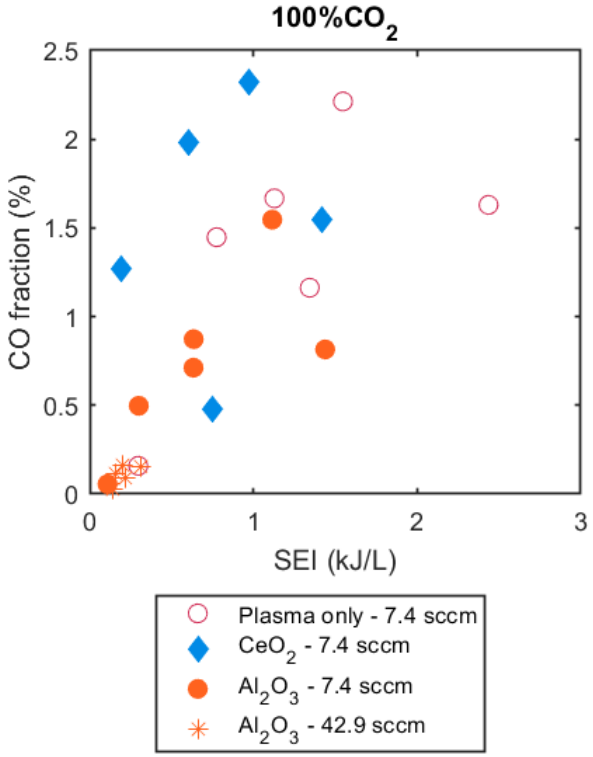

Figure 8.19: CO fraction as a function of SEI for plasma only, CeO_2 (SA) and Al_2O_3 at 7.4 sccm and plasma only and Al_2O_3 at 42.9 sccm in 100%CO_2 plasma in PB-DBD.

As expected, low flow rates results in a larger residence time, therefore a higher SEI and a stronger dissociation (Al_2O_3 experiments). At 7.4 sccm, the CO fraction in the downstream gas tends to be lower with 0.3 g of alumina than in plasma only. On the contrary, plasma with CeO_2 (SA) seems to increase the CO fraction These measurements should be performed again to confirm these trends and evaluate reproducibility error bars but similar results are reported by Ray et al. [180] when comparing several metal oxides including ceria and alumina in CO_2 decomposition with DBD. They suggested that the improved performance of ceria over alumina is due to the ability of O storage/release properties. However, as seen in the previous section, the charge transfer or current peaks should also be discussed. Figure 8.20 the Lissajous plots and envelope current peaks at applied voltage of 30 kV peak-to-peak and 750 Torr.

Plasma only displays a larger charge transfer by half voltage cycle than the rest of the samples. The time of ignition of the first filament seen both on the Lissajous (corners B and D) and on the current peaks envelope is very similar in the case of Al_2O_3 or empty reactor. Only the CeO_2 (SA) shows a higher breakdown voltage, especially at the corner B (positive half period of the voltage). This could be explained by a difference in local electric field enhancement in the presence of CeO_2 compared to Al_2O_3 as packing material affecting the breakdown voltage. However the permittivity of CeO_2 (ϵ_r ~23) is even higher than Al_2O_3 (ϵ_r ~11). More than an effect of electric field enhancement, the difference between the two packing material could point towards a higher surface charge density that each filament needs

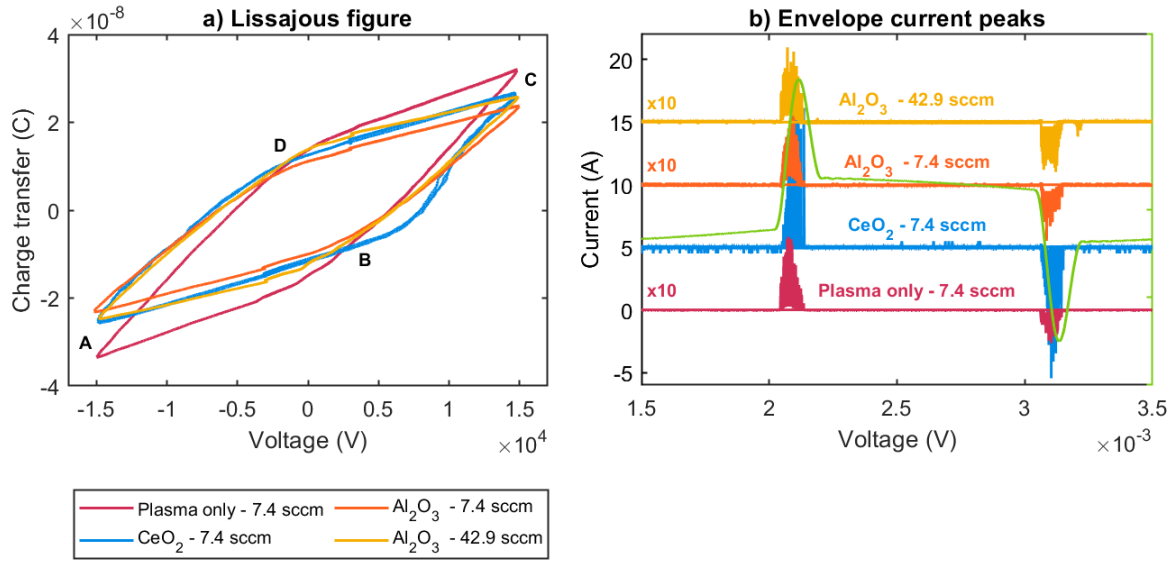

Figure 8.20: a) Lissajous plots of CO_2 plasma and the corresponding b) envelope of positive current peaks for plasma only and with 0.3 g of CeO_2 (SA) and Al_2O_3 at 7.4 sccm and 0.3 g Al_2O_3 at 42.9 sccm in PB-DBD configuration. Voltage: 15 kV amplitude (30 kV peak-to-peak); Pressure: 750 Torr. Envelope current peaks for plasma only, Al_2O_3 at 7.4 sccm and 0.3 g Al_2O_3 at 42.9 sccm are multiplied by 10.

to deposit on the surface of CeO_2 during its propagation because the capacitance of the CeO_2 surface is higher as shown in [181]. The envelope of current peaks confirms that plasma filaments are easier to ignite (and propagate) with Al_2O_3 than CeO_2 (SA) since the highest amplitude of peaks is seen with CeO_2. The others were magnified by ten for better comparison. The increase in flow rate does not change the current peaks amplitude nor the charge transfer as seen for Al_2O_3 at 7.4 and 42.9 sccm. This is explained by the fact that the envelope of current peaks mostly depends on the conditions required for the initiation of filament breakdown. The dissociation fraction is below a few percent for both 7.4 and 42.9 sccm so the breakdown field in the gas phase is not significantly different for both flows. The envelope is therefore only showing that surface charge on the Al_2O_3 particles is similar for both flows.

The reactor capacitance C_{cell} measured with Al_2O_3 is even lower than with CeO_2 (see table 8.5)

Conditions	calculated C_{cell} (pF)	C_{cell} from Lissajous (pF)
Empty reactor	1.05	1.14
Reactor filled with CeO_2 - 7.4 sccm	~4.9	0.95
Reactor filled with Al_2O_3- 7.4 sccm	~4.09	0.85
Reactor filled with Al_2O_3- 42.9 sccm	~4.09	0.76

Table 8.5: Reactor capacitance values calculated with reactor dimensions and obtained from Lissajous slope (m) in figure 8.20 during plasma OFF phase from (using a linear fit from point A to B where the slope is obtained from $y = mx + b$) in CO_2 plasma in PB-DBD.

As discussed in the previous section, this could be due to the fact that Al_2O_3 particles prevent the plasma from igniting over the whole length of the electrodes. As the relative permittivity of Al_2O_3 is lower than the one of CeO_2, the increase of capacitance value due to the presence of the material in the gas gap compensate less the reduction of effective length of the reactor, which could explain the slightly lower values of C_{cell} with Al_2O_3 than with CeO_2. It is however important to note that with Al_2O_3 the reduction of effective length of the reactor is not associated with higher currents peaks as in the case of CeO_2. It would seem that with the alumina particles the plasma cannot be ignited everywhere in the reactor, but where they can, the ignition occurs in a similar way as in the empty reactor (similar

breakdown field). To better understand this effect, the distribution of Al_2O_3 and CeO_2 particles in the reactor should be visualised when the plasma is on and correlated with the plasma filament breakdown zones whcih would require a planar packed bed - DBD reactor as in [182].

In summary, CeO_2 (SA) is a good material that promotes the conversion of CO_2 with plasma but it is still difficult to conclude whether this is due to its influence on the plasma development or to a real surface reactivity. The electrical data clearly shows that CeO_2 (SA) affects the initiation and propagation of plasma filaments in the PB-DBD. The reduction of reactor capacitance in presence of high permittivity materials (both CeO_2 and Al_2O_3) could only be explained by assuming that the plasma ignite only in a part of the reactor, reducing the 'effective' length of the electrode in front of which surface charges accumulate. However this does not result in the same behaviour of maximum of current peaks with both CeO_2 and Al_2O_3. The highest CO_2 conversion is obtained with CeO_2 which is also the packing material inducing the highest maxima of current peaks but the complexity of the filament breakdown and propagation mechanism do not allow to draw a definite correlation between these two observations.

8.6.2 CO_2-CH_4 plasma

The addition of methane to the gas mixture can lead to a change in the plasma characteristics due to the presence of H_2, H or even water. Hence, 30% of methane was added to the gas mixture with CO_2. This will also help to understand the results obtained in University of Bucharest. Figure 8.21 shows the CO fraction as a function of SEI for 70%CO_2-30%CH_4 in plasma only and packed bed mode with CeO_2 (SA), CeO_2 (SA) no CO_2, CeO_2 (solgel) and CeO_2 (Urea precipitation) at 750 Torr.

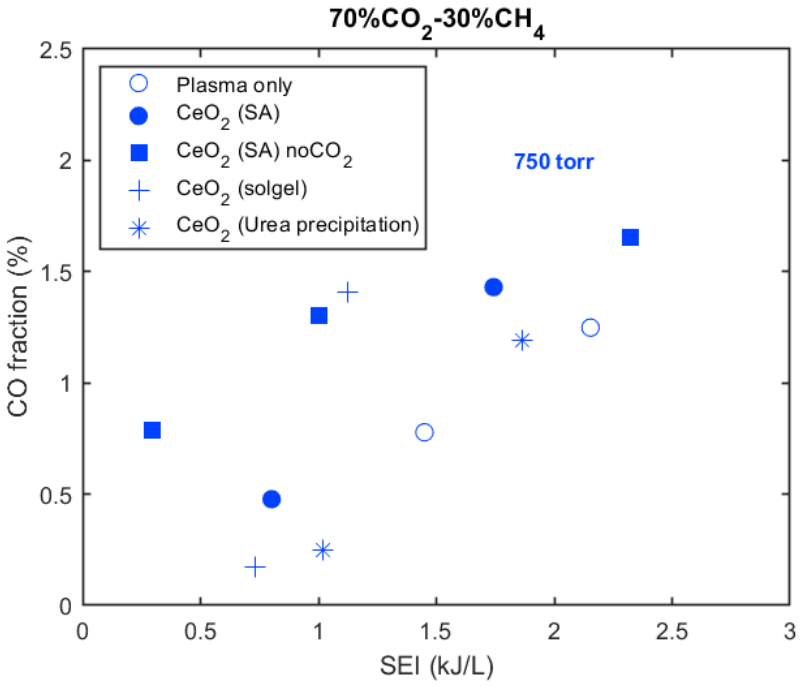

Figure 8.21: CO fraction as a function of SEI for 70%CO_2-30%CH_4 plasma in plasma only and packed bed mode with CeO_2 (SA), CeO_2 (SA) no CO_2, CeO_2 (solgel) and CeO_2 (Urea precipitation) at 750 Torr. Total flow rate: 7.4 sccm.

The results from 70%CO_2-30%CH_4 initial gas mixture are somewhat different to what has been observed for pure CO_2 plasma case. Of course, these observations have to be taken with caution because

the time was missing to perform reproducibility tests (explaining the absence of error bars) and the number of points measured is too limited to draw very affirmative conclusions. Nevertheless the following observations can be made:

- Plasma only and CeO_2 (Urea precipitation) experiments results in similar performance following similar trend.
- CeO_2 (SA), CeO_2 (SA) no CO_2 and CeO_2 (solgel) resulted in increased CO fraction.

By looking again to the electrical data, figure 8.22 shows the Lissajous figures and the envelope of the current peaks for the experiments for plasma only and with CeO_2 (SA), CeO_2 (SA) no CO_2, CeO_2 (solgel) and CeO_2 (Urea precipitation) in 70%CO_2-30%CH_4 plasma PB-DBD, 30 kV peak-to-peak, 750 torr. The main characteristics obtained in pure CO_2 remain here. From the Lissajous figure, ΔQ for plasma only is larger than for the packed bed with ceria materials, and the value of C_{cell} is higher with plasma only and CeO_2 urea, than with other CeO_2 materials. Regarding the envelope of the current peaks, the CeO_2 (SA) is again inducing by far the largest current peak amplitudes. However a few differences appear when adding CH_4 compared to the pure CO_2 case:

- The current peaks amplitudes in CeO_2 (SA) no CO_2 and CeO_2 (urea precipitation) increased in comparison to CO_2 plasma case (figure 8.17b) and are now higher than for plasma only (especially the CeO_2 (SA) no CO_2 case).
- Some small current peaks are observed through the whole applied voltage period in the case of CeO_2 (SA) and CeO_2 (SA) no CO_2.
- Maxima of current peaks seem to be higher during negative half period of the applied voltage compared to the pure CO_2 case with CeO_2 packing material but not with plasma only.

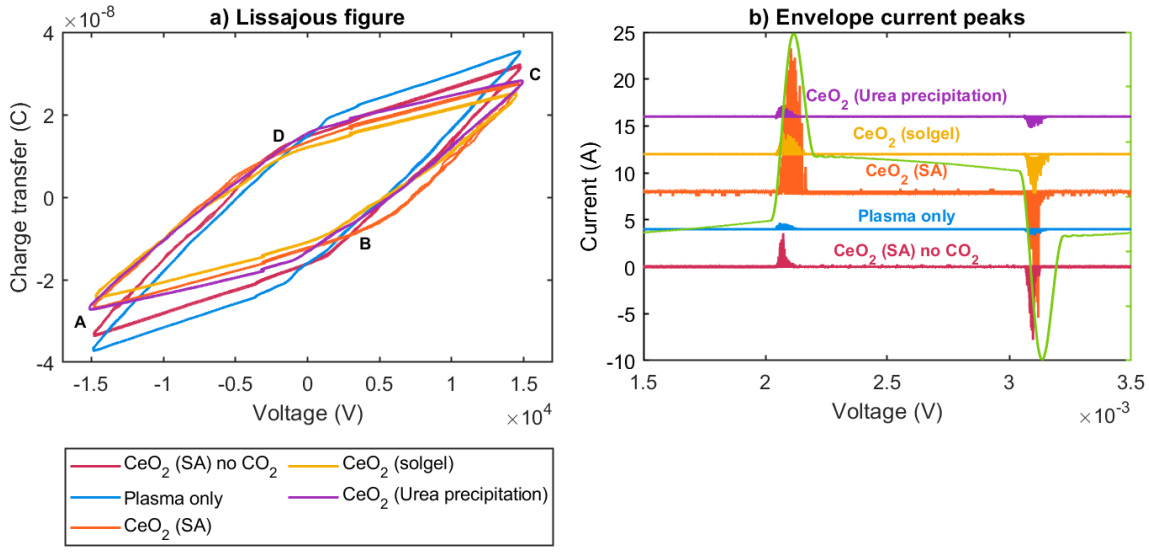

Figure 8.22: a) Lissajous figure and b) envelope of the current in the positive V from experiments for plasma only and with CeO_2 (SA), CeO_2 (SA) no CO_2, CeO_2 (solgel) and CeO_2 (Urea precipitation) in 70%CO_2-30%CH_4 plasma PB-DBD, 15 kV amplitude (30 kV peak-to-peak), 750 torr. The envelope corresponds to the accumulation of 1000 periods. The envelope is offset for clarity. One voltage cycle (green) is presented for further discussion.

The appearance of small current peaks throughout the period of the applied voltage in the presence of CeO_2 (SA) suggests the possibility that charges accumulated on the CeO_2 surface are sufficient to generate small plasma discharges even when the applied voltage is relatively low. This phenomenon was already visible in the case of CeO_2 (SA) in pure CO_2 (see figure 8.17) but is more clearly visible here in the presence of CH4 on both CeO_2 (SA) materials.

The presence of hydrogenated species from methane decomposition could also affect the charge adsorption on CeO_2. It is known for instance that water on surfaces makes streamer breakdown more difficult as shown in [183]. In chapter 5 the formation of water and OH groups on CeO_2 surface under CO_2-CH_4 plasma has been shown. The appearance of larger current peaks especially during negative half period with all the CeO_2 packing materials could be a consequence of water adsorbed on the surface. Interestingly, the appearance of these extra bursts of high current events correspond to the cases for which an increased formation of CO is observed in figure 8.21. However more measurements would be needed to confirm the beneficial effect of these strong current events on the conversion of CO_2 in presence of CeO_2.

Conditions	**calculated C_{cell} (pF)**	**C_{cell} from Lissajous (pF)**
Empty reactor	1.05	1.14
Reactor filled with CeO_2 (SA) no CO_2	~4.9	1.15
Reactor filled with CeO_2 (SA)	~4.9	0.96
Reactor filled with CeO_2 (solgel)	~4.9	0.9
Reactor filled with CeO_2 (Urea precipitation)	~4.9	0.83

Table 8.6: Reactor capacitance values calculated with reactor dimensions and obtained from Lissajous slope (m) in figure 8.22a during plasma OFF phase (using a linear fit from point A to B where the slope is obtained from $y = mx + b$) in 70%CO_2-30%CH_4 plasma in PB-DBD.

8.7 Conclusions

The packing of cerium oxide in a DBD reactor has mostly a positive effect on the conversion of CO_2 but it remain difficult to know if this beneficial effect is due to surface reactivity or to a modification of streamer breakdown mechanism. DRIFT spectra allowed to demonstrate that formates species are surface intermediates in DRM reaction on CeO_2 during CO_2-CH_4 plasma with two different configurations: DBD at atmospheric pressure and DC glow discharge at low pressure. Carbonates are the main source of the formates structure in CeO_2 which decline with time. This suggests that despite the difference in conditions and discharges presented in this work, one at atmospheric pressure (DBD) and the other at low pressure (DC glow discharge), the formation of formates probably follow the same mechanism.

In general, the presence of hydrogenated compounds on the surface can obviously induce chemical reactions but also affect the energy of adsorption of charges on the surface and thus the initiation of the plasma. Moreover, even for a given material, the conversion may vary according to the morphology (size, surface area, etc.) or composition (Zr) and the way the plasma can ignite in between the material particles. Throughout this chapter, the electrical data have shown to provide valuable information about how the energy is being deposited in the plasma/catalytic system for a given power transferred. The envelope of current peaks is only the accumulation maximum amplitudes over 1000 periods, so the precise number of current peaks and their amplitude during each period of voltage can vary a lot from cycle to cycle. To go deeper in the statistical behaviour of the filaments it would require to analyse the distribution of charge transferred per filaments as function of time as done in [178] but this is very time consuming. Using the current envelope already gives quick information about how the filaments generally occur in a particular configuration.

The difficulty to interpret better the change in the current envelope observed throughout this chapter

comes from the changes of structure of the particle bed happening during the plasma exposure.Indeed, despite the flow going from top to bottom of the reactor, the cerium oxide (and alumina) powder can stick to the dielectric and slowly move up because of electrostatic forces. Evidence of such phenomena is depicted in figure 8.23 and it was observed not only in LPP for the PB-DBD but also in the DBD in University of Bucharest (see also the next chapter 9 with the FB-DBD configuration with Al_2O_3). The plasma induce a negative charge on the particle of the packing material causing electrostatic repulsion between the particles and often causing the powder to stick to the glass wall of the reactor even after the plasma is turned off. Such phenomena can definitely have an influence on the current peaks, the total amount of charge transferred over time and generally, affect how the streamers will ignite. In other works, glass wool is often use to maintain the powder bed in place and avoid the displacement of the catalyst particles. However it is then questionable whether the plasma ignites more inside the glass wool or really in between the catalyst particles. More detailed investigation should focus on how the streamer really ignite in the core of packed bed configuration depending on catalyst particles macroscopic morphology.

Beyond these uncertainties as to how the streamers (plasma filaments) are initiated in the catalytic bed, the conversion performances were tested with different ceria materials where commercial CeO_2 resulted in the best performance. The reasons behind this are not clear, however, it seems that the surface area (the lower the better!) and amount of basic sites play an important role. In any case, through the testing of two different DBD configurations with very different energy range (from a few kJ/L to few tens of kJ/L), the same material, CeO_2 (SA) resulted in the largest conversion. This material happened to be the one also generating the largest current peaks amplitudes which could perhaps explain the improved CO_2 conversion. The structure of the ceria materials tested here was not permanently altered by the plasma as demonstrated by XRD analysis.

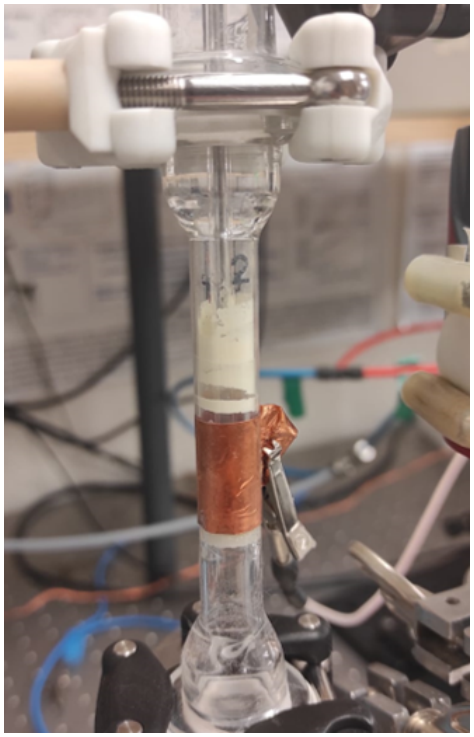

Figure 8.23: Picture of the PB-DBD reactor with CeO_2 (Urea precipitation) during 70%CO_2-30%CH_4 plasma experiments at 750 Torr.

To conclude, figure 8.24 shows the data extracted using the PIONEER database tool for only CO_2 plasma in DBD (without catalyst) across different conditions. The purpose of this graph is to show that our configuration in empty reactor is consistent to what has been reported in the literature. Definitely,

the results from this work fall in the low range of SEI along with some reported by Brehmer et al. (see figure 8.15).

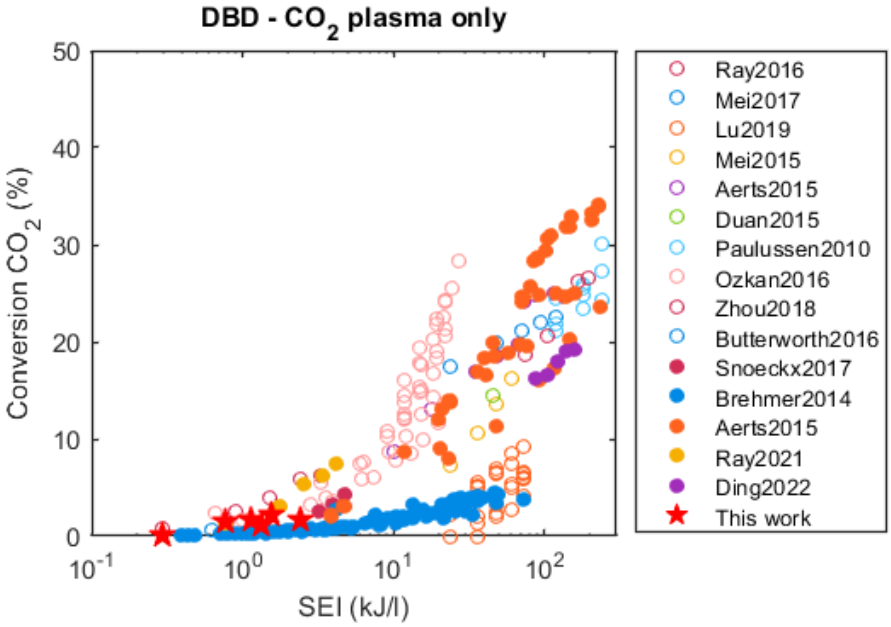

Figure 8.24: Conversions of CO_2 as a function of SEI for DBD plasmas in pure CO_2 extracted from literature using the PIONEER database tool (www.db.co2pioneer.eu, date of extraction: 21/02/2023). Data from this work are shown as red stars.

Chapter 9

Fluidized bed - DBD with Alumina particles

Contents

9.1 Introduction

Fluidized beds coupled with plasma reactors are still a novelty in the field of plasma catalysis and very few are reported for CO_2 conversion [54–56]. In this thesis, we focused on the fluidized bed coupled with a DC glow discharge as plasma source mainly for fundamental studies as reported in chapter 7. Hereinafter, fludized bed is combined with DBD plasma reactor to evaluate the performance and to compare with the literature. In this chapter, we present the experimental results from Fluidized bed - DBD (FB-DBD) varying different conditions with CO_2, CO_2-CH_4 and CO_2-H_2 plasmas. The minimum fluidization velocity is calculated and subsequently measured using CO_2 gas and alumina. CO fractions and electrical data are used for the discussion. Finally we provide a comparison between fluidized bed - DBD and packed bed - DBD.

9.2 Experimental procedure

Alumina particles are tested as fluidizing material in a fluidized bed - DBD reactor at atmospheric pressure. In the previous chapter CO_2 conversion was not improved by Al_2O_3 particles in packed bed configuration but the goal here is to evaluate if the fluidization of dielectric particle can affect the properties of the plasma as it has been done with glow discharge fluidized bed in chapter 7.

The schematic of the configuration is shown in figure 9.1. The same material (neutral γ-Al_2O_3) used in FB-GD experiments in chapter 7 is tested at atmospheric pressure in a DBD configuration. The

experiments are compared with 0.3 and 0.5 g of alumina bed with the empty reactor under the same conditions of pressure, applied voltage and total flow rate.

CO_2 only and CO_2-CH_4 gases are sent from the bottom of the reactor at different flow rates. The minimum fluidization velocity is calculated and subsequently measured using CO_2 gas and alumina as explained in section 9.3.

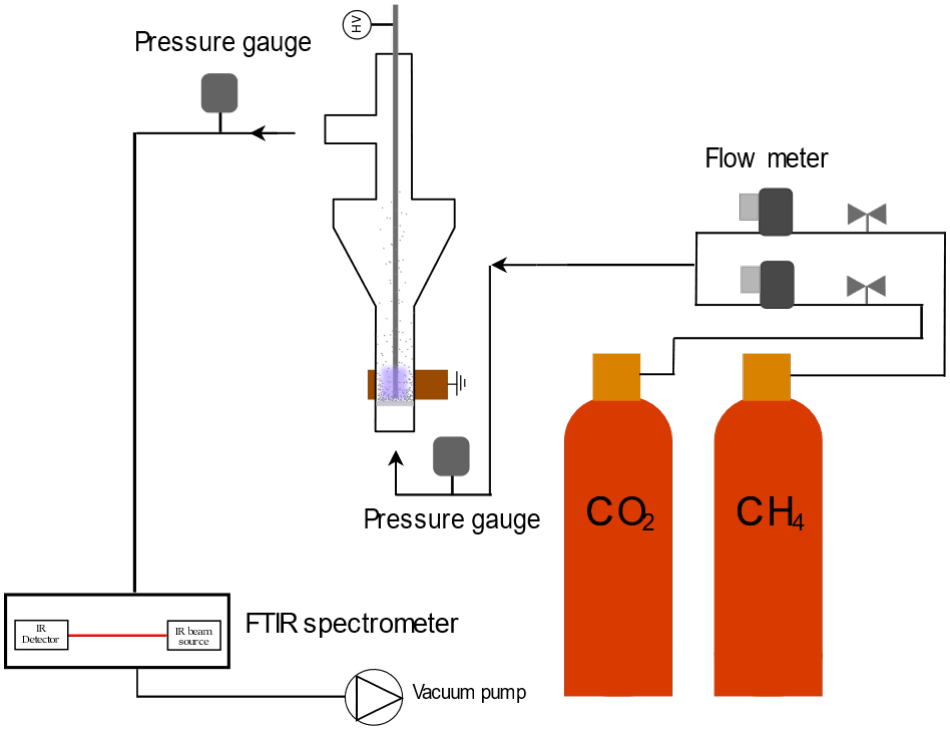

Figure 9.1: Schematic of the setup used for the testing of Al_2O_3 at atmospheric pressure.

The exit of the reactor was connected to the entrance of an IR cell to analyse the downstream gas with an ARCoptix FTIR. The CO fraction was estimated by the area of the band 2182 cm^{-1} and extrapolated by a linear regression obtained by CO calibration in O_2 gas. Details on the calibration are described in the experimental chapter 2.

The schematic of the electric circuit is the same as shown in figure 8.4a from chapter 8. The voltage was varied from 25 to 30 kV peak-to-peak. The power measurements were performed by plotting Lissajous figures to estimate the average power (figure 8.4b). The measurements of the current were done using a Rogowski coil between the ground electrode of the reactor and the measurement capacitor. The envelope of the current peaks corresponds to the accumulation of 1000 periods.

9.3 Measurement of u_{mf}

The minimum fluidization velocity (u_{mf}) is defined as the superficial gas velocity at which the drag force of the upward moving gas becomes equal to the weight of the particles in the bed. It is one of the most important parameters associated with a fluidized bed system and it has to be calculated and measured before carrying out any catalytic testing. There are plenty of equations reported in the literature as reviewed here [108]. In our case, the bed voidage at minimum fluidization (ϵ_{mf}) and sphericity (φ) of alumina particles remain unknown. Therefore, the equation adapted for coarse particles extracted from the book by Kuni et al. is used here to estimate u_{mf} without knowing these two parameters [17]:

$$Re_{mf} = [28.7^2 + 0.0494 \cdot Ar]^{1/2} - 28.7 \tag{9.1}$$

$$\frac{d_P u_{mf} \rho_g}{\mu} = \left[28.7^2 + 0.0494 \left(\frac{d_p^3 \rho_g (\rho_s - \rho_g) g}{\mu^2}\right)\right]^{1/2} - 28.7 \tag{9.2}$$

Table 9.1 compiles the experimental values regarding diameter of alumina particles, density of the bulk alumina, gas density and viscosity.

Parameters	**Value**
Particle diameter d_p	1.05 x 10^5 m
Al_2O_3 density ρ_s	1.720 kg/m^3
CO_2 gas density ρ_g	1.87 kg/m^3
CO_2 gas viscosity μ	1.47 x 10^5 kg/ms
Gravitational acceleration g	9.81 m/s^2

Table 9.1: Experimental values for the estimation of u_{mf}

Substituting the values from the table 9.1 in equation 9.2, the minimum fluidization velocity results in:

$$u_{mf} = 0.01083\ m/s = 65\ cm/min \tag{9.3}$$

Considering the radial area of the reactor ($A_{reactor}$), then the volumetric flow rate (ϕ_{mf}) in sccm is:

$$\begin{aligned} \phi_{(mf)} &= u_{mf} \cdot A_{reactor} \\ &= 65\ cm/min \cdot 0.6594\ cm^2 \\ &= 42.86\ sccm \end{aligned} \tag{9.4}$$

To test this estimation, we measure the pressure drop as a function of gas velocity based on a procedure described in ASTM D7743 – 12 for Geldart B type of particles. Small increments of CO_2 gas flow are sent to the empty reactor that result in a pressure drop caused by the embedded porous glass disk. The pressure drop is measured by two pressure gauges located in the gas line at the entrance and exit of the reactor. The gradual increments are done every 1.48 sccm (Δu = 2.24 cm/min) of CO_2 until reaching 3 times the estimated ϕ_{mf} which is 128.76 sccm corresponding to u = 195.16 cm/min.

$$\delta P \uparrow_{empty\ reactor} = P_{\phi} - P_{750\ Torr} \tag{9.5}$$

Then, 0.3 g of Al_2O_3 are added to the reactor and the same procedure is repeated:

$$\delta P \uparrow_{alumina} = P_{\phi} - P_{750\ Torr} \tag{9.6}$$

Then, $\delta P \uparrow_{empty\ reactor}$ is subtracted from $\delta P \uparrow_{alumina}$ to leave the pressure drop (ΔP) caused only by the bed. The velocity where the pressure drop begins to remain constant is the u_{mf}.

$$\Delta P = \delta P \uparrow_{alumina} - \delta P \uparrow_{empty\ reactor} \tag{9.7}$$

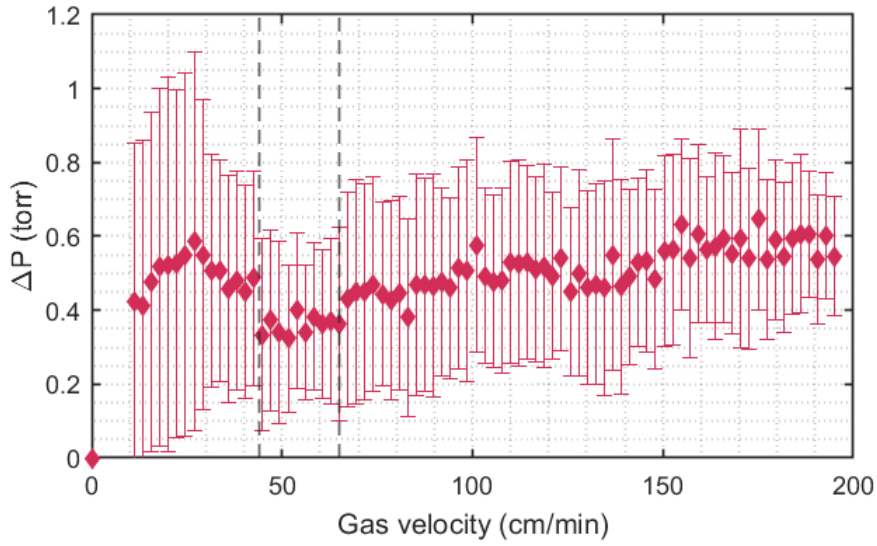

Figure 9.2: Pressure drop as a function of gas velocity caused by the presence of 0.3 g Al_2O_3 bed. The error bars represent +/- standard deviation from 3 separated measurements.

Figure 9.2 shows the pressure drop as a function of gas velocity caused by the presence of 0.3 g Al_2O_3 bed. Until ~40 cm/min, the pressure drop increases rapidly probably due to the porous glass disk. Around 44 cm/min, the pressure drop stabilizes and remains constant (between the vertical dashed lines) until 65 cm/min. This point corresponds to the value estimated in 9.4. The powder starts to slightly expand indicating that at 65 cm/min is the minimum velocity required for the bed to fluidize. After this point, the pressure drop continues increasing. To position our finding in the literature d_p^* and u^* are estimated using the Archimedes (equation 2.14) and Reynolds number (equation 2.13):

$$d_p^* = Ar^{1/3} \tag{9.8}$$

$$u^* = \frac{Re}{Ar^{1/3}} \tag{9.9}$$

The values obtained are $d_p^* = 5.524$ and $u^* = 0.0261$. They are represented by a red star in figure 9.3.

The values estimated fall in the region expected for the size of the Al_2O_3 particles although they barely fall into the Geldart B category. A bubbling regime is recommended for a better dispersion in the reactor but due to the low catalytic activity of neutral Al_2O_3, a reduced flow rate is indeed beneficial for the conversion by plasma means.

In summary, a total flow rate of 42.8 sccm of CO_2 is used for the rest of the experiments herein reported.

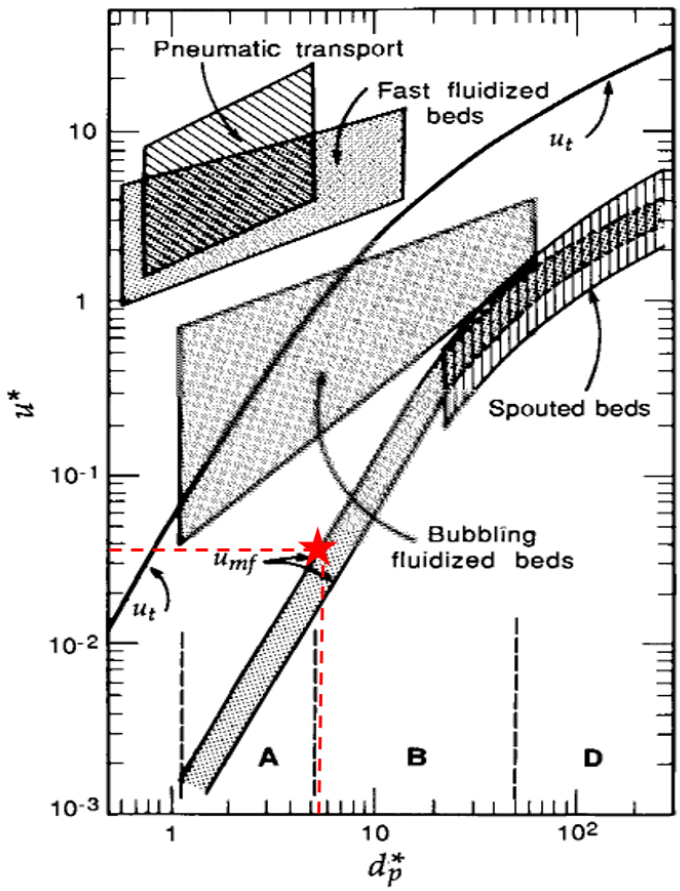

Figure 9.3: u^* as a function of d_p^* for Geldart group A, B and D. The estimated value is represented by the red star. Figure extracted from [17].

9.4 CO_2 plasma in FB-DBD

CO_2 plasma was tested at different conditions to obtain CO fractions in different values of SEI (table 9.2). The results of the experiments are shown in figure 9.4.

Parameters	Value
Voltage amplitude (peak-to-peak)	12.5,13.5 and 15 kV (25, 27 and 30 kV)
Pressure	450, 550, 650 and 750 torr
Flow rate	42.9 and 128.7 sccm
Amount of Al_2O_3	0, 0.3 and 0.5 g

Table 9.2: Parameters tested during CO_2 plasma in FB-DBD with Al_2O_3 particles.

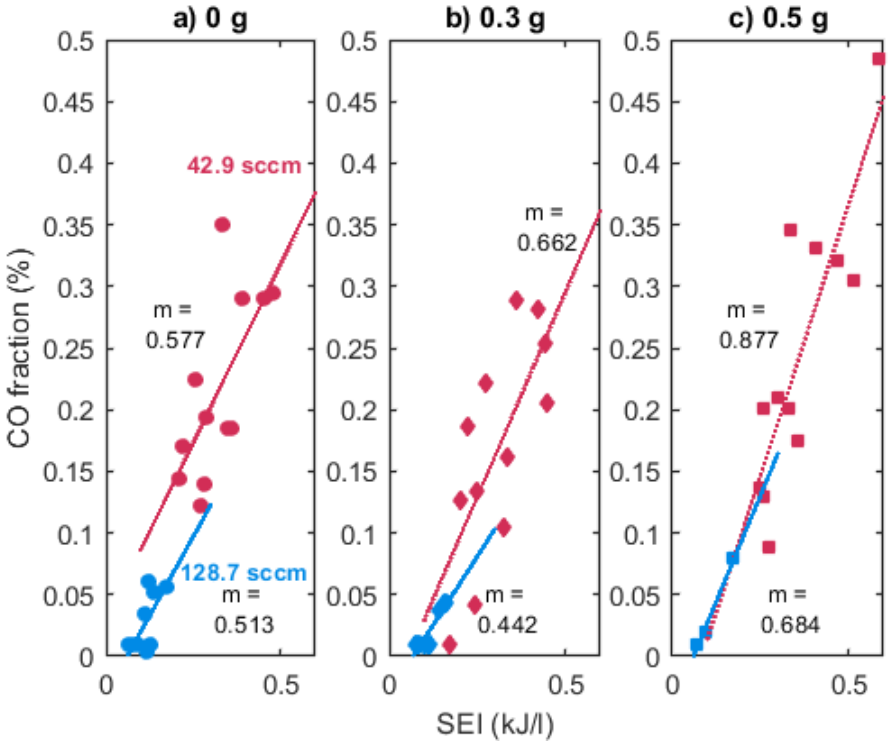

Figure 9.4: CO fractions as a function of SEI for a) 0 g (empty reactor), b) 0.3 and c) 0.5 g of alumina for 42.9 sccm (red) and 128.7 sccm (blue) gas flow rate. The linear fitting is represented by a straight dotted line along the slope next to the corresponding fit.

Here, two flow rates are compared: ϕ_{mf} = 42.9 sccm in red and 3*ϕ_{mf} = 128.7 sccm in blue. The largest flow at 128.7 sccm results into less than 0.1% CO fraction. When the flow rate is reduced to 42.9 sccm, the CO fraction ranges 0.1 - 0.4 % for empty reactor. With 0.3 g, the CO fraction range is reduced to 0.1-0.3 % while with 0.5 g of alumina, the CO fraction extends to almost 0.5%. A linear fitting is performed ($y = mx+b$) and the slope (m) is shown in the same figure next to the corresponding fit. For empty reactor, the slope is basically the same corresponding to 0.5 l/kJ for both flows. This indicates that the CO fraction depends mostly on the residence time in this case. The slopes differ in the case of 0.3 g and 0.5 g of alumina, with 0.66 and 0.87 for 42.9 sccm, meaning about 50% more than for 128.7 sccm. m increases with respect to empty reactor at the same flow showing clearly the increase of CO fraction with less energy input. In the case of 128.7 sccm, m does not follow a clear trend with increasing quantity of Al_2O_3 but the very small range of CO fraction obtained with this flow makes the accuracy of the slopes questionable. The scattering of the data would require to confirm these results with more measurements but the increase of CO_2 conversion with Al_2O_3 at 42.9 sccm seems significant and was not observed in packed bed configuration in the previous chapter. We turn to the electrical data, specifically the Lissajous figures in Figure 9.5a_1 for these 3 cases with flow rates at 42.9 in CO_2 plasma to gain insights on the plasma behaviour.

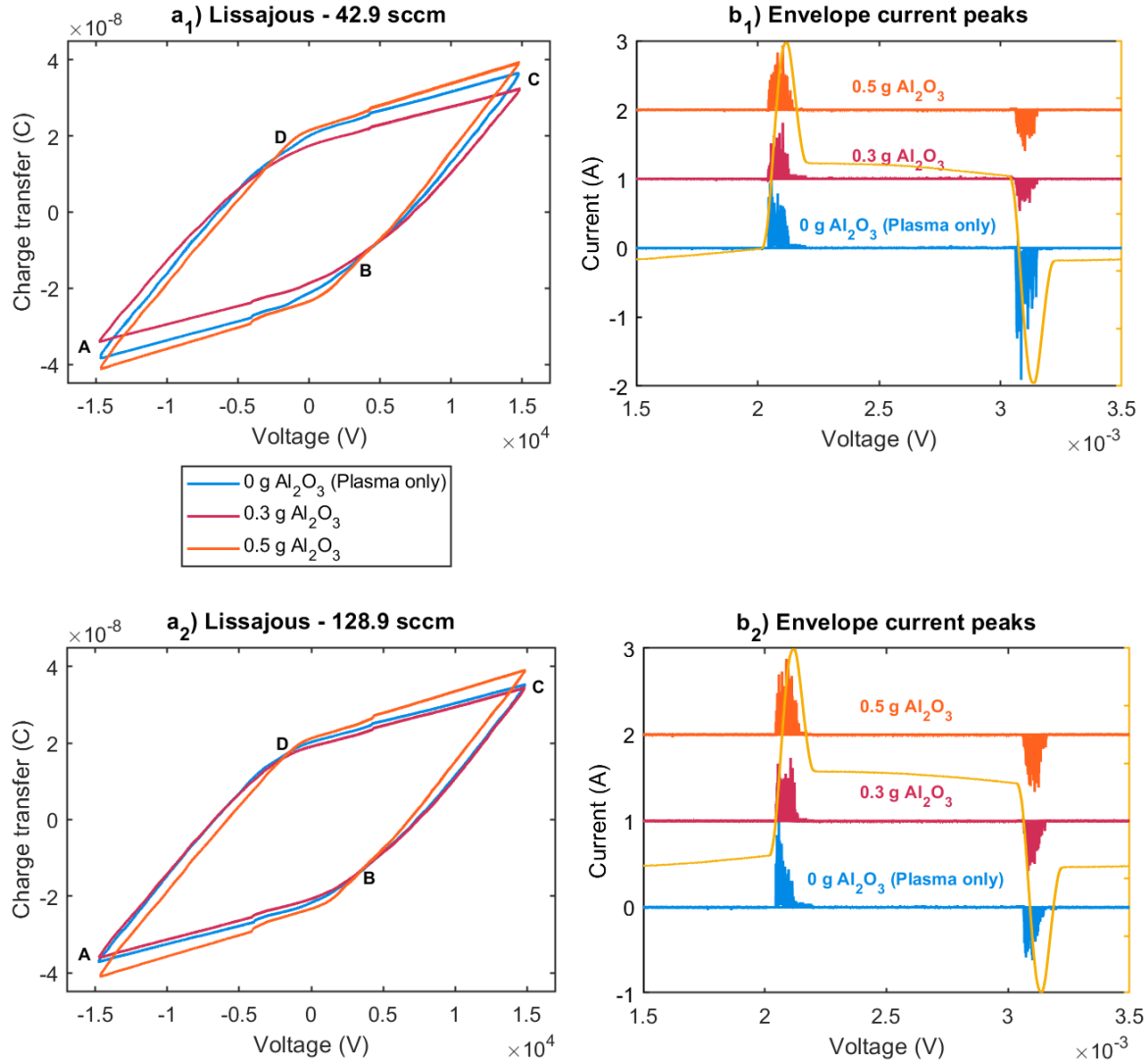

Figure 9.5: Lissajous plots of CO_2 plasma at a_1) 42.9 sccm and a_2) 128.9 with the corresponding envelope current peaks in b_1) and b_2), respectively for 0 g Al_2O_3 (plasma only), 0.3 and 0.5 g of Al_2O_3. Voltage: 15 kV amplitude (30 kV peak-to-peak); Pressure: 750 torr.

The charge transfer is similar with 0.5 g Al_2O_3 and empty reactor while it is lower with 0.3 g of Al_2O_3. At 128.9 sccm (figure 9.5a_2), 0.5 g Al_2O_3 transfers a bit more charge while the other two cases are very similar. The capacitance of the reactor C_{cell} shown in table 9.3 are also very similar in the 3 cases. The presence of Al_2O_3 particles seems to have less influence on the effective length of the reactor in fluidized bed configuration than in packed bed configuration (see figure 8.20 from chapter 8). This is consistent with the idea that when the particle bed is too dense, plasma filaments have difficulty initiating. On the contrary, when the bed is fluidized, the entire surface of the glass tube facing the ground electrode is accessible to the streamers at some point in time and thus the effective capacity of the reactor is very similar to that of the empty reactor.

Looking at the current peaks envelope in figure 9.5b, the amplitude is almost 1 A for 0.5 g Al_2O_3 and plasma only at both flow rates. Only 0.3 g of alumina results in slightly less charge transferred in the plasma. These differences between the three configurations are minimal and in general much less marked than the differences observed in the packed bed configuration. The moving particles in the fluidized bed

Conditions	**calculated C_{cell} (pF)**	**C_{cell} Lissajous (pF)** *42.9 sccm*	**C_{cell} Lissajous (pF)** *128.9 sccm*
Empty reactor	1.05	1.01	0.96
Reactor filled with 0.3 g Al_2O_3	~4.09	0.95	0.98
Reactor filled with 0.5 g Al_2O_3	~4.09	1.12	1.12

Table 9.3: Reactor capacitance values calculated with reactor dimensions and obtained from Lissajous slope (m) in figure 9.5a_1 and a_2 during plasma OFF phase from (using a linear fit from point A to B where the slope is obtained from $y = mx + b$) in CO_2 plasma in FB-DBD.

leave much more gas space for the plasma filaments to develop in a manner very similar to what they do in the empty reactor, despite the fact that the alumina particles are being negatively charged. This very weak influence of alumina particles in fluidized bed configuration is perhaps due to a limitation of the reactor used in this work. Indeed, the height of the electrodes used ($L = 2.1\ cm$) is small because of the power limitations of the high voltage generator used. As a result, the particles in the fluidized bed leave the discharge zone quickly. Moreover, the electrostatic repulsion phenomenon clearly modifies the way the powder moves when the plasma is on. Figure 9.6 shows the bed with fresh alumina and flowing gas, then with plasma on and finally when the plasma is off again.

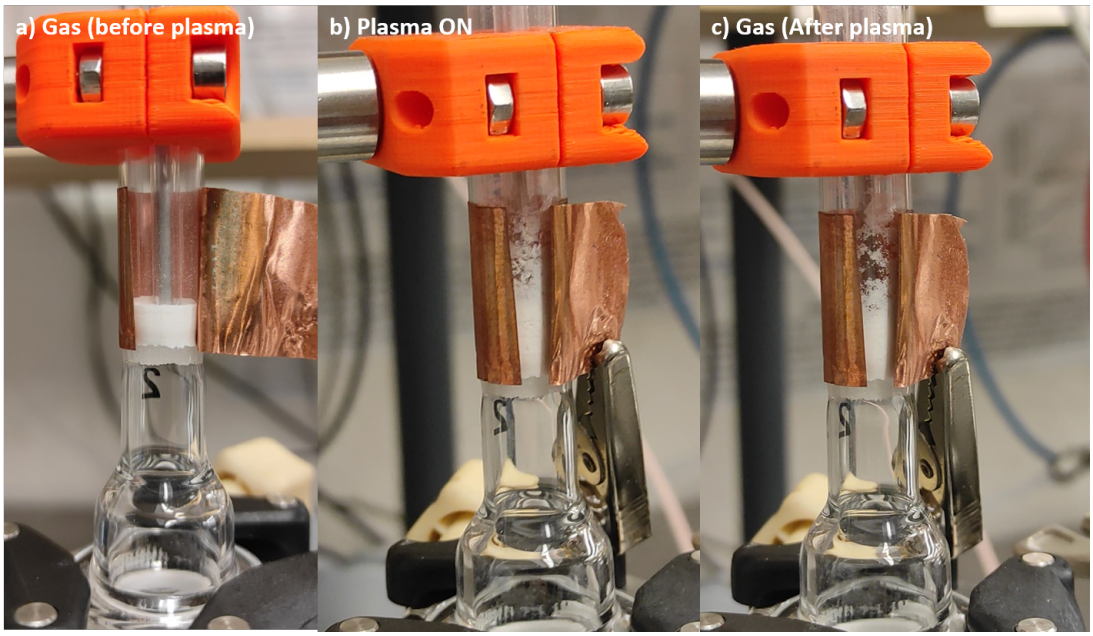

Figure 9.6: Picture of FB-DBD with fresh Al_2O_3 in a) gas (before plasma), b) Plasma is on and c) gas again (after plasma).

When the plasma is ignited, the particles start to move randomly and do not follow a typical movement going upward and downward from a conventional fluidized bed. The plasma discharges are capable of charging the Al_2O_3 particles a large part of them stick to the surface of the glass wall. When the plasma is switched off and only gas is flowing, most of the particles remain in the surface and do not fall down to the embedded porous glass disk. Subsequent experiments with the same material allow the material to maintain the electrostatic charge and move outside the discharge zone and remain there. This effect has already been reported in other FB-DBD [56]. Clearly, the negative charge of the particles could have an influence on how the discharge propagates from one glass wall to the other passing through moving Al_2O_3 negative solid particles. However in our small reactor configuration, a significant proportion of the particles are as a result out of the discharge zone which probably diminish their effect on the discharge. Despite that, the flow imposed based on the u_{mf} seems still essential in the moving of the particles

affecting the resulting CO fraction, and the alumina particles that were not increasing the conversion in packed bed configuration seem to be beneficial in fluidized bed configuration.

9.5 CO_2-CH_4 plasma in FB-DBD

The addition of CH_4 in the initial gas mixture is tested. Here, 70%CO_2-30%CH_4 and 95%CO_2-5%CH_4 are tested varying the SEI. Besides, another material is tested here as catalyst composed of 10% wt Ni/Al_2O_3. Figure 9.7 displays the CO fraction as a function of SEI for 70%CO_2-30%CH_4 and 95%CO_2-5%CH_4 initial gas mixtures.

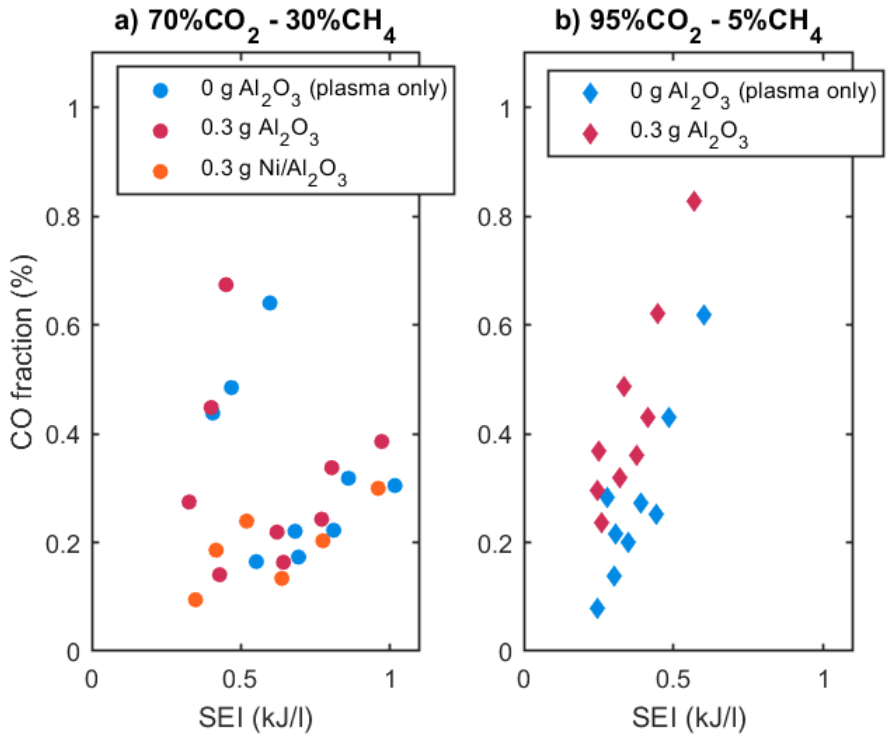

Figure 9.7: CO fraction as a function of SEI for a) 70%CO_2-30%CH_4 and b) 95%CO_2-5%CH_4 initial gas mixtures.

The comparison of both gas mixtures, one at 95%CO_2 and other at 70%CO_2 demonstrate that the dilution of CO_2 in the initial gas mixture does not help to increase the CO fraction. Actually, it does not help either on terms of energy input into the gas. Around 1 kJ/l only 0.4% fraction is obtained for 70%CO_2 while for 95%CO_2, only half of kJ/l is needed to generate 0.8% CO fraction.

Regarding the CO fractions for 70%CO_2-30%CH_4 initial gas mixture, no clear trend is observed among plasma only, 0.3 of Al_2O_3 and 0.3 g of Ni/Al_2O_3. The Lissajous figure do not show significant difference amongst the 5 experiments presented in figure 9.8a. It is worth to mention that in 70%CO_2-30%CH_4 experiments the amplitude of current peaks can reach 2 A except with plasma only. In the presence of alumina, with Ni or without, the amplitude is very similar. Nonetheless, the conversion of CO_2 does not seem altered in this gas initial concentration.

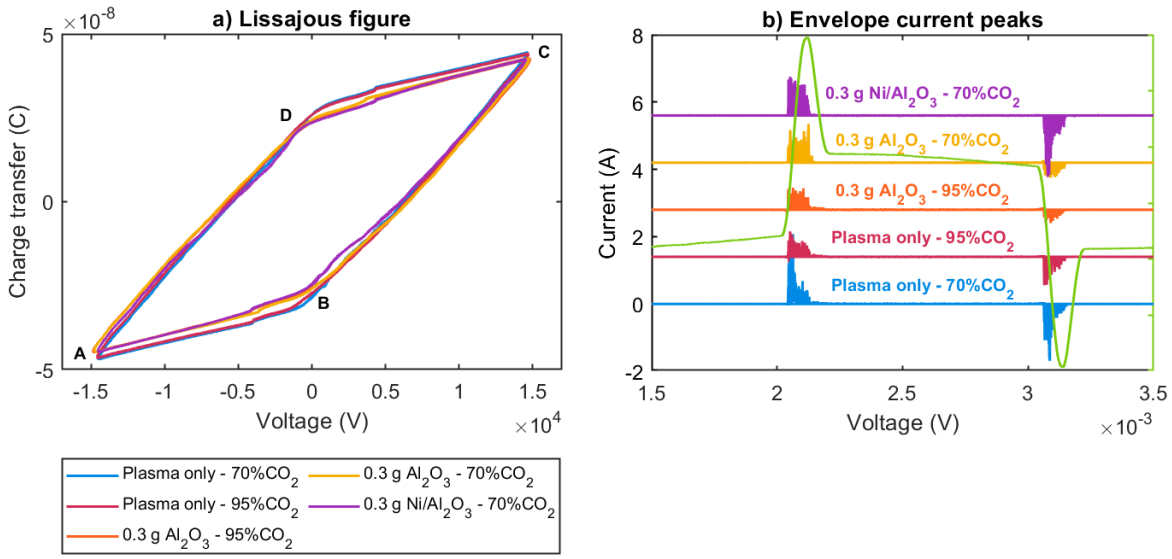

Figure 9.8: a) Lissajous plots of CO_2-CH_4 plasma and the corresponding b) envelope of current peaks for plasma only, 0.3 g Al_2O_3 and 0.3 g Ni/Al_2O_3. Voltage: 15 kV amplitude (30 kV peak-to-peak); Pressure: 750 torr.

Conditions	**calculated C_{cell} (pF)**	**C_{cell} Lissajous (pF)** *$70\%CO_2$-$30\%CH_4$*	**C_{cell} Lissajous (pF)** *$95\%CO_2$-$5\%CH_4$*
Empty reactor	1.05	1.00	0.99
Reactor filled with 0.3 g Al_2O_3	~4.09	1.09	1.14
Reactor filled with 0.3 g Ni/Al_2O_3	-	1.21	-

Table 9.4: Reactor capacitance values calculated with reactor dimensions and obtained from Lissajous slope (m) in figure 9.8a during plasma OFF phase from (using a linear fit from point A to B where the slope is obtained from $y = mx + b$) in CO_2-CH_4 plasma in FB-DBD.

For $95\%CO_2$-$5\%CH_4$, neither the envelope of current peaks nor the Lissajous figures show significant difference in the presence of alumina in comparison to plasma only. The increase of CO fraction with Al_2O_3 particles in the discharge when the initial concentration of CH_4 is very low (5%) could be the result of more efficient CH_x species oxidation. On the contrary, with $30\%CH_4$ the CO fraction appears to be diminished.

9.6 CO_2-H_2 plasma in FB-DBD

CO_2 methanation is tested in FB-DBD configuration. For this reaction, $20\%CO_2$ was mixed in $80\%H_2$ gas and the pressure and applied voltage was varied at 42.9 sccm total flow rate. Figure 9.9 shows the CO fraction as a function of SEI. CO fraction does not exceed 0.1 % in Plasma only and plasma with 0.3 g despite the dilution of $20\%CO_2$ into H_2. Meanwhile, 0.3 g of Ni/Al_2O_3 does not lead to almost any CO formation. At the same time no infrared bands are seen in the IR spectra that correspond to CH_4.

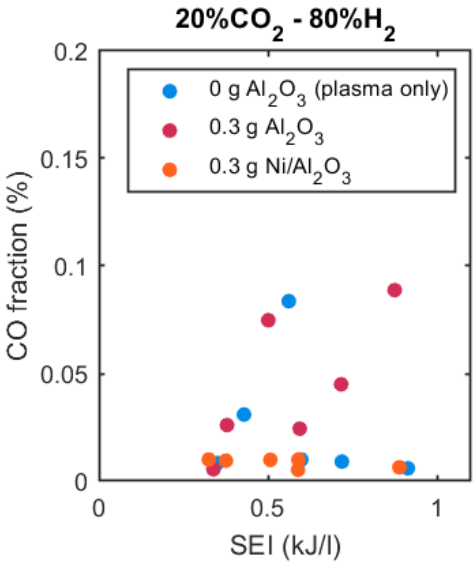

Figure 9.9: CO fraction as a function of SEI for 20%CO_2-80%H_2 initial gas mixture for 0 g Al_2O_3 (plasma only), 0.3 g of Al_2O_3 and 0.3 g Ni/Al_2O_3.

The dilution of CO_2 in the total gas flow rate is expected to result in an increase in the CO fraction. To ease the discussion, figure 9.10 shows a comparison in terms of CO yield for 20%CO_2-80%H_2 and 100%CO_2 as a function of SEI. CO can only come from CO_2 conversion, then:

$$Yield\ of\ CO\ (\%) = \frac{[CO]_{out}}{[CO_2]_{in}} * 100 \tag{9.10}$$

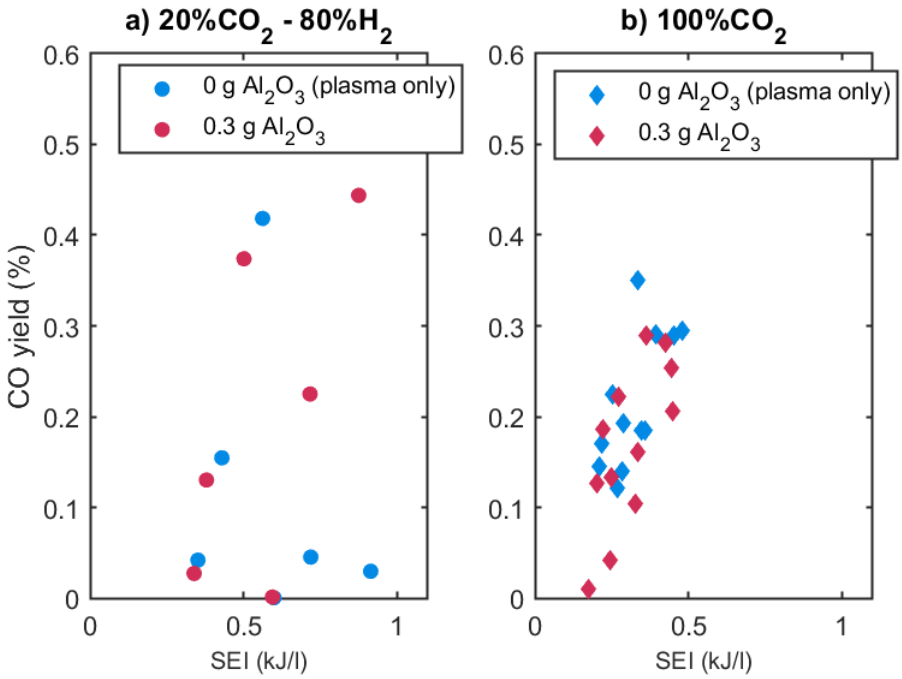

Figure 9.10: CO yield as a function of SEI in kJ/l for a) 20%CO_2-80%H_2 and b) 100%CO_2 initial concentrations for 0 g (plasma only), 0.3 g of Al_2O_3 and 0.3 g Ni/Al_2O_3.

No effect of the alumina particles is seen on the CO yield. No more than 0.5 kJ/l are needed to yield at most 0.35 % CO in pure CO_2 plasma while around 0.8 kJ/L are needed to give 0.45% CO yield in case of 20%CO_2-80%H_2. Definitely other reactions are taking place in high quantities of H_2 like water formation which does not occur in pure CO_2 plasma which consumes energy. Nonetheless, it is interesting to compare the Lissajous figures and envelope of current peaks as shown in figure 9.11 for 20%CO_2-80%H_2 and 100%CO_2 initial concentrations.

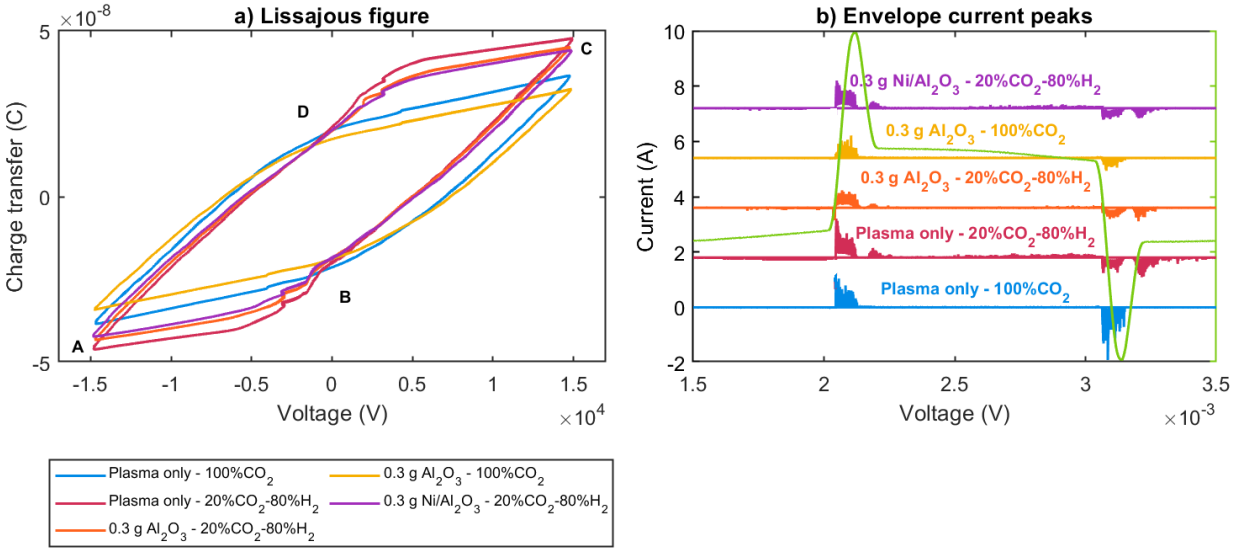

Figure 9.11: a) Lissajous plots of CO_2-CH_4 plasma and the corresponding b) envelope of positive current peaks for plasma only, 0.3 g Al_2O_3 and 0.3 g Ni/Al_2O_3. Voltage: 15 kV amplitude (30 kV peak-to-peak); Pressure: 750 torr.

The charge transfer per half cycle at constant applied voltage is always higher in 20%CO_2-80%H_2 with or without particles in the reactor. This corresponds to a lower breakdown field in this gas mixture compared to pure CO_2. The current peak envelope shows that for the three measurements in 20%CO_2-80%H_2 the plasma starts with larger current peaks followed by smaller current peaks during the rest of the voltage cycle. The reason of this behaviour is unclear, but shows a clear difference with the pure CO_2 case. The amplitude of the peaks reaches over 1 A in the case of 20%CO_2-80%H_2 plasma and less than 1 A in 100%CO_2. It could perhaps be a consequence of water adsorption on the glass surface in CO_2/H_2 mixtures. Another observation that can be made in the envelope of the current peaks is that current peaks are also ignited along the whole voltage cycle in 20%CO_2-80%H_2 plasma alone. Most of the current peaks are present obviously at the rise or decline of the voltage half cycle but some small peaks are formed throughout the voltage cycle. These small current peaks are in fact elementary filaments. Less of these peaks are observed when Al_2O_3 or Ni/Al_2O_3 particles are present in the discharge zone.

Conditions	**calculated C_{cell} (pF)**	**C_{cell} Lissajous (pF)** *100%CO_2*	**C_{cell} Lissajous (pF)** *20%CO_2-80%H_2*
Empty reactor	1.05	1.00	1.03
Reactor filled with 0.3 g Al_2O_3	~4.09	0.95	0.98
Reactor filled with 0.3 g Ni/Al_2O_3	-	-	1.04

Table 9.5: Reactor capacitance values calculated with reactor dimensions and obtained from Lissajous slope (m) in figure 9.11a during plasma OFF phase from (using a linear fit from point A to B where the slope is obtained from $y = mx + b$) in CO_2-H_2 plasma compared with only CO_2 plasma in FB-DBD.

9.7 Comparison FB vs PB

Al_2O_3 is tested in fluidized bed mode and packed bed mode in DB discharges. Both plasma regions have the same volume (1.38 cm^3) and dimensions, therefore, the capacitance of the reactor is the same. Figure 9.12 shows a comparison on the CO fraction for both configurations as a function of SEI.

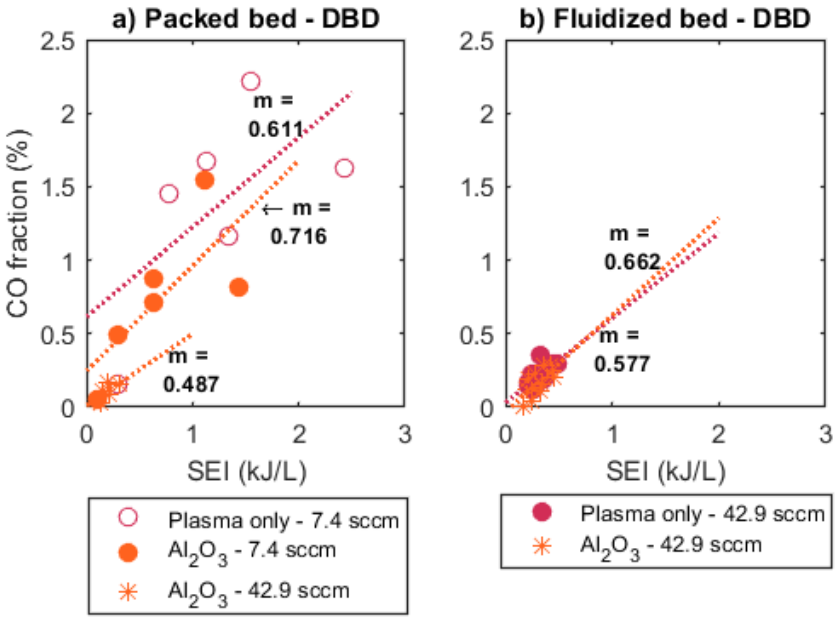

Figure 9.12: CO fraction as a function of SEI for a) packed bed - DBD in plasma only, Al_2O_3 at 7.4 and 42.9 sccm and b) fluidized bed - DBD in plasma only and Al_2O_3 at 42.9 sccm in 100%CO_2 plasma.

In the PB-DBD at 7.4 sccm, there is a reduction in CO fraction in the downstream gas when plasma only is compared with plasma with 0.3 g of alumina. The increase in flow rate (42.9 sccm) necessary to reach fluidization regime does not help the dissociation of CO_2 due to the very short residence time in the discharge volume. It would have been interesting to compensate this short residence time by a larger power input but the generator used could not provide enough power, and the glass cover of the inner electrode was cracking easily when increasing too much the power.

Comparing the CO fraction at very small SEI, with the same quantity of alumina and flow rate, the slope is 0.66 for FB while 0.48 for PB. In these conditions of low SEI, the FB configuration seems to improve the performance in comparison to the packed bed.

The mode of coupling between plasma source and catalyst has a considerable influence on the dissociation as observed closely to the same data but in figure 9.13. The same conditions are tested in reactors with the same dimensions in the discharge volume with 100%CO_2 plasma, 42.9 sccm total flow rate and with 0.3 g of Al_2O_3. The main difference is the packing of the material. Fluidization of alumina particles helps in the dissociation of CO_2 resulting in higher CO fractions. Although, the SEI seems to be proportional. Looking at the electrical data in figure 9.14a, we notice a difference in the Lissajous shape across the three cases corresponding to the ease with which plasma filaments can ignite.

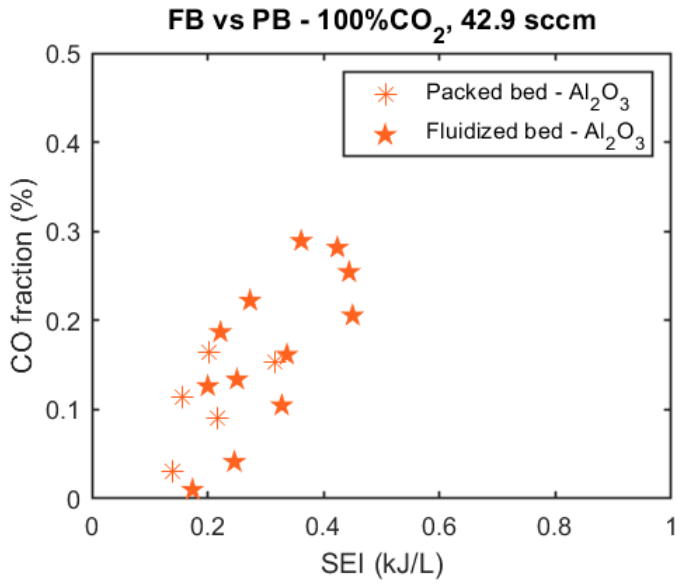

Figure 9.13: CO fraction as a function of SEI with packed bed - DBD and fluidized bed - DBD configurations for 100%CO_2 plasma and flow rate at 42.9 sccm.

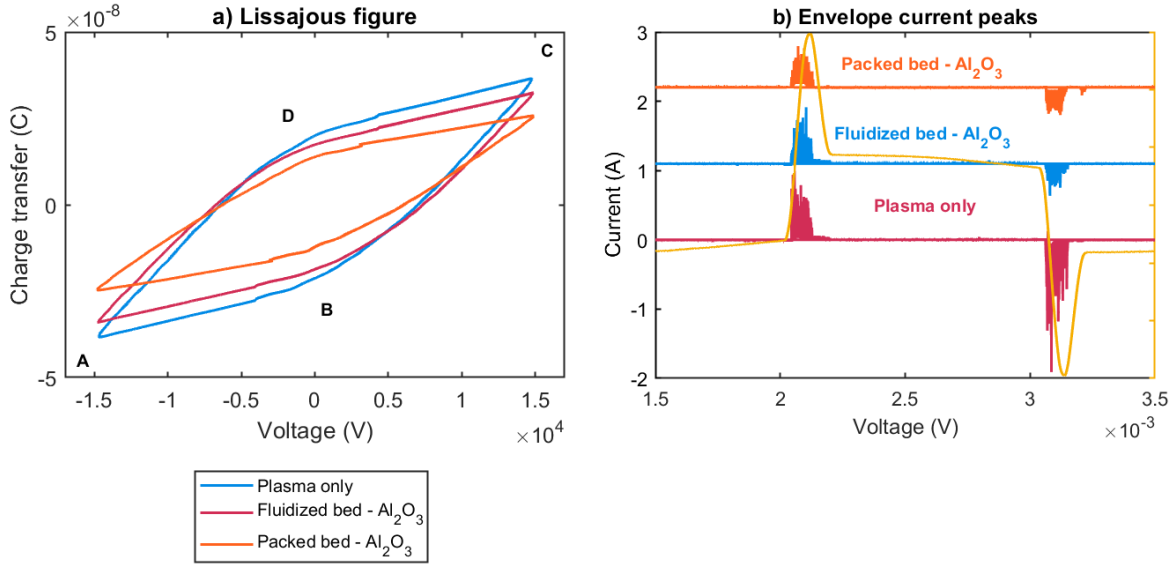

Figure 9.14: a) Lissajous plots and the corresponding b) envelope of positive current peaks for 100%CO_2 plasma only, 0.3 g Al_2O_3 in fludized bed and packed bed with flow rate of 42.9 sccm. Voltage: 15 kV amplitude (30 kV peak-to-peak); Pressure: 750 Torr.

Plasma only shows the highest charge transfer by half period being packed bed with alumina the lowest. However, the slope of plasma phase off is slightly flatter in case of packed bed - Al_2O_3 in comparison to plasma only and fluidized bed - Al_2O_3. Similarly, the slope in the plasma phase on in the rise of the applied voltage. This confirm the change of effective length of the reactor corresponding to the surface of glass over which the plasma filaments can deposit charges as described in [18].

9.8 Conclusions

Fluidized bed - DBD reactor was studied for conversion of CO_2 in several gas mixtures and conditions using alumina as fluidizing material. The minimum fluidization velocity was estimated and confirmed by measurement of the pressure drop at different velocities. However, during plasma, the alumina particles followed a different behaviour because of electrostatic forces. Even after plasma, particles remained negatively charged and sticking to the glass walls preventing the good fluidization of the bed. Nonetheless, it was observed a limited benefit of the fluidization of alumina in the plasma volume in comparison to plasma alone. The presence of alumina varied the capacitance of the reactor during the plasma off proving the importance to check the effective volume of the active plasma zone when comparing different packing materials and configurations.

The addition of 5%CH_4 to the initial gas mixture resulted in an increment of CO fraction in the downstream gas in comparison to only CO_2 plasma or 70%CO_2-30%CH_4. The addition of H_2 for CO_2 methanation reaction did not result in higher yield of CO compared to the addition of CH_4. Probably, the formation of water was the easier route for O atoms to react given that CH_4 was barely detected in the infrared spectra even in the presence of Ni/Al_2O_3 as catalyst. Also, the presence of H_2 lead to an increase of current peak through the whole voltage period not only during the rising in voltage, either in positive and negative polarity. Finally, the most striking result here is the demonstration of the improvement in the dissociation of CO_2 thorough CO fraction in fluidized bed - DBD in comparison to the packed bed for 100%CO_2. We assume that the movement of alumina in the plasma volume does not intervene in the charge transfer to the gas which benefits more than a fixed bed of alumina.

The results shown in this chapter were the very first one obtained in a fluidized bed DBD reactor at LPP. It appears that the small volume of the reactor used (needed for the limited power of the generator available) was a strong limitation to draw more conclusions from this preliminary study. Indeed, the small ground electrode height was not enough to keep all the particles in the plasma region when the fluidization occurs, especially when electrostatic repulsion tends to stick the particles to the walls. Measurements at higher power would be also beneficial to investigate a larger range of CO fraction and to be able to compare more convincingly the packed bed and the fluidized bed configuration. Nevertheless the results of this chapter are very promising about the possible gain obtained with fluidized bed configuration in DBDs.

Chapter 10

Conclusions

The aim of this thesis was to study the interaction of a catalytic material under plasma conditions and the application of fluidized bed reactors for CO_2 conversion. Well characterized CO_2 and CO_2-CH_4 plasmas in DC glow discharges were used to elucidate the processes occurring in a catalytic surface and to evaluate the impact of a moving catalytic material in the plasma itself. For sure the main interest was to focus on simple materials used as catalysts but without a metallic active phase ensuring that the effect of the material in the plasma region and conversion is well understood. The main conclusions are summarized in the following:

- ✓ **Downstream gas characterization.** The downstream gas from CO_2-CH_4 plasmas was characterized by FTIR spectroscopy and Mass spectrometry through different conditions (initial concentrations, current, pressures and flow rates). With 70%CO_2-30%CH_4 initial gas mixture we began to observe traces attributed to C_2 hydrocarbons by IR spectroscopy and MS. These traces grew with increasing CH_4 concentration in the initial gas mixture. The presence of the glass sampler holder with CeO_2 pellet does not change significantly the gas composition. Therefore, the gas temperature, reduced electric field (E/N), etc. of the plasma tested here was the same as the plasma used during the *in situ* FTIR transmission experiments. These results paved the way for subsequent experiments dedicated to the detail description of adsorbates formed during CO_2 and CO_2-CH_4 plasmas with a catalytic surface as CeO_2.

- ✓ **Plasma-surface catalytic interaction.** Tridentate carbonates and Hydrogen carbonates are the main adsorbate species present in CeO_2 surface from gaseous CO_2 interaction. Water traces are known to be the hydroxyl source for the formation of hydrogen carbonates but they are detrimental in larger concentrations. Carbonates are sensitive to temperature, partial pressure changes and ion bombardment (*e.g.* O_2^+) and/or electronically excited species (*e.g.* $O(^1D)$) upon CO_2 and O_2 plasma exposure. However, formates are the species formed during CO_2-CH_4 plasma. Formates are generated mainly from tridentate carbonates reacting with hydrogen either from the surface or in the plasma phase. This reaction was further confirmed by O_2-CH_4 plasma experiments in CeO_2 surface. By using a very well characterized plasma source to study the interaction with a relatively simple catalytic surface, it could be shown under certain conditions that the effect of the plasma on the adsorbed species was not simply a heating effect, or a reduction in the pressure of the adsorbing molecules. Thus, in particular with the various plasmas used for 'cleaning' the surface (O_2, N_2, Ar, He, N_2/H_2) and for conditions of pressure and current guaranteeing a minimal effect of the temperature, it appeared that excited species, that it is vibrational states, electronic or radicals, were to be essential in the desorption (or the destruction) of carbonates.

  The same surface processes observed for formates and tridentate carbonates in the glow discharge,

are also suggested at atmospheric pressure by tests performed *ex situ* in CeO_2 using DRIFTS for surface analysis in PB-DBD experiments.

✓ **Fluidizing bed plasma reactors.** Throughout the experiments performed in DBD and glow discharges, it was found that the plasma can be modified by interacting with powder materials. The plasma can induce a negative charge on the particle of the fixed material (for CeO_2) and fluidizing material (for Al_2O_3) causing electrostatic repulsion between particles and often causing the powder to stick to the walls of the reactor even after the plasma is turned off. The degree of affectation varies depending on the plasma source:

1. *Fluidizing bed in DC glow discharge.* In the FB - glow discharge, the presence of Al_2O_3 particles fluidizing inside the reactor constrains the plasma region spatially inducing an improvement in terms of conversion of CO_2. By OES analysis of the plasma, the gas temperature was found to be relatively unchanged despite the contraction of the plasma region corresponding to higher current density. The reduced electric field is enhanced by the large density of Al_2O_3 particles in the lower part of the FB-glow discharge. Most importantly, O atoms density seem to decrease in the presence of fluidizing particles in the plasma region because the increase of surface area where O atoms can recombine to O_2. This leads to an increase of CO density which is confirmed in the downstream gas by FTIR spectroscopy analysis.
2. *Fluidizing bed in DBD.* In the case of DBD reactors, the negative charging of the material placed in the plasma region affected the good fluidization of the bed. Ultimately, this had an influence on the current peaks, total amount of charge transferred over time and generally, how the streamers are ignited. Nonetheless, the fluidized bed resulted in a positive impact on the dissociation of CO_2 when fluidized bed was compared to a packed bed with the same material (Al_2O_3).

The combined work performed through this thesis was able to demonstrate that: (1) formates are surface intermediates in DRM reaction on CeO_2 during CO_2-CH_4 plasma; and (2) the packing mode of catalytic material has a clear influence on the plasma properties during the testing of two different plasma configurations: DBD at atmospheric pressure and DC glow discharge at low pressure. This proves that the combination of different plasma sources to investigate the plasma chemistry is necessary to obtain consistent and reliable results, not only in the plasma/gas phase but also during plasma/surface interactions as it was reported here.

Additionally, the flexibility in our DC glow discharge setup gave us the chance to show that in our plasma conditions the impact of pellets and powders on the plasma properties is minimal. In turn, the species on the catalyst surface were studied in detail while having a good knowledge of the conditions to which the surface is exposed as the study of the plasma kinetics in CO_2 and CO_2-CH_4 plasmas was thoroughly done in very similar glow discharges as described in [16, 87].

Future work

The results presented here open the door for future experimental work. Firstly, the *in situ* FITR transmission experiments performed on CeO_2 only can now be performed with real catalysts, meaning that an active phase is supported on CeO_2. This could be a good way to study in detail catalysts that have resulted in improved performance for DRM plasma reaction. Also, other reactions can be investigated as CO_2 methanation or H_2 production from ammonia decomposition.

Secondly, the characterization of CeO_2, Al_2O_3 and catalysts tested here was somewhat weak. The ceria pellets were characterized using XRD, surface analysis by BET theory, XPS, etc. but these techniques were not fully capable to capture any modification after plasma exposure. This does not mean

that the surface of CeO_2 was not reduced or modified by the plasma as the main products of DRM reaction are CO and H_2. Both molecules are known to be reducing agents and the IR measurements performed here were not able to capture a clear effect of the surface interaction with CO and H_2. For sure, *in situ* experiments on the ceria pellet with laser Raman spectroscopy could provide evidence of such reduction and investigate structural evolution by looking below 1000 cm^{-1} where the vibrations of the Ce-O network are shown. Oxygen vacancies formation can be followed by a red-shift of the D band due to an increase in the relative intensity of the component at 550 cm^{-1} compared to the one at 590 cm^{-1} [184].

Regarding the fluidized bed plasma reactors, the results show promising application, however more work needs to be done to conclusively confirm the positive enhancement of CO_2 dissociation. The small volume of the FB-DBD reactor used in this work (needed for the limited power of the generator available) was a strong limitation to draw more conclusions from this preliminary study. Indeed, the small ground electrode height was not enough to keep all the particles in the plasma region when the fluidization occurs, especially when electrostatic repulsion tends to stick the particles to the walls. Applying a negative DC field above the ground electrode could maybe help repelling the particles that are trying to stick on the glass above the plasma region and make them fall back in the DBD plasma region.

For the FB-GD, the life time of the reactor is for now mostly limited by the high current density at the position of the porous glass disk. It has to be reminded that the position of the porous glass disk between the two electrodes led to an enhanced of the electron density that possibly trigger the extensive carbon deposition and melting of the glass when CH_4 was added to the initial gas mixture. This could be prevented by changing the glow discharge source to Radio-frequency discharge with 2 ground electrodes placed outside the glass tube and right above the glass disk. The plasma homogeneity and operating pressure would be similar to the glow discharge conditions. Although, the performance could turn out to be different but the study of initial gas mixtures richer in CH_4 are worth the effort as some work has already been done for CO_2-CH_4 in RF [87].

Additionally, plasma-surface interaction modelling could provide meaningful insights as the type of mechanisms (Langmuir-Hishelwood or Eley-Ridel) was not fully confirmed for formates formation. Also, it would be interesting to pinpoint which electronically and vibrationally excited species in O_2 and N_2 plasmas are involved in the desorption of carbonates and formates from the surface and elucidate why Ar and He plasma were not able to aid in this process. Finally, the origin of bands at 1430, 1665 and 2818 cm^{-1} would be interested to clarify with more experiments.

Evidently, *in situ* plasma experiments were a good starting point for the comprehension on the plasma-surface catalytic interaction. The complexity of 'inhomogeneous plasma/support/promoter/active phase' system makes it almost impossible to identify the microscopic mechanisms really responsible for the macroscopic performances observed in reactors dedicated to CO_2 conversion applications. Even if the relevance of the reactions observed under low pressure conditions is questionable compared to the mechanisms occurring on catalysts at higher pressure, the use of low pressure model systems proves to be very informative on the understanding of the plasma/catalyst interaction thanks to the possibility of detailed characterization of the plasma phase to which the catalyst is exposed.

Fluidized bed configurations deserve to be studied in more detail but beyond this very particular configuration, it is important to better understand how the macroscopic geometry (typically between 1 and 100μm) of the catalysts (and/or their support) influences plasma development. The impact of this 'geometric' parameter, whether beneficial or detrimental to the CO_2 conversion performance, can hide the true chemical activity of the catalyst. It is therefore essential to better understand the influence of the macroscopic surface state of the catalyst on plasma behaviour in order to identify the most efficient active phases relevant for methanation or DRM.

Appendix A

Reduced Electric Field (E/N) calculation

Assuming excitation comes mainly due to electron impact, for a given specie X, line intensity I is given by:

$$I_X = h\nu_{ij} * n_e * k_e^X * \frac{A_{ij}^X}{\Sigma A_i^X + \Sigma_Q k_Q^X [n_Q]} * [n_X] \tag{A.1}$$

where: $h\nu_{ij}$ is the wavelength of the given transition, n_e is the electron density, k_e^X is the electron impact excitation rate coefficient, A_{ij}^X is the Einstein coefficient of transition, ΣA_i^X is the sum of possible radiative de-excitation, k_Q^X is the collisional quenching coefficient of level i by specie Q, $[n_Q]$ is the density of Q and $[n_X]$ is the density of X.

The fourth term can be simplified as a_X, the equation above can be written as:

$$I_X = h\nu_{ij} * n_e * k_e^X * a_X * [n_X] \tag{A.2}$$

By substituting this equation for oxygen atoms (O777 and O844 emission lines) and to estimate the ratio we have:

$$\frac{I_O^{777nm}}{I_O^{844nm}} = \frac{k_e^{O777}}{k_e^{O844}} * \frac{a_O^{777nm}}{a_O^{844nm}} * \frac{\lambda_O^{777nm}}{\lambda_O^{844nm}} \tag{A.3}$$

Since k_e^X depends on the Electron Energy Distribution Function (EEDF):

$$k_e^X = \sqrt{\frac{2e}{m}} \int_{\epsilon th}^{\infty} \sigma(\epsilon)_i f(\epsilon) \epsilon d\epsilon \tag{A.4}$$

and using a simulation with LoKI-B on the EEDF for several E/N for pure CO_2 plasmas, an equivalent relation between experimental and simulated can be done:

$$\left(\frac{k_e^{O777}}{k_e^{O844}}\right)_{exp} = \left(\frac{k_e^{O777}}{k_e^{O844}}\right)_{sim} \tag{A.5}$$

Assuming $\frac{a_O^{777nm}}{a_O^{844nm}}$ to be similar and $\frac{\lambda_O^{777nm}}{\lambda_O^{844nm}}$ is roughly 1, then equation A.3 (figure A.1) is simplified as a rough relation with intensity ratio as:

$$\frac{k_e^{O777}}{k_e^{O844}} \approx \frac{I_O^{777nm}}{I_O^{844nm}} \tag{A.6}$$

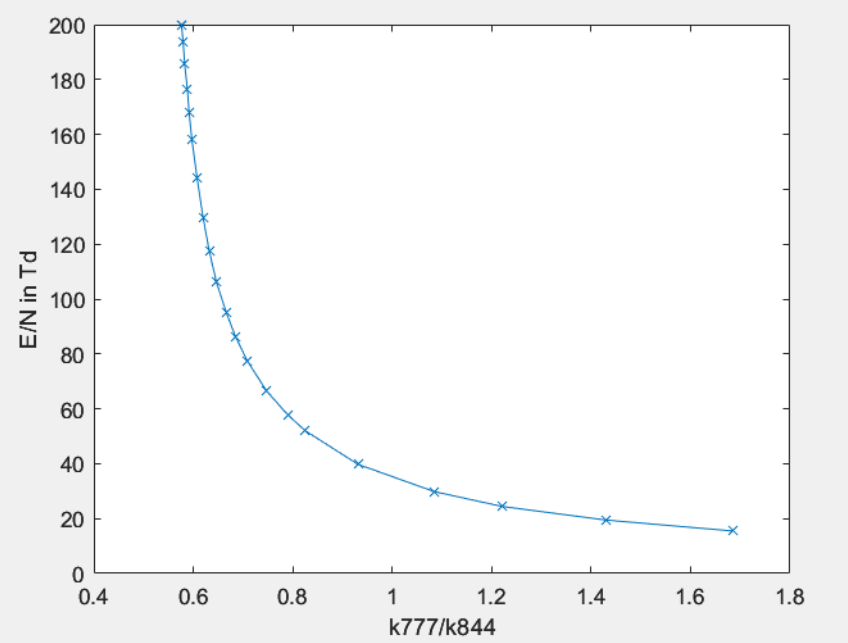

Figure A.1: Reduced electric field as a function of excitation coefficient ratio of kO777/kO844.

The same principle can be applied for the measurement of X species density with the aid of an actinometer. Ar, Ne or Xe are the typical gases used and the amount added must be known. Instead of using the ratio of two lines of the same species, the ratio of line intensity X over the intensity of actinometer results in the X density ($[X]$). In CO_2 plasmas, the Oxygen atom density is of particular interest [95]. Rearranging the different terms of the equation A.1 and A.4 and using argon as actinometer where [Ar] is constant, the O atom density can be obtained from expression:

$$[O] = \frac{I_O}{I_{Ar}} \frac{C_{Ar} \cdot h\nu_{ij}^{Ar}}{C_O \cdot h\nu_{ij}^{O}} \frac{k_e^{Ar}}{k_e^{O}} \frac{a_{ij}^{Ar}}{a_{ij}^{O}} \cdot [Ar] - \frac{k_{de}^{O}}{k_e^{O}} [O_2] \tag{A.7}$$

where the last term represents the contribution of dissociative excitation.

The line intensity strongly depends on excitation cross-sections of the atomic species ($\sigma(\epsilon)$) and of the actinometer, the accuracy of the computed EEDF and collisional quenching coefficients k_Q. More information can be found in Edmond Baratte thesis regarding the detailed analysis using actinometry for oxygen density in CO_2-CH_4 plasmas [87].

Appendix B

Ceria preparation by sol-gel method

The methodology for ceria preparation was based on solgel method reported in [81].

1. 4.35 g of cerium nitrate ($Ce(NO_3)_3 \cdot 6H_2O$) were added to 100 ml of distilled water by stirring for 30 min followed by the addition of ammonium hydroxide solution 25% (5 drops per minute). The reaction was carried out at 60°C.

2. The resulting solution turned into pale-pink-coloured sol which was further stirred continuously for one day. Finally, the sol got transformed into white-coloured sol.

3. The sol was then aged at room temperature for another 2 days until it reached a gel state.

4. The resulting gel was then washed thoroughly with ethanol and distilled water to remove the impurities.

5. The gel was dried at >80°C overnight in air. The obtained powder was ground using a mortar and pestle and finally calcinated at 550°C for 3 h in air. The final cerium oxide obtained an homogeneous yellow color.

Appendix C

Capacitance calculation

The capacitance of the DBD reactor used at LPP for the packed bed and fluidized bed configurations was calculated based on a cylindrical capacitor. The capacitance is calculated considering concentric cylinder of radius a and length L by conducting to a inner cylinder of radius b. We assume that L is much larger than b. The magnitude of charge Q on each cylinder is:

$$Q = \lambda L \tag{C.1}$$

where λ is the charge per unit length. Considering the electric field between cylinders:

$$E(r) = \frac{\lambda}{2\pi\epsilon_0 r} \tag{C.2}$$

ϵ_0 corresponds to the vacuum permittivity (8.85e-12 F/m). For the electric potential between cylinders we use V(a) = 0:

$$V(r) = -\int_a^r E(r)dr = -\frac{\lambda}{2\pi\epsilon_0} ln\frac{r}{a} \tag{C.3}$$

$$V \equiv V_+ + V_- = V(a) - V(b) = \frac{Q}{2\pi\epsilon_0 L} ln\frac{b}{a} \tag{C.4}$$

Then, the capacitance for a cylindrical geometric is calculated :

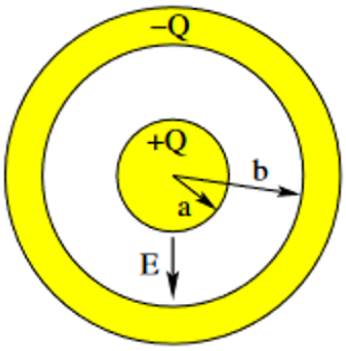

Figure C.1: Schematic of cylindrical capacitors

$$C \equiv \frac{Q}{V} = \frac{2\pi\epsilon_0 L}{ln\frac{r}{a}} \tag{C.5}$$

The capacitance of the whole empty reactor (C_{cell}) is considered a series of capacitors where the total capacitance is calculated from:

$$\frac{1}{C_{cell}} = \frac{1}{C_1} + \frac{1}{C_2} + \frac{1}{C_3} \tag{C.6}$$

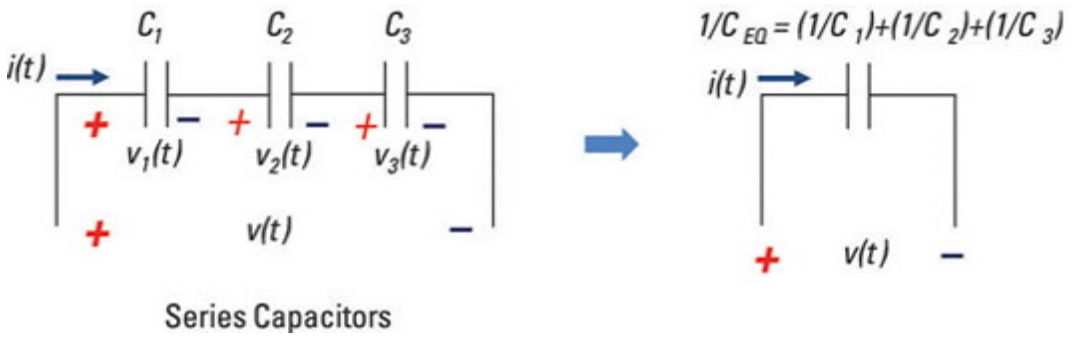

Figure C.2: Schematic of capacitors in series.

where:
C_1 = capacitance of inner glass tube (HV electrode)
C_2 = capacitance of gas gap
C_3 = capacitance of outer glass tube

Appendix D

Main processes for H_2 and H_2O

The figures presented here are the result from the 0D model of the plasma only for 95%CO_2-5%CH_4 at 30 mA, 20 sccm from 1 to 6 Torr based on work from [87]. The intention is to enrich the discussion on the FB-GD from section 7.4.4.

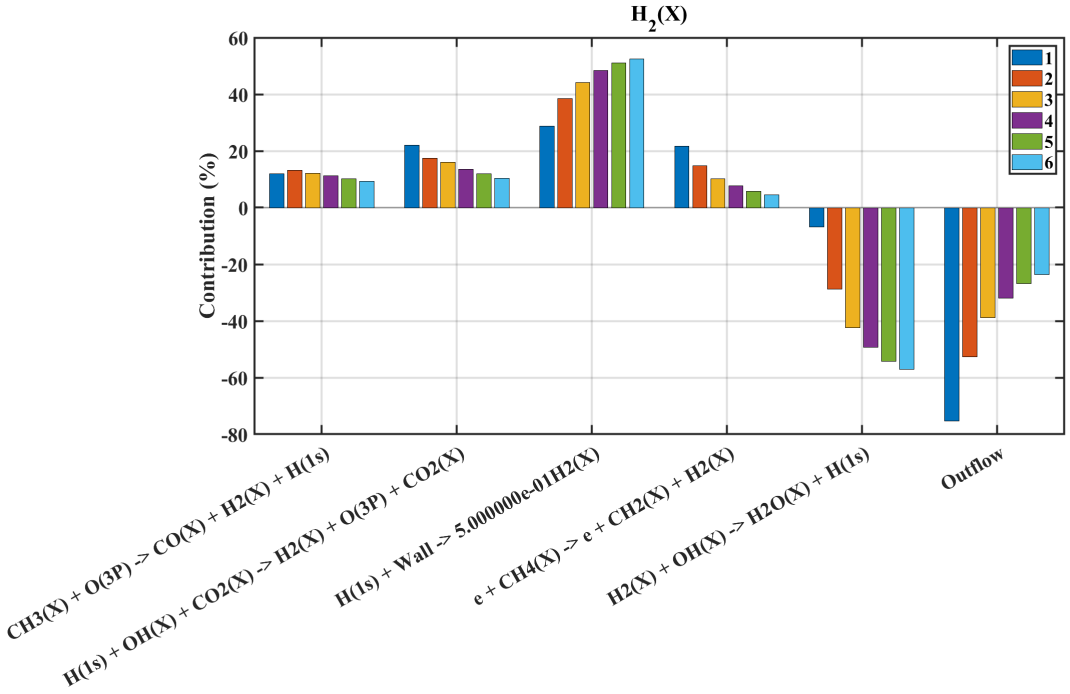

Figure D.1: Evolution of contribution of the main creation and destruction processes for H_2 for 95%CO_2-5%CH_4 plasma at 30 mA, 20 sccm from 1 to 6 Torr.

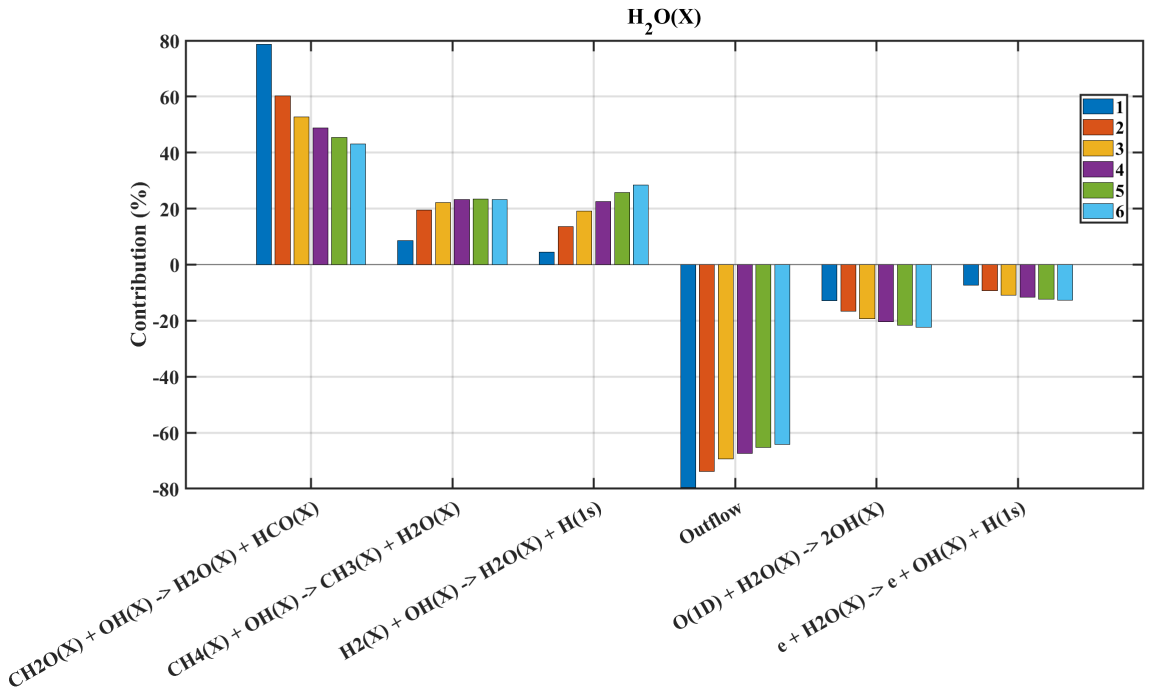

Figure D.2: Evolution of contribution of the main creation and destruction processes for H_2O for 95%CO_2-5%CH_4 plasma at 30 mA, 20 sccm from 1 to 6 Torr.

Bibliography

[1] C. Division and U. N. Environment, *Emissions Gap Report 2021: The Heat Is On*, 2021.

[2] B. L. M. Klarenaar, "Vibrational kinetics of CO_2 in non-thermal plasma," Ph.D. dissertation, 2018.

[3] Z. Wang, Y. Zhang, E. C. Neyts, X. Cao, X. Zhang, B. W. Jang, and C. J. Liu, "Catalyst Preparation with Plasmas: How Does It Work?" *ACS Catalysis*, vol. 8, no. 3, pp. 2093–2110, 2018.

[4] R. A. Spragg, "IR spectrometers," *Encyclopedia of Spectroscopy and Spectrometry*, pp. 419–427, 2016.

[5] S. Yamada, Y. Morita, A. Nezu, and H. Akatsuka, "Nonequilibrium characteristics in the rotational temperature of CO excited states in microwave discharge CO_2 plasma," *Japanese Journal of Applied Physics*, vol. 60, no. 4, 2021.

[6] U. P. Fringeli, *ATR and reflectance IR spectroscopy, applications*, 3rd ed. Elsevier Ltd., 2016. [Online]. Available: http://dx.doi.org/10.1016/B978-0-12-803224-4.00104-7

[7] Å. Kvick, "X-ray diffraction, materials science applications," *Encyclopedia of Spectroscopy and Spectrometry*, pp. 648–655, 2016.

[8] A. Fridman, *Plasma Chemistry*. Cambridge University Press, May 2008. [Online]. Available: https://doi.org/10.1017/cbo9780511546075

[9] M. A. Damen, "Absorption spectroscopy on O_2 production in an atmospheric pressure dielectric barrier discharge in CO_2," 2013.

[10] U. Kogelschatz, "Dielectric-barrier discharges: Their History, Discharge Physics, and Industrial Applications," *Plasma Chemistry and Plasma Processing*, vol. 23, no. 1, pp. 1–46, 2003.

[11] R. Cocco, S. B. Karri, and T. Knowlton, "Introduction to fluidization," *Chemical Engineering Progress*, vol. 110, no. 11, pp. 21–29, 2014.

[12] M. Menéndez, J. Herguido, A. Bérard, and G. S. Patience, "Experimental methods in chemical engineering: Reactors—fluidized beds," *Canadian Journal of Chemical Engineering*, vol. 97, no. 9, pp. 2383–2394, 2019.

[13] N. Răduţoiu and C. M. Teodorescu, "Satellites in Ce 3d X-ray photoelectron spectroscopy of ceria," *Digest Journal of Nanomaterials and Biostructures*, vol. 8, no. 4, pp. 1535–1549, 2013.

[14] M. Atoji, "Magnetic and crystal structures of CeC_2, PrC_2, NdC_2, TbC_2, and HoC_2 at low temperatures," *The Journal of Chemical Physics*, vol. 46, no. 5, pp. 1891–1901, Mar. 1967. [Online]. Available: https://doi.org/10.1063/1.1840950

[15] A. Bosak, M. Krisch, M. Mohr, J. Maultzsch, and C. Thomsen, "Elasticity of single-crystalline graphite: Inelastic x-ray scattering study," *Physical Review B*, vol. 75, no. 15, Apr. 2007. [Online]. Available: https://doi.org/10.1103/physrevb.75.153408

[16] A.-S. Morillo-Candas, "Investigation of fundamental mechanisms of CO_2 plasmas," Ph.D. dissertation, 2019.

[17] O. Kunii, Daizo and Levenspiel, *Fluidization engineering*. Butterworth-Heinemann, 1991.

[18] A. Bogaerts, E. C. Neyts, O. Guaitella, and A. B. Murphy, "Foundations of plasma catalysis for environmental applications," *Plasma Sources Science and Technology*, vol. 31, no. 5, 2022.

[19] F. Brehmer, S. Welzel, M. C. Van De Sanden, and R. Engeln, "CO and byproduct formation during CO_2 reduction in dielectric barrier discharges," *Journal of Applied Physics*, vol. 116, no. 12, 2014. [Online]. Available: http://dx.doi.org/10.1063/1.4896132

[20] P. Styring, E. A. Quadrelli, and K. Armstrong, *Carbon Dioxide Utilisation: Closing the Carbon Cycle: First Edition*, 1st ed. Elsevier, 2014.

[21] J. O. D. O. Rtiz, R. O. J. Ackson, M. Hall, and K. Campus, "Understanding Eunice Foote's 1856 experiments: Heat adsorption by atmospheric gases," *Royal society*, vol. 1857, no. August 1856, pp. 159–160, 2020.

[22] J. R. Fleming, *Historical perspectives on climate change*. Oxford University Press, 1998.

[23] R. Slade and A. Bauen, "Micro-algae cultivation for biofuels: Cost, energy balance, environmental impacts and future prospects," *Biomass and Bioenergy*, vol. 53, no. 0, pp. 29–38, 2013. [Online]. Available: http://dx.doi.org/10.1016/j.biombioe.2012.12.019

[24] C. Chen, J. F. Khosrowabadi Kotyk, and S. W. Sheehan, "Progress toward Commercial Application of Electrochemical Carbon Dioxide Reduction," *Chem*, vol. 4, no. 11, pp. 2571–2586, 2018. [Online]. Available: https://doi.org/10.1016/j.chempr.2018.08.019

[25] A. Galadima and O. Muraza, "Catalytic thermal conversion of CO_2 into fuels: Perspective and challenges," *Renewable and Sustainable Energy Reviews*, vol. 115, no. August, p. 109333, 2019. [Online]. Available: https://doi.org/10.1016/j.rser.2019.109333

[26] F. Saladin and I. Alxneit, "Temperature dependence of the photochemical reduction of CO_2 in the presence of H_2O at the solid/gas interface of TiO_2," *Journal of the Chemical Society - Faraday Transactions*, vol. 93, no. 23, pp. 4159–4163, 1997.

[27] A. D. Kamkeng, M. Wang, J. Hu, W. Du, and F. Qian, "Transformation technologies for CO_2 utilisation: Current status, challenges and future prospects," *Chemical Engineering Journal*, vol. 409, no. September 2020, p. 128138, 2021. [Online]. Available: https://doi.org/10.1016/j.cej.2020.128138

[28] S. G. Hong, H. Jeon, H. S. Kim, S. H. Jun, E. Jin, and J. Kim, "One-pot enzymatic conversion of carbon dioxide and utilization for improved microbial growth," *Environmental Science and Technology*, vol. 49, no. 7, pp. 4466–4472, 2015.

[29] P. R. Yaashikaa, P. Senthil Kumar, S. J. Varjani, and A. Saravanan, "A review on photochemical, biochemical and electrochemical transformation of CO_2 into value-added products," *Journal of CO_2 Utilization*, vol. 33, no. March, pp. 131–147, 2019. [Online]. Available: https://doi.org/10.1016/j.jcou.2019.05.017

[30] A. Saravanan, P. Senthil kumar, D. V. N. Vo, S. Jeevanantham, V. Bhuvaneswari, V. Anantha Narayanan, P. R. Yaashikaa, S. Swetha, and B. Reshma, "A comprehensive review on different approaches for CO_2 utilization and conversion pathways," *Chemical Engineering Science*, vol. 236, p. 116515, 2021. [Online]. Available: https://doi.org/10.1016/j.ces.2021.116515

[31] H. H. Kim, Y. Teramoto, A. Ogata, H. Takagi, and T. Nanba, "Plasma Catalysis for Environmental Treatment and Energy Applications," *Plasma Chemistry and Plasma Processing*, vol. 36, no. 1, pp. 45–72, 2016.

[32] J. C. Whitehead, "Plasma catalysis: A solution for environmental problems," *Pure and Applied Chemistry*, vol. 82, no. 6, pp. 1329–1336, 2010.

[33] K. P. Francke, H. Miessner, and R. Rudolph, "Cleaning of air streams from organic pollutants by plasma-catalytic oxidation," *Plasma Chemistry and Plasma Processing*, vol. 20, no. 3, pp. 393–403, 2000.

[34] L. R. Winter, B. Ashford, J. Hong, A. B. Murphy, and J. G. Chen, "Identifying surface reaction intermediates in plasma catalytic ammonia synthesis," *ACS Catalysis*, vol. 10, no. 24, pp. 14 763–14 774, 2020.

[35] C. Du, D. Ma, J. Wu, Y. Lin, W. Xiao, J. Ruan, and D. Huang, "Plasma-catalysis reforming for H_2 production from ethanol," *International Journal of Hydrogen Energy*, vol. 40, no. 45, pp. 15 398–15 410, 2015. [Online]. Available: http://dx.doi.org/10.1016/j.ijhydene.2015.09.096

[36] H. Kušić, N. Koprivanac, and B. R. Locke, "Decomposition of phenol by hybrid gas/liquid electrical discharge reactors with zeolite catalysts," *Journal of Hazardous Materials*, vol. 125, no. 1-3, pp. 190–200, 2005.

[37] C. Okolie, Y. Lyu, L. Kovarik, E. Stavitski, and C. Sievers, "Coupling of Methane to Ethane, Ethylene, and Aromatics over Nickel on Ceria–Zirconia at Low Temperatures," *ChemCatChem*, vol. 10, no. 12, pp. 2700–2708, 2018.

[38] G. Chen, V. Georgieva, T. Godfroid, R. Snyders, and M. P. Delplancke-Ogletree, "Plasma assisted catalytic decomposition of CO_2," *Applied Catalysis B: Environmental*, vol. 190, pp. 115–124, 2016. [Online]. Available: http://dx.doi.org/10.1016/j.apcatb.2016.03.009

[39] E. C. Neyts, K. Ostrikov, M. K. Sunkara, and A. Bogaerts, "Plasma Catalysis: Synergistic Effects at the Nanoscale," *Chemical Reviews*, vol. 115, no. 24, pp. 13 408–13 446, 2015.

[40] M. Shearn, X. Sun, M. David, A. Yariv, and A. Scherer, "Advanced Plasma Processing: Etching, Deposition, and Wafer Bonding Techniques for Semiconductor Applications," *Semiconductor Technologies*, no. June 2014, 2010.

[41] H. Randhawa, "Review of plasma-assisted deposition processes," *Thin Solid Films*, vol. 196, no. 2, pp. 329–349, 1991.

[42] X. Hu, X. Jia, X. Zhang, Y. Liu, and C. jun Liu, "Improvement in the activity of Ni/ZrO_2 by cold plasma decomposition for dry reforming of methane," *Catalysis Communications*, vol. 128, no. May, pp. 1–4, 2019.

[43] E. C. Neyts, "Plasma-Surface Interactions in Plasma Catalysis," *Plasma Chemistry and Plasma Processing*, vol. 36, no. 1, pp. 185–212, 2016.

[44] K. M. Bal and E. C. Neyts, "Modelling molecular adsorption on charged or polarized surfaces: A critical flaw in common approaches," *Physical Chemistry Chemical Physics*, vol. 20, no. 13, pp. 8456–8459, 2018.

[45] R. Tschiersch, S. Nemschokmichal, M. Bogaczyk, and J. Meichsner, "Surface charge measurements on different dielectrics in diffuse and filamentary barrier discharges," *Journal of Physics D: Applied Physics*, vol. 50, no. 10, 2017.

[46] C. Du, R. Qiu, and J. Ruan, *Plasma fluidized bed*. Springer, 2018.

[47] M. Ceppelli, T. P. Salden, L. M. Martini, G. Dilecce, and P. Tosi, "Time-resolved optical emission spectroscopy in CO_2 nanosecond pulsed discharges," *Plasma Sources Science and Technology*, vol. 30, no. 11, 2021.

[48] S. Kelly, A. Van De Steeg, A. Hughes, G. Van Rooij, and A. Bogaerts, "Thermal instability and volume contraction in a pulsed microwave N_2 plasma at sub-atmospheric pressure," *Plasma Sources Science and Technology*, vol. 30, no. 5, 2021.

[49] M. Budde, L. M. Martini, M. Ceppelli, S. Quercetti, and R. Engeln, "Absolute OH density measurements in a CO_2-H_2O glow discharge by laser-induced fluorescence spectroscopy," *Plasma Sources Science and Technology*, vol. 31, no. 5, 2022.

[50] M. Karches and P. R. Von Rohr, "Microwave plasma characteristics of a circulating fluidized bed-plasma reactor for coating powders," *Surface and Coatings Technology*, vol. 142-144, pp. 28–33, 2001.

[51] R. Jafari, M. Tatoulian, and F. Arefi-Khonsari, "Improvement of the stability of plasma polymerized acrylic acid coating deposited on PS beads in a fluidized bed reactor," *Reactive and Functional Polymers*, vol. 71, no. 4, pp. 520–524, 2011.

[52] D. Butscher, T. Schlup, C. Roth, N. Müller-Fischer, C. Gantenbein-Demarchi, and P. Rudolf Von Rohr, "Inactivation of microorganisms on granular materials: Reduction of *Bacillus amyloliquefaciens* endospores on wheat grains in a low pressure plasma circulating fluidized bed reactor," *Journal of Food Engineering*, vol. 159, pp. 48–56, 2015. [Online]. Available: http://dx.doi.org/10.1016/j.jfoodeng.2015.03.009

[53] J. O. Pou, C. Colominas, and R. Gonzalez-Olmos, "CO_2 reduction using non-thermal plasma generated with photovoltaic energy in a fluidized reactor," *Journal of CO_2 Utilization*, vol. 27, no. August, pp. 528–535, 2018. [Online]. Available: https://doi.org/10.1016/j.jcou.2018.08.019

[54] T. Kroker, T. Kolb, A. Schenk, K. Krawczyk, M. Młotek, and K. H. Gericke, "Catalytic conversion of simulated biogas mixtures to synthesis gas in a fluidized bed reactor supported by a DBD," *Plasma Chemistry and Plasma Processing*, vol. 32, no. 3, pp. 565–582, 2012.

[55] Q. Wang, Y. Cheng, and Y. Jin, "Dry reforming of methane in an atmospheric pressure plasma fluidized bed with Ni/γ-Al_2O_3 catalyst," *Catalysis Today*, vol. 148, no. 3-4, pp. 275–282, 2009.

[56] N. Bouchoul, H. Touati, E. Fourré, J. M. Clacens, and C. Batiot-Dupeyrat, "Efficient plasma-catalysis coupling for CH_4 and CO_2 transformation in a fluidized bed reactor: Comparison with a fixed bed reactor," *Fuel*, vol. 288, no. September 2020, 2021.

[57] X. T. Y. Sun, J. Wu, Y. Wang, J. Li, N. Wang, J. Harding, S. Mo, L. Chen, P. Chen, M. Fu, D. Ye, J. Huang, "Plasma-catalytic CO_2 hydrogenation over a Pd/ZnO catalyst: *In situ* probing of gas-phase and surface reactions," *JACS Au*, 2022.

[58] S. Xu, S. Chansai, Y. Shao, S. Xu, Y. chi Wang, S. Haigh, Y. Mu, Y. Jiao, C. E. Stere, H. Chen, X. Fan, and C. Hardacre, "Mechanistic study of non-thermal plasma assisted CO_2 hydrogenation over Ru supported on MgAl layered double hydroxide," *Applied Catalysis B: Environmental*, vol. 268, no. January, p. 118752, 2020. [Online]. Available: https://doi.org/10.1016/j.apcatb.2020.118752

[59] R. Dębek, F. Azzolina-Jury, A. Travert, F. Maugé, and F. Thibault-Starzyk, "Low-pressure glow discharge plasma-assisted catalytic CO_2 hydrogenation—The effect of metal oxide support on the performance of the Ni-based catalyst," *Catalysis Today*, vol. 337, no. March, pp. 182–194, 2019. [Online]. Available: https://doi.org/10.1016/j.cattod.2019.03.039

[60] H. Chen, Y. Mu, Y. Shao, S. Chansai, H. Xiang, Y. Jiao, C. Hardacre, and X. Fan, "Nonthermal plasma (NTP) activated metal–organic frameworks (MOFs) catalyst for catalytic CO_2 hydrogenation," *AIChE Journal*, vol. 66, no. 4, pp. 1–11, 2020.

[61] N. K. Alexander Parastaev and E. J. Hensen, "Mechanistic study of catalytic CO_2 hydrogenation in a plasma by operando DRIFT spectroscopy," *Journal of Physics D: Applied Physics*, 2021. [Online]. Available: https://doi.org/10.1088/1361-6463/abeb96

[62] D. Qin, D. Xie, H. Zheng, Z. Li, J. Tang, and Z. Wei, "In-Situ FTIR Study of CO_2 Adsorption and Methanation Mechanism Over Bimetallic Catalyst at Low Temperature," *Catalysis Letters*, 2021. [Online]. Available: https://doi.org/10.1007/s10562-021-03539-2

[63] H. Chen, Y. Mu, Y. Shao, S. Chansai, S. Xu, C. E. Stere, H. Xiang, R. Zhang, Y. Jiao, C. Hardacre, and X. Fan, "Coupling non-thermal plasma with Ni catalysts supported on BETA zeolite for catalytic CO_2 methanation," *Catalysis Science and Technology*, vol. 9, no. 15, pp. 4135–4145, 2019.

[64] D. Aceto, M. C. Bacariza, A. Travert, C. Henriques, and F. Azzolina-Jury, "Thermal and Plasma-Assisted CO_2 Methanation over Ru/Zeolite: A Mechanistic Study Using In-Situ Operando FTIR," *Catalysts*, vol. 13, p. 481, 2 2023. [Online]. Available: https://doi.org/10.3390/catal13030481

[65] F. Azzolina-Jury and F. Thibault-Starzyk, "Mechanism of low pressure plasma-assisted co_2 hydrogenation over ni-usy by microsecond time-resolved ftir spectroscopy," *Topics in Catalysis*, vol. 60, pp. 1709–1721, 12 2017. [Online]. Available: https://doi.org/10.1007/s11244-017-0849-2

[66] F. Azzolina-Jury, D. Bento, C. Henriques, and F. Thibault-Starzyk, "Chemical engineering aspects of plasma-assisted CO_2 hydrogenation over nickel zeolites under partial vacuum," *Journal of CO_2 Utilization*, vol. 22, no. June, pp. 97–109, 2017. [Online]. Available: https://doi.org/10.1016/j.jcou.2017.09.017

[67] P. Ferreira-Aparicio and I. Rodriguez-Ramos, "Mechanistic aspects of the dry reforming of methane over ruthenium catalysts," *Applied Catalysis A: General*, vol. 202, pp. 183–196, 2000. [Online]. Available: https://doi.org/10.1016/s0926-860x(00)00525-1

[68] L. Liu, S. Das, T. Chen, N. Dewangan, J. Ashok, S. Xi, A. Borgna, Z. Li, and S. Kawi, "Low temperature catalytic reverse water-gas shift reaction over perovskite catalysts in DBD plasma," *Applied Catalysis B: Environmental*, vol. 265, no. December 2019, p. 118573, 2020. [Online]. Available: https://doi.org/10.1016/j.apcatb.2019.118573

[69] V. T. Sagar and A. Pintar, "Enhanced surface properties of CeO_2 by MnO_x doping and their role in mechanism of methane dry reforming deduced by means of in-situ DRIFTS,"

Applied Catalysis A, General, vol. 599, no. April, p. 117603, 2020. [Online]. Available: https://doi.org/10.1016/j.apcata.2020.117603

[70] T. Zhang, X. Li, Y. Qiu, P. Su, W. Xu, H. Zhong, and H. Zhang, "Multilayered Zn nanosheets as an electrocatalyst for efficient electrochemical reduction of CO_2," *Journal of Catalysis*, vol. 357, pp. 154–162, 2018. [Online]. Available: https://doi.org/10.1016/j.jcat.2017.11.003

[71] T. Yabe, K. Yamada, K. Murakami, K. Toko, K. Ito, T. Higo, S. Ogo, and Y. Sekine, "Role of Electric Field and Surface Protonics on Low-Temperature Catalytic Dry Reforming of Methane," *ACS Sustainable Chemistry and Engineering*, vol. 7, no. 6, pp. 5690–5697, 2019.

[72] R. Vakili, R. Gholami, C. E. Stere, S. Chansai, H. Chen, S. M. Holmes, Y. Jiao, C. Hardacre, and X. Fan, "Plasma-assisted catalytic dry reforming of methane (DRM) over metal-organic frameworks (MOFs)-based catalysts," *Applied Catalysis B: Environmental*, vol. 260, no. September 2019, p. 118195, 2020. [Online]. Available: https://doi.org/10.1016/j.apcatb.2019.118195

[73] Z. Sheng, H. H. Kim, S. Yao, and T. Nozaki, "Plasma-chemical promotion of catalysis for CH_4 dry reforming: Unveiling plasma-enabled reaction mechanisms," *Physical Chemistry Chemical Physics*, vol. 22, no. 34, pp. 19 349–19 358, 2020. [Online]. Available: https://doi.org/10.1039/d0cp03127e

[74] J. V. Turnhout, D. Aceto, A. Travert, P. Bazin, F. Thibault-Starzyk, A. Bogaerts, and F. Azzolina-Jury, "Observation of surface species in plasma-catalytic dry reforming of methane in a novel atmospheric pressure dielectric barrier discharge in situ ir cell," *Catalysis Science and Technology*, vol. 12, pp. 6676–6686, 10 2022.

[75] D.-Y. Kim, A. Saito, K. Sasaki, and T. Nozaki, "In situ infrared absorption probing of plasma catalysis: vibrationally-excited species induced mars–van krevelen type mechanism," *Plasma Sources Science and Technology*, vol. 31, no. 12, p. 124005, Dec. 2022. [Online]. Available: https://doi.org/10.1088/1361-6595/acab28

[76] K. Chang, H. Zhang, M. J. Cheng, and Q. Lu, "Application of Ceria in CO_2 Conversion Catalysis," *ACS Catalysis*, vol. 10, no. 1, pp. 613–631, 2020.

[77] A. Salcedo and B. Irigoyen, "Unraveling the Origin of Ceria Activity in Water-Gas Shift by First-Principles Microkinetic Modeling," *Journal of Physical Chemistry C*, vol. 124, no. 14, pp. 7823–7834, 2020.

[78] C. Schilling and C. Hess, "Elucidating the Role of Support Oxygen in the Water-Gas Shift Reaction over Ceria-Supported Gold Catalysts Using Operando Spectroscopy," *ACS Catalysis*, vol. 9, no. 2, pp. 1159–1171, 2019.

[79] J. Q. Zhong, Z. K. Han, K. Werner, X. Y. Li, Y. Gao, S. Shaikhutdinov, and H. J. Freund, "Water-Assisted Homolytic Dissociation of Propyne on a Reduced Ceria Surface," *Angewandte Chemie - International Edition*, vol. 59, no. 15, pp. 6150–6154, 2020.

[80] A. M. Hernández-Giménez, D. Lozano-Castelló, and A. Bueno-López, "Effect of CO_2, H_2O and SO_2 in the ceria-catalyzed combustion of soot under simulated diesel exhaust conditions," *Applied Catalysis B: Environmental*, vol. 148-149, no. 2, pp. 406–414, 2014.

[81] K. Sakthiraj and B. Karthikeyan, "Synthesis and characterization of cerium oxide nanoparticles using different solvents for electrochemical applications," *Applied Physics A: Materials Science and Processing*, vol. 126, no. 1, pp. 1–10, 2020.

[82] A. S. Morillo-Candas, V. Guerra, and O. Guaitella, "Time Evolution of the Dissociation Fraction in rf CO_2 Plasmas: Impact and Nature of Back-Reaction Mechanisms," *Journal of Physical Chemistry C*, vol. 124, no. 32, pp. 17 459–17 475, 2020.

[83] B. L. Klarenaar, A. S. Morillo-Candas, M. Grofulović, M. C. Van De Sanden, R. Engeln, and O. Guaitella, "Excitation and relaxation of the asymmetric stretch mode of CO_2 in a pulsed glow discharge," *Plasma Sources Science and Technology*, vol. 28, no. 3, 2019.

[84] M. Grofulović, T. Silva, B. L. Klarenaar, A. S. Morillo-Candas, O. Guaitella, R. Engeln, C. D. Pintassilgo, and V. Guerra, "Kinetic study of CO_2 plasmas under non-equilibrium conditions. II. Input of vibrational energy," *Plasma Sources Science and Technology*, vol. 27, no. 11, 2018.

[85] T. Silva, M. Grofulović, B. L. Klarenaar, A. S. Morillo-Candas, O. Guaitella, R. Engeln, C. D. Pintassilgo, and V. Guerra, "Kinetic study of low-temperature CO_2 plasmas under non-equilibrium conditions. I. Relaxation of vibrational energy," *Plasma Sources Science and Technology*, vol. 27, no. 1, 2018.

[86] X. Chen, Z. Sheng, S. Murata, S. Zen, H. H. Kim, and T. Nozaki, "CH_4 dry reforming in fluidized-bed plasma reactor enabling enhanced plasma-catalyst coupling," *Journal of CO_2 Utilization*, vol. 54, no. June, p. 101771, 2021. [Online]. Available: https://doi.org/10.1016/j.jcou.2021.101771

[87] E. Baratte, "An experimental and numerical investigation of the fundamental mechanisms in CO_2-CH_4 plasmas," Ph.D. dissertation, 2023.

[88] Y. Sun, J. Li, P. Chen, B. Wang, J. Wu, M. Fu, L. Chen, and D. Ye, "Reverse water-gas shift in a packed bed DBD reactor: Investigation of metal-support interface towards a better understanding of plasma catalysis," *Applied Catalysis A: General*, vol. 591, no. December 2019, p. 117407, 2020. [Online]. Available: https://doi.org/10.1016/j.apcata.2019.117407

[89] X. Zhu, J. H. Liu, X. S. Li, J. L. Liu, X. Qu, and A. M. Zhu, "Enhanced effect of plasma on catalytic reduction of CO_2 to CO with hydrogen over Au/CeO_2 at low temperature," *Journal of Energy Chemistry*, vol. 26, no. 3, pp. 488–493, 2017. [Online]. Available: http://dx.doi.org/10.1016/j.jechem.2016.11.023

[90] D. Ray and C. Subrahmanyam, "CO_2 decomposition in a packed DBD plasma reactor: Influence of packing materials," *RSC Advances*, vol. 6, no. 45, pp. 39 492–39 499, 2016. [Online]. Available: http://dx.doi.org/10.1039/C5RA27085E

[91] T. Frost, *Quantitative analysis*, 3rd ed. Elsevier Ltd., 2016. [Online]. Available: http://dx.doi.org/10.1016/B978-0-12-803224-4.00263-6

[92] F. Thibault-Starzyk and F. Maugé, "Part One Molecular / Local Spectroscopies," *Characterization of Solid Materials and Heterogeneous Catalysts: From Structure to Surface Reactivity*, pp. 1–48, 2012.

[93] B. L. Klarenaar, R. Engeln, D. C. Van Den Bekerom, M. C. Van De Sanden, A. S. Morillo-Candas, and O. Guaitella, "Time evolution of vibrational temperatures in a CO2 glow discharge measured with infrared absorption spectroscopy," *Plasma Sources Science and Technology*, vol. 26, no. 11, 2017.

[94] I. E. Gordon, L. S. Rothman, C. Hill, R. V. Kochanov, Y. Tan, P. F. Bernath, M. Birk, V. Boudon, A. Campargue, K. V. Chance, B. J. Drouin, J. M. Flaud, R. R. Gamache, J. T. Hodges, D. Jacquemart, V. I. Perevalov, A. Perrin, K. P. Shine, M. A. Smith, J. Tennyson, G. C. Toon, H. Tran,

V. G. Tyuterev, A. Barbe, A. G. Császár, V. M. Devi, T. Furtenbacher, J. J. Harrison, J. M. Hartmann, A. Jolly, T. J. Johnson, T. Karman, I. Kleiner, A. A. Kyuberis, J. Loos, O. M. Lyulin, S. T. Massie, S. N. Mikhailenko, N. Moazzen-Ahmadi, H. S. Müller, O. V. Naumenko, A. V. Nikitin, O. L. Polyansky, M. Rey, M. Rotger, S. W. Sharpe, K. Sung, E. Starikova, S. A. Tashkun, J. V. Auwera, G. Wagner, J. Wilzewski, P. Wcisło, S. Yu, and E. J. Zak, "The HITRAN2016 molecular spectroscopic database," *Journal of Quantitative Spectroscopy and Radiative Transfer*, vol. 203, pp. 3–69, 2017.

[95] A. S. Morillo-Candas, C. Drag, J. P. Booth, T. C. Dias, V. Guerra, and O. Guaitella, "Oxygen atom kinetics in CO_2 plasmas ignited in a DC glow discharge," *Plasma Sources Science and Technology*, vol. 28, no. 7, 2019.

[96] R. L. Fitzgerald, C. L. O'Neal, B. J. Hart, A. Poklis, and D. A. Herold, "Comparison of an ion-trap and a quadrupole mass spectrometer using diazepam as a model compound," *Journal of analytical toxicology*, vol. 21, no. 6, pp. 445–450, 1997.

[97] P. R. Griffiths, *IR spectroscopic data processing*, 3rd ed. Elsevier Ltd., 2016. [Online]. Available: http://dx.doi.org/10.1016/B978-0-12-409547-2.12149-3

[98] A. Filtschew, K. Hofmann, and C. Hess, "Ceria and Its Defect Structure: New Insights from a Combined Spectroscopic Approach," *Journal of Physical Chemistry C*, vol. 120, no. 12, pp. 6694–6703, 2016.

[99] D. Louër, "Powder X-ray diffraction, applications," *Encyclopedia of Spectroscopy and Spectrometry*, pp. 723–731, 2016.

[100] R. Bardestani, G. S. Patience, and S. Kaliaguine, "Experimental methods in chemical engineering: specific surface area and pore size distribution measurements—BET, BJH, and DFT," *Canadian Journal of Chemical Engineering*, vol. 97, no. 11, pp. 2781–2791, 2019.

[101] F. Dumeignil, J. F. Paul, and S. Paul, "Heterogeneous Catalysis with Renewed Attention: Principles, Theories, and Concepts," *Journal of Chemical Education*, vol. 94, no. 6, pp. 675–689, 2017.

[102] M. H. Engelhard, T. C. Droubay, and Y. Du, "X-ray photoelectron spectroscopy applications," *Encyclopedia of Spectroscopy and Spectrometry*, pp. 716–724, 2016.

[103] M. Černák, D. Kováčik, J. Ráhel', P. St'ahel, A. Zahoranová, J. Kubincová, and A Tóth and L' Černáková, "Generation of a high-density highly non- equilibrium air plasma for high-speed large-area flat surface processing," *plasma physics and controlled fusion*, vol. 53, p. 8, 2011.

[104] R. Brandenburg, C. Wilke, and K. Weltmann, "The Role of Acidification for Antimicrobial Activity of Atmospheric Pressure Plasma in Liquids," *Plasma Processes and Polymers*, vol. 7, pp. 250–257, 2010.

[105] K.-D. Weltmann, K. Fricke, M. Stieber, R. Brandenburg, T. V. Woedtke, U. Schnabel, and A. P. Sources, "New Nonthermal Atmospheric-Pressure Plasma Sources for Decontamination of Human Extremities," *IEEE Transactions on Plasma Science*, vol. 40, no. 11, pp. 2963–2969, 2012.

[106] R. Brandenburg, "Dielectric barrier discharges: progress on plasma sources and on the understanding of regimes and single filaments," *Plasma Sources Science and Technology*, vol. 27, no. 7, 2018.

[107] W. Luyben, *Chemical Reactor, Design and Control*, 2007.

[108] A. Anantharaman, R. A. Cocco, and J. W. Chew, "Evaluation of correlations for minimum fluidization velocity (Umf) in gas-solid fluidization," *Powder Technology*, vol. 323, pp. 454–485, 2018.

[109] K. L. Pan, W. C. Chung, and M. B. Chang, "Dry reforming of CH_4 with CO_2 to generate syngas by combined plasma catalysis," *IEEE Transactions on Plasma Science*, vol. 42, no. 12, pp. 3809–3818, 2014.

[110] W. C. Chung and M. B. Chang, "Dry reforming of methane by combined spark discharge with a ferroelectric," *Energy Conversion and Management*, vol. 124, pp. 305–314, 2016. [Online]. Available: http://dx.doi.org/10.1016/j.enconman.2016.07.023

[111] A. M. Ghorbanzadeh, S. Norouzi, and T. Mohammadi, "High energy efficiency in syngas and hydrocarbon production from dissociation of CH_4-CO_2 mixture in a non-equilibrium pulsed plasma," *Journal of Physics D: Applied Physics*, vol. 38, no. 20, pp. 3804–3811, 2005.

[112] Y. Zeng, X. Zhu, D. Mei, B. Ashford, and X. Tu, "Plasma-catalytic dry reforming of methane over γ-Al_2O_3 supported metal catalysts," *Catalysis Today*, vol. 256, no. P1, pp. 80–87, 2015. [Online]. Available: http://dx.doi.org/10.1016/j.cattod.2015.02.007

[113] M. A. Malik and X. Z. Jiang, "The CO_2 reforming of natural gas in a pulsed corona discharge reactor," *Plasma Chemistry and Plasma Processing*, vol. 19, no. 4, pp. 505–512, 1999.

[114] C. Li, K.-i. Maruya, and T. Onishi, "Dioxygen Adsorption on Well-Outgassed and Partially Reduced Cerium Oxide Studied by FT-IR," no. 10, pp. 7683–7687, 1989.

[115] C. Binet, A. Badri, and J. C. Lavalley, "A spectroscopic characterization of the reduction of ceria from electronic transitions of intrinsic point defects," *Journal of Physical Chemistry*, vol. 98, no. 25, pp. 6392–6398, 1994.

[116] Y. Mordekovitz, L. Shelly, B. A. Rosen, and S. Hayun, "Surface properties of Ca, Ti-doped CeO_2 and their influence on the reverse water-gas shift reaction," *Journal of the American Ceramic Society*, vol. 104, no. 5, pp. 2337–2347, 2021.

[117] G. N. Vayssilov, M. Mihaylov, P. S. Petkov, K. I. Hadjiivanov, and K. M. Neyman, "Reassignment of the vibrational spectra of carbonates, formates, and related surface species on ceria: A combined density functional and infrared spectroscopy investigation," *Journal of Physical Chemistry C*, vol. 115, no. 47, pp. 23 435–23 454, 2011.

[118] J. P. Booth, D. Marinov, M. Foucher, O. Guaitella, D. Bresteau, L. Cabaret, and C. Drag, "Gas temperature measurements in oxygen plasmas by high-resolution Two-Photon Absorption Laser-induced Fluorescence," *Journal of Instrumentation*, vol. 10, no. 11, 2015.

[119] J. P. Booth, O. Guaitella, A. Chatterjee, C. Drag, V. Guerra, D. Lopaev, S. Zyryanov, T. Rakhimova, D. Voloshin, and Y. Mankelevich, "Oxygen (3P) atom recombination on a Pyrex surface in an O_2 plasma," *Plasma Sources Science and Technology*, vol. 28, no. 5, p. 55005, 2019. [Online]. Available: http://dx.doi.org/10.1088/1361-6595/ab13e8

[120] C. Li, K. Domen, K. ichi Maruya, and T. Onishi, "Spectroscopic identification of adsorbed species derived from adsorption and decomposition of formic acid, methanol, and formaldehyde on cerium oxide," *Journal of Catalysis*, vol. 125, no. 2, pp. 445–455, 1990.

[121] K. Mudiyanselage, A. E. Baber, Z. Liu, S. D. Senanayake, and D. J. Stacchiola, "Isolation and characterization of formates on CeO_x–cu_yo/cu(1 1 1)," *Catalysis Today*, vol. 240, pp. 190–200, Feb. 2015. [Online]. Available: https://doi.org/10.1016/j.cattod.2014.06.001

[122] S. Rousseau, O. Marie, P. Bazin, M. Daturi, S. Verdier, and V. Harlé, "investigation of methanol oxidation over au/catalysts using operando IR spectroscopy: Determination of the active sites, intermediate/spectator species, and reaction mechanism," vol. 132, no. 31, pp. 10 832–10 841, Jul. 2010. [Online]. Available: https://doi.org/10.1021/ja1028809

[123] P. G. Lustemberg, M. V. Bosco, A. Bonivardi, H. F. Busnengo, and M. V. Ganduglia-Pirovano, "Insights into the nature of formate species in the decomposition and reaction of methanol over cerium oxide surfaces: A combined infrared spectroscopy and density functional theory study," *The Journal of Physical Chemistry C*, vol. 119, no. 37, pp. 21 452–21 464, Sep. 2015. [Online]. Available: https://doi.org/10.1021/acs.jpcc.5b05070

[124] F. Chen, D. Liu, J. Zhang, P. Hu, X.-Q. Gong, and G. Lu, "A DFT+U study of the lattice oxygen reactivity toward direct CO oxidation on the CeO_2 (111) and (110) surfaces," *Physical Chemistry Chemical Physics*, vol. 14, no. 48, pp. 16 573–16 580, 2012.

[125] A. F. Silva, A. S. Morillo-Candás, A. T. del Caz, L. L. Alves, O. Guaitella, and V. Guerra, "A reaction mechanism for vibrationally-cold low-pressure CO_2 plasmas," *Plasma Sources Science and Technology*, vol. 29, no. 12, p. 125020, Dec. 2020. [Online]. Available: https://doi.org/10.1088/1361-6595/abc818

[126] M. Mikhail, P. D. Costa, J. Amouroux, S. Cavadias, M. Tatoulian, S. Ognier, and M. E. Gálvez, "Electrocatalytic behaviour of $CeZrO_x$-supported Ni catalysts in plasma assisted CO_2 methanation," *Catalysis Science & Technology*, vol. 10, no. 14, pp. 4532–4543, 2020. [Online]. Available: https://doi.org/10.1039/d0cy00312c

[127] S. Agarwal, L. Lefferts, and B. L. Mojet, "Ceria Nanocatalysts : Shape Dependent Reactivity and Formation of OH," pp. 1–12, 2012.

[128] S. Agarwal, L. Lefferts, B. L. Mojet, D. A. J. M. Ligthart, E. J. M. Hensen, D. R. G. Mitchell, W. J. Erasmus, B. G. Anderson, E. J. Olivier, J. H. Neethling, and A. K. Datye, "Exposed surfaces on shape-controlled ceria nanoparticles revealed through AC-TEM and water-gas shift reactivity," *ChemSusChem*, vol. 6, no. 10, pp. 1898–1906, Sep. 2013. [Online]. Available: https://doi.org/10.1002/cssc.201300651

[129] A. Badri, C. Binet, and J.-C. Lavalley, "An FTIR study of surface ceria hydroxy groups during a redox process with H_2," *Journal of the Chemical Society, Faraday Transactions*, vol. 92, no. 23, p. 4669, 1996. [Online]. Available: https://doi.org/10.1039/ft9969204669

[130] L. Mino, G. Spoto, and A. M. Ferrari, "CO_2 capture by TiO_2 anatase surfaces: A combined DFT and FTIR study," *Journal of Physical Chemistry C*, vol. 118, no. 43, pp. 25 016–25 026, 2014.

[131] D. C. Sorescu, W. A. Al-Saidi, and K. D. Jordan, "CO_2 adsorption on TiO_2 (101) anatase: A dispersion-corrected density functional theory study," *The Journal of Chemical Physics*, vol. 135, no. 12, p. 124701, Sep. 2011. [Online]. Available: https://doi.org/10.1063/1.3638181

[132] N. D. Parkyns, "The surface properties of metal oxides. part II. an infrared study of the adsorption of carbon dioxide on γ-alumina," *J. Chem. Soc. A*, vol. 0, no. 0, pp. 410–417, 1969. [Online]. Available: https://doi.org/10.1039/j19690000410

[133] C. Li, Y. Sakata, T. Arai, K. Domen, K. ichi Maruya, and T. Onishi, "Adsorption of carbon monoxide and carbon dioxide on cerium oxide studied by Fourier-transform infrared spectroscopy. Part 2.—Formation of formate species on partially reduced CeO_2 at room temperature," *Journal*

of the Chemical Society, Faraday Transactions 1: Physical Chemistry in Condensed Phases, vol. 85, no. 6, p. 1451, 1989. [Online]. Available: https://doi.org/10.1039/f19898501451

[134] S. Agarwal, L. Lefferts, and B. L. Mojet, "Ceria nanocatalysts: Shape dependent reactivity and formation of OH," *ChemCatChem*, vol. 5, no. 2, pp. 479–489, Dec. 2012. [Online]. Available: https://doi.org/10.1002/cctc.201200491

[135] T. Shido and Y. Iwasawa, "Reactant-Promoted Reaction Mechanism for Water-Gas Shift Reaction on Rh-Doped CeO_2," *Journal of Catalysis*, vol. 141, no. 1, pp. 71–81, May 1993. [Online]. Available: https://doi.org/10.1006/jcat.1993.1119

[136] J. Liu, E. Zhan, W. Cai, J. Li, and W. Shen, "Methanol Selective Oxidation to Methyl Formate over ReO_x/CeO_2 Catalysts," *Catalysis Letters*, vol. 120, no. 3-4, pp. 274–280, Oct. 2007. [Online]. Available: https://doi.org/10.1007/s10562-007-9280-9

[137] L. Luo, J. D. LaCoste, N. G. Khamidullina, E. Fox, D. D. Gang, R. Hernandez, and H. Yan, "Investigate interactions of water with mesoporous ceria using in situ VT-DRIFTS," *Surface Science*, vol. 691, p. 121486, Jan. 2020. [Online]. Available: https://doi.org/10.1016/j.susc.2019.121486

[138] C. Binet, M. Daturi, and J.-C. Lavalley, "IR study of polycrystalline ceria properties in oxidised and reduced states," *Catalysis Today*, vol. 50, no. 2, pp. 207–225, Apr. 1999. [Online]. Available: https://doi.org/10.1016/s0920-5861(98)00504-5

[139] M. M. Hussain, M. M. Rahman, and A. M. Asiri, "Efficient 2-nitrophenol chemical sensor development based on Ce_2O_3 nanoparticles decorated cnt nanocomposites for environmental safety," *PLoS ONE*, vol. 11, no. 12, pp. 1–17, 2016.

[140] M. H. Pham, V. Goujard, J. M. Tatibouët, and C. Batiot-Dupeyrat, "Activation of methane and carbon dioxide in a dielectric-barrier discharge-plasma reactor to produce hydrocarbons - Influence of La_2O_3/γ-Al_2O_3 catalyst," *Catalysis Today*, vol. 171, no. 1, pp. 67–71, 2011. [Online]. Available: http://dx.doi.org/10.1016/j.cattod.2011.03.015

[141] N. R. Pinhão, A. Janeco, and J. B. Branco, "Influence of helium on the conversion of methane and carbon dioxide in a dielectric barrier discharge," *Plasma Chemistry and Plasma Processing*, vol. 31, no. 3, pp. 427–439, 2011.

[142] L. M. Zhou, B. Xue, U. Kogelschatz, and B. Eliasson, "Nonequilibrium plasma reforming of greenhouse gases to synthesis gas," *Energy and Fuels*, vol. 12, no. 6, pp. 1191–1199, 1998.

[143] D. Hu, C. Liu, L. Li, K. L. Lv, Y. H. Zhang, and J. L. Li, "Carbon dioxide reforming of methane over nickel catalysts supported on TiO_2 (001) nanosheets," *International Journal of Hydrogen Energy*, vol. 3, pp. 21 345–21 354, 2018.

[144] A. V. Volynets, D. V. Lopaev, T. V. Rakhimova, A. A. Chukalovsky, Y. A. Mankelevich, N. A. Popov, A. I. Zotovich, and A. T. Rakhimov, "N_2 dissociation and kinetics of N(4S) atoms in nitrogen DC glow discharge," *Journal of Physics D: Applied Physics*, vol. 51, p. 364002, 2018.

[145] I. N. Brovikova and E. G. Galiaskarov, "Kinetic Characteristics of Production and Loss of Nitrogen Atoms in N_2 Plasma," *High Temperature*, vol. 39, no. 6, pp. 809–814, 2001. [Online]. Available: https://doi.org/10.1023/a:1013174518832

[146] C. D. Pintassilgo and V. Guerra, "Modelling of the temporal evolution of the gas temperature in N_2 discharges," *Plasma Sources Science and Technology*, vol. 26, no. 5, p. 055001, Mar. 2017. [Online]. Available: https://doi.org/10.1088/1361-6595/aa5db2

[147] M. W. Millard, P. P. Yaney, B. N. Ganguly, and C. A. DeJoseph, "Diode laser absorption measurements of metastable helium in glow discharges," *Plasma Sources Science and Technology*, vol. 7, no. 3, pp. 389–394, Aug. 1998. [Online]. Available: https://doi.org/10.1088/0963-0252/7/3/017

[148] N. Dyatko, Y. Ionikh, and A. Napartovich, "Influence of nitrogen admixture on plasma characteristics in a dc argon glow discharge and in afterglow," *Atoms*, vol. 7, no. 1, p. 13, Jan. 2019. [Online]. Available: https://doi.org/10.3390/atoms7010013

[149] C. Ferreira, J. Loureiro, and A. Ricard, "Populations in the metastable and the resonance levels of argon and stepwise ionization effects in a low-pressure argon positive column," *Journal of applied physics*, vol. 57, no. 1, pp. 82–90, 1985.

[150] A. P. Yalin, Y. Z. Ionikh, and R. B. Miles, "Gas temperature measurements in weakly ionized glow discharges with filtered rayleigh scattering," *Appl. Opt.*, vol. 41, no. 18, pp. 3753–3762, Jun 2002. [Online]. Available: https://opg.optica.org/ao/abstract.cfm?URI=ao-41-18-3753

[151] A. I. Pushkarev, A. M. Zhu, X. S. Li, and R. V. Sazonov, "Methane conversion in low-temperature plasma," *High Energy Chemistry*, vol. 43, pp. 156–162, 5 2009.

[152] G. Scarduelli, G. Guella, I. Mancini, G. Dilecce, S. D. Benedictis, and P. Tosi, "Methane oligomerization in a dielectric barrier discharge at atmospheric pressure," *Plasma Processes and Polymers*, vol. 6, pp. 27–33, 1 2009.

[153] C. Binet, A. Badri, M. Boutonnet-Kizling, and J. C. Lavalley, "FTIR study of carbon monoxide adsorption on ceria: CO_2 $^{2-}$ carbonite dianion adsorbed species," *Journal of the Chemical Society, Faraday Transactions*, vol. 90, no. 7, pp. 1023–1028, 1994.

[154] T. Tabakova, F. Boccuzzi, M. Manzoli, and D. Andreeva, "FTIR study of low-temperature water-gas shift reaction on gold/ceria catalyst," *Applied Catalysis A: General*, vol. 252, pp. 385–397, 10 2003.

[155] S. Agarwal, X. Zhu, E. J. Hensen, B. L. Mojet, and L. Lefferts, "Surface-Dependence of Defect Chemistry of Nanostructured Ceria," *Journal of Physical Chemistry C*, vol. 119, no. 22, pp. 12 423–12 433, 2015.

[156] B. Kozanoglu, J. W. Chanes, D. G. Cuautle, and J. S. Jean, "Hydrodynamics of large particle fluidization in reduced pressure operations: an experimental study," *Powder technology*, vol. 125, pp. 55–60, 2002.

[157] T. Silva, M. Grofulović, L. Terraz, C. D. Pintassilgo, and V. Guerra, "Dynamics of Gas Heating in the Afterglow of Pulsed CO_2 and CO_2–N_2 Glow Discharges at Low Pressure," *Plasma Chemistry and Plasma Processing*, vol. 40, no. 3, pp. 713–725, 2020. [Online]. Available: https://doi.org/10.1007/s11090-020-10061-7

[158] A. Tejero-Del-Caz, V. Guerra, D. Gonçalves, M. L. D. Silva, L. Marques, N. Pinhão, C. D. Pintassilgo, and L. L. Alves, "The LisbOn KInetics Boltzmann solver," *Plasma Sources Science and Technology*, vol. 28, 2019.

[159] S. Kelly and J. A. Sullivan, "CO_2 Decomposition in CO_2 and CO_2/H_2 Spark-like Plasma Discharges at Atmospheric Pressure," *ChemSusChem*, vol. 12, pp. 3785–3791, 2019.

[160] W. Ding, M. Xia, C. Shen, Y. Wang, Z. Zhang, X. Tu, and C. J. Liu, "Enhanced CO_2 conversion by frosted dielectric surface with ZrO_2 coating in a dielectric barrier discharge reactor," *Journal of CO_2 Utilization*, vol. 61, no. 2, p. 102045, 2022. [Online]. Available: https://doi.org/10.1016/j.jcou.2022.102045

[161] N. Lu, C. Zhang, K. Shang, N. Jiang, J. Li, and Y. Wu, "Dielectric barrier discharge plasma assisted CO_2 conversion: Understanding the effects of reactor design and operating parameters," *Journal of Physics D: Applied Physics*, vol. 52, no. 22, 2019.

[162] A. R. Abrahamsen and D. Geldart, "Behaviour of gas-fluidized beds of fine powders part I. Homogeneous expansion," *Powder Technology*, vol. 26, no. 1, pp. 35–46, 1980.

[163] D. Mei, G. Duan, J. Fu, S. Liu, R. Zhou, R. Zhou, Z. Fang, P. J. Cullen, and K. K. Ostrikov, "CO_2 reforming of CH_4 in single and double dielectric barrier discharge reactors: Comparison of discharge characteristics and product distribution," *Journal of CO2 Utilization*, vol. 53, no. August, p. 101703, 2021. [Online]. Available: https://doi.org/10.1016/j.jcou.2021.101703

[164] X. G. Zheng, S. Y. Tan, L. C. Dong, S. B. Li, H. M. Chen, and S. A. Wei, "Experimental and kinetic investigation of the plasma catalytic dry reforming of methane over perovskite $LaNiO_3$ nanoparticles," *Fuel Processing Technology*, vol. 137, pp. 250–258, 2015. [Online]. Available: http://dx.doi.org/10.1016/j.fuproc.2015.02.003

[165] D. Ray, P. M. K. Reddy, and C. Subrahmanyam, "Ni-Mn/γ-Al_2O_3 assisted plasma dry reforming of methane," *Catalysis Today*, vol. 309, no. March 2017, pp. 212–218, 2018. [Online]. Available: https://doi.org/10.1016/j.cattod.2017.07.003

[166] L. Brune, A. Ozkan, E. Genty, T. Visart De Bocarmé, and F. Reniers, "Dry reforming of methane via plasma-catalysis: Influence of the catalyst nature supported on alumina in a packed-bed DBD configuration," *Journal of Physics D: Applied Physics*, vol. 51, no. 23, 2018.

[167] A. H. Khoja, M. Tahir, and N. A. S. Amin, "Dry reforming of methane using different dielectric materials and DBD plasma reactor configurations," *Energy Conversion and Management*, vol. 144, pp. 262–274, 2017. [Online]. Available: http://dx.doi.org/10.1016/j.enconman.2017.04.057

[168] T. Garcia, B. Solsona, and S. H. Taylor, "Nano-crystalline ceria catalysts for the abatement of polycyclic aromatic hydrocarbons," *Catalysis Letters*, vol. 105, no. 3-4, pp. 183–189, 2005.

[169] A. Aranda, B. Puértolas, B. Solsona, S. Agouram, R. Murillo, A. M. Mastral, S. H. Taylor, and T. Garcia, "Total oxidation of naphthalene using mesoporous CeO_2 catalysts synthesized by nanocasting from two dimensional SBA-15 and three dimensional KIT-6 and MCM-48 silica templates," *Catalysis Letters*, vol. 134, no. 1-2, pp. 110–117, 2010.

[170] B. Puertolas, B. Solsona, S. Agouram, R. Murillo, A. M. Mastral, A. Aranda, S. H. Taylor, and T. Garcia, "The catalytic performance of mesoporous cerium oxides prepared through a nanocasting route for the total oxidation of naphthalene," *Applied Catalysis B: Environmental*, vol. 93, no. 3-4, pp. 395–405, 2010.

[171] Z. Cui, J. Gan, J. Fan, Y. Xue, and R. Zhang, "Size-Dependent Surface Basicity of Nano-CeO_2 and Desorption Kinetics of CO_2 on Its Surface," *Industrial and Engineering Chemistry Research*, vol. 57, no. 32, pp. 10 977–10 984, 2018.

[172] J. Sun, D. Yamaguchi, L. Tang, S. Periasamy, H. Ma, J. N. Hart, and K. Chiang, "Enhancement of oxygen exchanging capability by loading a small amount of ruthenium over ceria-zirconia on dry reforming of methane," *Advanced Powder Technology*, vol. 33, no. 2, p. 103407, 2022. [Online]. Available: https://doi.org/10.1016/j.apt.2021.103407

[173] M. Nizio, A. Albarazi, S. Cavadias, J. Amouroux, M. E. Galvez, and P. Da Costa, "Hybrid plasma-catalytic methanation of CO_2 at low temperature over ceria zirconia supported Ni catalysts," *International Journal of Hydrogen Energy*, vol. 41, no. 27, pp. 11 584–11 592, 2016. [Online]. Available: http://dx.doi.org/10.1016/j.ijhydene.2016.02.020

[174] P. A. Aldana, F. Ocampo, K. Kobl, B. Louis, F. Thibault-Starzyk, M. Daturi, P. Bazin, S. Thomas, and A. C. Roger, "Catalytic CO_2 valorization into CH_4 on Ni-based ceria-zirconia. Reaction mechanism by operando IR spectroscopy," *Catalysis Today*, vol. 215, pp. 201–207, 2013. [Online]. Available: http://dx.doi.org/10.1016/j.cattod.2013.02.019

[175] M. H. Yao, R. J. Baird, F. W. Kunz, and T. E. Hoost, "An XRD and TEM investigation of the structure of alumina-supported ceria-zirconia," *Journal of Catalysis*, vol. 166, no. 1, pp. 67–74, 1997.

[176] M. M. Khan, R. Siwach, S. Kumar, M. Ahamed, and J. Ahmed, "Frequency and temperature dependence of dielectric permittivity/electric modulus, and efficient photocatalytic action of fe-doped CeO_2 NPs," *Journal of Alloys and Compounds*, vol. 856, p. 158127, Mar. 2021. [Online]. Available: https://doi.org/10.1016/j.jallcom.2020.158127

[177] T. Yamamoto, H. Momida, T. Hamada, T. Uda, and T. Ohno, "First-principles study of dielectric properties of cerium oxide," *Thin Solid Films*, vol. 486, no. 1-2, pp. 136–140, Aug. 2005. [Online]. Available: https://doi.org/10.1016/j.tsf.2004.11.240

[178] O. Guaitella, F. Thevenet, C. Guillard, and A. Rousseau, "Dynamic of the plasma current amplitude in a barrier discharge: Influence of photocatalytic material," *Journal of Physics D: Applied Physics*, vol. 39, no. 14, pp. 2964–2972, 2006.

[179] X. Tu, H. J. Gallon, M. V. Twigg, P. A. Gorry, and J. C. Whitehead, "Dry reforming of methane over a Ni/Al_2O_3 catalyst in a coaxial dielectric barrier discharge reactor," *Journal of Physics D: Applied Physics*, vol. 44, no. 27, 2011.

[180] D. Ray, P. Chawdhury, K. V. Bhargavi, S. Thatikonda, N. Lingaiah, and C. Subrahmanyam, "Ni and Cu oxide supported γ-Al_2O_3 packed DBD plasma reactor for CO_2 activation," *Journal of CO_2 Utilization*, vol. 44, no. August 2020, 2021.

[181] T. Butterworth, R. Elder, and R. Allen, "Effects of particle size on CO_2 reduction and discharge characteristics in a packed bed plasma reactor," *Chemical Engineering Journal*, vol. 293, pp. 55–67, 2016. [Online]. Available: http://dx.doi.org/10.1016/j.cej.2016.02.047

[182] K. W. Engeling, J. Kruszelnicki, M. J. Kushner, and J. E. Foster, "Time-resolved evolution of micro-discharges, surface ionization waves and plasma propagation in a two-dimensional packed bed reactor," *Plasma Sources Science and Technology*, vol. 27, no. 8, p. 085002, Aug. 2018. [Online]. Available: https://doi.org/10.1088/1361-6595/aad2c5

[183] Z. Falkenstein and J. J. Coogan, "Microdischarge behaviour in the silent discharge of nitrogen - oxygen and water - air mixtures," *Journal of Physics D: Applied Physics*, vol. 30, no. 5, pp. 817–825, Mar. 1997. [Online]. Available: https://doi.org/10.1088/0022-3727/30/5/015

[184] S. Loridant, "Raman spectroscopy as a powerful tool to characterize ceria-based catalysts," *Catalysis Today*, no. April 2020, pp. 98–111. [Online]. Available: https://doi.org/10.1016/j.cattod.2020.03.044

ECOLE
DOCTORALE

Titre : Étude fondamentale des interactions plasma-surface catalytique pour la conversion du CO_2 et application des réacteurs à lit fluidisé

Mots clés : Plasma, catalyse, dioxide de carbone, lit fluidisé

Résumé : L'augmentation considérable des émissions de gaz à effet de serre tels que le CO_2 a causé un accroissement de la température moyenne mondiale responsable d'une crise environnementale. Une stratégie pour limiter ce problème est le recyclage du CO_2, en synthétisant des molécules à haute densité d'énergie de manière durable en fermant ainsi le cycle du carbone. Le CO_2 est une molécule qui nécessite une énorme quantité d'énergie pour être dissociée. Les plasmas froids représentent une technologie prometteuse pour activer cette dissociation à moindre coût énergétique. Il s'agit de gaz partiellement ionisés où les molécules neutres, les ions et les électrons sont hors équilibre thermodynamique et présentent une forte réactivité chimique, permettant de réaliser un grand nombre de réactions chimiques. Cependant, le plasma seul ne suffit pas, car il est peu sélectif, et l'association avec un catalyseur est nécessaire pour améliorer la conversion. Les processus fondamentaux qui se produisent sur une surface catalytique sous exposition au plasma doivent être élucidés en détail. De plus, les réacteurs à plasma à lit fluidisé ont été étudié comme technologie innovante. Ces résultats permettent de décrire l'interaction plasma-surface catalytique et l'effet des catalyseurs sur les propriétés des plasmas permettant une optimisation future des réacteurs à plasma à lit fluidisé qui s'avèrent très prometteurs.

Title : Fundamental study of plasma-catalytic surface interactions for CO_2 conversion and application of fluidized bed reactors

Keywords : Plasma, catalysis, carbon dioxide, fluidized bed

Abstract : The dramatic increase in emissions of greenhouse gases such as CO_2 has caused a rise in the global temperature responsible for an environmental crisis. One strategy is the recycling of CO_2, building molecules with high energy density in a sustainable way thus closing the carbon cycle. CO_2 is a molecule that requires an enormous amount of energy to break down. Cold plasmas represent a promising technology to activate this dissociation at a lower energy cost. These are partially ionized gases where neutral molecules, ions and electrons are out of thermodynamic equilibrium and exhibit high chemical reactivity, carrying out a large number of chemical reactions. However, the plasma alone is not enough, because it is not very selective, but the coupling with a catalyst is necessary to improve the conversion. The fundamental processes that occur on a catalytic surface under plasma exposure need to be elucidated in detail. In addition, fluidized bed plasma reactors have been studied as an innovative technology. These results help to describe the plasma-catalytic surface interaction and the effect of catalysts on the properties of plasmas allowing future optimization of fluidized bed plasma reactors which are proving very promising.

Institut Polytechnique de Paris
91120 Palaiseau, France